INELASTIC LIGHT SCATTERING IN LOW DIMENSIONAL SEMICONDUCTORS

thesis by

Morag Watt

Submitted for the degree of Doctor of Philosophy to the Electronics and Electrical Engineering Department of Glasgow University

December 1988

To my family

Acknowledgements

Now I can allow a little more emotion, a little less analysis and thank the many people who have contributed to this thesis.

As ever, my first thoughts are for my family. They have given me support and encouragement throughout my academic career and have strengthened me by their confidence in my ability. Without them, I might never have entered university, much less remained to pursue research. I have chosen to dedicate this work to them as a small expression of my feelings and I take this opportunity of thanking them.

At this point, I would like to mention Michael Haseler, who has stalwartly endured the sometimes anti-social demands of this work. I very much appreciate your support, Mike.

This work was begun in the Physics Department of St Andrews University and when I left there after two years, I left behind many friends. Nevertheless, the move to Glasgow University's Electronics and Electrical Engineering Department proved both a benefit and a stimulant and new friendships were not long in forming. I should like to extend my thanks to all who gave me their support both in St Andrews and in Glasgow. In particular, Hazel Arnot and Rebecca Cheung, who collaborated in the work of chapters 7 and 6, respectively, and who staunchly supported my experimental endeavours.

I am deeply grateful to three colleagues in Edinburgh for giving me both their time and help: Peter Hatton and Hugh Vass who helped me so greatly with the Raman scattering experiments and Tom Ryan who was involved in the x-ray diffraction experiments.

Whenever I remember the time before Doug Irons joined our group, I wonder how on earth we coped with the day-to-day disasters of running the lab. Certainly, I am amazed that there was any time for experimentation. I appreciate

your help, Doug, all the more for lacking it during the first two and a half years of this work.

Naturally, no acknowledgement would be complete without a tribute to one's supervisor. Hindsight has shown that I made a wise decision when I chose to do my PhD with Dr Sotomayor Torres; I never doubted that it would be the right choice. I greatly appreciate your help and encouragement, Clivia, and only wish that I had half your apparently– endless energy and enthusiasm. In particular, thank you for the time you have given me during the preparation of this thesis. I hope that you feel proud of the finished result.

TABLE OF CONTENTS

Appendices

List of Figures

Chapter 1

Chapter 2

Chapter 3

Chapter 4

Chapter 5

Chapter 6

Chapter 7

Chapter 8

List of Tables

List of Publications Arising from this Work

Chapter 5

M Watt, C M Sotomayor Torres, P D Hatton, H Vass, P A Claxton and J S Roberts; "Raman Scattering from GaInAs–InP Quantum Well Structures", Superlatt Microstr 3, 75, 1987

M Watt, C M Sotomayor Torres, P D Hatton, H Vass, P A Claxton and J S Roberts; "Raman Scattering in MBE GaInAs–InP Quantum Wells", J Physique Colloque 48, C5–483, 1987

Chapters 6 and 7

M Watt, C M Sotomayor Torres, R Cheung, C D W Wilkinson, H E G Arnot and S P Beaumont; "Raman Scattering Investigations of the Damage Caused by Reactive–Ion–Etching of GaAs", Superlatt Microstr 4, 243, 1988

M Watt, C M Sotomayor Torres, R Cheung, C D W Wilkinson, H E G Arnot and S P Beaumont; "Raman Scattering of Reactive–Ion–Etched GaAs", J Mod Opt 35, 365, 1988

Chapter 8

T W Ryan, P D Hatton, S Bates, M Watt, C M Sotomayor Torres, P A Claxton and J S Roberts; "X–Ray Scattering from a Single Quantum Well Heterostructure", Semicond Sci Technol 2, 241, 1987

Summary

Raman scattering is a powerful technique with which to study the lattice vibrations of semiconductors. Investigations of the phonons of GaInAs–InP heterostructures have shown that although the phonons in GaInAs quantum wells resembled those of bulk GaInAs, they were screened by free carriers. Raman scattering and photoluminescence techniques were employed to estimate the plasma density at which plasmon–phonon coupling became significant. Triple crystal x–ray diffraction measurements complemented the Raman scattering data and provided information on the GaInAs alloy composition and state of strain. It was found that although nominally lattice–matched to the underlying InP, the epitaxially–grown layers were tetragonally distorted in the direction of growth.

Assessment of sample damage produced by reactive–ion–etching (RIE) was undertaken as a prerequisite to the study of phonons in fabricated nanostructures. Structural damage to the crystal showed up as a relaxation of the crystalline selection rules allowing the observation of a symmetry–forbidden phonon. The intensity of this phonon correlated well with depth profiling of the damage. Optimised RIE conditions were found to produce negligible crystalline damage. The study of GaAs cylinders (with diameters of less than 100 nanometers) revealed an additional feature in the optical phonon region of their Raman spectra. This feature was identified as a surface phonon of the quantum cylinders. The experimentally–observed frequencies of the surface phonon peaks showed good agreement with calculated frequencies based on vibrations in small, geometrically–regular crystals.

The main contribution of this work is the study of the surface phonons of the GaAs quantum cylinders. This is the first time that surface phonons have been observed in small fabricated samples: all previous work has involved specially–prepared crystalline powders or else comparatively large slab geometries. The conclusion that can be drawn from this work is that the cylinders are not only well–defined (as observed from the SEM micrographs) but they are also crystalline. The implication is that such structures can now be fabricated at a sufficiently high level to allow progress in prototype devices such as the quantum dot laser.

CHAPTER 1

INTRODUCTION AND THEORY

1.1 Introduction

The semiconductor is a very versatile material. By introducing into it a variety of dopant atoms, it can be made to sustain a conductivity ranging from insulating to metallic. This adaptability has paved the way for the rapid progress from the invention of the transistor to the very large scale integrated circuitry that is commonplace today.

The backbone of the industry has been, and still is, Silicon. Nevertheless, in specialised areas, III– V semiconductors, GaAs, GaP, InP, AlGaAs and the like, are now competing for a share of the market. III– V semiconductors have two advantages over Silicon and one disadvantage. The favourable factors are that III– Vs tend to be direct– gap semiconductors (unlike Silicon which is indirect– gap) and that they have higher carrier mobilities which enables faster device operation. The disadvantage is that they are more expensive to produce. Given this disadvantage, the potential for III– V semiconductor devices lies in the regions where Silicon cannot compete. This is primarily in optoelectronic applications where most of the research effort is concentrated. A parallel programme of research into the fundamental behaviour of these materials has benefitted from this commercial impetus

particularly with regard to improved material quality.

Over the past decade, low dimensional semiconductor structures have proved to be a fertile ground for study. Electronic confinement of the order of a few atomic spacings has allowed research into the behaviour of two dimensionally–confined electrons and holes. Confinement of the lattice vibrational energies has also been observed and a whole new means of studying semiconductor phonons is now available.

The new periodicity of a superlattice reduces the Brillouin zone and allows light scattering experiments to probe phonons which otherwise have wavevectors inaccessibly far beyond the reach of the photon light line. This produces the first experimental comparison with neutron scattering data which, until now, has been the sole means of accessing these high wavevector phonons.

Inelastic light scattering is a term applied to a number of specific techniques. Raman scattering probes energies in the 1–100meV range and is the experimental technique used in this work. In any inelastic light scattering experiment, energy is exchanged between the incident photon and an excitation within the sample. Usually, the scattered light contains a range of different energies. Studying the energy spectrum of this scattered light allows information to be gleaned about the sample excitation involved in the scattering process.

In this thesis, new experimental results are reported on the phonons of GaInAs–InP heterostructures, Raman scattering assessment of Reactive–Ion–Etch (RIE) damage to the crystalline structure of GaAs and the phonon modes associated with very small structures of GaAs.

The work on GaInAs–InP heterostructures, discussed in chapter 5, presents information regarding the nature of the phonon modes of GaInAs when confined to two dimensions. Well–defined phonons at the bulk frequencies were observed in layers of GaInAs as thin as 25Å. The LO phonons were observed to be quenched in the layers and this was attributed to screening by a photoexcited electron–hole

plasma.

The work on RIE damage to GaAs is discussed in chapter 6. This work had the objective of assessing the extent of the damage in both a qualitative and a quantitative manner using Raman scattering. The results obtained are preliminary and initial conclusions suggest that little or no damage to the crystalline structure occurs as a result of the RIE process when the process is fully optimised.

An additional feature was observed in the Raman spectrum of very small GaAs structures and this is discussed in chapter 7. Both experimental and theoretical work support the identification of this feature as a surface phonon mode. It is hoped that further work in the near future will provide conclusive identification of the feature.

Chapter 8 provides an account of triple crystal x-ray work done in collaboration with colleagues at Edinburgh University. Tetragonal distortion of the lattice was observed in the GaInAs-InP samples used for the Raman scattering study presented in chapter 5. This work provided valuable characterisation of the samples which could not have been achieved by other means.

The three theory chapters, 1, 2 and 3, provide the neccessary background to the experimental work presented. The experimental arrangement is described in chapter 4 and conclusions to the work are presented in chapter 9. The rest of this chapter introduces some basic concepts in Raman scattering theory.

1.2 Properties of Long Wavelength Lattice Vibrations

In the simple one dimensional approximation, a crystal can be regarded as a linear chain of atoms. In this representation, a lattice vibration corresponds to harmonic oscillator vibrations of each of the atoms. This problem can be solved in terms of nearest neighbour force constants to yield the frequency dependence on wavevector, known as the dispersion relation, which is plotted in figure 1.1(a). If this picture is extended such that there are two atoms, of differing masses, per unit cell then a dispersion curve involving two branches exists. This is shown in figure 1.1(b) where one of the branches is labelled optical and the other acoustical. In general, if there are p atoms in the unit cell, there will be 3p branches to the dispersion relation: 3 acoustical and 3p−3 optical branches. Each branch supports N values of $\mathbf{q}$ where N is the number of primitive cells in the crystal and $\mathbf{q}$ is the wavevector of the vibration.

The energy of a lattice vibration is quantised and the quantum of energy is called the phonon. Thus the energy, E, of a vibration with frequency ω is given by:

$$E = (n + 1/2)\hbar\omega \qquad (1.1)$$

when the mode is occupied by n phonons. It is customary to call both the lattice vibrations and the quantised energy units phonons where the meaning is clear from the context. This practice is adopted here.

Calculations of the dispersion curves for real crystals must involve all three dimensions in order to incorporate the crystal symmetry and the differing lattice constants in each direction. An example of the phonon dispersion of GaAs is shown in figure 6.6(b). Here it can be seen that the acoustical and optical branches have each split into longitudinal and transverse components. This split is discussed in

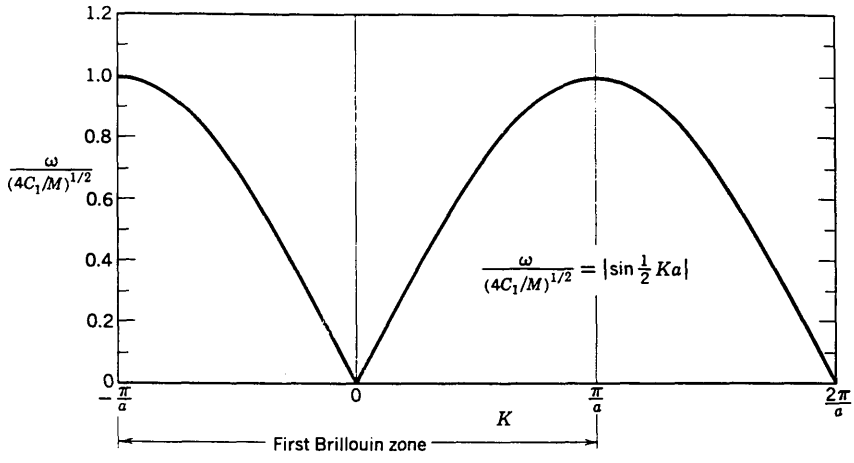

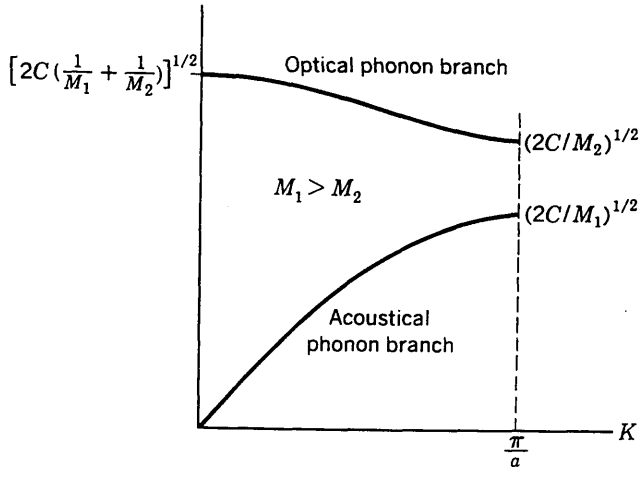

Figure 1.1 (a) Plot of ω versus K, for the 1D linear chain with one atom per unit cell. [after Kittel, 1976]

(b) Plot of ω versus K, for the 1D linear chain with two atoms per unit cell. [after Kittel, 1976]

K here is the same as q in the text.

section 2.2.

It is useful at this stage to compare the phonon wavevectors with the typical photon wavevectors involved in a light scattering experiment. The phonon extends throughout the Brillouin zone and the Brillouin zone boundary is given by π/a where a is the lattice constant. Thus for GaAs, where a = 5.653Å, $\pi/a = 5.6 \times 10^7$ cm^{-1}. Typical light scattering experiments are carried out in the visible region of the spectrum using available laser sources, e.g. Argon ion 4880Å or Krypton ion 6741Å lines. The photon wavevectors, given by $2\pi n/\lambda$, are equal to 5.6×10^5 cm^{-1} and 3.4×10^5 cm^{-1}, respectively, for these wavelengths in GaAs [values for refractive index, n, at each wavelength were taken from Aspnes and Studna, 1983]. As these values are two orders of magnitude smaller than the boundary of the Brillouin zone, it is clear that light scattering experiments which conserve momentum can only probe excitations close to the centre of the Brillouin zone, i.e. at around q = 0.

1.3 First Order Raman Scattering Theory

1.3.1 Historical Introduction

Brillouin [1914] made the first inroads into understanding the frequency spectrum of inelastically–scattered light. He calculated the spectrum due to the density fluctuations associated with sound waves and predicted a doublet split symmetrically around the frequency of the exciting light with an energy shift of less than 1 cm^{-1}. The Brillouin doublets were first observed experimentally by Gross [1930] who also observed an unshifted component of the incident light in the scattered spectrum. This unshifted component is the elastically–scattered light now referred to as Rayleigh scattering.

In parallel with the work on Brillouin scattering (as it is now known), Smekal [1923] predicted that a system with two quantised energy levels would exhibit sidebands in its scattered spectrum. The sidebands were subsequently observed by Raman and Krishnan [1928] in benzene where it was found that some of the spectral shifts corresponded exactly to some of the infra–red vibrational absorption energies. Inelastic light scattering in this energy regime (10 – 1000 cm^{-1}) is now called Raman scattering. It arises as a result of interaction of incident light with modulations in both space and time of the susceptibility of a medium via the interaction:

$$\mathbf{P} = \chi(\omega,\mathbf{k})\mathbf{E}$$

where **P** is the induced dipole moment, **E** is the electric field vector of the incident light and χ is the susceptibility tensor. This modulation can result from vibrations or other excitations such as excitons or plasmons. Early Raman scattering experiments

were done using arc lamp sources but the popularity of the technique declined in favour of infra-red spectroscopy due to the weak scattering involved. Revitalization came with the invention of the laser and its wide-spread availability as an intense monochromatic source of exciting light. Raman scattering is now a widely used investigative technique.

1.3.2 Scattering Cross Section

The basic concept of Raman scattering is simple. An incident photon, of frequency ω_i and wavevector $\mathbf{k}_i$, inelastically scattered by a medium, will either gain or lose energy. The spectral component which has lost energy to the medium is called the Stokes component, denoted by ω_s, and the spectral component that has gained energy from the medium is called the anti-Stokes component and is denoted by ω_{as}. Conservation of energy and wavevector lead to the first order expressions:

$$\omega = \omega_i - \omega_s \qquad \text{and} \qquad \omega = \omega_{as} - \omega_i \tag{1.2a}$$

where $\hbar\omega$ is the gain or loss of energy in the sample, together with

$$k_i = k_s + q \tag{1.2b}$$

where $\mathbf{q}$ is the wavevector of the excitation and $\mathbf{k}_s$ is the scattered photon wavevector. The intensity of the scattered light for any given energy shift $\hbar\omega$ depends on the quantised excitation energies of the scattering medium. It is only when $\hbar\omega$ equals some naturally-occuring excitation of the medium that significant scattering occurs. Thus measurement of the energy shifts $\hbar\omega_i - \hbar\omega_s$ or $\hbar\omega_{as} - \hbar\omega_i$ gives the energy of the excitation. The intensity ratio of the Stokes to

anti– Stokes components for phonon scattering is given by Hayes and Loudon [1978] as:

$$[n(\omega)+1] \;/\; n(\omega) \tag{1.3}$$

where

$$n(\omega) = \frac{1}{\exp(\hbar\,\omega/k_B T) - 1} \tag{1.4}$$

and is the Bose– Einstein distribution with k_B = Boltzmann constant and T = lattice temperature. The Bose– Einstein distribution can be used to describe phonons as they are bosons with zero spin.

The scattering cross section can be defined in three distinct ways [Hayes and Loudon, 1978].

$$\text{Spectral differential cross section} \equiv \frac{d^2\sigma}{d\Omega d\omega_s} \tag{1.5}$$

$$\text{Differential cross section} \equiv \frac{d\sigma}{d\Omega} = \int d\omega_s \frac{d^2\sigma}{d\Omega d\omega_s} \tag{1.6}$$

$$\text{Cross section} \equiv \sigma = \int d\Omega \frac{d\sigma}{d\Omega} \tag{1.7}$$

where $d\Omega$ is the solid angle element and the scattered frequency lies between ω_s and $\omega_s + d\omega_s$.

The spectral differential cross section contains the most information and is the rate of removal of energy from the incident beam as a result of scattering in volume v divided by the product $d\Omega d\omega_s$ (see figure 1.2 for definitions). It has the units of area/frequency. The differential cross section is the integral of the spectral

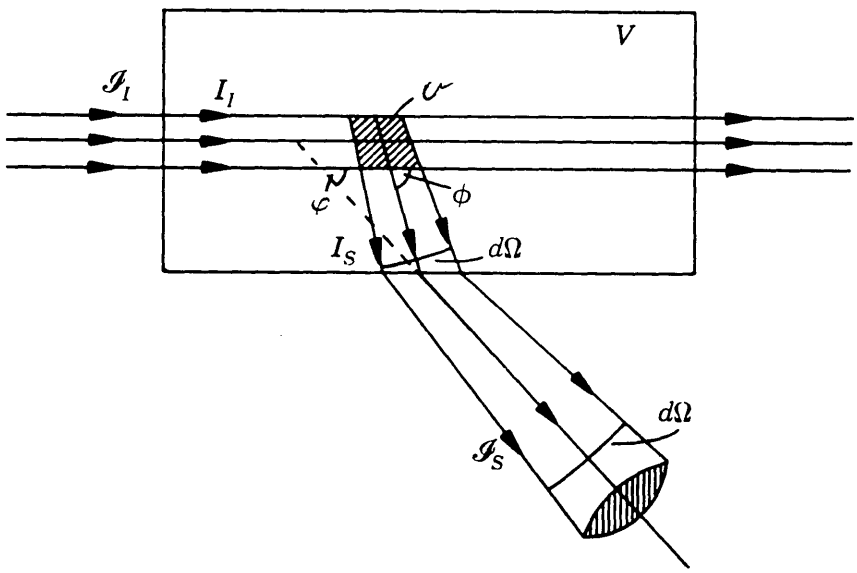

Figure 1.2 Schematic representation of the geometry of the scattering experiment which defines the variables used in equations 1.5 to 1.7. [after Hayes and Loudon, 1978]

differential cross section over the required frequency range. This range is often taken to be a single peak. The cross section is the integral of the differential cross section over all directions in space.

It is illuminating to study the classical expression for the differential cross section relating to elastic scattering by an atom. This is given by:

$$\frac{d\sigma}{d\Omega} = \frac{r_e^2 \omega_i^4}{(\omega_o^2 - \omega_i^2)^2 + \omega_i^2 \Gamma^2} (\epsilon_i \cdot \epsilon_s)^2 \qquad (1.8)$$

where the atom is represented by an electron of charge e and mass m in a harmonic oscillator potential whose natural frequency of oscillation, ω_o, is the main absorption frequency of the atom. The incident light has electric field vector E_i and causes forced vibrations at ω_i. Γ is the damping constant, ϵ_i and ϵ_s are unit vectors in the E_i and E_s directions respectively and E_s is the electric field vector of the scattered light. r_e is given by:

$$r_e = \frac{e^2}{4\pi \epsilon_o m c^2} \qquad (1.9)$$

Equation 1.8 does not take into account inelastic scattering as it does not contain the required anharmonic terms in the oscillator potential. It shows the dependence of the scattering cross section on the polarisation of the light, however, and also illustrates how the scattering intensity can be a strong function of the incident frequency, ω_i, thus leading to the resonance effects discussed in section 1.3.4.

Raman scattering is a three step process (as illustrated in figure 1.3) and as such it must be treated by third order perturbation theory. This calculation has been performed by Loudon [1963] for zinc–blende crystals. He calculated the probability

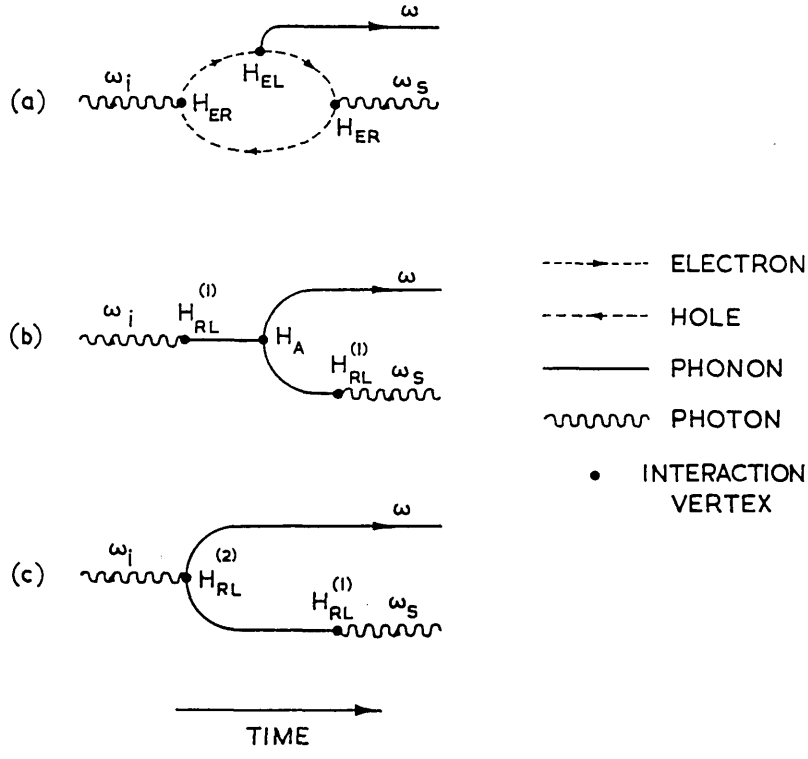

Figure 1.3 Schematic representation of three types of Raman scattering process. Process (a) is the dominant one where the incident light interacts with the crystal through the intermediary of the electrons. H_{EL}, $H_{RL}^{(1)}$ and H_{ER} represent the first order interactions of the electrons, lattice and radiation in an obvious notation. H_A is the three–phonon anharmonic interaction while $H_{RL}^{(2)}$ is the second order radiation–lattice interaction. [after Loudon, 1964]

per unit time, $1/\tau$, that one of the incident photons was destroyed in a Raman scattering process. This probability is given by Loudon [1964] as:

$$\frac{1}{\tau} = \frac{2\pi}{\hbar^6} \sum_{k,k_s} \left| \sum_{a,b} \frac{\langle n_i-1, n_s+1; n_o+1; 0 | H_I | a \rangle \langle a | H_I | b \rangle \langle b | H_I | n_i, n_s; n_o; 0 \rangle}{(\omega_a - \omega_i)(\omega_b - \omega_i)} \right|^2$$

$$\times \quad \delta(\omega_i - \omega_o - \omega_s) \qquad (1.10)$$

where n_i, n_s and n_o denote the numbers of incident photons, scattered photons and optic phonons present in the initial state. a and b run over complete sets of intermediate states for the whole system, the summation over $\mathbf{k}_s$ includes only directions within the solid angle $d\Omega$ and $H_I = H_{ER} + H_{EL}$ where these are the first order interactions between the electrons and the radiation and the electrons and the lattice, respectively (see also figure 1.3). The final zeros in the initial and final state quantum numbers show that the electrons start and finish in the ground state. If this expression is evaluated for the geometry given in figure 1.4 then the following expression for the scattering efficiency, S, is obtained [Loudon, 1964]:

$$S = \frac{e^4 \omega_s V(n_o+1) L d\Omega}{4\hbar^3 m^4 d^2 M c^4 \omega_o \omega_i} \left[|R^x_{yz}|^2 + |R^z_{xy}|^2 + |R^y_{xz}|^2 \right] \qquad (1.11)$$

where

e = electronic charge

m = electronic mass

M = atomic mass

d = lattice constant

V = crystal volume

L = length of the crystal in the direction of the incident light

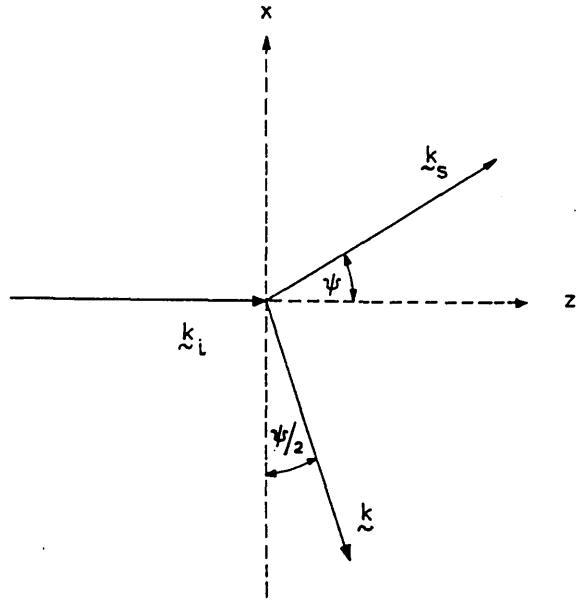

Figure 1.4 Schematic representation of the scattering geometry considered in calculating equations 1.11 to 1.15. [after Loudon, 1964]

ω_s = scattered photon frequency

ω_o = optic phonon frequency

ω_i = incident photon frequency

and

(n_o+1) = Stokes component of the Bose population factor

S is defined as the ratio of the number of scattered photons per unit time per unit cross sectional area in solid angle $d\Omega$ about the direction of observation, to the number of photons crossing unit area in unit time. R is the Raman tensor and its three components are equal for zinc–blende crystals.

$$R^{x}_{yz} = R^{x}_{yz}(-\omega_i, \omega_s, \omega_o)$$

$$= \frac{1}{V} \sum_{\alpha,\beta} \left[\frac{P^{z}_{o\beta}\, \Xi^{x}_{\beta\alpha}\, P^{y}_{\alpha o}}{(\omega_\beta+\omega_o-\omega_i)(\omega_\alpha-\omega_i)} + 5 \text{ similar terms} \right] \qquad (1.12)$$

The subscripts on the P and Ξ matrix elements refer to electron–hole pair states with energies $\hbar\omega_\alpha$ and $\hbar\omega_\beta$. o refers to the electronic ground state. The two subscripts on R are the polarisation directions of the incident and scattered photons, respectively, while the superscript gives the direction of polarisation of the phonon. The term given in full in 1.12, corresponds to the order of interaction shown in figure 1.3(a) while the other five terms refer to the other possible ordering of the interaction vertices. P is the electronic momentum operator which arises from the two H_{ER} matrix elements. The Ξ matrix elements are deformation potentials arising from H_{EL}.

Inspection of 1.11 shows that the scattering efficiency is determined by the Raman scattering tensors. It is these third order tensors that control whether or not

a phonon will scatter in any given scattering geometry, i.e., the crystalline selection rules discussed in the following section.

1.3.3 Raman Scattering Selection Rules

In any given crystal, the different phonon branches correspond to different symmetries of vibration of the atoms in the unit cell. They can therefore be represented by irreducible representations of the space group of the crystal lattice. If the phonon wavelengths are assumed infinite then the crystal point group will suffice to classify the phonon symmetries. This works well for centro-symmetric crystals but breaks down for piezoelectric crystals and therefore for all the III-V semiconductors. In the piezoelectric case, it is found that a) more first order Raman peaks are observed than would be expected and b) the expressions for the scattering efficiency have to be modified. It is still possible, however, to use the crystal point group as a basis for phonon classification if a) the extra peaks observed in the Raman spectra can be accounted for by lifting the group-theoretical degeneracy of the lattice vibrations and b) the scattering efficiency can be modified to incorporate the polarisation of the phonon. Thus S becomes [Loudon, 1964]:

$$S = A \left[\sum_{\substack{\sigma,\rho,\tau \\ = x,y,z}} e_i^{\sigma} R_{\sigma\rho}^{\tau} \xi^{\tau} e_s^{\rho} \right] \qquad (1.13)$$

and it is possible to identify a particular phonon symmetry by selecting the phonon unit polarisation vector ξ^{τ}. e_i^{σ} and e_s^{ρ} give the polarisations, σ and ρ, of the incident and scattered light, respectively, and A is a constant of proportionality. Equation 1.13 illustrates the result that a phonon can participate in a first order

scattering event if, and only if, its irreducible representation is the same as one of the irreducible representations of the polarisability tensor. Equation 1.13 also allows the determination of the Raman scattering selection rules.

Zinc–blende crystals have T_d point symmetry and the irreducible representations of the Raman–active lattice vibrations for this and all the other crystal symmetries have been collated by Loudon [1964]. The optical phonons of zinc–blende crystals can be shown to have F_2 symmetry (Γ_{15} in Bethe's notation) and the scattering efficiencies for these vibrations in the geometry given in figure 1.4 have been calculated by Loudon [1964] as:

$$S^l_{//} = A'd^2[e^y_i \sin(3\psi/2)]^2 \qquad (1.14a)$$

and

$$S^l_{\perp} = A'd^2[e^x_i \sin(\psi/2)]^2 \qquad (1.14b)$$

for the longitudinal vibrations and

$$S^t_{//} = Ad^2[\{e^y_i \cos(3\psi/2)\}^2 + \{e^x_i \sin\psi\}^2] \qquad (1.15a)$$

and

$$S^t_{\perp} = Ad^2[e^x_i \cos(\psi/2)]^2 \qquad (1.15b)$$

for the transverse vibrations where $S^l_{//} + S^t_{//} = S_{//}$ and $S^l_{\perp} + S^t_{\perp} = S_{\perp}$, the values for non–piezoelectric crystals, provided that $A = A'$.

For polar crystals, however, $A \neq A'$, because the macroscopic electric field which accompanies a polar lattice vibration provides an additional electron–lattice interaction (the Froehlich interaction). The effect of this additional interaction on the scattering efficiency of the modes and thus on the relative intensities of the modes

is described by the Faust–Henry coefficient, C, as discussed in section 2.2.1.

The immediate conclusion that can be drawn from 1.13 is that in backscattering from the (001) face of a zinc–blende crystal, the LO mode is allowed whereas the TO mode is forbidden. Also, since all the non–zero Raman tensor components are off–diagonal matrix elements, the LO mode can only be observed in the crossed polarisation $z(x,y)\bar{z}$; it is forbidden in $z(x,x)\bar{z}$. The standard notation used to represent scattering geometry is a(b,c)d, where a gives the direction of incidence of the exciting radiation and b gives its polarisation, c gives the polarisation of the scattered light and d is its direction. The selection rules can be used to identify features in the Raman spectrum.

1.3.4 Resonance Effects

Resonant effects occur when the frequency of the incident light approaches a critical frequency of the sample. This was shown in equation 1.8, which gave the expression for the differential cross section for elastic scattering by an atom. In that case, the term $(\omega_o^2 - \omega_i^2)^2$ appeared in the denominator of the expression where ω_o was an absorption frequency of the atom. Clearly, as ω_i approaches ω_o, the scattering cross section increases and the scattering process becomes more efficient. The physical reason behind this is that in resonance, real, rather than virtual, excited states are populated when ω_i is absorbed. The lifetimes within real excited states are much longer than those within virtual excited states (nanoseconds rather than femtoseconds). This means that the resonantly excited electron–hole pair has a higher probability of performing a scattering interaction before decaying thus the scattering efficiency increases.

This effect can also be seen by inspection of equation 1.10 which gives the scattering probability per unit time for inelastic scattering. The two terms $(\omega_a - \omega_i)$

and $(\omega_b - \omega_i)$ in the denominator of the expression, show the effect of choosing the incident light frequency such that it resonates with one of the real intermediate states of the system, a or b. It is possible to measure the resonant behaviour of Raman scattering and this has been done for GaAs by Trommer and Cardona [1978]. Their data is shown in figure 1.5. It can be seen that resonant enhancement of the TO phonons is apparent for all the E_0, $E_0+\triangle_0$, E_1 and $E_1+\triangle_1$ energy gaps.

In order to enhance the Raman scattering signal, measurements are often made at or near resonance. This can result in unwanted side effects such as the phonon broadening discussed in section 2.3 and it is important to consider such effects when interpreting experimental data.

1.3.4 Second–Order Raman Scattering

First–order Raman scattering involves the creation or destruction of a single excitation (say, a phonon). In second–order Raman scattering, two phonons participate in the scattering process. There are two ways in which this can occur. Two first–order Raman events can occur sequentially or else one Raman event can occur involving two phonons. In a crystal, the former process will give rise to a line spectrum containing features at the sum and difference values of the first–order spectrum. The latter process, however, is not bound by the first–order scattering selection rules as the two phonons can come from any region of the Brillouin zone provided that their wavevectors, $\mathbf{q}$ and $\mathbf{q}'$, satisfy $\mathbf{q} + \mathbf{q}' \simeq 0$. In this way, a continuous spectrum is produced which reflects the phonon density of states weighted by a factor which incorporates the $\mathbf{q} + \mathbf{q}' \simeq 0$ constraint.

Second–order Raman scattering theory is neccessarily more cumbersome than first–order theory as higher–order anharmonic terms must be included in the

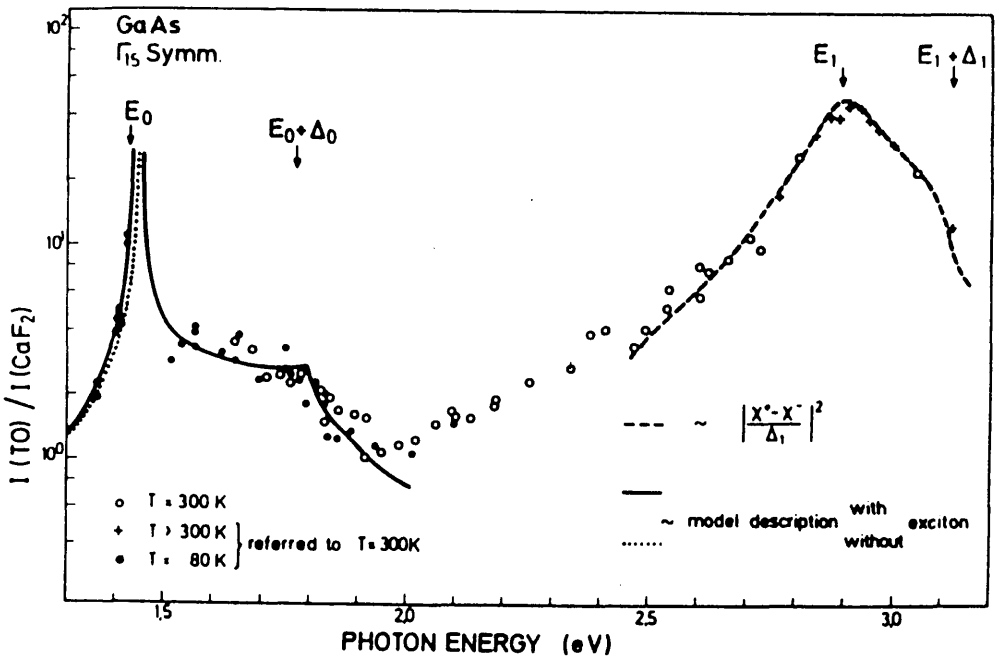

Figure 1.5 Resonance behaviour of Raman scattered intensity of TO phonons in GaAs showing enhancement near the crystalline energy gaps. [after Trommer and Cardona, 1978]

calculations. Theoretical and experimental aspects of resonant second–order Raman scattering have been considered by Cardona [1982] where the resonance can be expected to enhance the second–order scattering intensity. This technique has proved useful to study, e.g., crystalline disorder because of its extreme sensitivity to the perfection of the lattice [see, e.g., Wagner et al, 1987; also the discussion in section 2.5.5].

References

D E Aspnes and A A Studna; Phys Rev B27, 985, 1983

L Brillouin; Compt Rend 158, 1331, 1914

M Cardona; in "Light Scattering in Solids II: Basic Concepts and Instrumentation", edited by M Cardona and G Guentherodt, published by Springer– Verlag, Berlin, Heidelberg, New York, 1982; p19

E Gross; Nature 126, 201, 1930

W Hayes and R Loudon; "Scattering of Light by Crystals", published by John Wiley & Sons, New York, 1978; Chapter 1

C Kittel; "Introduction to Solid State Physics", 5th edition, published by John Wiley & Sons, New York, 1976; chapter 4

R Loudon; Proc Roy Soc A275, 218, 1963

R Loudon; Advan Phys 13, 423, 1964

A Smekal; Naturwiss 11, 873, 1923

R Trommer and M Cardona; Phys Rev B17, 1865, 1978

CHAPTER 2

3D PHONONS IN III– V SEMICONDUCTORS: THEORY AND REVIEW

2.1 Introduction

This chapter discusses some of the theoretical concepts that are specifically relevant to III– V semiconductors: in particular, the Froehlich interaction which removes the TO– LO degeneracy in III– V semiconductors and effects of alloying with regard to both the disorder of the alloy microstructure and the expected phonon behaviour of an alloy. In this chapter, only the three dimensional (3D) case is discussed; the difference between 3D and 2D phonon behaviour is covered in the following chapter. The emphasis is placed upon phonon behaviour which is observable and thus reference is made to published work wherever it supports or illuminates the discussion. Section 2.6, on phonons in alloy semiconductors, is predominantly a review of published opinion at the present time.

2.2 Electron – Phonon Interactions

2.2.1 Deformation Potential and Froehlich Interaction

The electron–phonon interaction in a polar crystal has two contributions: a short–range contribution from the deformation potential and a long–range contribution known as the Froehlich interaction.

The deformation potential contribution stems from the effect of the lattice atomic displacements on the periodic crystalline electrostatic potential. The relative movements of the two ions in the atomic cell modify the periodic potential of the crystal and thus enable coupling of the electrons to the lattice vibrations. The Froehlich interaction, on the other hand, arises from the interaction of the electrons with the macroscopic electric field produced by the lattice vibrations. As it is only the longitudinal phonons in a polar material which produce such an electric field, it is only the longitudinal modes which take part in the Froehlich interaction. A full theoretical treatment of both these interactions is given by Hayes and Loudon [1978]. The Froehlich coupling is described by a constant, α, given by:

$$\alpha = \frac{2m^*\omega_L}{\hbar} \times \frac{1}{2\hbar\omega_L^3} \times \frac{e^2}{4\pi\epsilon_o\epsilon_\infty} \times (\omega_L^2 - \omega_T^2) \qquad (2.1)$$

where

m^* = effective mass

e = electronic charge

ω_L = LO phonon frequency at the Brillouin zone centre

ω_T = TO phonon frequency at the Brillouin zone centre

ϵ_o = static dielectric constant

ϵ_∞ = dynamic dielectric constant

and all other constants have their usual meanings. This expression shows that α depends only on the LO– TO frequency difference at the centre of the Brillouin zone.

In the case of a non– polar crystal, e.g. Silicon or Germanium, there is no macroscopic electric field associated with the longitudinal modes so the Froehlich interaction vanishes leaving the longitudinal and transverse vibrations degenerate at the Brillouin Zone centre.

The relative intensities of the TO and LO modes are obtained via the Faust– Henry coefficient, C, given by Cardona [1982] as:

$$C = \frac{e^*(\partial\chi/\partial u)}{\mu(\omega_{TO})^2(\partial\chi/\partial E)} \qquad (2.2)$$

with

e^* = dynamical charge on one of the atoms

μ = reduced mass ($1/\mu = 1/M_a + 1/M_b$)

E = electrostatic field associated with the LO modes

χ = electric susceptibility of the material

u = atomic displacement

This dimensionless coefficient is a measure of the relative strength of the deformation potential coupling with respect to the electro– optic coupling and thus yields the relative intensity of the TO mode with respect to that of the LO mode. A list of both theoretical and experimental values for C is given in table 2.6 of Cardona [1982] for some III– V and II– VI binary semiconductors. All show an enhancement of the LO phonon intensity relative to that of the TO phonon.

2.2.2 Forbidden– Froehlich Interaction

It is possible to observe LO phonon scattering that is symmetry– forbidden in the first– order approximation. This scattering is induced by the Froehlich interaction and a theoretical description is given by Cardona [1982] of which the relevant points are summarised below.

Symmetry– forbidden LO scattering originates in the macroscopic electric field associated with LO phonons and thus in the Froehlich interaction. The electric field produces a modulation in the susceptibility of the material, χ, via the first– order electro– optic effect. If the expression for the Raman scattering cross– section is expanded in terms of the wavevector, q, a term is obtained in q which is proportional to χ. This contribution to the scattering cross– section would vanish in a first order approximation as q approaches zero (because only terms linear in q are considered, see chapter 1) thus making it a "forbidden" scattering mechanism. The effect of this term is strongly resonant near critical points in the Brillouin zone and is the source of the forbidden LO scattering.

This forbidden Froehlich interaction is induced by breaking the $q=0$ condition, specifically by impurity effects (extrinsic mechanism) and this mechanism has been investigated experimentally by Menendez and Cardona [1985] in GaAs, Menendez et al [1985] in CdHgTe and Kauschke et al [1987] in GaAs– AlGaAs superlattices. The forbidden Froehlich interaction has also a contribution from intrinsic (two– phonon) processes.

Interference effects between symmetry– allowed and symmetry– forbidden LO phonon scattering have been seen in both GaAs and InP [Menendez and Cardona, 1985 and Kauschke and Cardona, 1986, respectively] and have been used by the authors to investigate the competing mechanisms of forbidden scattering. In both GaAs and InP it was observed that most of the intensity from the forbidden LO phonon scattering resulted from impurity– induced Froehlich interactions with only a

small contribution (of about 20% in GaAs and 40% in InP) from the intrinsic intraband Froehlich interaction. These percentages depended strongly upon sample quality with these values being the largest obtained. This suggests that in the ideal case of zero impurities, all the forbidden– LO scattering intensity would come from the intrinsic mechanism. In the non– ideal case, as the crystal quality decreases, a larger percentage of the symmetry– forbidden intensity results from the impurity– induced Froehlich interaction.

The forbidden– Froehlich mechanism explains why the LO mode can appear with a strong intensity even when symmetry– forbidden in first– order. The fact that the coupling is via a Froehlich interaction rather than the deformation potential explains why only LO modes and not TO modes exhibit this type of behaviour.

2.3 Raman Linewidth and Lineshape

If the crystalline lattice is considered in the harmonic approximation discussed in section 1.2 then the normal modes obtained for the vibrations of the lattice are independent and therefore have an infinite lifetime. This has the effect of making the modes delta functions. This approximation is usually adequate to describe the phonons seen in Raman scattering if a broadening parameter is introduced to fit experimental data. In this case, a symmetric lineshape is obtained. When a more rigorous treatment of the lineshape is required then anharmonic contributions must be considered. The anharmonic coupling of the normal modes of the crystal destroys their independence and introduces both a finite lifetime for the phonon and linewidth broadening of the mode. The third order anharmonic term, for example, describes the decay of a one–phonon mode into a two–phonon state with conservation of wavevector (e.g. LO(Γ) decaying into 2LA(X)) [Pinczuk and Burstein, 1983].

Anharmonic coupling has been extensively studied in the case of the TO phonon mode of GaP. This mode is strongly asymmetric with a strong low–energy tail (see figure 2.1). The asymmetry was first interpreted as an anharmonic coupling by Barker [1968] who attributed the low energy tail to an interaction of the TO(Γ) with the combination mode TA(X) + LA(X). Strong coupling can be expected because the two modes are almost degenerate. This interpretation was further investigated by Weinstein and Piermarini [1975] who studied the evolution of the GaP TO mode as a function of hydrostatic pressure up to 135 kbar. They found that the asymmetry reduced sharply with increasing pressure such that the TO peak became symmetric at about 80 kbar. They related this result to the opposite signs of the pressure coefficients of the TO(Γ) mode and the TA(X) mode. This caused one phonon to increase in energy with pressure while the other decreased in energy with

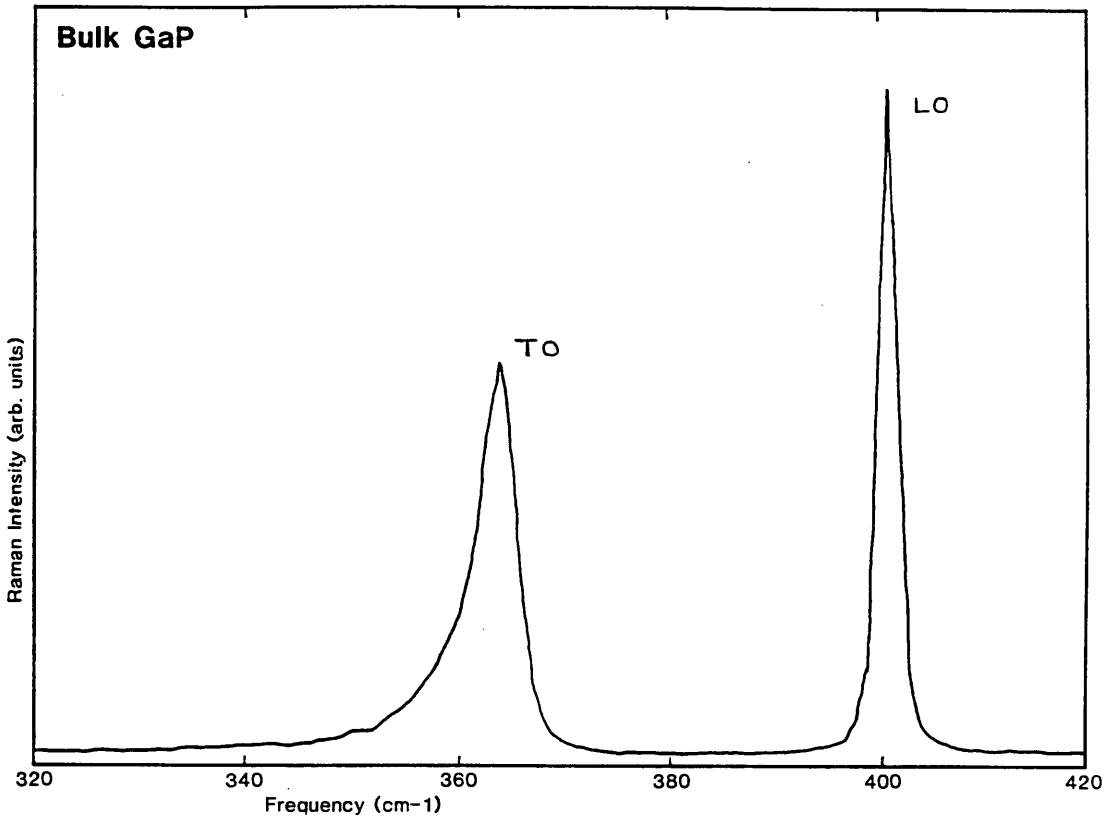

Figure 2.1 Room temperature Raman scattering from GaP showing asymmetry of TO mode. Laser line = 4880Å, resolution = 2.5 cm^{-1}. Spectrum recorded without polarisation analysis.

pressure thus removing the near–degeneracy of the modes and prohibiting the strong coupling.

The linewidth broadening discussed so far has been an intrinsic effect. There are extrinsic effects that also contribute to broadened Raman linewidths. The various effects of crystalline disorder on linewidth are discussed in section 2.5.4. In addition, if the phonon couples to another excitation, e.g. a plasmon, then its lineshape and frequency will alter. This so–called Fano asymmetry is discussed by Wagner [1986]. As the Fano asymmetry relates to heavily–doped samples ($n \geq 10^{19}$ cm^{-3}) it can be neglected for this work where nominally–undoped samples are used ($n \leqslant 10^{16}$ cm^{-3}).

2.4 Impurity Modes in Binary Compounds

The simplest model to investigate impurity mode effects in binary crystals is that of a single substitution of one atom. This has been investigated by Barker and Sievers [1975] and a summary of part of their excellent review article follows.

If a linear chain model is composed of atoms A and B with masses M_A and M_B, respectively, and having $M_A < M_B$ then the expected phonon density of states for an infinitely–long chain is given in figure 2.2. There are four types of impurity substitution that can be made: the lighter atom, atom A, can be substituted by impurity atom C, with either $M_C > M_A$ or $M_C < M_A$; similarly, the heavier atom, atom B, can be substituted by C such that $M_C > M_B$ or $M_C < M_B$. This yields four types of impurity mode behaviour which will be considered separately.

Localised Mode : $M_C < M_A$

If $M_C < M_A$ then a mode develops above the optical frequency band as shown by the upper solid curve in figure 2.3. This mode is localised in space at the impurity site and the localisation of the mode increases as M_C approaches zero with atom C taking an increasing share of the total amplitude of the impurity mode

Gap Mode : $M_C > M_A$

When $M_C > M_A$, a mode develops which lies in the gap between the acoustic and optic frequency bands (see lower solid curve, figure 2.3). This mode is less spatially localised than the localised mode mentioned above because it has only a limited range of allowed frequency values. The mode amplitude, therefore, spreads over the first few nearest neighbours of atom C.

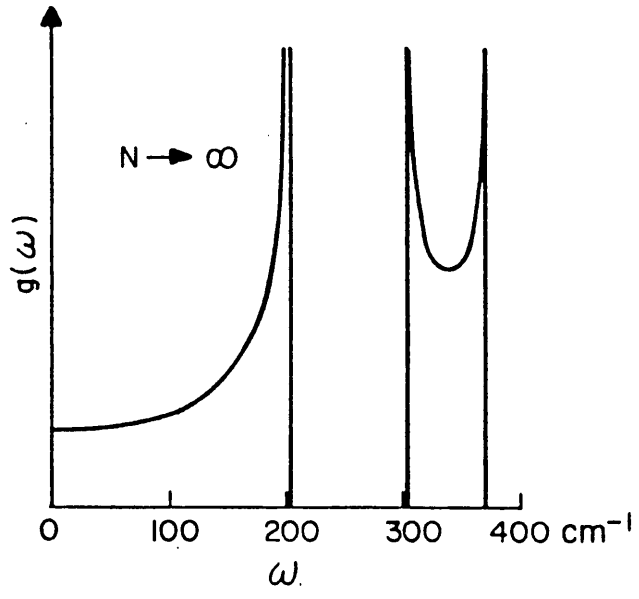

Figure 2.2 Theoretical phonon density of states calculated using the infinite diatomic linear chain model. [After Barker and Sievers, 1975].

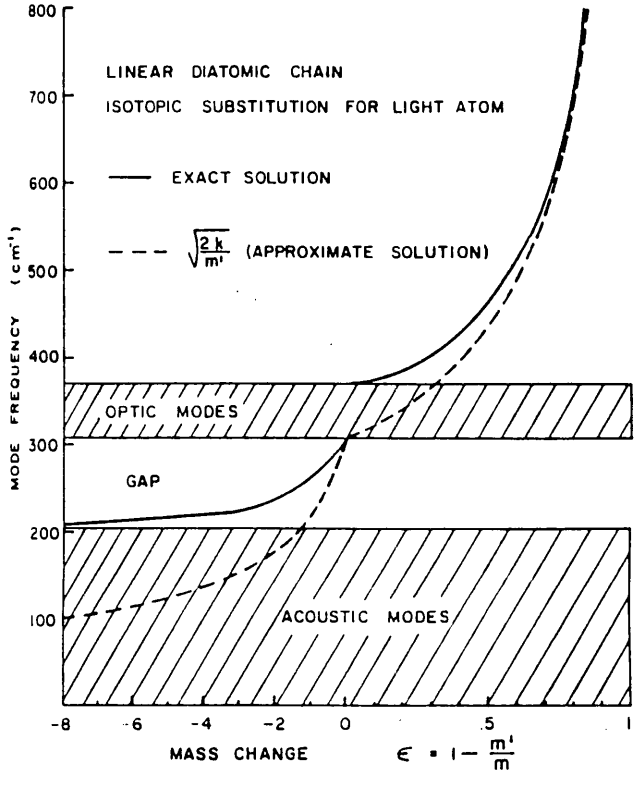

Figure 2.3 Localised (upper solid curve) and gap (lower solid curve) mode frequencies for light and heavy impurity substitutions of the lighter atom in the diatomic linear chain model. The dotted line shows an approximate solution discussed by the authors. [After Barker and Sievers, 1975].

Gap and Local Modes : $M_C < M_B$

Solving the linear chain model for the substitution of atom B with a lighter impurity atom, C, yields two modes: a local mode and a gap mode as shown in figure 2.4. The gap mode in this case has very different behaviour from the gap mode caused by light atom substitution as can be seen by comparison of figures 2.3 and 2.4. For this substitution regime, the gap mode moves asymptotically towards the centre of the gap as the impurity mass becomes lighter.

Resonant Modes : $M_C > M_B$

The behaviour of resonant modes is shown in figure 2.5. It is not possible to model this behaviour with the simple linear chain model which has constant force constants between the atoms, so Barker and Sievers [1975] modified the nearest neighbour force constants in a simple extension of the basic model and obtained the results shown in figure 2.5. The force constant on either side of the impurity was reduced and a parameter γ defined such that $\gamma = 1 - k'/k$ where k = old force constant and k' = new, redefined, force constant. As γ increases from 0 to 0.66, i.e. as the force constant is reduced, a gap mode appears with behaviour very similar to the gap mode caused by substituting M_A with $M_C > M_A$ (see figure 2.3). As γ increases above 0.66, however, the impurity mode drops into the acoustic continuum. This gives rise to a broad spectral peak consisting of an envelope of modes in which the impurity vibrates with a significantly enhanced amplitude. The figure shows vertical bars which correspond to the extent of the resonant band of the impurity.

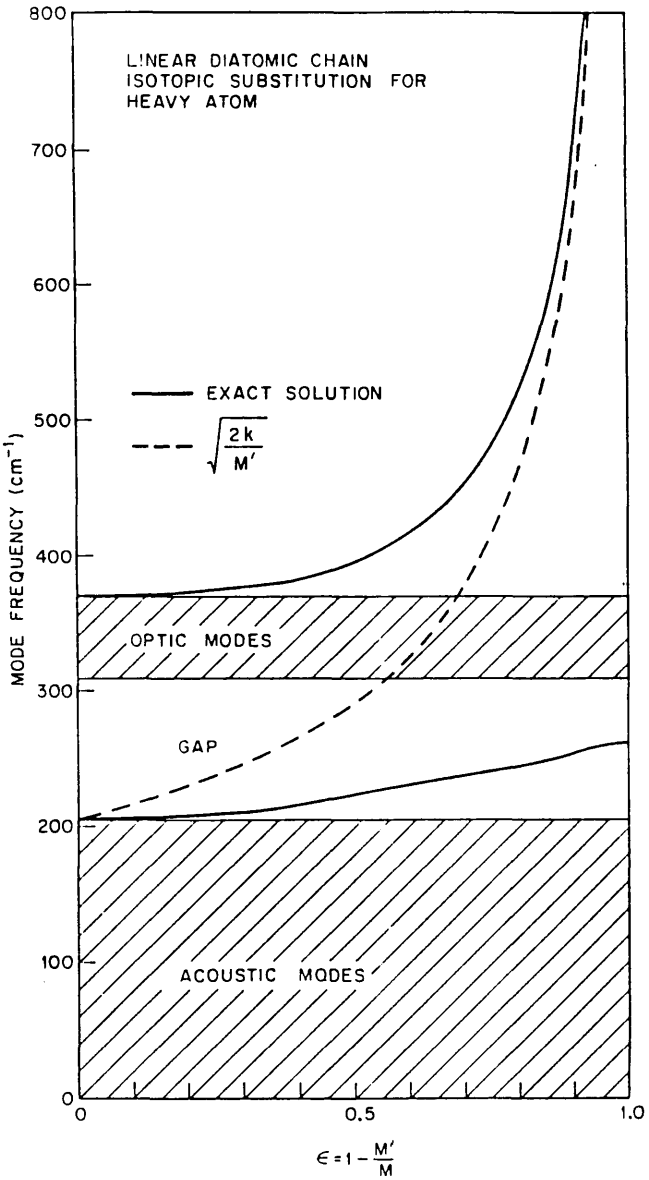

Figure 2.4 Local (upper solid curve) and gap (lower solid curve) mode solutions which occur together for light impurity substitution of the heavier atom in the diatomic linear chain model. The dotted line shows an approximate solution discussed by the authors. [After Barker and Sievers, 1975].

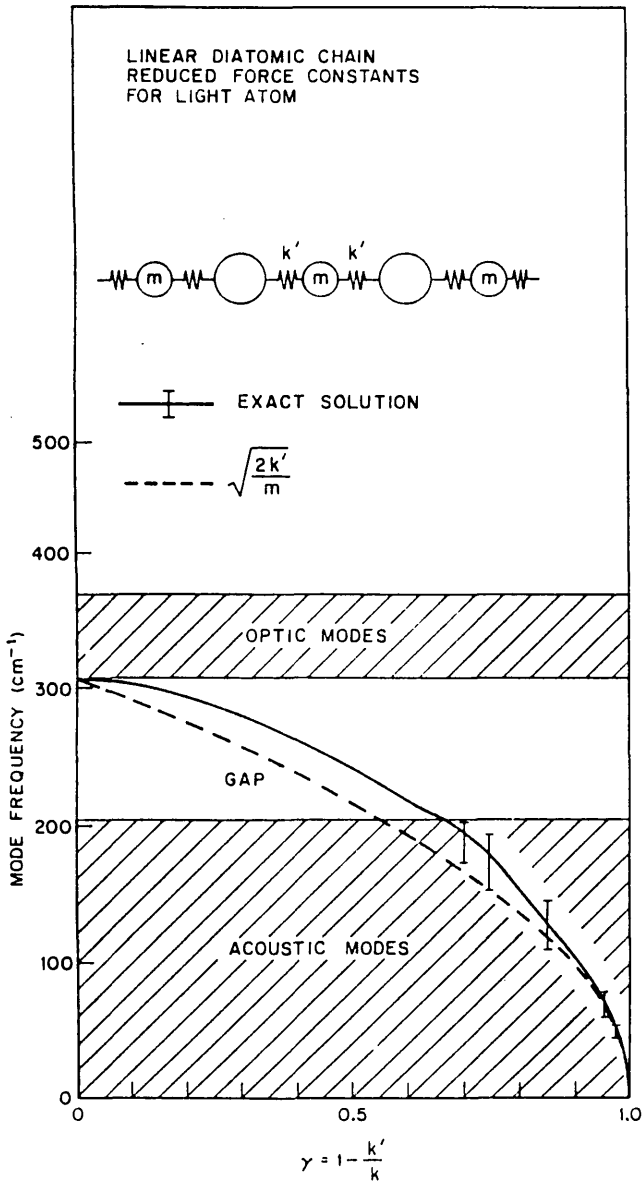

Figure 2.5 This diagram shows the defect modes arising from a force constant reduction. The mode decreases in frequency with decreasing force constant until it enters the acoustic band. Once within this band, an entire group of modes combines to form a "resonant mode". The width in frequency of this group is given by the vertical bars. The dotted line shows an approximate solution discussed by the authors. [After Barker and Sievers, 1975].

An example of the experimental observation of impurity vibrational modes can be seen in the work of Wagner et al [1986] where the local mode of Boron in crystalline Silicon was studied by Raman scattering to yield information about the properties of heavily–doped Silicon. The local vibrational mode of Boron was observed at higher energy than the optical phonon of Silicon. A partial list of impurity mode frequencies for III–V and II–VI compounds is given by Chang and Mitra [1971].

This simple 1D linear chain model can be extended to predict alloy phonon behaviour by considering the effect of adding progressively more impurity atoms to the chain. It successfully predicts the two–mode alloy behaviour for GaAsP (see section 2.6 for a discussion of two–mode behaviour).

2.5 Alloy Microstructure

The interest in ternary and quaternary alloy microstructure has been given impetus by the need to produce homogeneous alloys with reproducible and reliable properties. Alloy microstructure, clustering and disorder have a profound effect on many of the relevant properties of semiconductor alloys. Growth of better quality alloys which have good and consistent parameters is therefore an important part of the development of III– V semiconductors for commercial use. As such, this area of work is attracting the attention it merits from both industrial and academic sources. This can be seen most clearly in the very large numbers of publications in the fields of alloy growth and characterisation.

The quest for better material has led to much investigation of the microstructure of presently–available materials. Two interesting facts have emerged from these investigations: 1) it is energetically favourable for alloys to grow in a "clustered" form [Yamazaki et al, 1982] and 2) although the average bond length in the alloy changes smoothly from one end–point lattice parameter to the other, the individual bond lengths remain almost constant [Mikkelson and Boyce, 1983]. The implications of these facts for alloy microstructure are discussed below.

2.5.1 Clustering Effects

Yamazaki et al [1982] undertook a theoretical calculation of the excess free energy of mixing in III– V alloys. The excess free energy, $\triangle G_{ex}$, is given by:

$$\triangle G_{ex} = \triangle H_{ex} - T\triangle S_{ex} \qquad (2.3)$$

where $\triangle H_{ex}$ is the excess enthalpy, $\triangle S_{ex}$ is the excess entropy of mixing and T is the temperature. The authors calculated both $\triangle H_{ex}$ and $\triangle S_{ex}$ as a function of a clustering parameter, β. β was defined such that $\beta = 0$ would yield an entirely random atomic arrangement of the A and B atoms in the alloy $A_{1-X}B_XC$ while $\beta = 1$ would imply a saturation clustering such that the second neighbours of A atoms would always be A atoms etc. Given that a stable crystalline state is obtained when the excess free energy is a minimum, the authors calculated the clustering parameter corresponding to a minimum in the excess free energy, β_S, and compared it with the relative difference in the lattice constants of the two end members of the alloy. They found that β_S increased with the increase in the relative difference of the lattice constants suggesting that clusters are likely to be formed more easily when the relative difference of the lattice constants is large. An example of this can be found in the alloys of GaSb: GaPSb ($\triangle a/\bar{a} = 11.15\%$) has $\beta_S = 0.68$, GaAsSb ($\triangle a/\bar{a} = 7.52\%$) has $\beta_S = 0.39$ and GaAlSb ($\triangle a/\bar{a} = 0.65\%$) has $\beta_S = 0.0$. Thus GaPSb is most likely to cluster while GaAlSb will have entirely random ordering according to this model. Application of this method to $Ga_XIn_{1-X}As$ shows a maximum in β_S of 0.4 at $x = 0.5$ thus suggesting that GaInAs is very inclined to cluster when grown at the mid-range of composition.

An experimental study of the clustering parameter has been undertaken by Kakimoto and Katoda [1985] in which they investigated GaAlAs, GaInP, GaInAs and GaAsP using Raman spectroscopy. They were able to calculate a value for the clustering parameter by analysing the temperature dependence of the optic phonon intensity ratios. Their experimental values for the clustering parameters obtained for the four alloys agree very well with the theoretical values of Yamazaki et al [1982].

2.5.2 Bond Lengths

The tendency of an alloy to grow in clusters has been attributed to the relative difference in bond lengths between the end members of the alloy. In the simple virtual crystal approximation (VCA) [Nordheim, 1931] an alloy of $A_{1-x}B_xC$ has a single lattice parameter, C–C, and the bond lengths A–C and B–C are equal to half this value. Thus all atoms sit on the same lattice site as the binary and the bonds are stretched or compressed to suit. EXAFS work undertaken by Mikkelson and Boyce [1983] on GaInAs and more recently by Bunker et al [1988] on ZnMnSe has shown that although the C–B–C and C–A–C bond distances are equal to the VCA values, the individual A–C and B–C bond lengths remain almost the same as in the binary compound. This causes the A and B atoms to sit slightly displaced from the lattice sites resulting in a bending of the bonds which distorts the lattice from the tetragonal. The new structure is described in terms of a chalcopyrite crystal which is closely related to the zinc–blende structure but has a new unit cell of, say, $InGaAs_2$ and a slightly compressed lattice in one direction known as a tetragonal compression. Figure 2.6 shows the structure as given by Mikkelson and Boyce [1983].

Relating this information to the discussion in the previous section, the EXAFS data explains qualitatively why an alloy should cluster when its end members have very different lattice parameters. Clearly, if the bond lengths of the binaries do not change in the alloy then it is likely that there will be an energy advantage in clustering because local strains will be minimised. Conversely, if the end members of the alloy have similar lattice parameters then there will be no distortion of the lattice, hence no energy advantage in clustering and a truly random alloy will result.

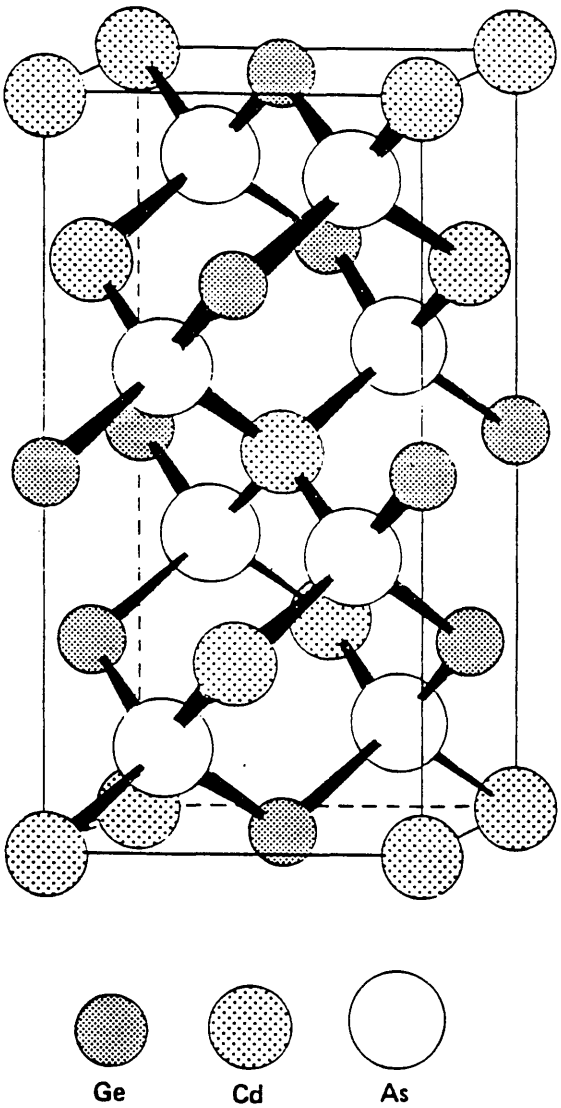

Figure 2.6 Schematic of the chalcopyrite crystal structure for $CdGeAs_2$ which is also the structure for $GaInAs_2$ if Cd is substituted by Ga and Ge by In. [After Mikkelson and Boyce, 1983].

2.5.3 Effect of Alloy Disorder on Energy Gap

The energy gap of a ternary alloy $A_{1-x}B_xC$ is generally given by:

$$E_g = a + bx + cx^2 \qquad (2.4)$$

where x = alloy composition

a = energy gap of material AC

b = difference in energy gap between BC and AC

c = bowing parameter, obtained experimentally and associated with the effective charge and the Phillips electronegativity [Van Vechten and Bergstresser, 1970]

This assigns a one–to–one correspondence between energy gap and composition. A recent study of GaInP suggests that equation 2.4 may be over–simplified. Gomyo et al [1987] discovered a 50meV difference in the energy gap of ordered and random $Ga_{0.5}In_{0.5}P$. The authors were able to produce material with one or the other energy gap by varying the MOVPE growth conditions. Electron diffraction measurements of the lower bandgap material yielded evidence of a crystalline period twice as large in one direction as the lattice constant and thus suggested an ordered growth in that direction. Similar measurements on the higher bandgap material showed no such structure thereby suggesting a random arrangement of the Ga and In atoms. The second piece of evidence put forward by the authors involved Zn diffusion into the lower energy gap material (ordered alloy). This was found to change the bandgap back to the higher value (disordered alloy). Parallels were drawn with the work of Laidig et al [1981] who discovered that Zn diffusion destroyed the ordering in $(AlAs)_m(GaAs)_n$ superlattice structures.

Clearly this work is still in its early stages and more experimental studies are

needed but it seems physically reasonable that an ordered crystal could possess a bandgap energy that is different to a disordered one. If this should prove to be the case then equation 2.4 must be applied with some caution taking into consideration the growth conditions.

2.5.4 Effect of Alloy Disorder on Phonon Linewidth

This section should be read in conjunction with section 2.3 which provides a fuller account of the main contributions to linewidth broadening. Substitutional alloy disorder or alloy potential fluctuations degrade the long range order of the crystal. In order to investigate this effect, Parayanthal and Pollack [1984] studied the Raman scattering lineshapes of a number of GaAlAs and GaInAs alloys. They correlated asymmetry (of typically Γ_a/Γ_b of 1.5) and broadening of the LO phonon modes (of typically $2 - 3\ cm^{-1}$) with a coherence length in the crystal exactly as was done by Tiong et al [1984] for ion-damaged samples (see chapter 6). The authors obtained a good fit of the model to the experimental data thereby demonstrating that the model was adequate to treat both substitutional and damage-induced disorder. Their interpretation of the phonon linewidth broadening has been independently corroborated by Kash et al [1987] using time-resolved Raman measurements. It is interesting to note that these fundamentally different types of crystalline disorder (alloy potential fluctuations, substitutional disorder, ion damage causing defects and dislocations) all produce a similar effect on the lattice vibrations and can be treated in the same manner.

2.5.5 Disorder–Activated Phonon Modes

The restriction that first order Raman scattering can involve only those phonon modes at $q=0$ in the Brillouin zone stems from the infinite crystal approximation and the conservation of momentum conditions (see chapter 1). If the disorder in a crystal is such that the infinite crystal approximation no longer holds good, then the $q=0$ condition is relaxed and phonon modes with $q\neq0$ may participate in the Raman scattering process. This relaxation is taken to its extreme in the case of amorphous crystals which have no long–range order and where the Raman signal reflects the entire phonon density of states [Brodsky, 1982; Rama Rao et al, 1983]. In the case of an alloy, the disorder is usually intermediate between the crystalline and the amorphous states and thus the Raman spectrum has strong crystalline features (which may be broadened as discussed above) and also contributions from the phonon density of states involving phonons at various points in the Brillouin zone.

There is always some allowed scattering from combinations of zone–edge phonons where $q'-q \approx 0$, meets the first order Raman scattering condition (where q' and q are the wavectors of the zone–edge phonons). This effect is usually very weak [see, e.g., Bedel et al, 1986]. When disorder breaks the crystalline structure, scattering from single zone–edge phonons can become allowed. These modes, the DALA mode (disorder activated longitudinal acoustic mode) and DATA mode (disorder activated transverse acoustic mode), have been observed in many III–V alloys [see, e.g., Kakimoto and Katoda, 1982, for DALA in GaInAs; Soni et al, 1986, for DALA in GaInAsP; Carles et al, 1980, for DATA and DALA in InPAs; Bedel et al ,1985, for DATA in GaInP]. These features are characteristically very broad and peak in intensity around the mid–range of alloy composition where the disorder can be expected to be greatest.

Disorder can destroy second–order Raman scattering in much the same way as it broadens first–order Raman scattering. Teicher et al [1984] looked at this effect

in two alloys: GaPAs and GaAlAs. The authors found qualitative differences in the two-phonon spectra of the alloys. In the GaAlAs, spectral features corresponding to combinations of GaAs-like and AlAs-like zone-edge phonons were visible which was not the case for GaPAs. This was interpreted by assuming a random distribution of the Ga and Al atoms in the GaAlAs alloy, thus allowing any given bond to participate in both GaAs-like and AlAs-like zone-edge phonon modes. In the case of GaPAs, clustering of the alloy introduces disorder into the crystal which has the general effect of broadening the modes, reducing the coherence length and causing an overall decrease in the two-phonon intensity. The specific effect of the clustering is to localise the zone-edge phonon within a cluster of either GaP or GaAs and thus reduce the possibility of combinations of GaP-like and GaAs-like modes.

2.6 Alloy One– Mode and Two– Mode Phonon Behaviour

Phonon modes in alloys or mixed crystals have long been of interest; in 1971, Chang and Mitra published a review of the experimental results and theoretical models up to that date. They concluded by stating empirical criteria for one– mode and two– mode phonon behaviour.

Ternary alloys display one mode phonon behaviour if they have one set of phonon frequencies, i.e. one TO and one LO, varying smoothly in frequency with the alloy composition. The crystal systems cited by Chang and Mitra [1971] as exhibiting one– mode behaviour have a common feature in that there is a frequency overlap of the restrahlen bands (which are bounded by the TO and LO frequencies) of the end members of the alloy and, in addition, the restrahlen bands are well– separated from the acoustical phonon continuum. The authors observed only two systems which exhibit one– mode behaviour and which violate this criterion: GaAsSb and GaInAs. This was attributed to a continuity in the one– phonon density of states of GaAs between the acoustical and optical branches which precludes the observation of a gap mode and thereby precludes two– mode behaviour (see below). Figure 2.7 shows a schematic of one– mode behaviour.

Two– mode behaviour has been seen in a number of ternary alloy semiconductors. Crystals which exhibit two– mode behaviour have an LO and a TO mode corresponding to each of the end members of the alloy, i.e., two LO modes and two TO modes throughout the entire range of alloy composition. The reason for this type of behaviour is attributed to the observed fact that for two– mode systems, the restrahlen bands of the end members of the alloy are well– separated in frequency, thus allowing the existence of both a local mode of A in BC and a gap mode of B in AC (see section 2.4 and figure 2.8).

In all cases, clustering of the alloy during growth will lead to volumes in the

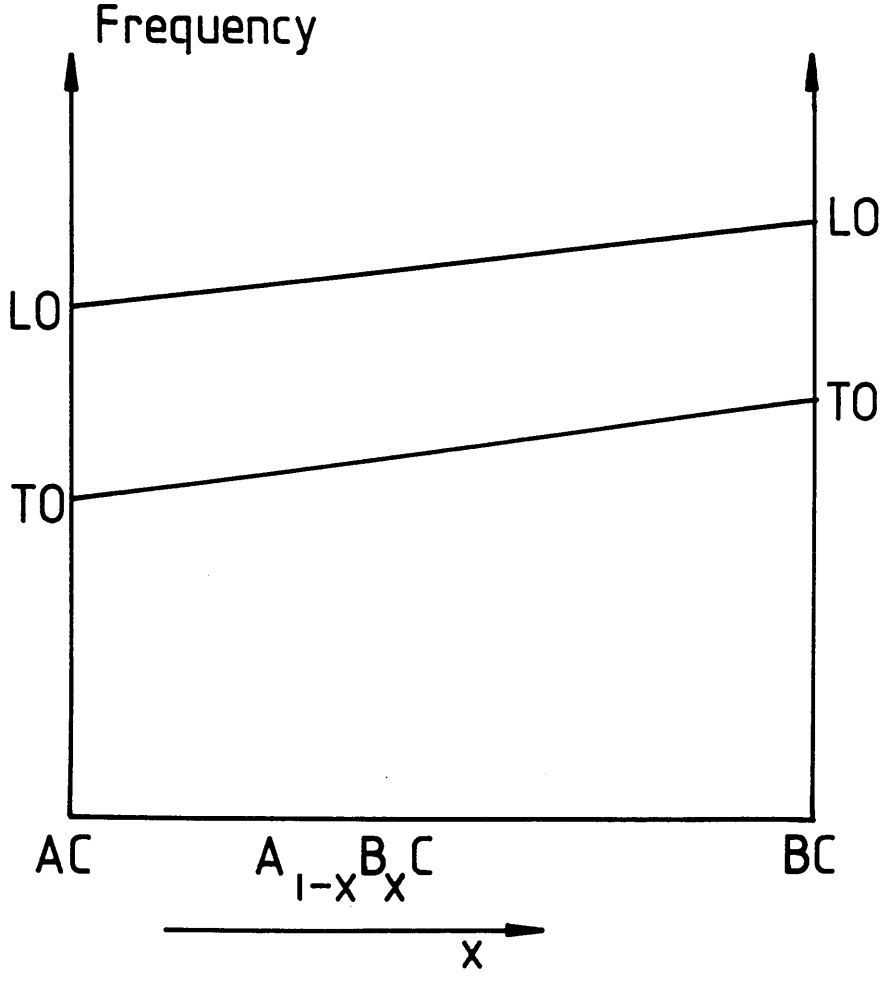

Figure 2.7 Schematic representation of one– mode alloy behaviour showing the evolution of one LO and one TO mode across the entire composition range.

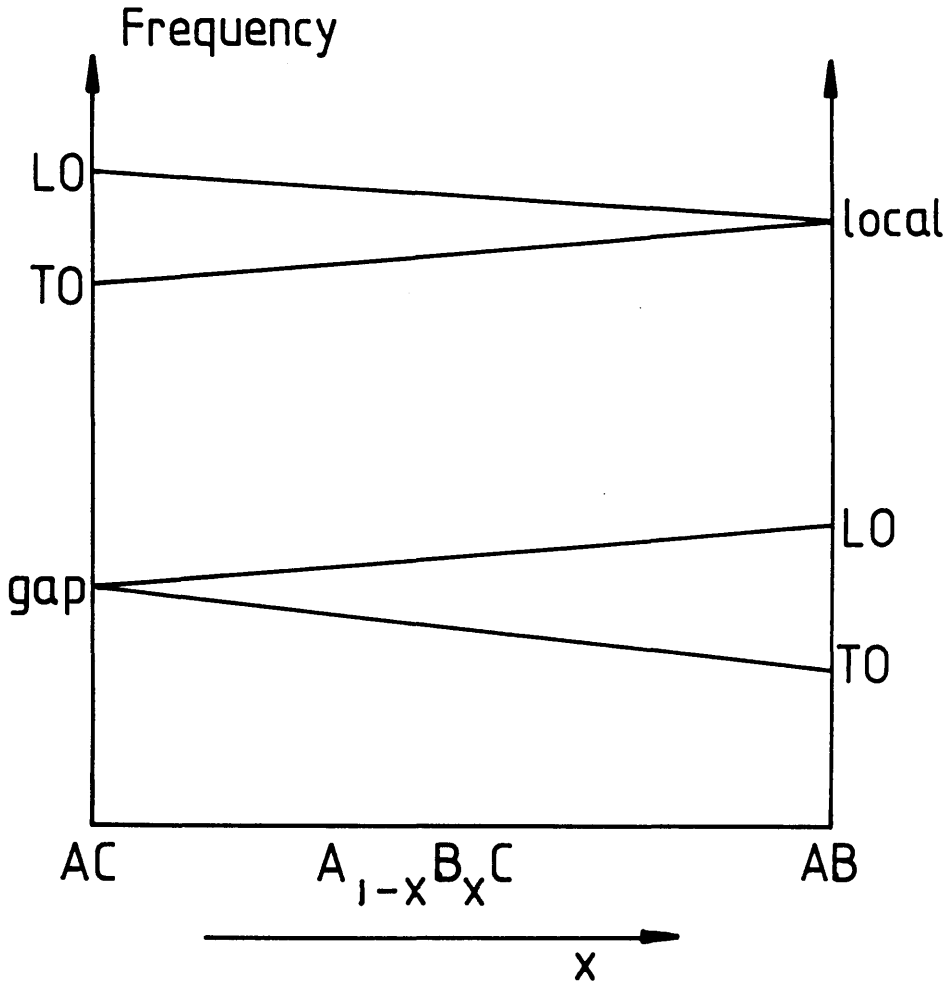

Figure 2.8 Schematic representation of two– mode alloy behaviour showing the evolution of two LO and two TO modes across the entire composition range. The upper two branches converge to the frequency of the local impurity mode of A in BC while the lower two branches converge to the frequency of the gap impurity mode of B in AC.

crystal of binary composition. These volumes will support binary phonons which will broaden and distort the phonon spectra obtained from the alloy. This effect has been investigated by Landa et al [1987] who studied the one–mode/two–mode behaviour of an alloy as a function of the lattice mismatch of its constituent binary compounds. The authors discovered an empirical rule for classifying alloy phonon behaviour based on the lattice mismatch of the binaries: if $\triangle a/a \leq 5\%$, the alloy showed two–mode behaviour, if $5\% < \triangle a/a < 7\%$, the alloy exhibited mixed–mode behaviour, while if $\triangle a/a \geq 7\%$ then one–mode behaviour was observed. This interpretation is consistent with both the work of Yamazaki et al [1982] on alloy clustering behaviour and that of Mikkelson and Boyce [1983] and Bunker et al [1988] on alloy bond lengths (see sections 2.5.1 and 2.5.2, respectively).

The different characteristics of these three types of phonon behaviour will be illustrated by looking at specific well–studied alloys: GaAlAs for two–mode behaviour, GaInP for one–mode behaviour and GaInAs as an example of mixed–mode behaviour which is discussed here because of its relevance to the work of chapter 5.

2.6.1 GaAlAs – Case Study of Two–Mode Behaviour

GaAlAs is perhaps the most thoroughly studied of all the alloys because of its importance in the semiconductor industry. It has classical two–mode behaviour with two LO modes and two TO modes throughout the entire composition range. Its mode frequencies as a function of composition are shown in figure 2.9. The frequencies are so well documented that Raman scattering measurements of the alloy phonons are used to calculate the composition of material down to a few percent of Al in GaAs [see e.g. Abstreiter et al, 1978].

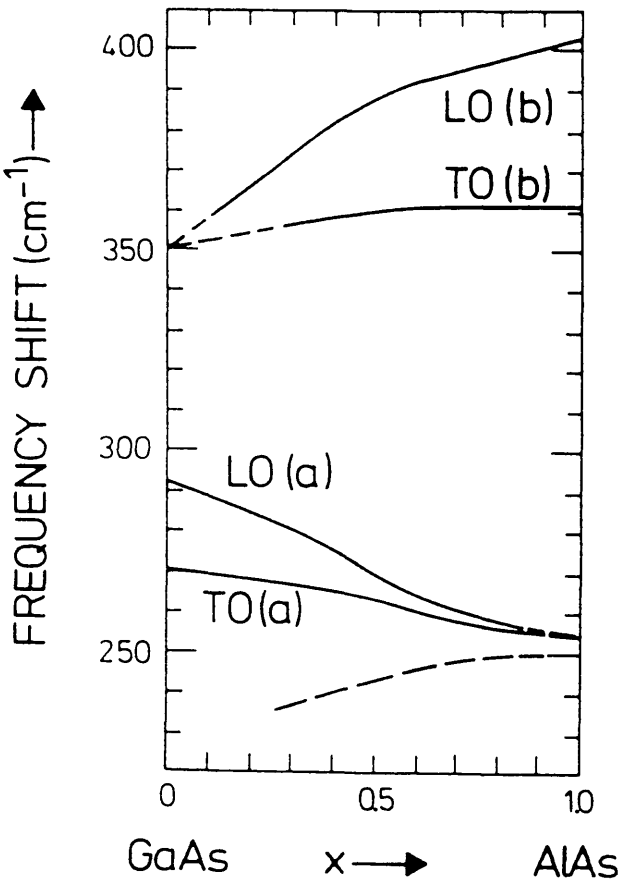

Figure 2.9 The variation of the mode frequencies of $Al_xGa_{1-x}As$ with x is shown. This plot is used to determine x in uncharacterised samples. [After Abstreiter et al, 1978].

2.6.2 GaInP – Case Study of One–Mode Behaviour

The first assignment of GaInP to one–mode behaviour was made by Lucovsky et al [1971]. The authors studied polycrystalline samples of GaInP using both the infra–red reflectivity technique and Raman scattering measurements and observed behaviour which they classified after Lucovsky et al [1968] as one–mode. This assignment was based on the behaviour of the dominant modes only; their spectra clearly show other modes assigned by later authors to a second LO and TO mode [see e.g. Bedel et al, 1984; Jusserand and Slempkes, 1984]. Subsequent Raman scattering studies of polycrystalline GaInP across the entire composition range were undertaken by Beserman et al [1976]. Two optic mode frequencies were observed which moved smoothly from one composition extreme to the other. One of these modes obeyed LO selection rules and the other obeyed TO selection rules thus the authors concluded in agreement with Lucovsky et al [1971] that GaInP was a one–mode alloy. They also observed a third peak, labelled X, which was situated between the LO and TO modes, which equalled the LO in intensity at the mid–range of alloy composition and which obeyed LO selection rules. They interpreted this feature as a disorder–induced coupling of the LO mode with non–zone–centre phonons. This mode was also reported by Bayramov et al [1981], again for polycrystalline GaInP, and with the same interpretation as to its origin.

In 1984, two papers were published refuting the idea that GaInP was a one–mode alloy and suggesting that it had two–mode behaviour. Bedel et al identified two LO modes and two TO modes across the whole range of composition. They compared the phonon intensities for single–crystal GaP, polycrystalline GaP and crystalline GaInP with the GaP phonon density of states in order to investigate the effect of strictly geometric disorder (polycrystalline GaP) with alloy substitutional disorder (crystalline GaInP). The peak labelled X by Beserman et al [1976] was

observed only in the spectrum of GaInP, thus suggesting that its origin did not lie with disorder–activated phonon coupling, and it was assigned by the authors to the second LO phonon mode. The second TO mode they estimated to be an order of magnitude weaker than the first TO mode and therefore not readily observable.

The second paper which identified two–mode behaviour in GaInP was by Jusserand and Slempkes [1984]. These authors studied GaInP as the limiting case of GaInAsP for low As concentration. They observed the InP LO mode to split into two components whenever Ga formed part of the quaternary composition. The intensity variation of both peaks with increasing Ga concentration led them to conclude that the split–off intensity was too large to be attributed to a local mode of Ga in InAsP and they assigned it to the second LO mode of GaInP. They identified the second TO mode as connecting the two impurity modes of Ga in InP and In in GaP and suggested that this would result in its intensity being very weak (see figure 2.10).

A third paper on GaInP appeared in 1984: Galtier et al published a work on both GaInP and GaAsP at atmospheric and high pressure. They studied polycrystalline GaInP and observed one–mode alloy behaviour with additional features at lower energy than the LO and the TO modes (BL and BT respectively, where BL corresponds to the mode labelled X by Beserman et al [1976]). The evolution of these modes as a function of hydrostatic pressure was monitored by Raman scattering at pressures up to 130 kbar. It was discovered that the LO–TO splitting increased as a function of pressure in contrast to all other measurements on both III–V and II–VI zinc–blende compounds (both of which exhibit a decrease in the LO–TO split which is linear in pressure squared). The authors concluded from this observation that the spectral peaks at high pressure in GaInP no longer corresponded to zone–centre phonon modes but instead to modes further out in the phonon dispersion curve. Theoretical modelling of the dispersion as a function of the alloy composition yielded a good fit to the experimental data and suggested that

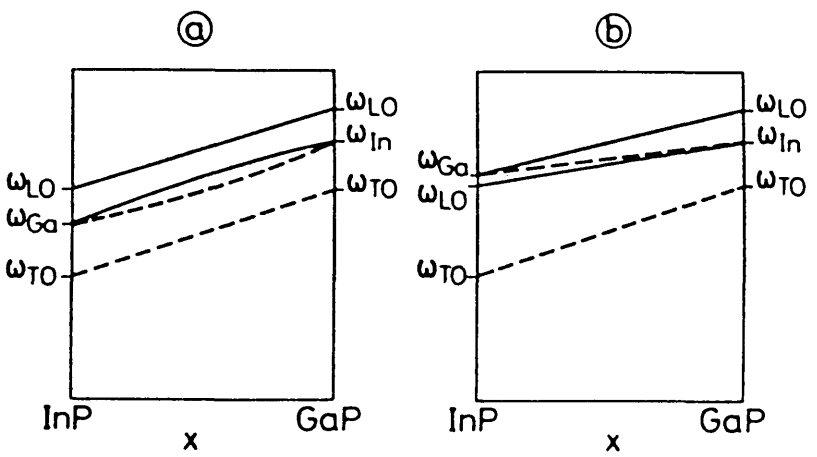

Figure 2.10 Schematic representation of the optical phonon energies in $In_{1-x}Ga_xP$ as a function of the alloy composition. (a) The one–mode behaviour model. (b) The modified two–mode behaviour model. Full lines correspond to the LO modes, dashed lines correspond to the TO modes. [After Jusserand and Slempkes, 1984]

even at atmospheric pressure, the phonons in a one–mode alloy do not have LO or TO zone–centre character. Galtier et al [1984] assign one–mode behaviour to GaInP on the basis of their observation of the LO – TO splitting. They are the only authors who do not base their assignment on the non–observance of two–mode behaviour.

Galtier et al [1984], however, remain alone in their assignment of one–mode behaviour to GaInP. Two recent works, Bedel et al [1985] and Wicks et al [1986] corroborate the identification of two–mode alloy behaviour. In one sense, the dispute is merely one of terminology: what Lucovsky et al [1971] call one–mode behaviour (despite their acknowledgement of TO(2) and LO(2) features), Bedel et al [1984] call two–mode behaviour; in the case of the former, the dominant modes serve to categorise the alloy, with the latter, all the modes are included, both weak and strong. The interpretation of Galtier et al [1984] is not so easily incorporated into this picture. The authors reported a fundamental difference in the nature of the modes for a one–mode alloy and independent corroboration of this must be made before significant conclusions can be drawn from their work.

In summary, GaInP is a one–mode alloy in the sense that one pair of optic frequencies dominates its spectrum. The optical modes can be interpreted, however, in terms of a two mode alloy with the usual two LO modes and two TO modes merely by considering one set of modes to be much weaker than the other.

2.6.3 GaInAs – Case Study of Mixed–Mode Behaviour

In the light of the discussion of one–mode phonon behaviour, mixed–mode behaviour can also be interpreted within the framework of two–mode behaviour. Mixed–mode behaviour is defined as the intermediate condition between one–mode and two–mode behaviour when the alloy shows one or the other type of behaviour

depending on composition. The definition is usually widened to include any departure from one– or two–mode behaviour.

The first reported study of the optical phonon modes of GaInAs was made by Brodsky and Lucovsky [1968] using infra–red reflectivity measurements. They observed a two–mode behaviour in InAs–rich samples, a one–mode behaviour in GaAs–rich samples and a smooth transition between the two. For GaInAs, two–mode behaviour, in the definition of Chang and Mitra [1971], is precluded because the restrahlen band of GaAs is not well separated from the phonon continuum; equally, one–mode behaviour cannot occur because the restrahlen bands of GaAs and InAs do not overlap. The result is the mixed–mode behaviour observed. The work on GaInP (see previous section) suggests that two–mode behaviour is the norm for a ternary alloy but that the observable modes are modified by the relative locations of the restrahlen regions of the end members of the alloy. This explains well the behaviour of GaInAs and is in agreement with a number of authors. Jain et al [1985] report that "the alloy $In_XGa_{1-X}As$ exhibits partially two–mode behaviour in which the GaAs–like LO and TO phonons are observed throughout the composition range but InAs–like LO and TO phonons are not observed for $X \leq 0.20$ because of their small oscillator strength"; Kakimoto and Katoda [1982] observe all four phonon modes in their GaInAs (i.e. two LO modes and two TO modes); the work of Davey et al [1987] and that of Carles et al [1985] support this interpretation. The results of Pearsall et al [1983], however, do not agree with this interpretation. The authors observed four optical phonon peaks in their Raman spectra of $Ga_{0.47}In_{0.53}As$: one LO, one TO and two which obeyed neither set of selection rules. The spectra of Pearsall et al [1983] are qualitatively different from any of the other published spectra in that their resolution of the alloy modes for this alloy composition is much better. This suggests a difference in the microscopic nature of the samples used by Pearsall et al and the quality of their samples should be tested by another technique prior to interpreting their Raman

scattering data. It is possible that their samples have excessive clustering which would tend to allow distinct phonon modes corresponding to the GaAs or InAs clusters and this may account for their unusually well– resolved spectra.

Recent work on GaInAs alloys has involved comparisons of the expected oscillator strengths with the observed phonon intensities in order to find the reason why some modes are weaker than others [Nash et al, 1987]. It was found that the polarisation field for the higher energy LO mode was larger than that for the lower energy LO mode thus enhancing the electron– phonon interaction for the higher energy branch. This is consistent with the intensities of the GaAs– like and InAs– like modes observed in Raman scattering and also with the magnetophonon resonance results of Sarkar et al [1985], Portal et al [1983] and Sugimasa et al [1985] all of which show a stronger signal from the higher– energy GaAs– like modes.

2.7 Summary

Throughout this chapter, GaInAs has been of particular interest. This alloy has been described as mixed–mode but, as has been shown here, it can be regarded as a two–mode alloy with one weak set and one strong set of phonons. The reason for the difference in the oscillator strengths of the two LO phonons is that the Froehlich coupling constant is much larger for GaAs–like phonons than for InAs–like phonons (0.05 as opposed to 0.01 [Nash et al, 1987]). Thus, the spectra of GaInAs given in chapter 5 (see e.g. figure 5.1) reflect this by exhibiting one dominant LO phonon and one weaker LO phonon.

The expected linewidths for the GaInAs phonons can be deduced, in part, by considering the alloy quality. The role of the growth method was studied by Parayanthal and Pollak [1984] for $Ga_{0.47}In_{0.53}As$–InP grown by MBE, MOCVD, VPE and LPE. They used the phonon confinement model described in section 6.2.2.1 to interpret their data in terms of alloy potential fluctuations leading to a length parameter describing the spatial extent of the potential fluctuations. The authors discovered that the MBE–grown samples exhibited the narrowest lines and lowest asymmetry ($\Gamma \approx 4cm^{-1}$, $\Gamma_a/\Gamma_b < 1.5$) while the MOCVD–grown samples showed the broadest and most asymmetric of the peaks ($\Gamma \approx 6cm^{-1}$, $\Gamma_a/\Gamma_b \approx 1.7$). If these values are considered in terms of a total alloy phonon region of about $45cm^{-1}$ from the InAs–like TO to the GaAs–like LO then it can be seen that this level of broadening (with spectral slitwidth contributions) is just sufficient to produce the continuous band that is observed experimentally. The typical resolution for the spectra shown in chapter 5 is $5cm^{-1}$. Nevertheless, since the four spectral peaks are not expected to be equally spaced in this region [Brodsky and Lucovsky, 1968] it is unlikely that improving instrumental resolution would be sufficient to yield a fully–resolved spectrum. Since the electron mobility at low temperatures is limited

by alloy potential fluctuations, the mobility can be taken as a measure of alloy quality and samples which have a high mobility are likely to exhibit narrow linewidths in their phonon spectra. In this case, the samples which are likely to show the best–defined phonon Raman spectra can be selected on the basis of their electron mobility.

References

G Abstreiter, E Bauser, A Fischer and K Ploog; Appl Phys 16, 352, 1978

A S Barker; Phys Rev 165, 917, 1968

A S Barker and A J Sievers; Rev Mod Phys 47 Suppl 2, S1, 1975

B H Bayramov, V V Toporov, Sh B Ubaydullaev, L Hildisch and E Jahne; S S Comm 37, 963, 1981

E Bedel, R Carles, G Landa and J B Renucci; Revue Phys Appl 19, 17, 1984

E Bedel, R Carles, A Zwick, M A Renucci and J B Renucci; Phys Stat Sol (b) 130, 467, 1985

E Bedel, G Landa, R Carles, J P Redoules and J B Renucci; J Phys C19, 1471, 1986

R Beserman, C Hirliman, M Balkanski and J Chevallier; S S Comm 20, 488, 1976

M H Brodsky; in "Light Scattering in Solids I", edited by M Cardona, published by Springer–Verlag, Berlin, Heidelberg, New York, 1982; p205

M H Brodsky and G Lucovsky; Phys Rev Lett 21, 990, 1968

B A Bunker, Q T Islam, P Bandyopadhyay and W F Pong; Superlatt Microstr 4, 489, 1988

M Cardona in "Light Scattering in Solids II: Basic Concepts and Instrumentation", edited by M Cardona and G Guentherodt, published by Springer–Verlag, Berlin, Heidelberg, New York, 1982; p19

R Carles, G Landa and J B Renucci; S S Comm 53, 179, 1985

R Carles, N Saint–Cricq, J B Renucci and R J Nicholas; J Phys C13, 899, 1980

I F Chang and S S Mitra; Adv Phys 20, 359, 1971

S T Davey, P C Spurdens, B Wakefield and A W Nelson; Appl Phys Lett 51, 758, 1987

P Galtier, J Chevallier, M Zigone and G Martinez; Phys Rev B30, 726, 1984

A Gomyo, T Suzuki, K Kobayashi, S Kawata, I Hino and T Yuasa; Appl Phys Lett 50, 673, 1987

W Hayes and R Loudon; "Scattering of Light by Crystals", published by John Wiley and Sons, New York, 1978; p182

K P Jain, R K Soni, S C Abbi and M Balkanski; Phys Rev B32, 1005, 1985

B Jusserand and S Slempkes; S S Comm 49, 95, 1984

K Kakimoto and T Katoda; Appl Phys Lett 40, 826, 1982

K Kakimoto and T Katoda; Japn J Appl Phys 24, 1022, 1985

J A Kash, S S Jha and J C Tsang; Phys Rev Lett 58, 1869, 1987

W Kauschke and M Cardona; Phys Rev B33, 5473, 1986

W Kauschke, A K Sood, M Cardona and K Ploog; Phys Rev B36, 1612, 1987

W Laidig, N Holonyak, M D Camras, K Hess, J J Coleman, P D Dapkus and J Bardeen; Appl Phys Lett 38, 776, 1981

G Landa, R Carles and J B Renucci; Proc 18th ICPS, Stockholm, Vol 2, edited by O Engstroem, published by World Scientific, Singapore, 1987; p1361

"Landolt–Boernstein Numerical Data and Functional Relationships in Science and Technology. Group III: Crystal and Solid State Physics" Vol 17a: Physics of Group IV Elements and III–V Compounds, edited by O Madelung, published by Springer–Verlag, Berlin, Heidelberg, New York, 1982; sections 2.10, 2.11, 2.14 and 2.16

G Lucovsky, M H Brodsky and E Burstein in "Localised Excitations in Solids", edited by R F Wallis, published by Plenum, New York, 1968; p592

G Lucovsky, M H Brodsky, M F Chen, R J Chicotka and A T Ward; Phys Rev B4, 1945, 1971

J Menendez and M Cardona; Phys Rev B31, 3696, 1985

J Menendez, M Cardona and L K Vodopyanov; Phys Rev B31, 3705, 1985

J C Mikkelson and J B Boyce; Phys Rev B28, 7130, 1983

K J Nash, M S Skolnick and S J Bass; Semicond Sci Technol 2, 329, 1987

L Nordheim; Ann Physik 9, 607, 1931

P Parayanthal and F H Pollack; Phys Rev Lett 52, 1822, 1984

T P Pearsall, R Carles and J C Portal; Appl Phys Lett 42, 436, 1983

A Pinczuk and E Burstein in "Light Scattering in Solids I: Introductory Concepts", edited by M Cardona, published by Springer–Verlag, Berlin, Heidelberg, New–York, 1983; p23

J C Portal, J Cisowski, R J Nicholas, M A Brummell, M Razeghi and M A Poisson; J Phys C16, L573, 1983

C S Rama Rao, S Sundaram, R L Schmidt and J Comas; J Appl Phys 54, 1808, 1983

C K Sarkar, R J Nicholas, J C Portal, M Razeghi, J Chevrier and J Massies; J Phys C18, 2667, 1985

R K Soni, S C Abbi, K P Jain, M Balkanski, S Slempkes and J L Benchimol; J Appl Phys 59, 2184, 1986

T Sugimasa, T Yamasaki, H Hazama, T Imachi and C Hamaguchi; Jpn J Appl Phys 25, Suppl 25−1, 55, 1985

M Teicher, R Beserman, M V Klein and H Morkoc; Phys Rev B29, 4652, 1984

K K Tiong, P M Amirtharaj, F H Pollack and D E Aspnes; Appl Phys Lett 44, 122, 1984

J A Van Vechten and T K Bergstresser; Phys Rev B1, 3351, 1970

J Wagner; Private communication, 1986

B A Weinstein and G J Piermarini; Phys Rev B12, 1172, 1975

G W Wicks, D P Bour, J R Shealy and J T Bradshaw; in "Gallium Arsenide and Related Compounds", Inst Phys Conf Series 83, edited by W T Lindley, published by IOP Publishing Ltd, Bristol, 1987; p257

S Yamazaki, M Kishi and T Katoda; Phys Stat Sol (b) 113, 421, 1982

CHAPTER 3

PHONONS IN III–V LOW DIMENSIONAL SYSTEMS: THEORY AND REVIEW

3.1 Introduction

The initial proposal for a semiconductor superlattice was put forward by Esaki and Tsu [1969]. The idea was to fabricate thin layers of alternating semiconductors thus producing a periodic modulation of the energy gap of the material (see figure 3.1). This modulation resulted in novel electronic properties such as the confinement of carriers into a two dimensional electron or hole gas (2DEG or 2DHG) in which the carriers are trapped in one or other of the layers. Once in a layer of dimensions smaller than their de Broglie wavelengths (say approx. 50 Å), the carriers experience electronic quantum–mechanical confinement resulting in discrete energy levels and a density of states different from that of the bulk (see figure 3.2). An overview of many of the implications of this for electrical devices such as the HEMT is given by Esaki [1986].

The evolution of high–precision growth methods suitable for semiconductors has enabled layered structures such as the heterojunction, quantum well and superlattice to be realised experimentally. The growth methods (molecular beam epitaxy (MBE), metalorganic chemical vapour deposition (MOCVD), and, more recently, metalorganic

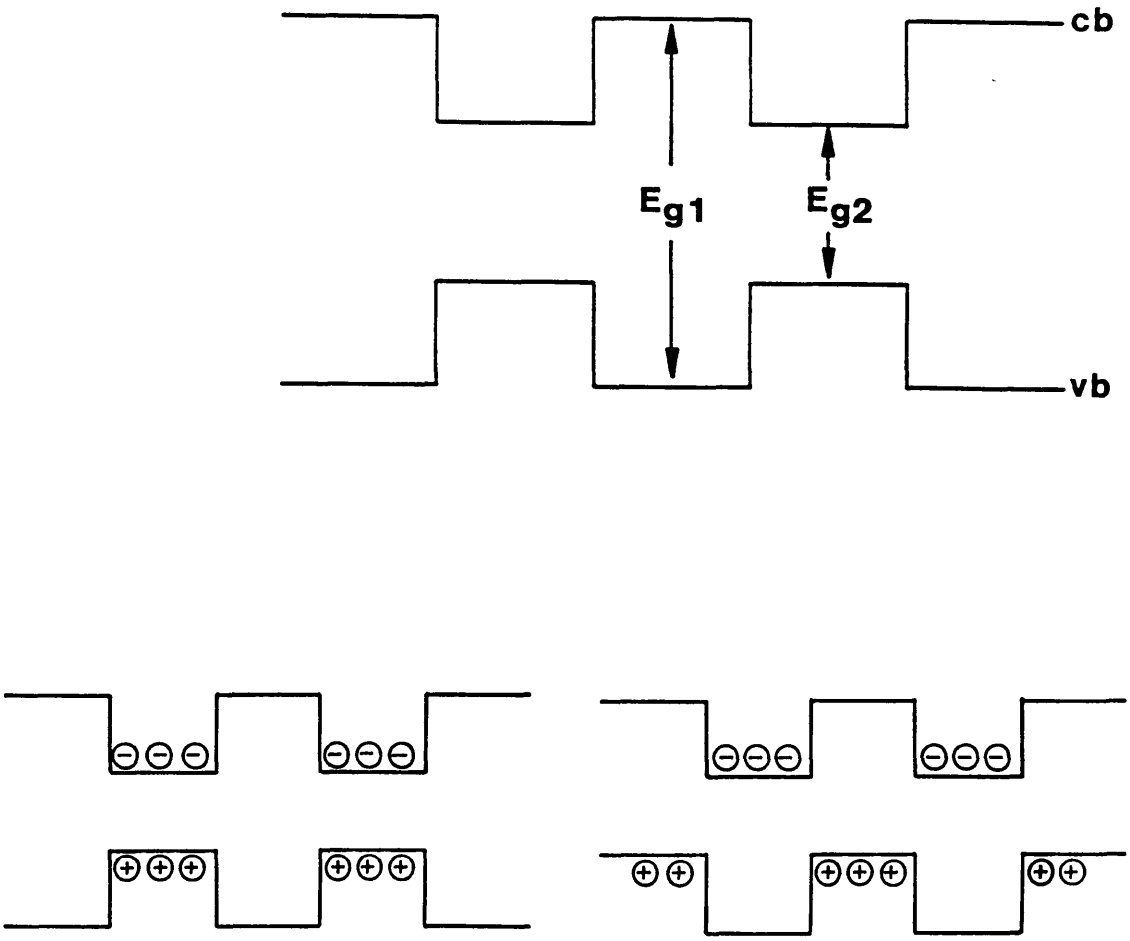

Figure 3.1 Schematic representation of a semiconductor superlattice comprising alternating layers of material with energy gaps E_{g1} and E_{g2}. Electrons and holes can be confined either in the same layer (type one superlattice, lower left) or in alternate layers (type two superlattice, lower right).

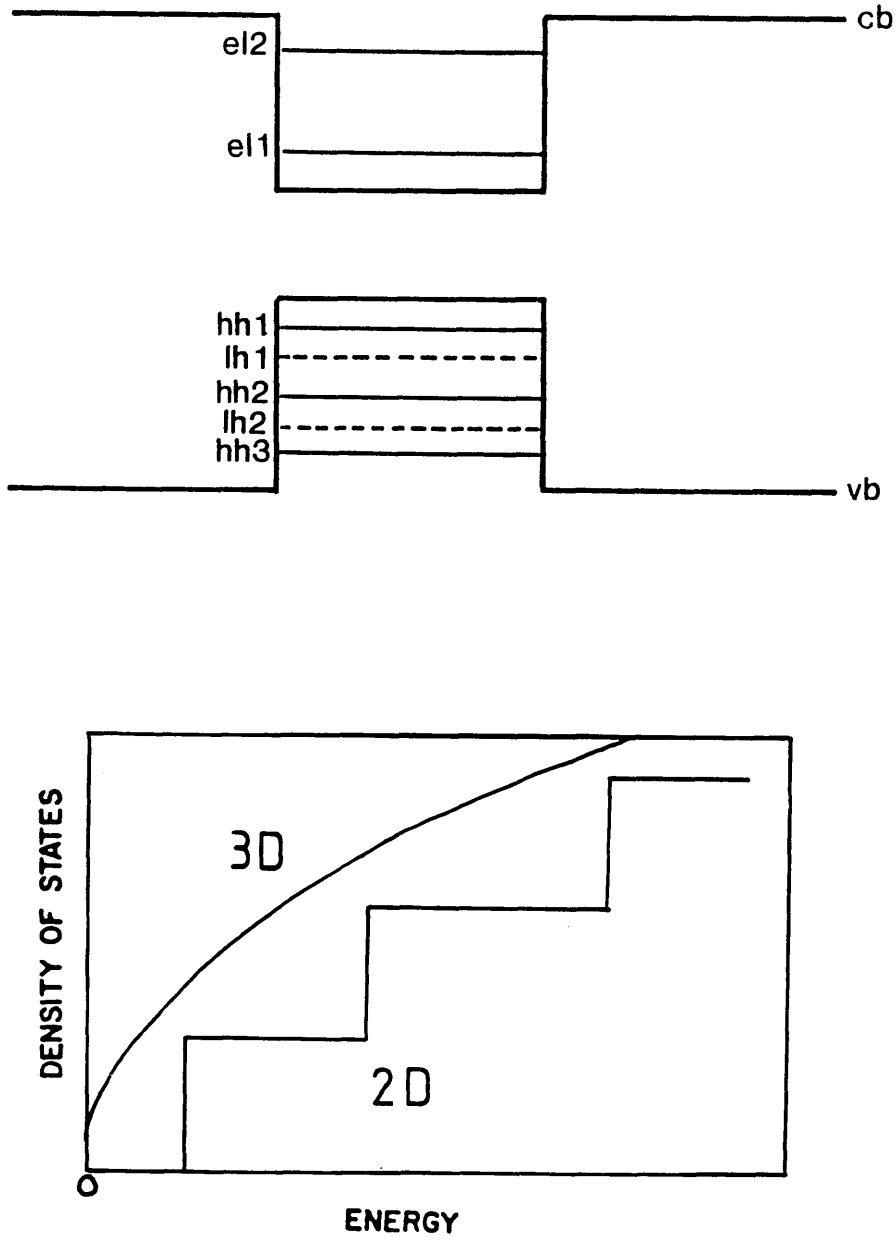

Figure 3.2 Upper Schematic representation of the discrete electron and hole energy levels confined in a quantum well.

Lower Comparison of the theoretical density of states for three dimensional (3D) and two dimensional (2D) systems.

MBE (MOMBE)) all allow single atomic layers to be deposited on a prepared substrate. Thus, for example, GaAs is grown by MBE from two solid sources, one of Gallium and one of Arsenic. These are heated to produce a flux of atoms. The two atomic beams are then directed onto a preheated substrate where the epitaxial growth takes place. Typical growth rates are of the order of a few microns per hour at temperatures in the region of 500–700°C. Layered structures are formed by allowing a sequence of different atomic beams to impinge onto the substrate. Although simple in concept, these growth methods are far from easy in practice and stringent purity and high vacuum conditions are required to produce good quality material [see e.g. Ploog, 1987; Claxton et al, 1987].

The debate on which growth technique produces the best quality material has raged as long as the growth methods have existed. The consensus of opinion is that MBE–grown samples have a better interface quality between the layers. This is evident in the fact that most published work on short period superlattices (where interface quality is crucial) has involved MBE–grown samples [see e.g. Sood et al, 1985; Jusserand et al, 1986; Sapriel et al, 1988].

Some of the optical properties of the quantum well structure have already been exploited to produce, for example, the quantum well laser. These have two advantages over the normal bulk semiconductor laser: the emission frequency can be varied by varying the well width and, secondly, the layered structure can be used as a light guide for the laser output thus forming a basic unit for optical integration.

New physical phenomena arise when very low dimensions are achieved. The quantum Hall effect was first demonstrated by von Klitzing et al [1980] in the 2DEG formed in a Silicon MOSFET. Subsequent studies by Tsui et al [1982] on GaAs–AlGaAs 2D systems uncovered the fractional quantum Hall effect.

The growth and fabrication of low dimensional structures are dogged by the same problems as bulk materials. Defects, such as dislocations in a crystalline lattice, act as carrier traps thereby degrading both the electrical and the optical quality of

the material. Dislocations arise when a local strain in the lattice is relaxed by atoms moving away from their lattice sites to some intermediate position (see Figure 3.3). In order to avoid dislocations within a crystal, the lattice constant of each of the epitaxial layers must be the same and must also match that of the substrate. Clearly, this condition imposes a constraint on those structures which can be grown successfully. Figure 3.4 shows the range of lattice constants that occur in III– V binaries. The lattice constants of various alloy compositions are given by the solid lines. It can be seen that GaAs and AlAs have very similar lattice constants hence it is relatively easy to grow high quality GaAs– AlGaAs heterostructures.

The choice of substrate material is important to the crystal quality because it defines the lattice parameter of the epitaxial layer. It is usual to grow a few microns of buffer layer material on the substrate before growing the structure or device required. The buffer layer is designed as an intermediary to distance the impurities and dislocations of the substrate from the heterostructure. Matching the lattice parameter of an alloy to that of the substrate is crucial. If the wrong alloy composition is obtained then its lattice parameter will be correspondingly affected giving two possible growth conditions. If the mismatch is slight or the layer thin, the alloy will grow in a strained state. If the mismatch is large, or the layer thicker than the critical thickness, a relaxed layer with dislocations will be grown [Marzin, 1987]. The substrate is therefore an important factor in the quality of an overgrown layer and care should be taken to include the substrate contribution to any experimental results; for example, the one– mode/two– mode alloy behaviour discussed in section 2.6 could have a contribution from strain imposed on the epitaxial layer by a mismatched substrate.

The interest of the present work is to study the effect of low dimensions on the phonon behaviour of semiconductors. The rest of this chapter is devoted to a review of the predicted and observed effects of phonon behaviour in low dimensional systems.

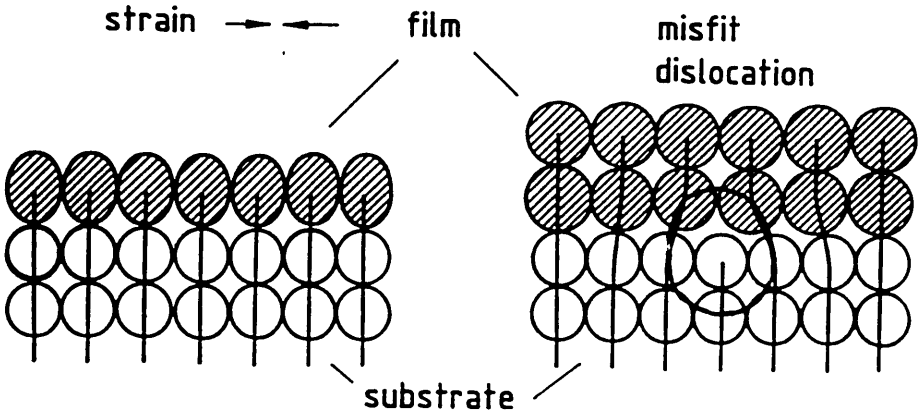

Figure 3.3 Lattice mismatch accommodation by strain (left) or misfit dislocation (right) [after Kasper, 1987].

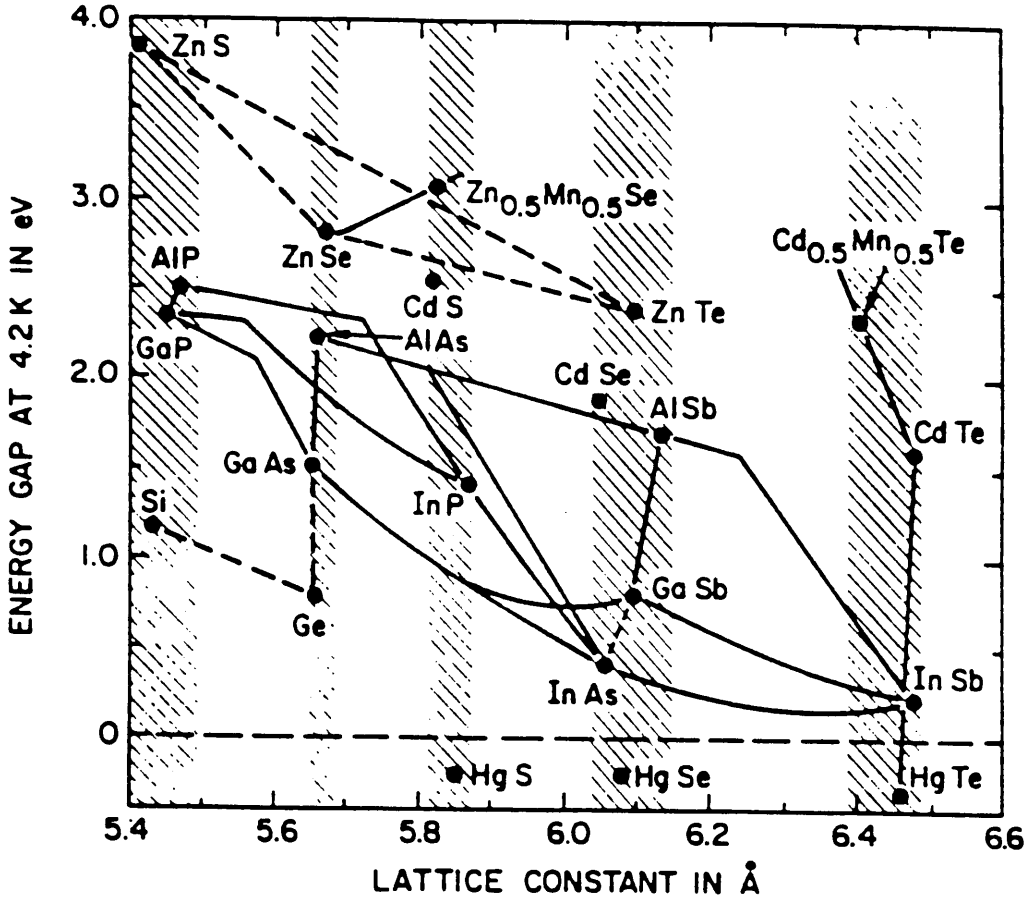

Figure 3.4 Energy gap as a function of the lattice constant for a number of III– V and II– VI semiconductors [after Esaki, 1986].

3.2 Phonons in Two Dimensions

The new periodicity along the growth axis of a semiconductor superlattice gives rise to a folding of the Brillouin zone such that the edge of the Brillouin zone moves from π/a to π/d, where a is the lattice constant and d is the superlattice period. When the superlattice period is sufficiently small, the carriers are able to tunnel quantum mechanically from one well to another thus altering the semiconductor band structure into a series of minibands with minigaps [Chang, 1985] (see figure 3.5). In a similar manner, the phonon dispersion curves must also be accommodated within the smaller Brillouin zone and it will be shown that this can result in either folding or confinement of the modes [Klein, 1986].

The phonon dispersion curve for GaAs is shown in figure 3.6. It can be seen that for each phonon mode there is a corresponding frequency range. Phonons can propagate through a layered structure if there is an overlap in the frequency range of that mode for each layer. If there is no frequency overlap then the phonons will be confined to one or the other of the layers. This concept is shown schematically in figure 3.7 for GaAs–InAs, a structure difficult to realise physically because of its large lattice mismatch. A full theoretical treatment of the phonon modes in superlattices has been published by Yip and Chang [1984]. This discussion is limited to simple models which can be applied to specific problems.

3.2.1 Propagating Modes

Experimental observations of propagating modes in semiconductor superlattices have been confined largely to the zone–folded acoustic modes. The reason for this is that the acoustical frequency ranges always overlap consequently propagating

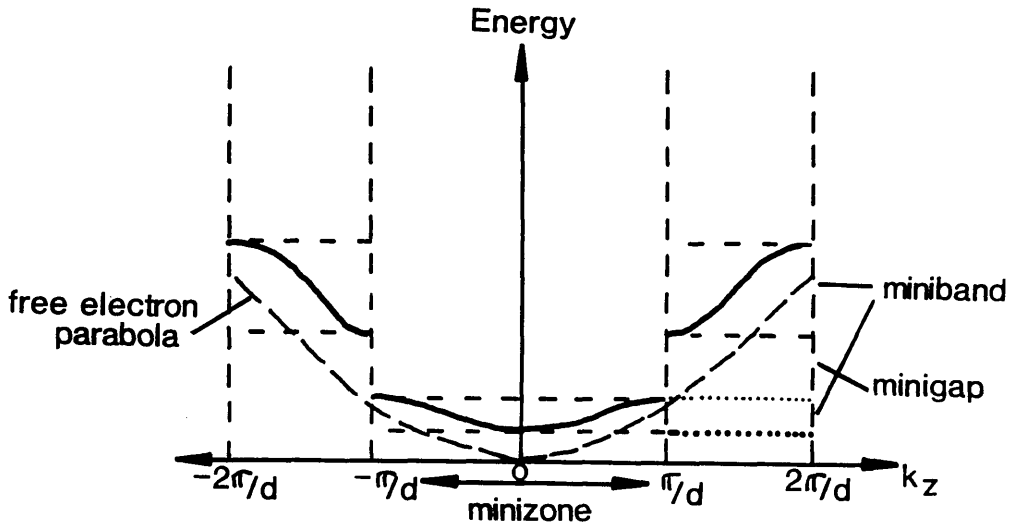

Figure 3.5 Schematic representation of the effect of the superperiodicity on the conduction band of a semiconductor. Note that the band splits into minibands separated by minigaps.

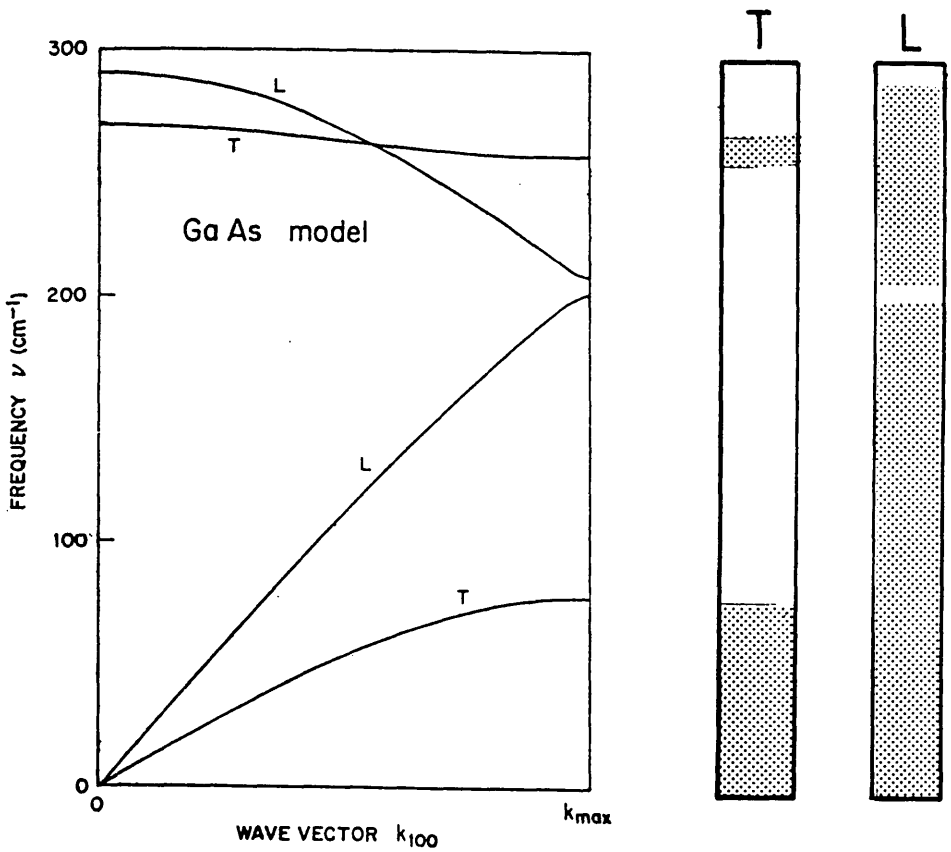

Figure 3.6 GaAs phonon dispersion curves modelled by Barker et al [1978] together with the phonon ranges of the TO and LO modes.

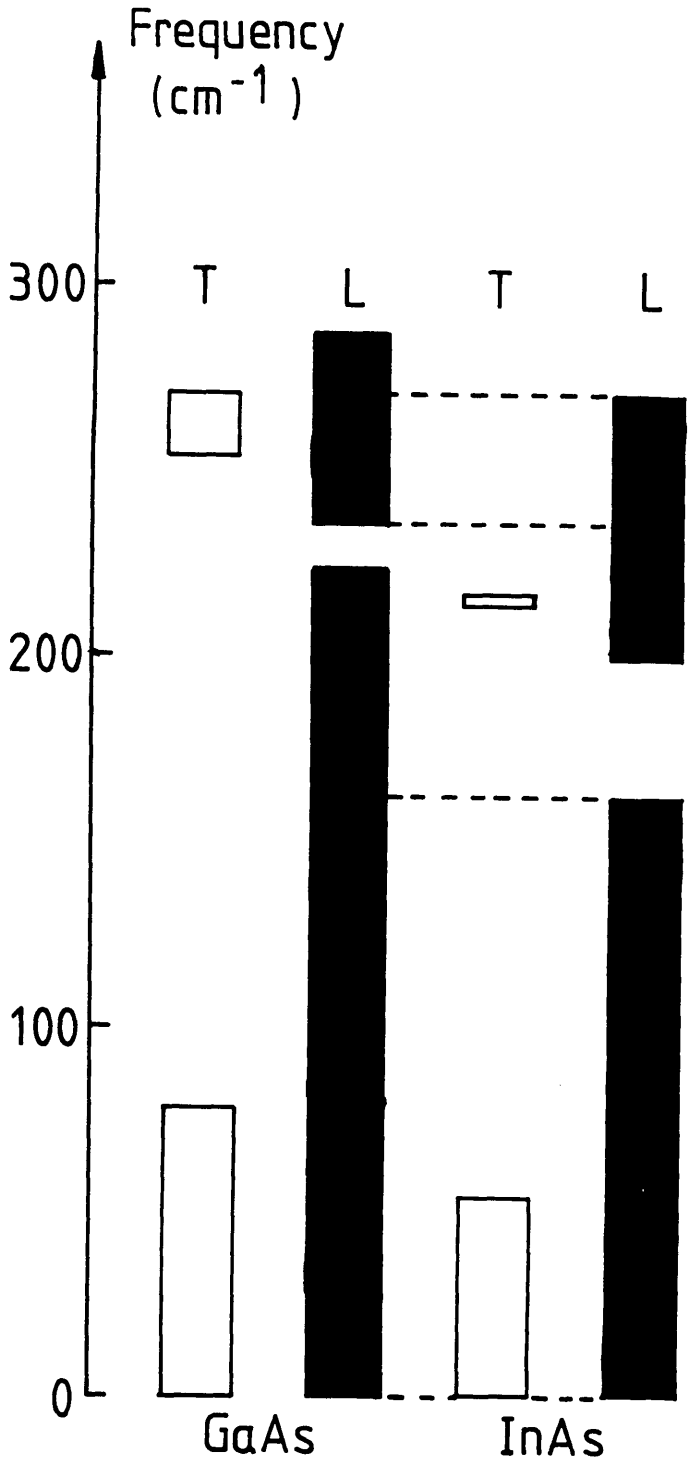

Figure 3.7 Comparison of the phonon frequency ranges of GaAs and InAs. The dashed lines show the boundaries of propagating longitudinal modes. Outwith the dashed region, the modes are confined. Note that there exist both propagating and confined LO modes but only confined TO modes.

acoustic modes always exist. It is rarer for the optical frequency ranges in a semiconductor superlattice to overlap since they have a flatter dispersion. As a result, most observations of optical phonons in superlattices have been of confined modes.

Raman scattering is a most appropriate technique to investigate the zone–folded modes as it primarily reflects the phonon density of states around $q = 0$. The reduced Brillouin zone has the effect of bringing more modes to the zone–centre thereby causing a previously forbidden scattering mechanism to become allowed (see figure 3.8). This manifests itself in new features in the Raman spectrum which appear as narrow doublets at low energy.

The first Raman scattering observation of the folded acoustic phonons was reported by Colvard et al [1980]. The authors studied a superlattice of GaAs–AlAs and observed a doublet in the low energy region of the spectrum. They assigned the two new lines to scattering from the folded longitudinal acoustic (LA) phonons and obtained a good fit to their data by modelling their system with a Kronig–Penney model for the electrons and an elastic continuum for the phonons. A model which has been used extensively to predict the folded–modes frequencies is the layered elastic continuum model [Rytov, 1956] described in section 3.2.2. Section 3.2.4 describes the one dimensional (1D) linear chain model first used by Barker et al [1978] for the study of zone–folded effects.

3.2.2 Layered Elastic Continuum

This one dimensional (1D) model was developed by Rytov [1956] to describe acoustic vibrations in layered media. It is valid for low energy phonons where the dispersion is almost linear (below about 100 cm^{-1}). It has been successfully applied to the analysis of folded acoustic modes in semiconductor superlattices of

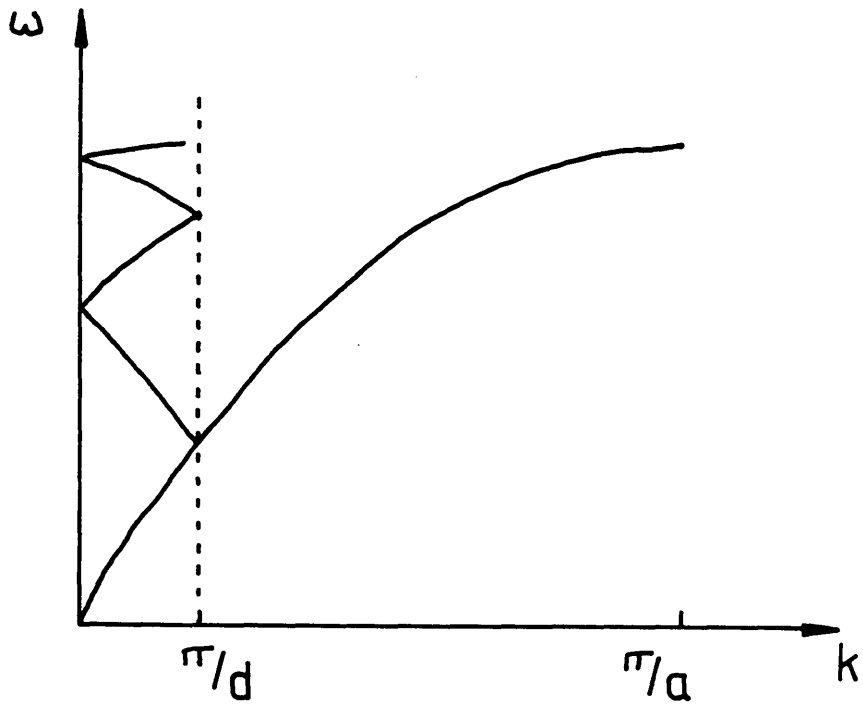

Figure 3.8 Schematic representation of the folding of an acoustic phonon dispersion curve into the reduced Brillouin zone.

GaAs– AlAs [Colvard et al, 1980], GaAs– AlGaAs [Sapriel et al, 1983; Colvard et al, 1985], Si– SiGe [Brugger et al, 1986; Lockwood et al, 1986], GaInAs– InP [Davey et al, 1987] and GaInAs– AlInAs [Davey et al, 1987]. The application of the model to semiconductor superlattices has been discussed fully by Jusserand and Pacquet [1985] and is outlined below.

The model describes vibrations with wavelengths longer than the lattice parameter such that the two layers can be regarded as effective media and characterised by their densities, ρ_1 and ρ_2, and their elastic constants, C_1 and C_2, respectively. The analagous case of an electron in a superlattice uses the effective mass and the electrostatic potential as the relevant parameters to characterise each layer for the Kronig– Penney model.

Considering propagation along the z (or growth) direction, the Lagrangian density equation for acoustic vibrations can be written as:

$$L = \frac{\rho(z)(\partial u/\partial t)^2}{2} - \frac{C(z)(\partial u/\partial z)^2}{2} \qquad (3.1)$$

where ρ (and C) take on the values of ρ_1 and ρ_2 (and C_1 or C_2) depending on whether z is in layer 1 or layer 2. The equation of motion is:

$$\frac{\partial}{\partial t}[\rho(z)(\partial u/\partial t)] - \frac{\partial}{\partial z}[C(z)(\partial u/\partial z)] = 0 \qquad (3.2)$$

which reduces within each layer to:

$$\rho_1(\partial^2 u_1/\partial t^2) = C_1(\partial^2 u_1/\partial z^2) \qquad (3.3a)$$

and

$$\rho_2(\partial^2 u_2/\partial t^2) = C_2(\partial^2 u_2/\partial z^2) \qquad (3.3b)$$

thus recovering the bulk equations with linear dispersion curves given by:

$$\omega = q\sqrt{(C_1/\rho_1)} \tag{3.4a}$$

and

$$\omega = q\sqrt{(C_2/\rho_2)} \tag{3.4b}$$

where q is the phonon wavevector.

Continuity of stress and displacement across the superlattice interfaces imply that:

$$u_1 = u_2 \tag{3.5}$$

and

$$C_1(\partial u_1/\partial z) = C_2(\partial u_2/\partial z) \tag{3.6}$$

with the latter resulting from equation 3.1. The periodicity of the superlattice allows the use of Bloch waves to provide appropriate solutions and thus:

$$u(z+d) = u(z)e^{iQd} \tag{3.7}$$

where

$d = d_1 + d_2 =$ superlattice period

$Q =$ superlattice wavevector

If the acoustic vibration is written as a linear combination of a forwards–propagating and backwards–propagating plane wave with wavevector q_1 or q_2 then:

$$u_1(z) = (\lambda_1 e^{iq_1 z} + \mu_1 e^{-iq_1 z})e^{-i\omega t} \qquad (3.8a)$$

and

$$u_2(z) = (\lambda_2 e^{iq_2 z} + \mu_2 e^{-iq_2 z})e^{-i\omega t} \qquad (3.8b)$$

This gives rise to four continuity equations, two for $z=0$ and two for $z=d$. Solving for these yields:

$$\cos(Qd) = \cos(q_1 d_1 + q_2 d_2) - \frac{\epsilon^2}{2}\sin(q_1 d_1)\sin(q_2 d_2) \qquad (3.9)$$

where

$$\epsilon = (C_1\rho_1 - C_2\rho_2)/(C_1\rho_1 + C_2\rho_2) \qquad (3.10)$$

Because ϵ is small for III–V semiconductors the dispersion curve differs very little from a folded bulk dispersion curve which is given by :

$$\omega = v_s q \qquad (3.11)$$

where

$$d/v_s = d_1/v_1 + d_2/v_2$$

and v_1 and v_2 are the sound velocities in media 1 and 2 respectively ($v = \sqrt{(C/\rho)}$). The only effect of the two–layered structure is to open up minigaps at the zone–edge and zone–centre. This is illustrated in figures 3.9(a) and 3.9(b) for the example of the GaInAs–InP sample (PMB121) discussed in chapter 5. Both the folded dispersion curve (according to equation 3.9) and the bulk dispersion (given by equation 3.11) are plotted. It can be seen that over most of the reduced Brillouin zone the bulk dispersion is a good approximation. The parameters used in the calculation are given in table 3.1, and the computer program is contained in

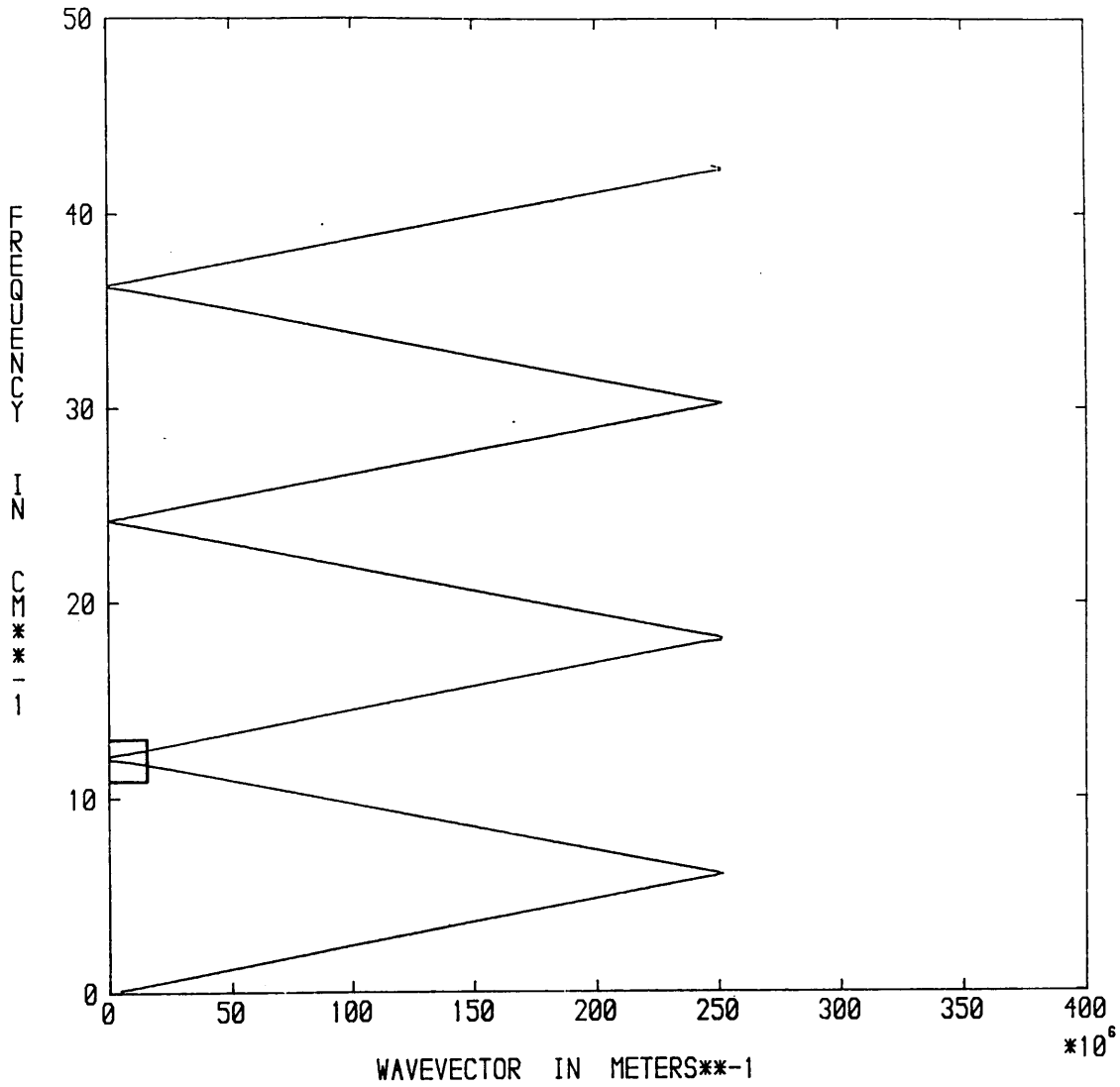

Figure 3.9 (a) Plot of the folded acoustic phonons expected for PMB121 versus wavevector perpendicular to the layers. Two curves are shown superimposed: the superlattice modes according to equation 3.9 and the folded bulk dispersion from equation 3.11. Note that the two traces are indistinguishable on this scale.

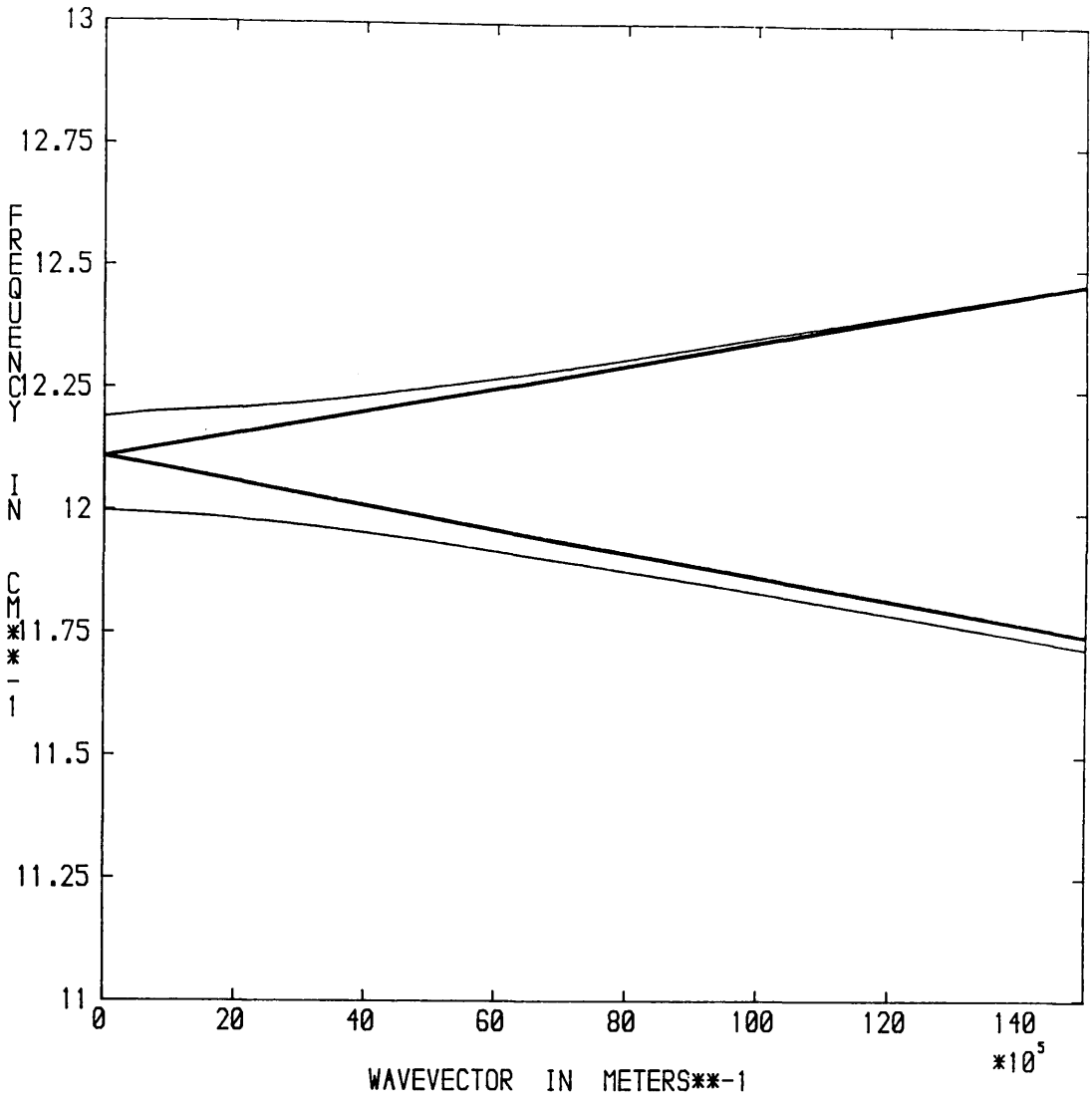

Figure 3.9(b) An expansion of the square marked on (a). The thinner line results from equation 3.9 while the thicker line is simply the folded bulk dispersion curve. Here the effect of the superlattice can be seen clearly in the minigap that has opened at the zone–centre.

Table 3.1

Parameters used in the Calculation of the Folded Acoustic Phonon Dispersion for Sample PMB121.

Parameter	GaInAs, layer 1	InP, layer 2
C_{11}	9.96×10^{10} Nm^{-2}	10.22×10^{10} Nm^{-2}
ρ	5.503×10^{3} kgm^{-3}	4.81×10^{3} kgm^{-3}
d	25×10^{-10} m	100×10^{-10} m
v	4.25×10^{3} $msec^{-1}$	4.61×10^{3} $msec^{-1}$

All values taken from Landolt–Boernstein and extrapolated where necessary for $Ga_{0.47}In_{0.53}As$.

Appendix A.

Although many experimental observations of the folded modes were made before 1986, there were none which clearly showed the coupled–phonon gap at the zone centre. The first Raman scattering observations of the zone–centre minigap were made by Jusserand et al [1986] who employed a forward scattering geometry in GaAs–AlAs superlattices in order to probe wavevectors very close to zero. Their experimental data was in good agreement with the gap sizes predicted by the elastic continuum model described above.

3.2.3 Confined Modes

Confined phonon modes in superlattices exist when there is no overlap of the phonon frequency range belonging to each of the constituent layers. Such modes are generally in the optical region of the spectrum. In this case, a given mode in one layer cannot exist in the neighbouring layers and therefore cannot propagate in the direction of growth. Since the mode is unable to propagate through the layers, it does not experience the additional periodicity of the superlattice; it will be unaffected by the reduced Brillouin zone and cannot have a folded dispersion curve as described in sections 3.2.1 and 3.2.2 for the acoustic modes. Equally, however, the mode cannot be described within the infinite crystal approximation as the layer thickness is small. The best analogy for such a mode is that of an electronic quantum well: an electron in a quantum well can have only discrete energy levels and, similarily, it can be shown that confined phonons have discrete vibrational energies which are virtually dispersionless. A small dispersion arises from the very weak interaction between layers of the same type.

Raman scattering observations of confined optical phonons have been made by a number of authors. The first study by Jusserand et al [1984] demonstrated the

existence of up to three confined LO modes in GaAs– AlGaAs superlattices. Complementary work by Zucker et al [1984] also on GaAs– AlGaAs superlattices involved a right– angle geometry for Raman scattering and probed the phonon modes parallel to the layers as well as those in the growth direction. The authors found that confined phonons in superlattice layers behaved as those in thin ionic slabs and could be described by the theory developed by Fuchs and Kliewer [1965]. The major feature of such slab modes is that the longitudinal vibration occurs at the bulk TO frequency while the transverse vibration occurs at the bulk LO frequency. Zucker et al [1984], however, unlike Jusserand et al [1984], saw only the highest energy confined optical mode with no evidence for any others.

A combined investigation of both the folded acoustic and the confined optic modes was undertaken by Colvard et al [1985] in which the authors studied GaAs– AlGaAs superlattices and were able to observe four confined longitudinal optical phonons. The authors used both the linear chain model (see section 3.2.4) and the dielectric continuum model (see section 3.3.1) to fit their data. Similar work by Sood et al [1985] demonstrated not only confined longitudinal optical phonons but also confined transverse optical phonons.

3.2.4 Linear Chain Model

The 1D linear chain model has been applied to superlattices by Barker et al [1978]. The 1D model is adequate to incorporate the superlattice effects as the superperiodicity is also 1D. It is particularly appropriate for the discussion of superlattice interfaces as discussed in section 3.3.2.

The simplest form of the model considers a binary– binary superlattice and involves only nearest neighbour interactions (i.e. force constants and lattice parameters). It can be written as follows [Jusserand and Paquet, 1985].

The complex dispersion curve of a linear chain with two atoms per unit cell

(masses M_A and M_B) is given by:

$$\cos(qa) = 1 - \frac{(M_A + M_B)\omega^2}{\alpha} + \frac{M_A M_B \omega^4}{2\alpha^2} \qquad (3.12)$$

where

α = force constant

a = lattice constant

If the longitudinal displacements of atoms A and B are denoted by U and V respectively, then the displacements within any given unit cell can be written as:

$$U = \alpha(1 + e^{-ika}) \qquad (3.13a)$$

$$V = 2\alpha - M_A\omega^2 \qquad (3.13b)$$

If, instead of an infinite chain of $-A-B-A-B-A-$, a superlattice of $-A-B-A-B-A-C-A-C-A-B-$ is considered, where A is the common atom (e.g. AlAs–GaAs), then equations 3.13 still apply but must be subscripted by 1 or 2 depending on whether the atom is in AB or AC. Thus for the j–th atom in medium 1, the displacement is given by the linear combination:

$$U_{j1} = \lambda_1\alpha(1 + e^{-iq_1a_1})e^{ijq_1a_1} + \mu_1\alpha(1 + e^{iq_1a_1})e^{-ijq_1a_1} \qquad (3.14a)$$

and

$$V_{j1} = \lambda_1(2\alpha - M_A\omega^2)e^{ijq_1a_1} + \mu_1(2\alpha - M_A\omega^2)e^{-ijq_1a_1} \qquad (3.14b)$$

where λ and μ must be continuous across the superlattice interface. When the interface continuity equations have been solved together with the secular equation,

the following dispersion relation is obtained:

$$\cos(Qd) = \cos(n_1 q_1 a)\cos(n_2 q_2 a) - \frac{(1 - \cos(q_1 a)\cos(q_2 a))\, \sin(n_1 q_1 a)\sin(n_2 q_2 a)}{\sin(q_1 a)\sin(q_2 a)} \qquad (3.15)$$

This has been plotted by Jusserand and Paquet [1985] for the case that A, the common atom, is the heaviest. Their diagram is shown in figure 3.10 and shows only confined optical phonons for the case of non−overlap of the AB and AC phonon frequency regions. Both confined and propagating optical phonons are present for the case of some overlap of the frequency ranges. An illustration of the atomic displacements associated with three specific modes is given in part (c) of figure 3.10.

It is possible to extend this simple model by using a three dimensional (3D) lattice mapped on to a 1D linear chain thereby preserving the 3D parameters. This calculation has been performed for GaAs−AlAs by Molinari et al [1986] and has proved to reproduce fairly well the expected superlattice phonon dispersion curves although the authors offer no direct comparison with experiment.

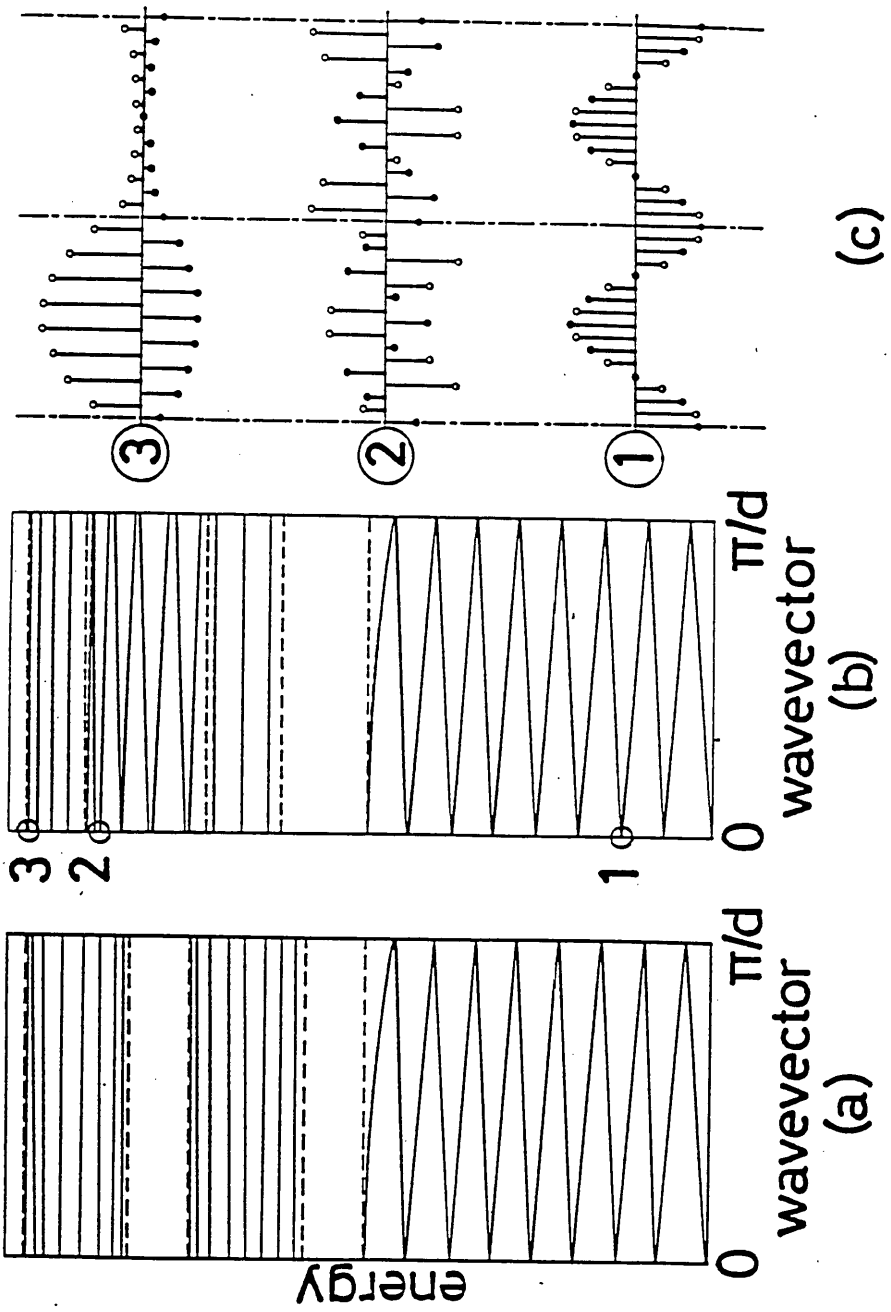

Figure 3.10 Schematic dispersion curves of two superlattices made of bulk materials with (a) not overlapping and (b) overlapping optical branches. (c) shows typical eigendisplacements for the modes labelled in (b) [after Jusserand and Paquet, 1985].

3.3 Interface Modes

As well as sustaining both propagating and confined phonon vibrations, the layered nature of a superlattice, with its many interfaces, means that it can also support interface phonons. These are defined as modes with an exponentially– decreasing amplitude of vibration away from the interface. The nature of these modes is closely related to that of the surface modes discussed in chapter 7 and their theoretical description is therefore qualitatively similar.

Interface phonons have been observed in GaAs– AlGaAs superlattices using Raman scattering by a number of authors [Sood et al, 1985(b); Arora et al, 1987; Gammon et al, 1987]. The modes can be described by a dielectric continuum model which is discussed in section 3.3.1. The model predicts interface modes which have wavevectors parallel to the interface and therefore parallel to the superlattice layers. These modes should be strictly forbidden for Raman scattering in the backscattering geometry, nevertheless, all three observations of the interface modes have been performed in the backscattering geometry. This apparent anomaly is interpreted as a breakdown of wavevector– conservation arising from impurities and defects at the interface [Sood et al, 1985(b)]. A more detailed investigation into the nature of the wavevector– conservation breakdown has been discussed by Gammon et al [1988] who studied GaAs– AlGaAs interface phonons by Raman scattering both with and without an applied external magnetic field. They observed an enhancement in intensity of the interface mode when the experiment was performed with the magnetic field but have been unable so far to resolve the nature of the defect(s) involved.

3.3.1 Dielectric Continuum Model

This theory is based on the surface vibrations of ionic slabs, first discussed by Fuchs and Kliewer [1965], and later extended to superlattices [Camley and Mills, 1984]. The dispersion of the interface modes can be written as follows if retardation effects (polaritons) can be neglected (i.e. if the interface wavevector $q \gg \omega_{TO}/c$ which is generally true for these experiments [Zucker et al, 1984]).

$$\cos(q_z D) = \frac{(\eta^2 + 1)\sinh(q_x d_1)\sinh(q_x d_2) + \cosh(q_x d_1)\cosh(q_x d_2)}{2\eta} \qquad (3.16)$$

where

d_1 and d_2 = layer thicknesses of materials 1 and 2 respectively

$D = d_1 + d_2$ = superlattice period

q_z and q_x = phonon wavevectors perpendicular and parallel to the layers, respectively

$\eta = \epsilon_1(\omega)/\epsilon_2(\omega)$ = the ratio of the frequency dependant dielectric constants for the two materials

and, for a binary semiconductor,

$$\epsilon(\omega) = \epsilon_\infty \frac{(\omega_L^2 - \omega^2)}{(\omega_T^2 - \omega^2)}$$

or, for a two-mode alloy,

$$\epsilon(\omega) = \epsilon_\infty \frac{(\omega_{L1}^2 - \omega^2)(\omega_{L2}^2 - \omega^2)}{(\omega_{T1}^2 - \omega^2)(\omega_{T2}^2 - \omega^2)}$$

This relation (3.16) predicts interface modes in the vicinity of the optical modes of each layer i.e. a GaAs-like and an AlAs-like mode for the GaAs-AlAs

superlattices and a GaAs– like mode from the wells together with both a GaAs– like mode and an AlAs– like mode from the AlGaAs barriers in GaAs– AlGaAs superlattices. All three predicted modes have been observed by Arora et al [1987] for a GaAs– AlGaAs superlattice and the experimental frequencies agree well with those calculated using the dielectric continuum model.

Calculations of the expected interface mode frequencies for GaInAs– InP superlattices have been undertaken by Portal et al [1984] as an aid to interpreting their magnetophonon resonance data. A subsequent publication by Nash et al [1987], however, points out a mistake in the calculation and hence the calculation will be undertaken here for one of the samples of interest: PMB121. The parameters are given in table 3.2 and the results are shown in figures 3.11 and 3.12 for three values of q_x. Figure 3.11 shows the variation in η as a function of ω. The interface modes will exist where $\eta < 0$. It can be seen in figure 3.12 that a gap has opened between the symmetric and antisymmetric branches of the interface modes and this is attributable to the different thicknesses of the two layers [Camley and Mills, 1984].

The mode that would be most easily seen in this GaInAs– InP system would be the high– frequency mode between the LO and the TO of the InP. The other two modes would be masked by the broad alloy structure discussed in section 5.2 of this work. In addition, the interface modes have been observed only when the incident laser light has been in resonance with the excitons in the wells [Sood et al, 1985; Arora et al, 1987; Gammon et al, 1987]. This is comparatively simple for the case of GaAs– AlGaAs where the exciton resonances can be reached easily using a dye laser together with photon counting techniques. The GaInAs– InP exciton resonance, however, lies at 1.34 μm at 4K [Roberts, 1988] and is therefore well outside the capability of the available instrumentation both with regard to excitation sources and detectors. It seems likely that other experimental techniques (such as far infra– red spectroscopy) will be needed to observe the interface modes of this sample.

Table 3.2

Calculation of the Interface Phonons for Sample PMB121.

Parameters used.

Parameter	GaInAs, layer 1	InP, layer 2
d	25 Å	100 Å
ω_L	ω_{L1} = 232 cm^{-1} (a) ω_{L2} = 265 cm^{-1} (a)	348 cm^{-1} (a)
ω_T	ω_{T1} = 226 cm^{-1} (b) ω_{T2} = 254 cm^{-1} (b)	304 cm^{-1} (a)
ϵ_∞	11.62 (c)	9.61 (d)
n	4.35 (e)	3.851 (f)

(a) Data obtained from Raman scattering experiments undertaken in this work

(b) Pearsall et al [1983]

(c) Landolt– Boernstein [1982], interpolated from the binary values

(d) Landolt– Boernstein [1982]

(e) Aspnes and Studna [1983], interpolated from the binary values

(f) Palik [1985]

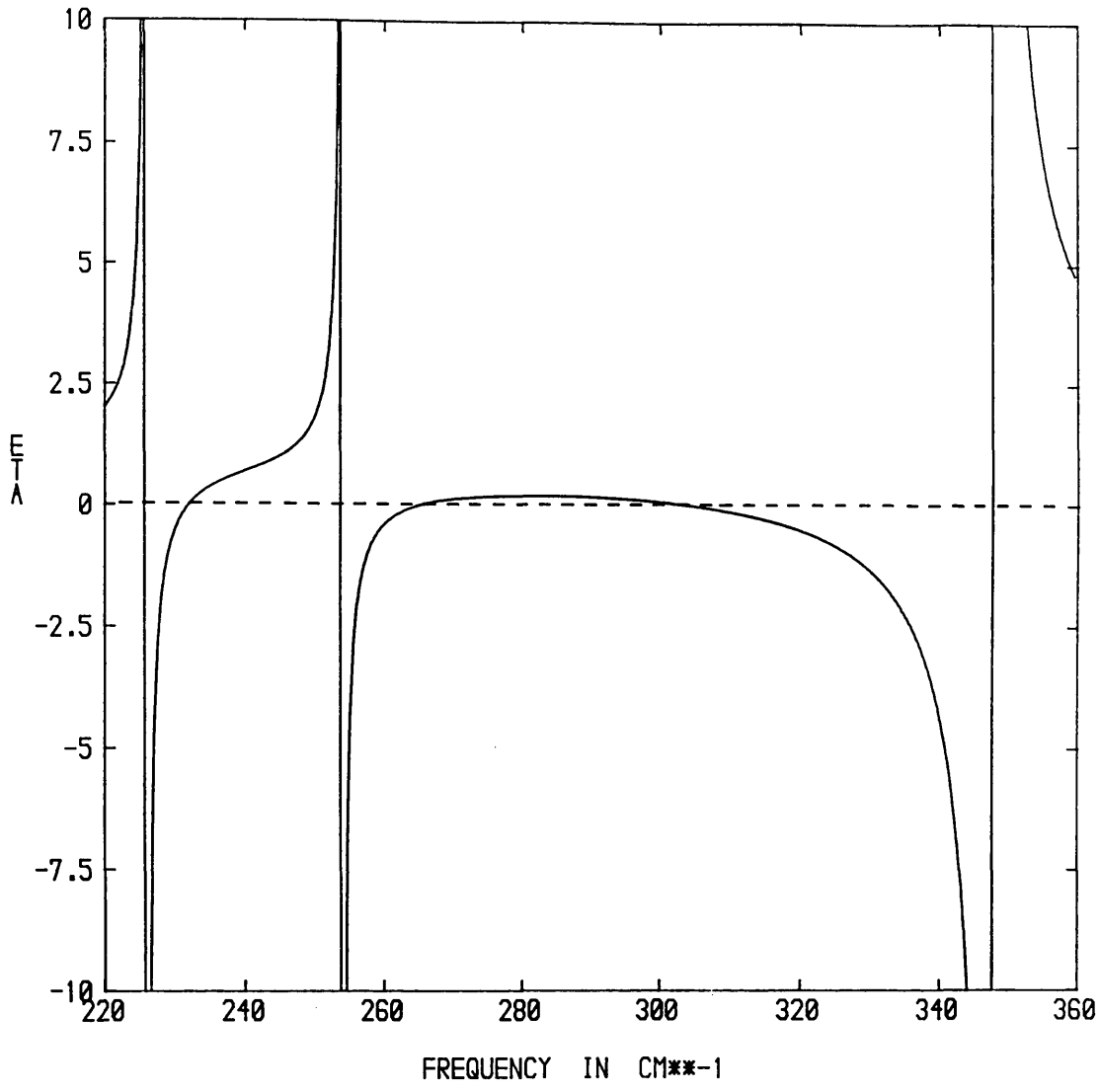

Figure 3.11 Plot of η (where $\eta = \epsilon(\text{GaInAs})/\epsilon(\text{InP})$) as a function of frequency. Interface modes exist wherever $\eta < 0$.

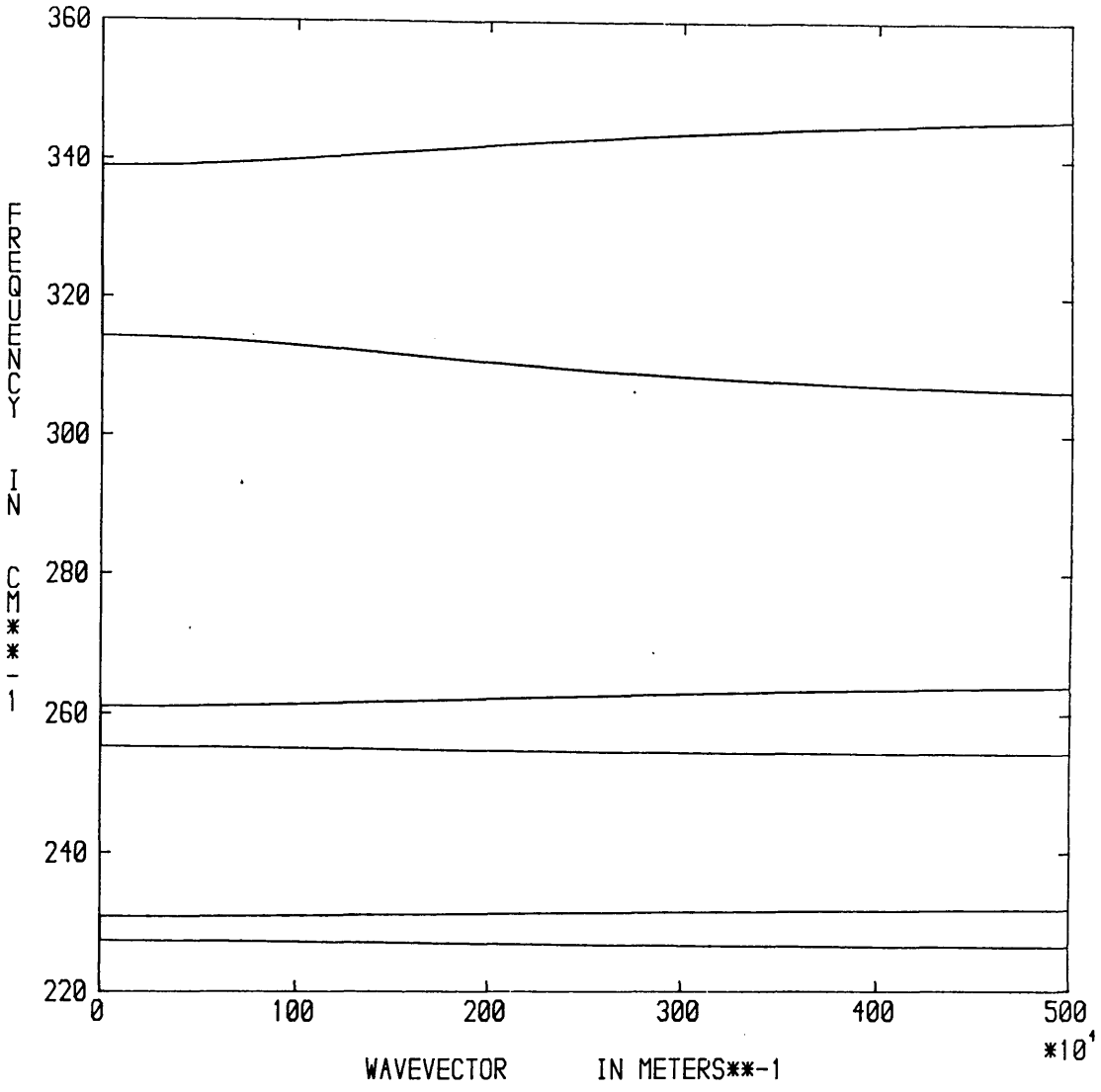

Figure 3.12(a) Interface mode frequency (calculated from equation 3.16 for PMB121) plotted as a function of q_z, the wavevector perpendicular to the layers. q_x, the wavevector parallel to the layers is taken as 5×10^5 m^{-1}.

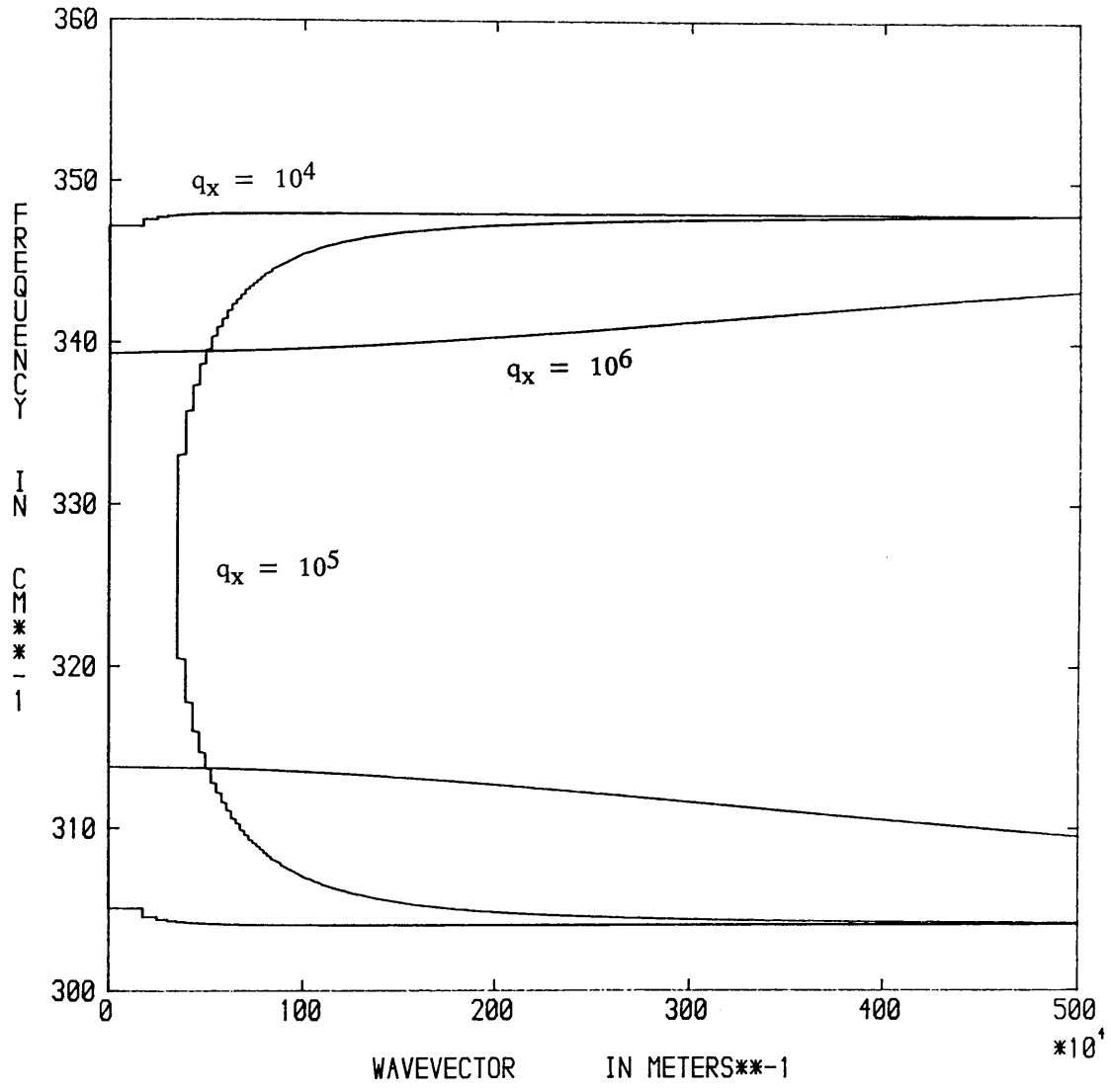

Figure 3.12(b) One of the three interface modes plotted as a function of q_z for three different values of q_x. Note that for $q_x = 10^5\ m^{-1}$, there is no frequency gap predicted for the interface modes.

3.3.2 Linear Chain Model

This model was discussed in section 3.2.4 in connection with confined optical phonons. It is, however, also of use in the description of interface modes in superlattice systems. Fasolino et al [1986] used the linear chain model to investigate interface modes in InAs– GaSb systems. This system differs from GaAs– AlGaAs and GaInAs– InP in that it does not possess an atom common to each layer. Its interfaces consist of either GaAs or InSb bonds and will therefore have characteristic frequencies of vibration that are quite distinct from those of the layers (see figure 3.13). As yet there is no direct comparison of the predictions of the linear chain model with either experimental data or the dielectric continuum model (since different systems have been investigated). The model is likely to be more appropriate for very narrow superlattices where a dielectric constant for each layer cannot be assumed because the layers are too narrow and where the role of each atomic bond has a strong influence on the resultant dispersion.

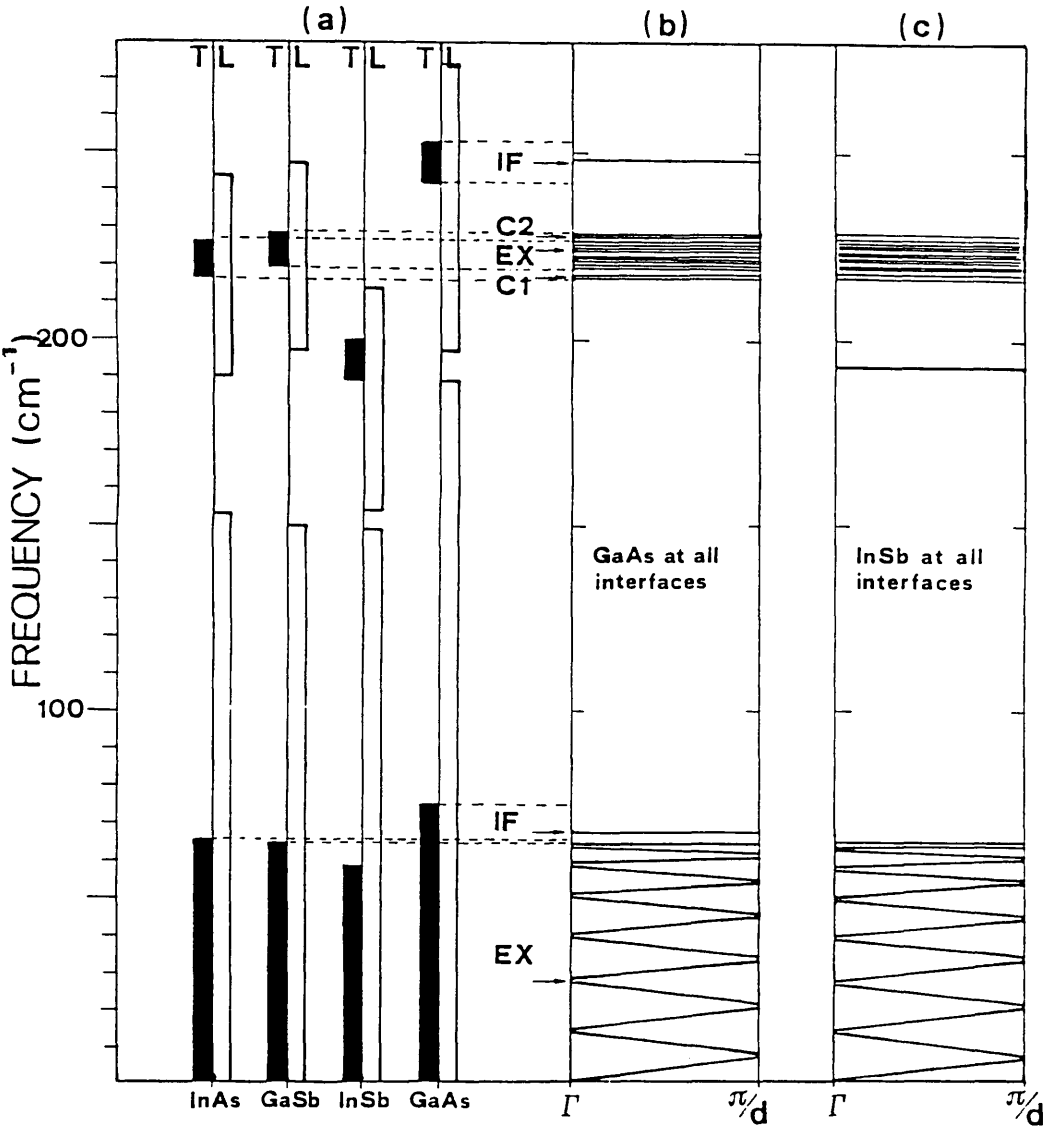

Figure 3.13 Interface modes for GaSb– InAs superlattices calculated by Fasolino et al [1986] using the linear chain model. The dashed lines indicate how the character of the superlattice modes (either confined, C, interface, IF, or extended/propagating, EX) is strictly related to their energy with respect to the bulk continua.

References

G Abstreiter; in "Physics and Applications of Quantum Wells and Superlattices", edited by E E Menendez and K von Klitzing, published by Plenum Press, 1987; p301

A K Arora, A K Ramdas, M R Melloch and N Otsuka; Phys Rev B36, 1021, 1987

D E Aspnes and A A Studna; Phys Rev B27, 985, 1983

A S Barker, J L Merz and A C Gossard; Phys Rev B17, 3181, 1978

H Brugger, G Abstreiter, H Jorke, H J Herzog and E Kasper; Phys Rev B33, 5928, 1986

R E Camley and D L Mills; Phys Rev B29, 1695, 1984

L L Chang; in "Molecular Beam Epitaxy and Heterostructures", edited by K Ploog, published by Martinus Nijhoff, Dordrecht, Netherlands, 1985; p461

P A Claxton, J S Roberts, J P R David, C M Sotomayor Torres, M S Skolnick, P R Tapster and K J Nash; J Cryst Growth 81, 288, 1987

C Colvard, R Merlin, M V Klein and A C Gossard; Phys Rev Lett 45, 298, 1980

C Colvard, T A Gant, M V Klein, R Merlin, R Fischer, H Morkoc and A C Gossard; Phys Rev B31, 2080, 1985

S T Davey, P C Spurdens, B Wakefield and A W Nelson; Appl Phys Lett 51, 758, 1987(a)

S T Davey, E G Scott, B Wakefield and G J Davies; Semiconductor Sci Technol 2, 683, 1987(b)

L Esaki; IEEE J Quantum Electron QE-22, 1611, 1986

L Esaki and R Tsu; IBM Res Note, RC-2418, 1969

A Fasolino, E Molinari and J C Maan; Phys Rev B33, 8889, 1986

R Fuchs and K L Kliewer; Phys Rev 140, A2076, 1965

D Gammon, R Merlin and H Morkoc; Phys Rev B35, 2552, 1987

D Gammon, L Shi, R Merlin, G Ambrazevicius, K Ploog and H Morkoc; Superlatt Microstr 4, 405, 1988

B Jusserand, F Alexandre, J Dubard and D Paquet; Phys Rev B33, 2897, 1986

B Jusserand and D Paquet; Proc Les Houches Winterschool on "Heterojunctions and Semiconductor Superlattices", edited by G Allen, G Bastard, N Boccara, M Lannoo and M Voos, published by Springer– Verlag, Berlin, Heidelberg, New York, 1985; p342

B Jusserand, D Paquet and A Regreny; Phys Rev B30, 6245, 1984

E Kasper; in "Physics and Applications of Quantum Wells and Superlattices", edited by E E Menendez and K von Klitzing, published by Plenum Press; 1987; p101

M V Klein; IEEE J Quantum Electron QE–22, 1760, 1986

"Landolt– Boernstein Numerical Data and Functional Relationships in Science and Technology. Group III: Crystal and Solid State Physics" Vol 17a: Physics of Group IV Elements and III– V Compounds, edited by O Madelung, published by Springer– Verlag, Berlin, Heidelberg, New York, 1982; sections 2.10, 2.11, 2.14 and 2.16

D J Lockwood, M W C Dharma– wardana, J M Barbeau and D C Houghton; Phys Rev B34, 3024, 1986

J Y Marzin; in "Optical Properties of Narrow– Gap Low– Dimensional Structures", NATO ASI Series B Physics Vol 152, edited by C M Sotomayor Torres, J C Portal, J C Maan and R A Stradling, published by Plenum Press, London New York, 1987; p99

E Molinari, A Fasolino and K Kunc; Superlatt Microstr 2, 397, 1986

K J Nash, M S Skolnick and S J Bass; Semicond Sci Technol 2, 329, 1987

E D Palik (editor); "Handbook of Optical Constants of Solids", published by Academic Press, 1985; p510

T P Pearsall, R Carles and J C Portal; Appl Phys Lett 42, 436, 1983

K Ploog; in "Physics and Applications of Quantum Wells and Superlattices", edited by E E Menendez and K von Klitzing, published by Plenum Press, 1987; p43

J C Portal, G Gregoris, M A Brummell, R J Nicholas, M Razeghi, M A Di Forte– Poisson, K Y Cheng and A Y Cho; Surf Sci 142, 368, 1984

J S Roberts; private communication, 1988

S M Rytov; Sov Phys– Acoust 2, 68, 1956

J Sapriel, J C Michel, J C Toledano, R Vacher, J Kervarec and A Regreny; Phys Rev B28, 2007, 1983

J Sapriel, E V K Rao, F Brillouet, J Chavignon, P Ossart, Y Gao and P Krauz; Superlatt Microstr 4, 115, 1988

A K Sood, J Menendez, M Cardona and K Ploog; Phys Rev Lett 54, 2111, 1985(a)

A K Sood, J Menendez, M Cardona and K Ploog; Phys Rev Lett 54, 2115, 1985(b)

D C Tsui, H L Stoermer and A C Gossard; Phys Rev Lett 48, 1559, 1982

K von Klitzing, G Dor da and M Pepper; Phys Rev Lett 45, 494, 1980

S K Yip and Y C Chang; Phys Rev B30, 7037, 1984

J E Zucker, A Pinczuk, D S Chemla, A Gossard and W Wiegmann; Phys Rev Lett 53, 1280, 1984

CHAPTER 4

EXPERIMENTAL METHOD

4.1 Experimental Apparatus Overview

This chapter is concerned with the experimental methodology used in this work. Details are given of the type of equipment used together with some comments on the manner of operation if this differs from the normal case or is particularly relevant. The chapter is subdivided into sections corresponding to the different components of the apparatus.

In an inelastic light scattering experiment three basic components are needed: a) a light source, b) a means of dispersing the scattered light and c) suitable detection of the dispersed light. Function a) can be obtained by a laser or an incoherent source such as an arc lamp. Filtering, beam–steering and focussing optics will also be needed. Function b) is usually performed by a spectrometer together with appropriate collection optics. The detector in function c) will depend on the wavelength range to be studied and the signal strength; its output must be recorded in some manner to correlate with another variable, be it scattered wavelength or incident wavelength, to produce the desired spectrum. A schematic of the experimental arrangement used for the experiments in this work is shown in figure 4.1. The laser and prism filter are discussed in section 4.3, the detection system is

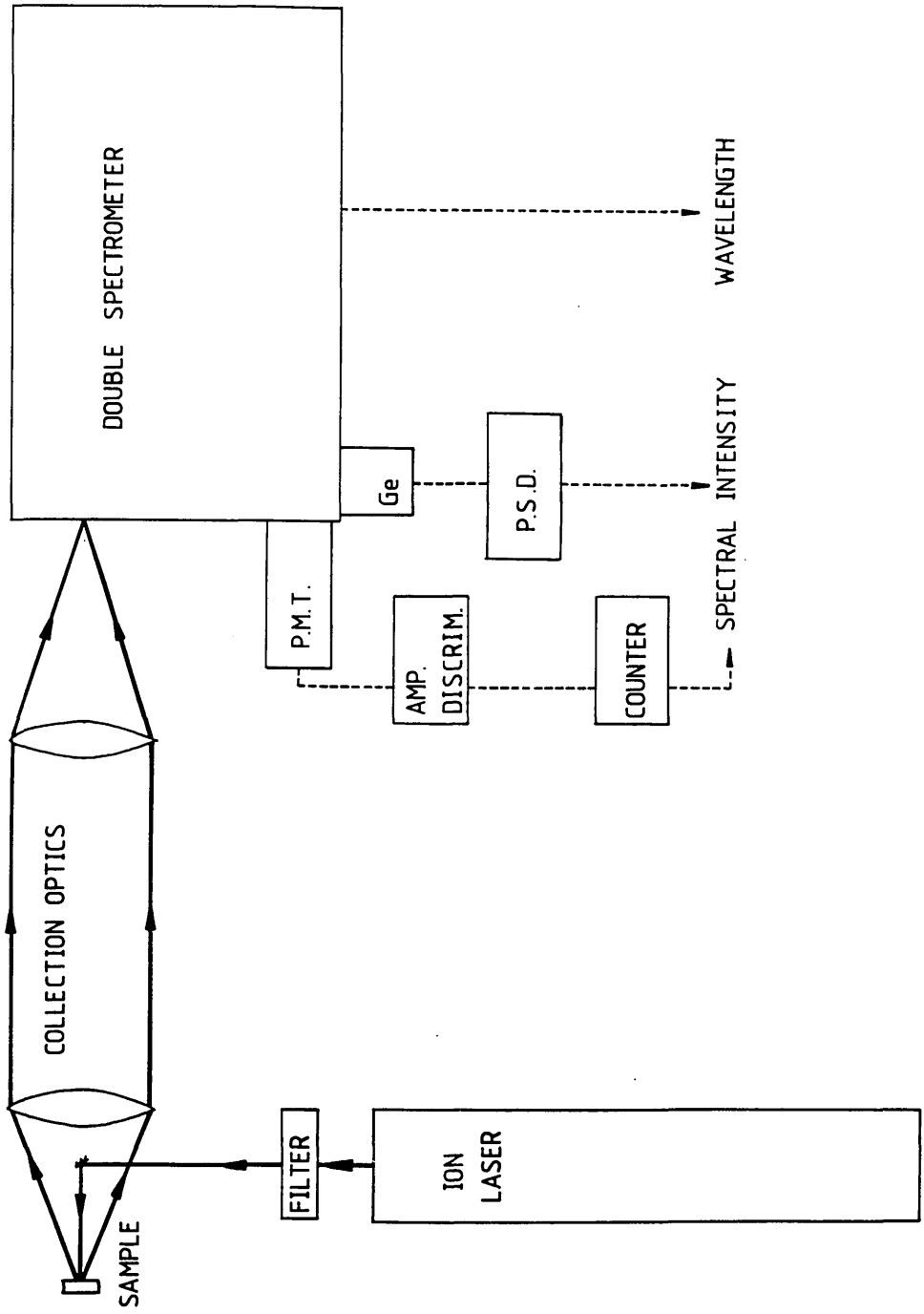

Figure 4.1 Schematic representation of experimental set–up for Raman scattering or Photoluminescence spectroscopy showing the photomultiplier tube (PMT) with its amplifier/discriminator and pulse counter, the Germanium detector (Ge) and the phase–sensitive detection unit (PSD). A backscattering geometry is depicted.

discussed in section 4.2, the spectrometer in section 4.4 and the data–recording system in section 4.5. The other aspects of the apparatus will be covered here.

The samples were always cleaned before use in acetone and then methanol. They were mounted vertically on metallic mounts using either heat–sink compound or a very thin layer of Bostick. As most III–V semiconductors are opaque in the visible region of the spectrum, a backscattering geometry was used for the Raman scattering experiments. There is some experimental advantage in using a "nearly–backscattering" geometry rather than true backscattering and so unless otherwise stated, it is this "nearly–backscattering" geometry that is used throughout this work. The main advantage arises from the reduction in both the reflected and Rayleigh scattered light that reach the spectrometer entrance slit. This permits a lower background count and signal detection closer to the laser frequency. A second advantage is the fact that this geometry allows the directing optics to be located outwith the solid angle of the collection optics and thus a greater collection efficiency is possible. Typically, the incident light would have an angle of 50 to 60° to the sample surface. This geometry is made possible by the high refractive index of most III–V semiconductors (e.g. 4.33 in GaAs at 4880Å) which causes the light to be bent towards the normal within the sample thus minimising the effect of the "nearly–backscattering" geometry. The usual notation is used throughout to identify the spectra (see section 1.3.3).

Raman scattering cross–sections are small in comparison with, say, emission cross sections, and thus a high power density of incident laser light is needed to produce a detectable signal. This is why a laser was used in preference to an arc lamp source. The power density that can be used is limited by sample heating effects. This limitation can be overcome by using a line rather than a point focus. The beam was focussed onto the sample in either a spot or a line which was then transferred by means of the collection optics to a similarly focussed spot on the entrance slit of the spectrometer. In order to collect as much of the scattered light

as possible, lenses of 10cm diameter were used for the collection optics. A pair of such lenses were used: the first had the sample at its focal length and provided a collection angle of F1.6, the collimated beam from this lens was focussed by the second lens onto the spectrometer slit. The second lens provided all the fine adjustment ne cessary to couple the signal into the spectrometer. This arrangement also enabled any polarisation analysis components to be conveniently located between the lenses and also allowed for a variable distance between the sample and the spectrometer, e.g. when working inside or outside the cryostat. The lenses were made of optical crown (type HC 519604). This was chosen to combine a flat optical transmission between 400nm and 1.8μm with low cost. The transmission over this range was in excess of 90%.

The extreme weakness of the Raman signal, together with its close proximity to the laser line (typically one might scan from 5cm^{-1} which is only 1.2Å removed from the 4880Å laser line) requires that a double spectrometer be used to provide extremely good stray light rejection. In addition to this, an extremely sensitive detection method, such as the photon counting system described in section 4.2, is needed to detect these signals. It was neccessary to record most spectra with the room darkened to eliminate background noise from the room lights which would otherwise have swamped the signal. For work in the near infra-red (900nm-1.5μm), photomultiplier tubes that are sufficiently sensitive for this type of Raman scattering work are unavailable. Photoluminescence emission (PL) in this region was detected by a Germanium detector with phase sensitive detection. Its spectral response is given in figure 4.2 for operation at 300K. It is possible to operate the detector cooled to 77K which reduces the noise. This, however, shifts the peak of the spectral response to shorter wavelengths. The photoluminesence data discussed in chapter 5 were recorded with the detector at 300K. The rest of the experimental set-up for the PL measurements was exactly the same as for the Raman work.

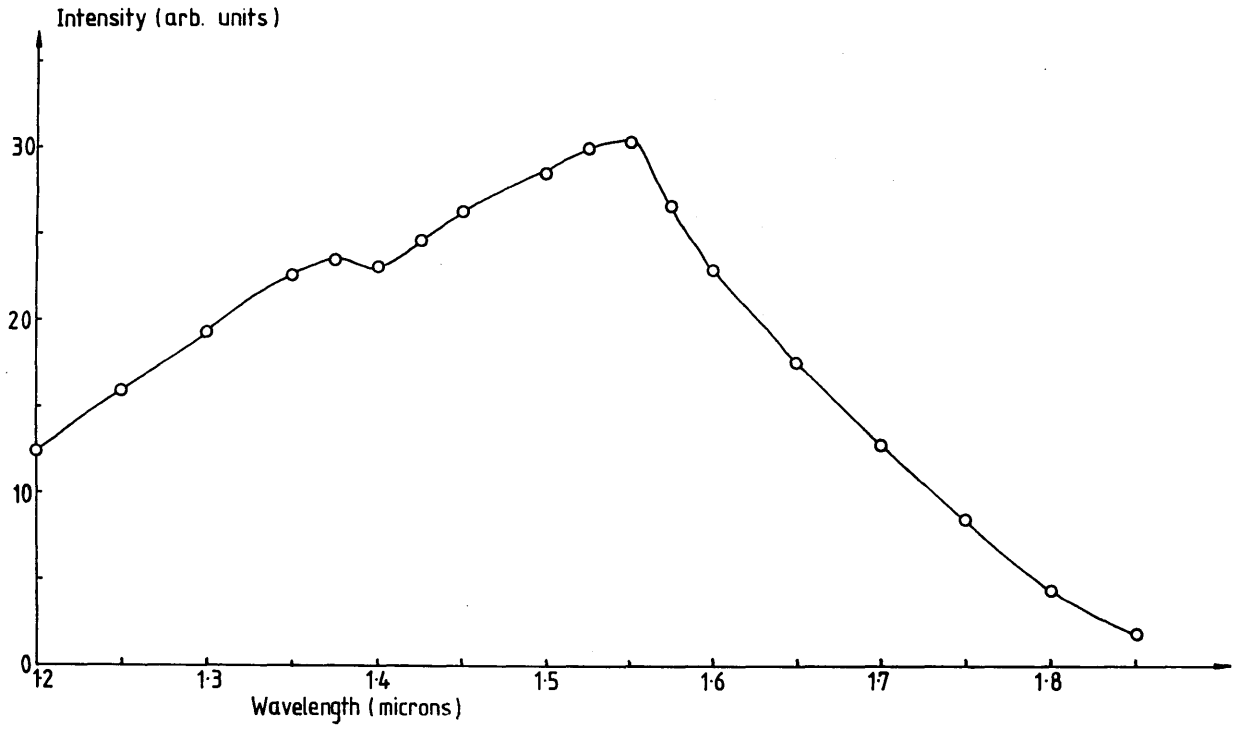

Figure 4.2 Blackbody calibration of the spectral response using the Germanium detector operated at 300K and the infra–red gratings.

The initial means of recording spectra was on a chart recorder with the analogue output from the detector connected across the y− input and an analogue output proportional to the wavelength connected to the x− input of the chart recorder. This latter output was available from an interface box made in the electronic workshop of the Physics department of St Andrews University. This box gave an analogue output proportional to the number of stepper motor pulses sent to the spectrometer and hence proportional to the wavelength increment. This method was unsatisfactory since there was no means whereby the data could be stored and processed and no method of extending the count time to detect very weak structure. A small improvement on this was obtained by feeding both analogue outputs to a BBC microcomputer which enabled data− collection times to be extended. This was only a temporary measure and a permanent solution was found by using an IBM Model 30 microcomputer to record the spectra digitally. This system was designed to be very flexible incorporating both detector outputs and either wavelength or wavenumber scanning increments together with a number of analogue input parameters such as laser power and cryostat temperature. The computerisation and software are discussed in section 4.5.

4.2 Photon Counting Techniques

Photon counting is a technique used in conjunction with a very sensitive photomultiplier tube when the light flux is weak. It is highly developed in astronomical applications and many articles on the statistics of the essentially random nature of counting photons have this application in mind.

All photomultiplier tubes have background noise (dark current). This current has many sources: external radiation that produces electrons at the photocathode and dynodes, leakage currents, thermal emission from the dynodes or photocathode. Due to the nature of the photomultiplier tube gain, each electron that is produced in the tube will undergo gain and thus produce a short pulse of electrons at the anode of the tube. The nearer the photocathode the electron is produced, the bigger this pulse will be. It therefore follows that electrons produced at the photocathode produce the largest pulses at the anode. Since all the light signal is converted to electrons at the photocathode, rather than at the dynode chains, this implies that pulses produced by photons will be larger than all the noise pulses excepting those originating at the photocathode itself. An electronic discriminator can therefore be used to "pass" all output pulses above a certain size and "reject" all others. The probability of counting a noise pulse is thereby limited to those originating at the photocathode and the signal to noise ratio increases as a result. In order to favour this method of operation, the gain between the photocathode and the first dynode chain is made larger than the gain between the dynodes thus emphasising the difference between pulses of different origin.

A number of photomultiplier tubes were used during the course of this work. All were Hamamatsu R943–02 type tubes with a Cs–activated GaAs photocathode. This type of tube is designed specifically for photon–counting applications as it has a gain of 5×10^5 and a very low dark noise. Its spectral response is given in figure

4.3. The tube was cooled to about −20°C in a Pacific Instruments thermoelectrically−cooled housing with a built−in amplifier and discriminator. The cooling is neccessary to keep the dark noise to a minimum level. Table 4.1 shows the different characteristics and lifetime of each of the tubes. Several tests were performed on each new tube to assess its performance with respect to the manufacturer's specification. All tests were performed with the tube already cooled and under no illumination unless otherwise stated.

4.2.1 Photomultiplier Tube Tests

The four tests used routinely to characterise the photomultiplier tubes are detailed separately below.

Bleeder Current

The bleeder current flows through the dynode chain as a result of the HT applied to the photocathode. The dynode chain is shown schematically in figure 4.4. The total dynode chain resistance is 4.8×10^6 Ω and thus with an applied voltage of −1500V, the bleeder current ought to be 0.31mA. If the bleeder current is measured to be greater than this value then a source for the leakage current must be sought. If, for example, the photomultiplier tube shield were externally grounded, say by water causing a short circuit to the grounded housing, then an additional current would flow from the cathode through R17 to the grounded shield. This current would have a value of 0.15mA and thus be detected as an increase in the bleeder current drawn from the power supply. The importance of this measurement is tied to the importance of the tube shield: if the photocathode is at a very high

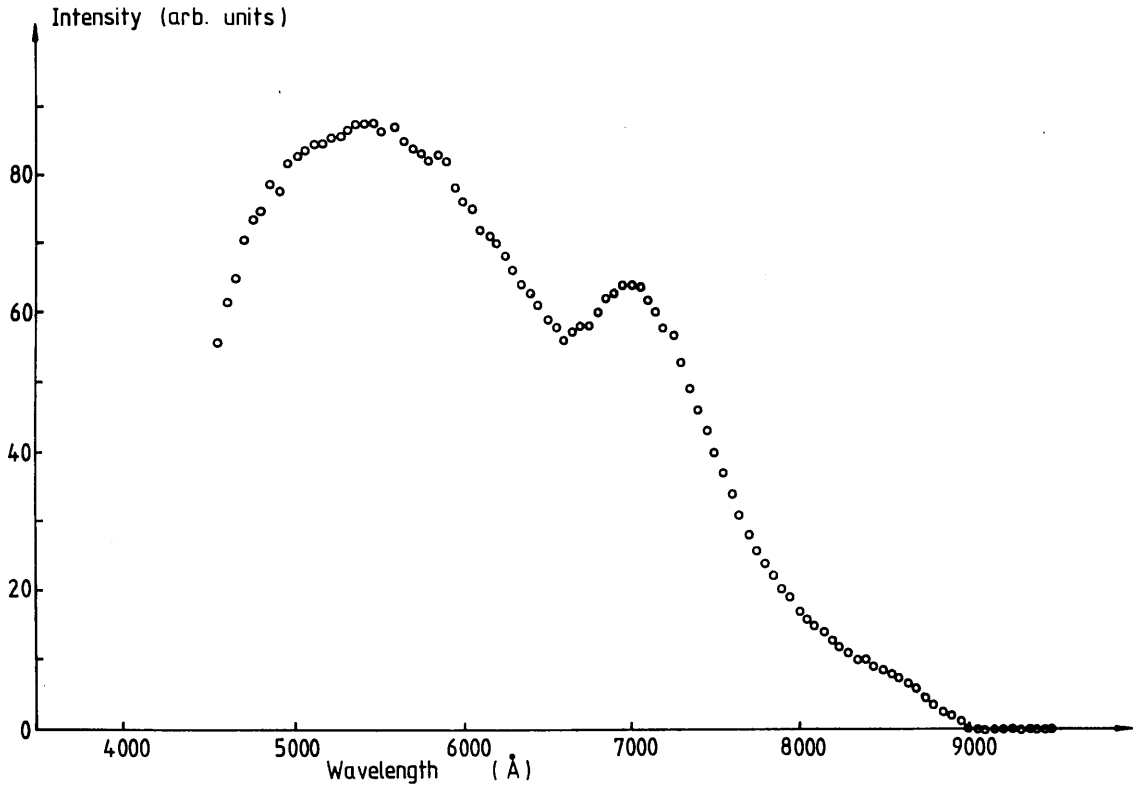

Figure 4.3 Blackbody calibration of the spectral response of the photomultiplier tube R943−02 and the visible gratings. No data is recorded for wavelengths less than 4500Å because the blackbody source was at too low a temperature to yield enough intensity at short wavelengths. (The peak of intensity is at approximately 2μm for the temperature of 1173K used.)

Table 4.1

Specifications of the photomultiplier tubes used in this work.

Serial Number:	EA1456	EA2183	EA3666	EA3743	EA3843	EA4135
Tube Number:	1	2	3	4	5	6
Dates from:	20.11.85	14.10.86	26.1.87	9.3.87	15.5.87	20.1.88
until:	17.9.86	4.12.86	9.3.87	14.4.87	27.11.87	present
Cathode Luminous Sensitivity (μA/lm)	550	no spec.#	652	599	666	737
Anode Luminous Sensitivity (A/lm)	195		505	433	261	285
Anode Dark Current (nA)	5.5		3.6	0.66	1.4	1.9
*R/Wx10^{-3}	590		580	583	602	590
Test Voltage (V)	1500		1500	1500	1500	1500
Cause of Failure	1	2	2	3	4	–

Key

* Ratio of red light sensitivity to white light sensitivity.
\# This was a used tube loaned by Hakuto International, the Hamamatsu distributers.

Cause of failure:

1. HT shield round tube at ground potential resulting in a loss of sensitivity of the photocathode.
2. Dark count too high.
3. Thermal crack of tube envelope at pins.
4. Cathode crack: reason unknown but after thermal and mechanical shock.

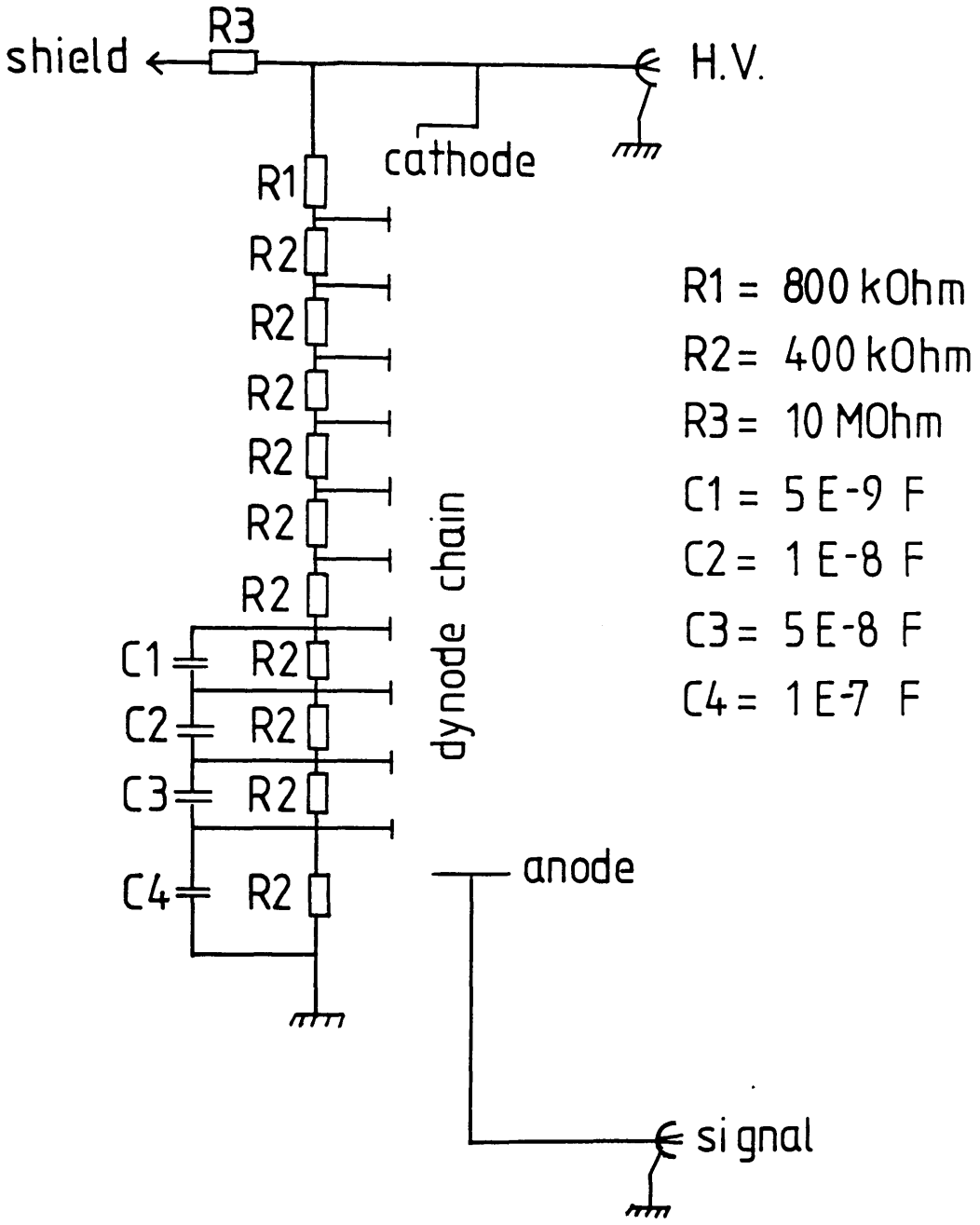

Figure 4.4 Schematic representation of Hamamatsu R943–02 photomultiplier tube dynode chain.

potential with respect to its surrounding environment then the potential gradient across the tube wall will cause scintillations in the glass of the wall and increase the dark noise. If this is allowed to continue for a sufficiently long time, then ionic conduction through the glass will permanently damage the photocathode [RCA Photomultiplier Handbook, 1980]. It is to prevent such an occurrence that the R943−02 has a conductive coating, on the outside of the tube, which is connected to the cathode potential. It is also why the mu−metal shield (which protects electrons from deflections due to external magnetic fields) is kept at cathode potential through R17. The slow loss of sensitivity of tube EA1456 is attributed to the fact that R17 was open circuit and the shield was thus effectively at ground potential. This loss of sensitivity began in the red region of the spectrum and spread to lower wavelengths; eventually light that was plainly visible to the human eye did not register on the photocathode. Tests of the bleeder currents of tubes 3 to 6 produced no anomalous results (see figure 4.5).

Dark Count with respect to Time

This was measured for tubes 3 and 5 and is shown in figures 4.6(a) and 4.6(b). In the case of tube 3, the dark current was unacceptably high and increased with time causing the tube to be rejected and returned to the manufacturers. Tube 5 showed what could be termed "normal" characteristics in its noise versus time dependence in that the dark count increased with time fairly rapidly and then saturated in a period of one to two hours. This was attributed to a fault within the Model 33 cooling unit. Immediately after the high voltage was applied, the initially cold tube rose in temperature as a result of the power dissipation of the bleeder current. A temperature equilibrium was then reached with the cooler which did not have the power to maintain the required temperature. This temperature rise and

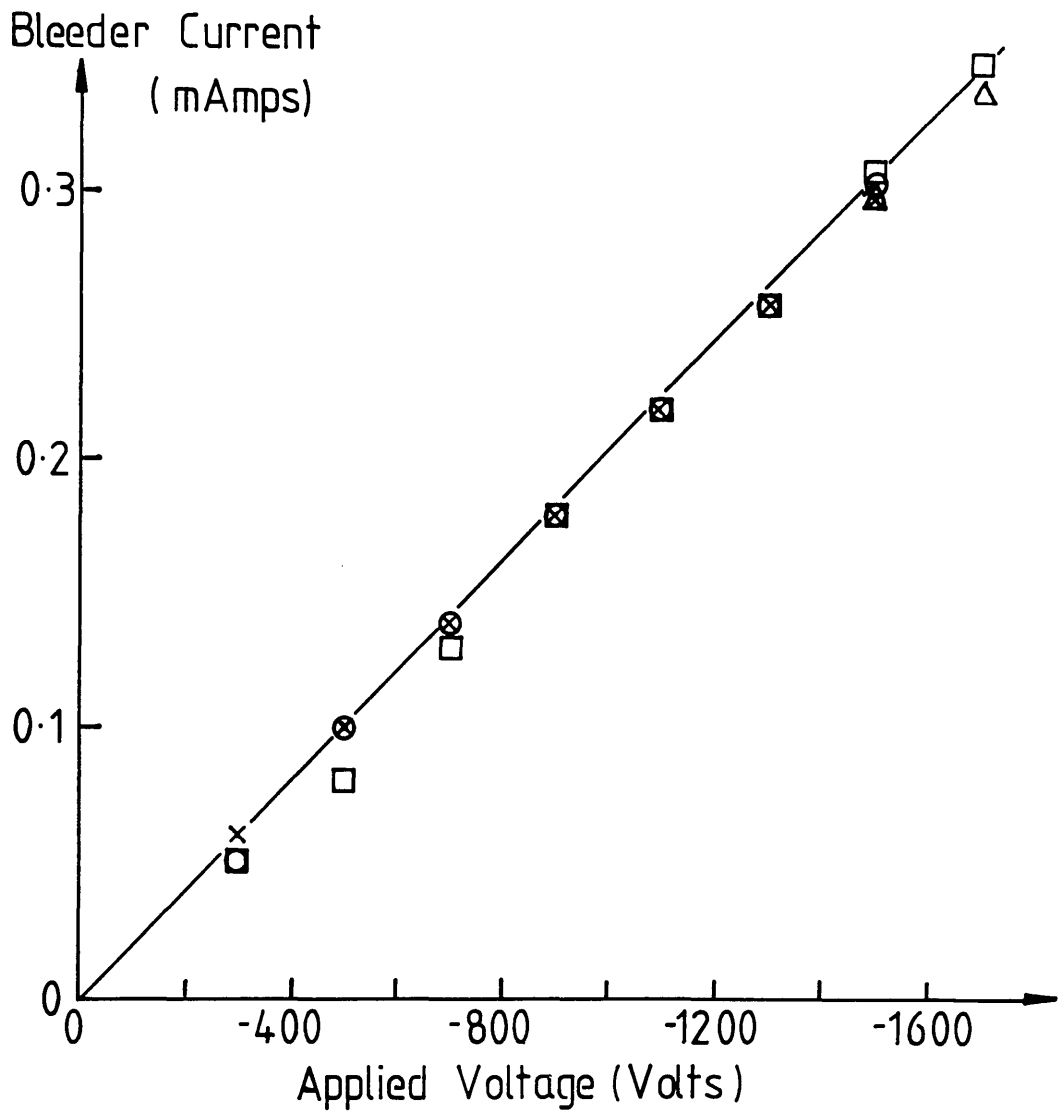

Figure 4.5 Bleeder current plotted as a function of applied voltage for four photomultiplier tubes: x tube 3, O tube 4, □ tube 5, △ tube 6. The solid line is the theoretical value from Ohm's law.

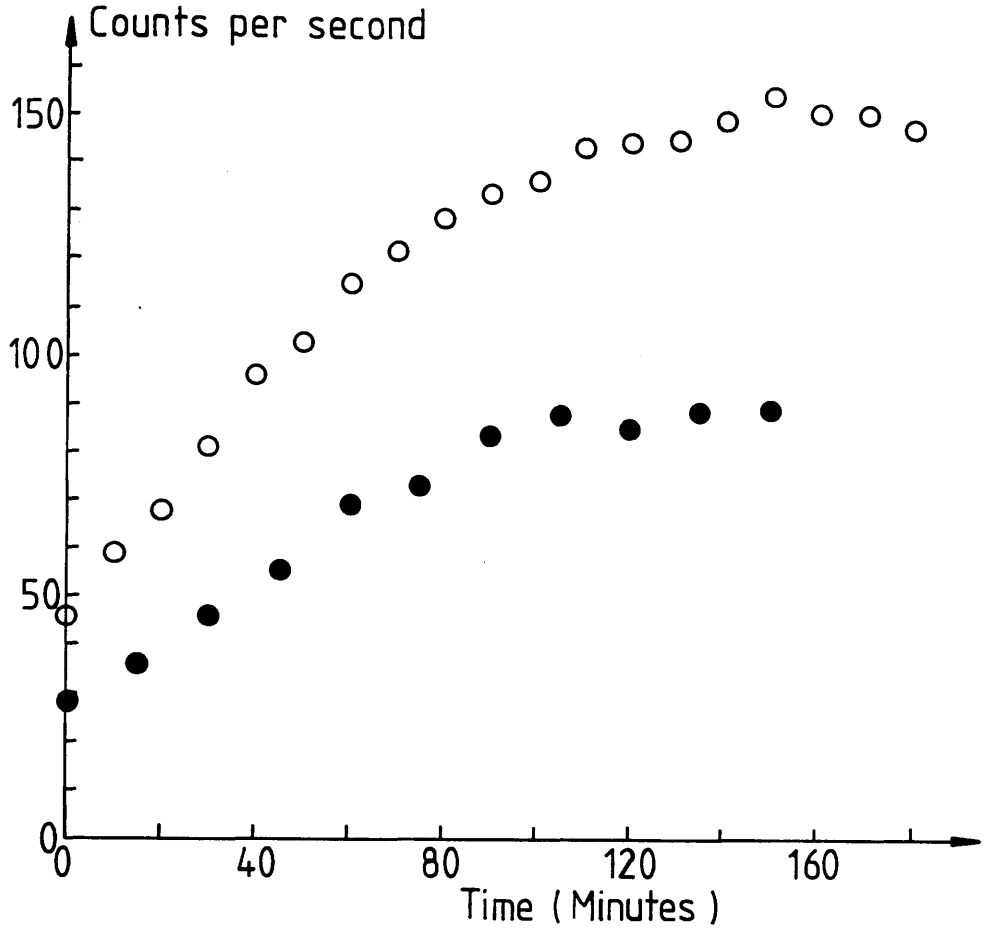

Figure 4.6(a) Dark count as a function of time for tube 3 with an applied voltage of −1500V and discriminator settings of −50.4mV (open circles) and −75.6mV (full circles).

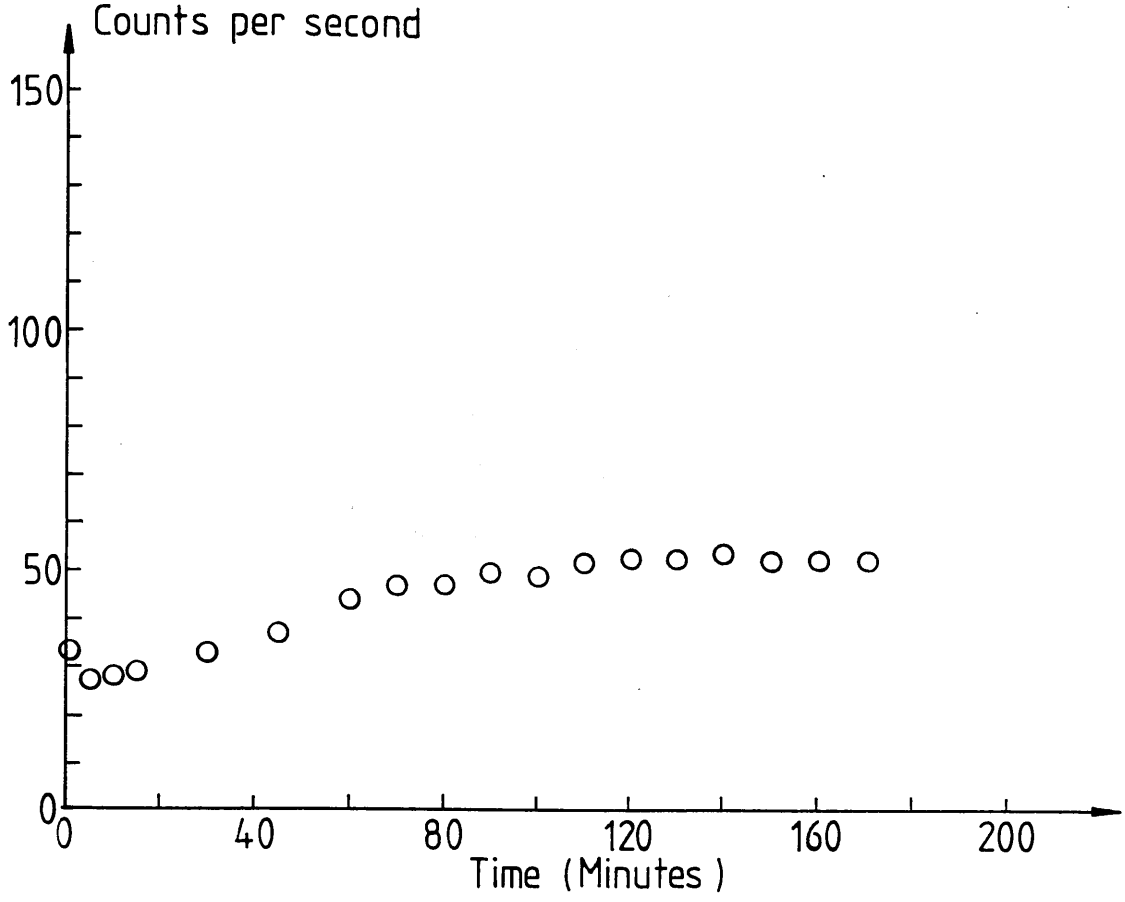

Figure 4.6(b) Dark count as a function of time for tube 5 with an applied voltage of −1500V and a discriminator setting of −24mV.

equilibrium was reflected in the dark noise versus time characteristics of the tube output since dark noise varies by almost an order of magnitude per 10°C in the range +20°C to −20°C [RCA Photomultiplier Handbook, figure 16, 1980].

Noise with respect to Discriminator Level

Much of the theory of discriminating the output of a photomultiplier tube centres on the optimum level for the discriminator [see e.g. Foord et al, 1969; Meade, 1981; Nakamura, 1968]. The reason for this is obvious if one looks at the pulse height analysis spectrum of the tube output supplied as part of the specification of each new photomultiplier tube (see, e.g. figure 4.7). Signal pulses are generally larger than dark pulses as discussed above. In this particular case, most of the dark pulses fall in channels 0 to 60 while the peak of the signal pulses falls around channel 200. Thus by discriminating against any pulse lower than channel 60, it is possible to increase the signal to noise ratio. This is very easily seen using a pulse height analyser but becomes less clear when using an amplifier discriminator in photon−counting mode. Meade [1981] speaks of a "knee" in the discriminator versus signal curve reporting that this "knee" will give the optimum signal to noise ratio: such a "knee" is not evident in figure 4.8. There is moreover a problem in setting the discriminator level too high in that the observable output may become only a small fraction of the incident light intensity upon the tube thus making it possible to overexpose the photocathode causing permanent damage and loss of sensitivity to the tube while unaware of the overexposure. For this reason, therefore, and because of the lack of any clear "knee" of optimum discriminator level in figure 4.8, the minimum discriminator setting available was used (−25mV) as it was found to provide an adequate signal to noise ratio.

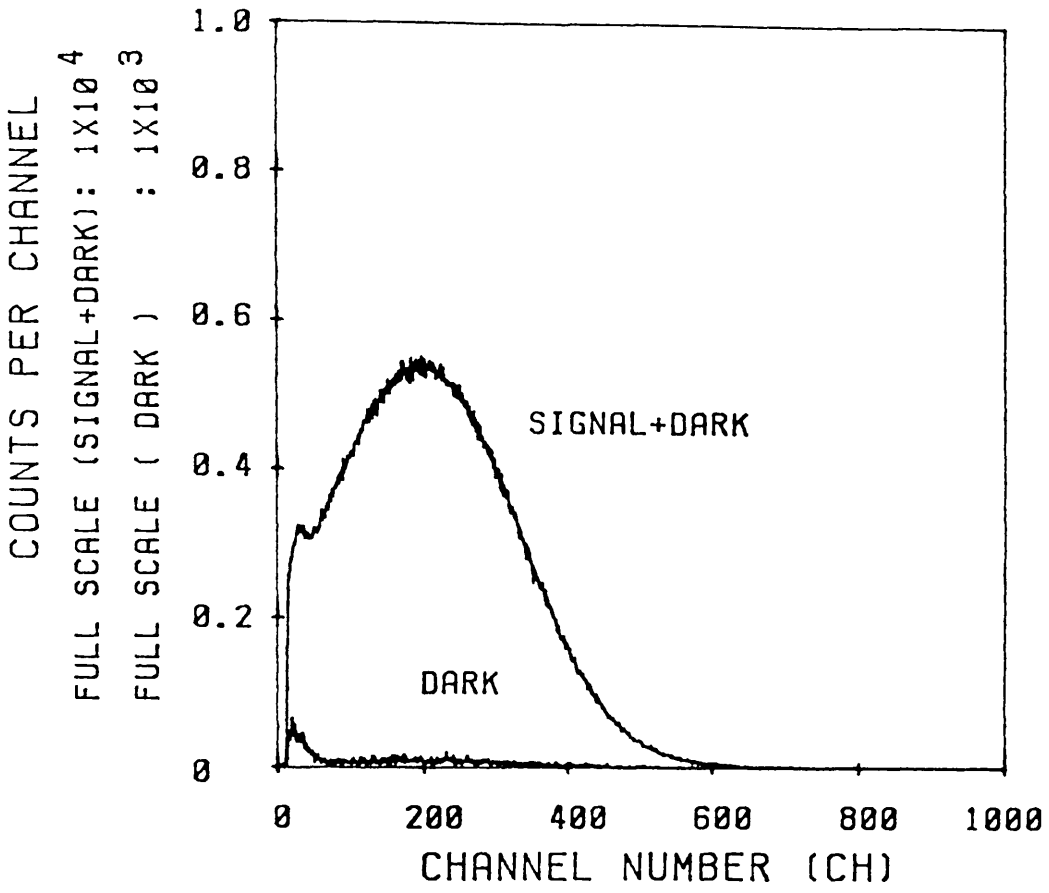

WAVELENGTH OF INCIDENT LIGHT	:	800 (nm)
APPLIED VOLTAGE	:	1790 (V)
LOWER LEVEL DISCRI.	:	60 (CH)
SIGNAL+DARK COUNTS	:	5080 (cps)
DARK COUNTS	:	9 (cps)
LIVE TIME	:	300 (sec.)
P.H.A.	:	NAIG-E SERIES
TEST DATE	:	DEC./23/'87
TEMP.	:	-20°C
TESTED BY	:	A.K.

Figure 4.7 Manufacturer's specification supplied with photomultiplier tube EA4135 (tube 6).

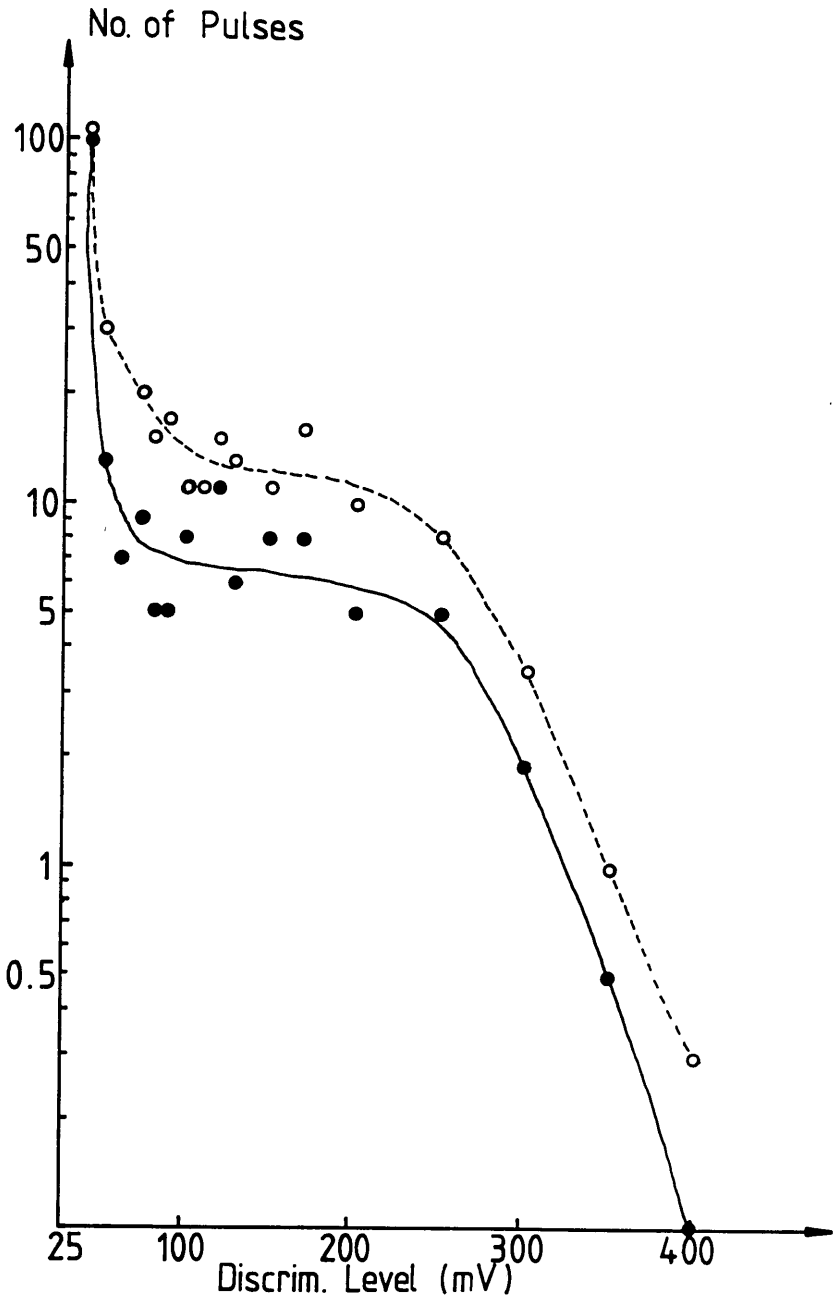

Figure 4.8 Pulse height analysis data for tube 3. The number of pulses in each voltage interval of the discriminator level is plotted against the discriminator level. The voltage interval is given by the difference between adjacent points on the voltage scale. Full circles are the dark noise pulses, open circles are with light applied. Enough light was allowed to fall on the photocathode to cause the count rate to double. For this low level of light, no significant difference in the shape of the curves is observed. The lines are a guide to the eye.

Dark count versus discriminator level setting measurements were taken for two tubes, 4 and 6, and the results are shown in figures 4.9(a) and 4.9(b) respectively. There is no evidence from either of these graphs to suggest that operating the tube at a higher voltage would improve the signal to noise ratio; indeed the main conclusion one can draw from this data is that higher operating voltages cause much larger noise pulses and the task of discriminating against these would be more difficult.

In summary, therefore, the failure rate of these photomultiplier tubes is rather higher than one would wish. It is not easy to combat this problem since sudden thermal shock cannot always be avoided (e.g. power failure, coolant failure) and dark noise behaviour is as much a function of the manufacturing process as of the subsequent treatment of the tube. Certain action can be taken: the dynode resistors can be checked to see that they have the correct values, the housing can be kept dry by removing the tube every few months and replacing the water–absorbent material kept with the tube in its housing, unneccessary thermal cycling of the tube can be prevented by switching off the cooling as seldom as possible. These measures may reduce the likelihood of tube failure but are unlikely to remove it completely.

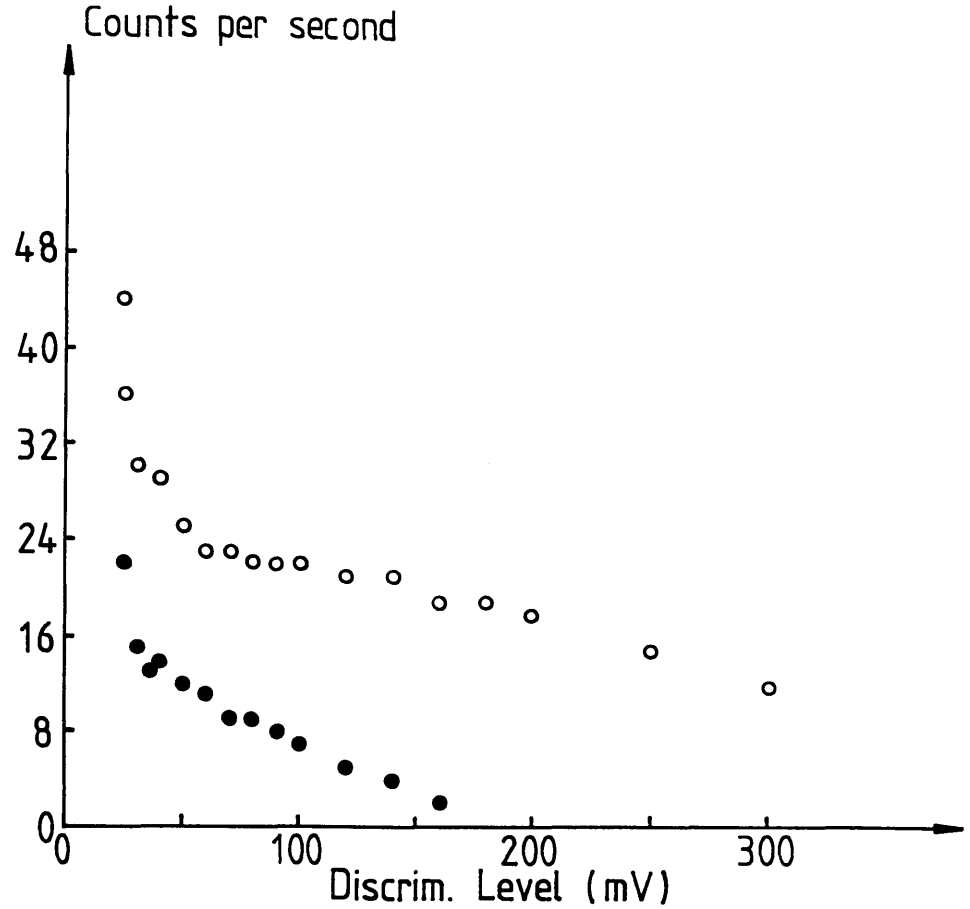

Figure 4.9(a) Dark count as a function of discriminator level for tube 4. Open circles denote an applied voltage of −1720V, full circles denote an applied voltage of −1500V.

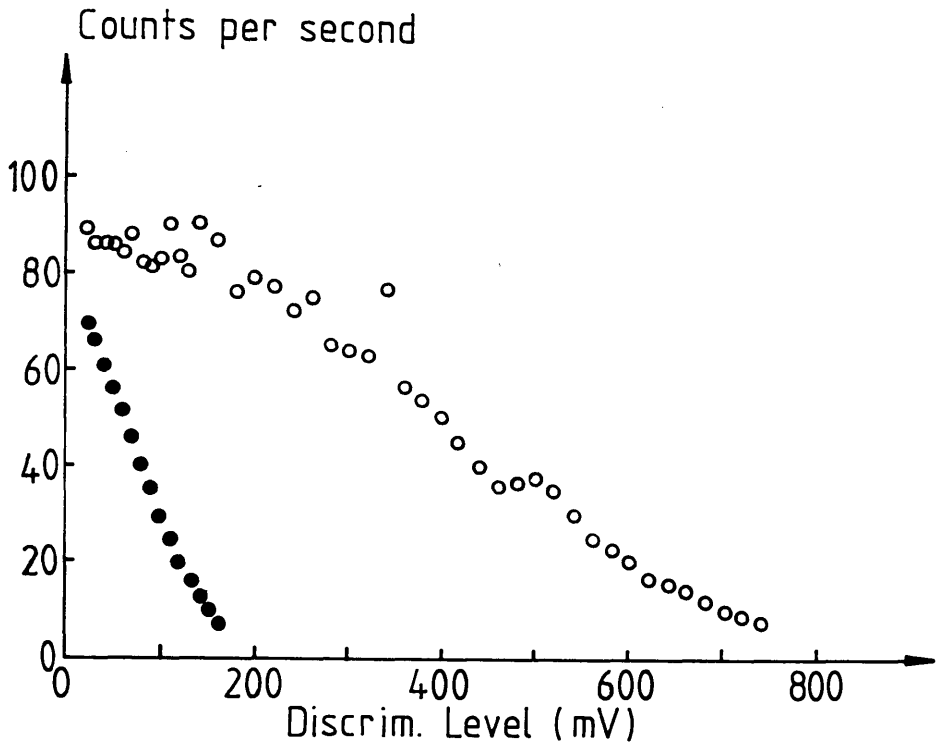

Figure 4.9(b) Dark count as a function of discriminator level for tube 6. Open circles denote an applied voltage of −1790V, full circles denote an applied voltage of −1500V.

4.3 Laser

Several laser systems have been used for this work. From October 1985 until September 1987, a Coherent CR−2000K supergraphite Krypton ion laser was used as the excitation source. The wavelengths used were 4762, 4825, 5309 and 6471Å. The laser tube was seven years old − very old by ion laser tube standards − and it had deteriorated with age. This resulted in poor reliability and lengthy periods of repair work. From October 1987, the work was done using a new Spectra−Physics model 2030 Argon ion laser. A single set of mirrors enabled lasing in the blue/green region of the spectrum on ten separate lines of which the 4545, 4880 and 5145Å were used. A second set of mirrors designed for the U.V. enabled lasing from 3511 to 3638Å on a number of lines. These could be selected to lase separately, as with the visible lines, by using an intracavity prism filter. Both ion lasers were capable of pumping the dye laser, a Coherent CR−599.

The experiments done in Edinburgh in collaboration with Dr Peter D Hatton used a Spectra−Physics Krypton ion and a Spectra−Physics Argon ion laser as excitation sources.

In each case, it was necessary to use a prism monochromator to filter the laser beam and thus remove plasma line emissions from the laser tube. The plasma lines exist throughout the spectrum and are often many times stronger than the signal. The Spectrolab prism monochromator used here had a maximum transmission of 82% and an almost flat spectral response from 350nm to 900nm. The transmission, however, depended on the beam size and so this maximum was seldom achieved and transmission of around 50% was usual.

4.4 Spectrometer Theory, Resolution and Calibration

The spectrometer used was a Jobin–Yvon Ramanor U1000. This is a 1m focal length double grating spectrometer, i.e., two single spectrometers side by side with the gratings attached to a single shaft to eliminate any relative movement. The image of the exit slit of the first spectrometer falls upon the entrance slit of the second spectrometer; the light path is shown in figure 4.10. The gratings are coupled additively in that the second grating further disperses the light incident upon it.

The gratings in the spectrometer are interchangeable. At present, two pairs of gratings are available: a holographic pair, with 1800 grooves/mm and a pair ruled with 600 grooves/mm and blazed at 26.75°. This latter pair has a peak efficiency at 1.5μm and is used primarily for the photoluminesence work on GaInAs–InP; the efficiency of this pair is shown in figure 4.11(a). The holographic gratings are efficient throughout the visible region of the spectrum with the efficiency given in figure 4.11(b).

The linear dispersion, D, of a plane grating single spectrometer is given by:

$$D = dx/d\lambda = nf/(d\cos\theta) \qquad (4.1)$$

where

x = the direction of dispersion

λ = wavelength

f = focal length of exit mirror

n = order in which grating is used

d = grating period

θ = angle which diffracted light makes with the normal.

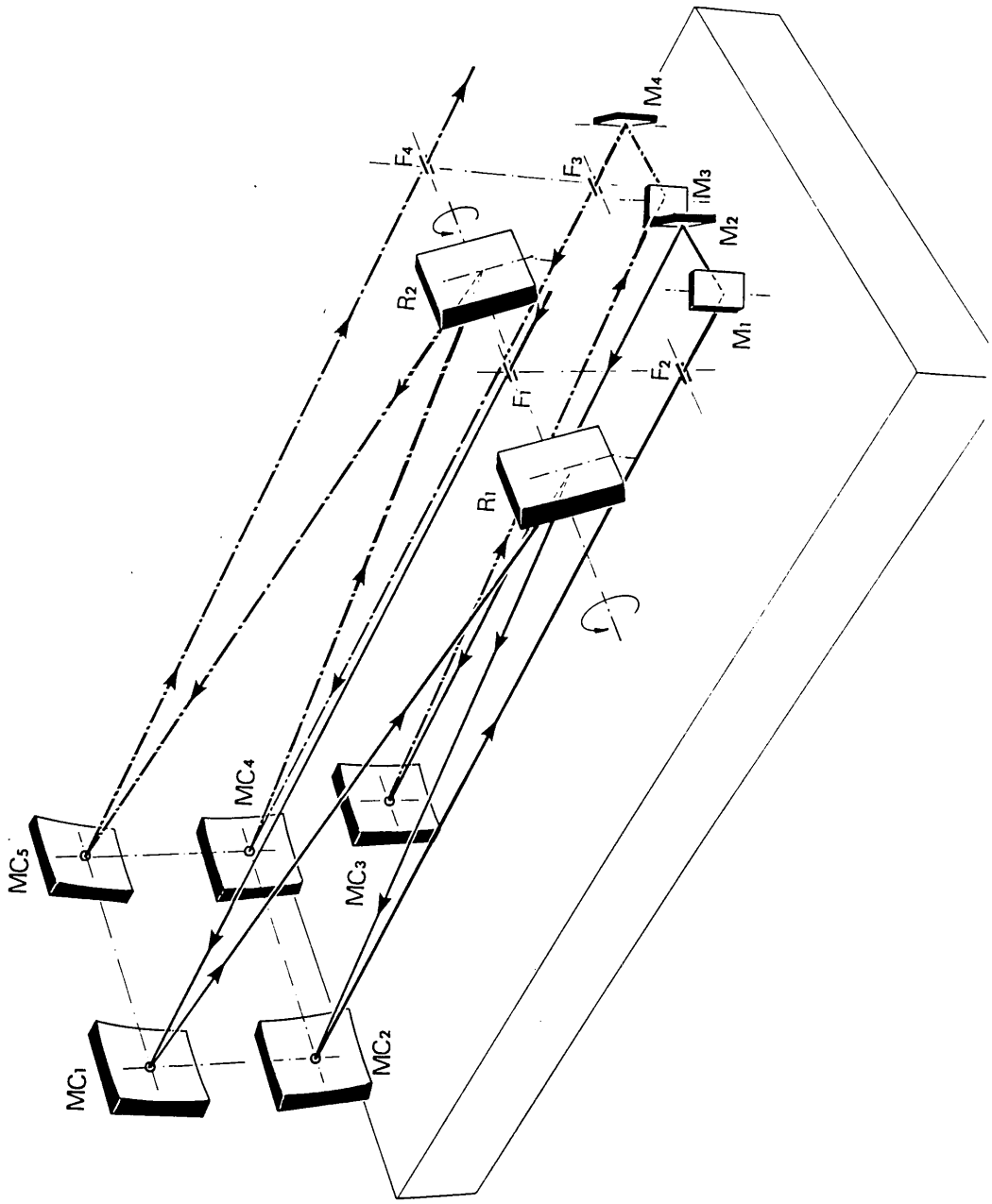

Figure 4.10 Schematic representation of the light path within the double spectrometer.

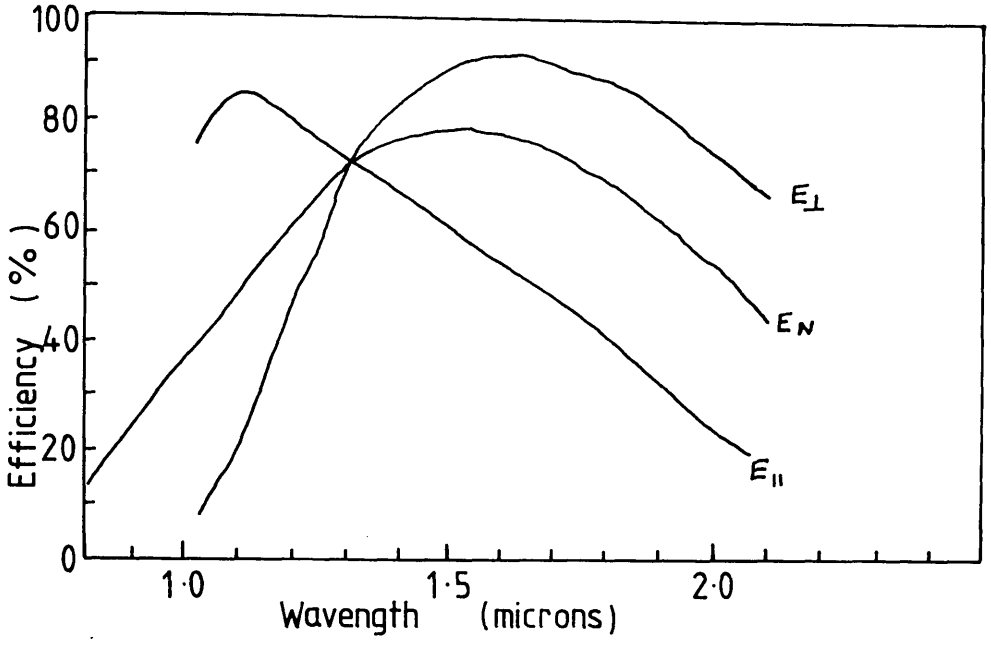

Figure 4.11(a) Grating efficiency curves for the infra–red gratings showing the efficiency for light polarised parallel to the grooves, perpendicular to the grooves and for unpolarised light ($E_{||}$, $E_\perp$ and E_N respectively).

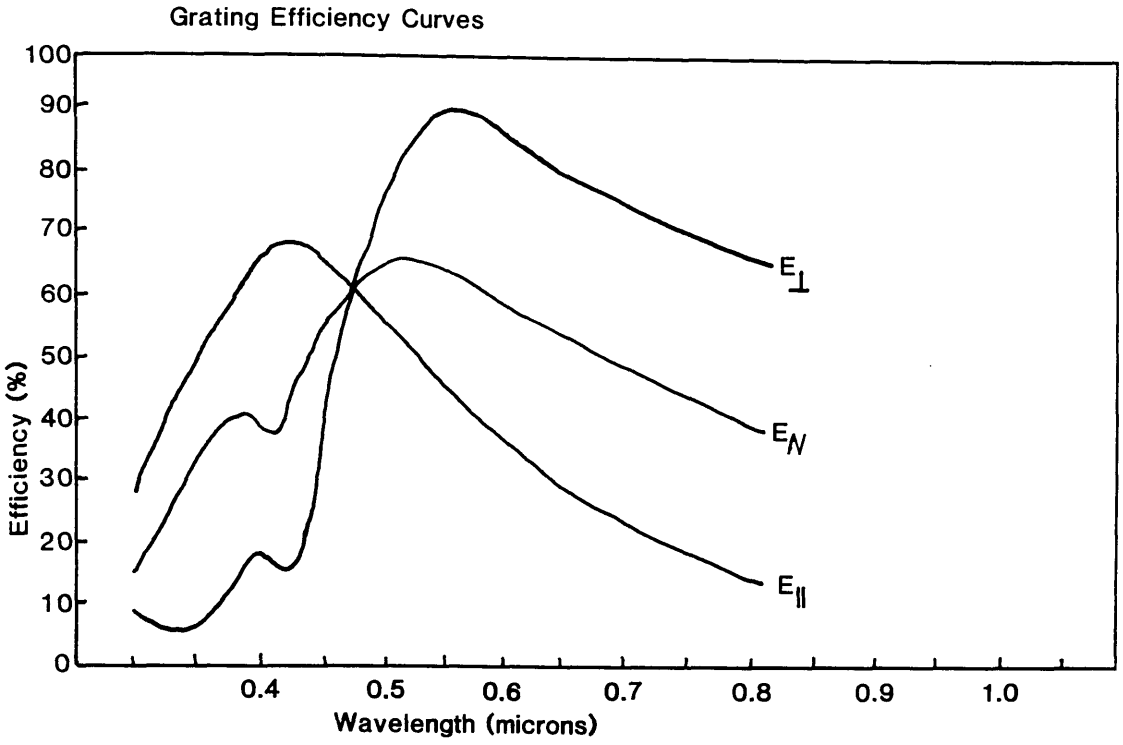

Figure 4.11(b) Grating efficiency curves for the visible gratings showing the efficiency for light polarised parallel to the grooves, perpendicular to the grooves and for unpolarised light ($E_{||}$, $E_{\perp}$ and E_N respectively).

Christensen and Potter [1963] have shown that the resolution of a double grating spectrometer may be treated as an extension of the single grating case by either considering the effects of a second spectrometer on the output of the first or by incorporating the dispersion effects of both gratings into the above formula by doubling the dispersion, D. The optimum performance can be shown to be obtained when all the slits are the same width. This assumes perfect coupling between the two spectrometers with the image of the second slit falling exactly on the third slit. In practice, this is not always the case because thermal effects cause the mirrors to move relative to one another. This can be adjusted by small movements of mirrors MC3 and MC4 of figure 4.10. Moving MC3 will affect the coupling of light from the first to the second spectrometer; moving MC4 will change the position of the light image with respect to slit 4, the final exit slit. If these mirrors are incorrectly placed then signal is lost within the spectrometer and the observed light intensity drops sharply.

Given that the static resolution, SR, is given by:

$$\begin{aligned} SR &= \text{reciprocal angular dispersion} \times \text{slitwidth} \\ &= d\lambda/dx \times \text{slitwidth} \\ &= 2.43\ \text{Å/mm} \times \text{slitwidth} \end{aligned} \qquad (4.2)$$

and the dynamic resolution, DR, is given by:

$$DR = \text{scan rate} \times \text{timeconstant of detection system} \qquad (4.3)$$

then the total resolution, R = SR + DR, and typical curves are shown in figure 4.12.

Control of the spectrometer is via a microprocessor unit called the Spectralink which operates the stepper motor drive. This unit retains a memory in RAM of the

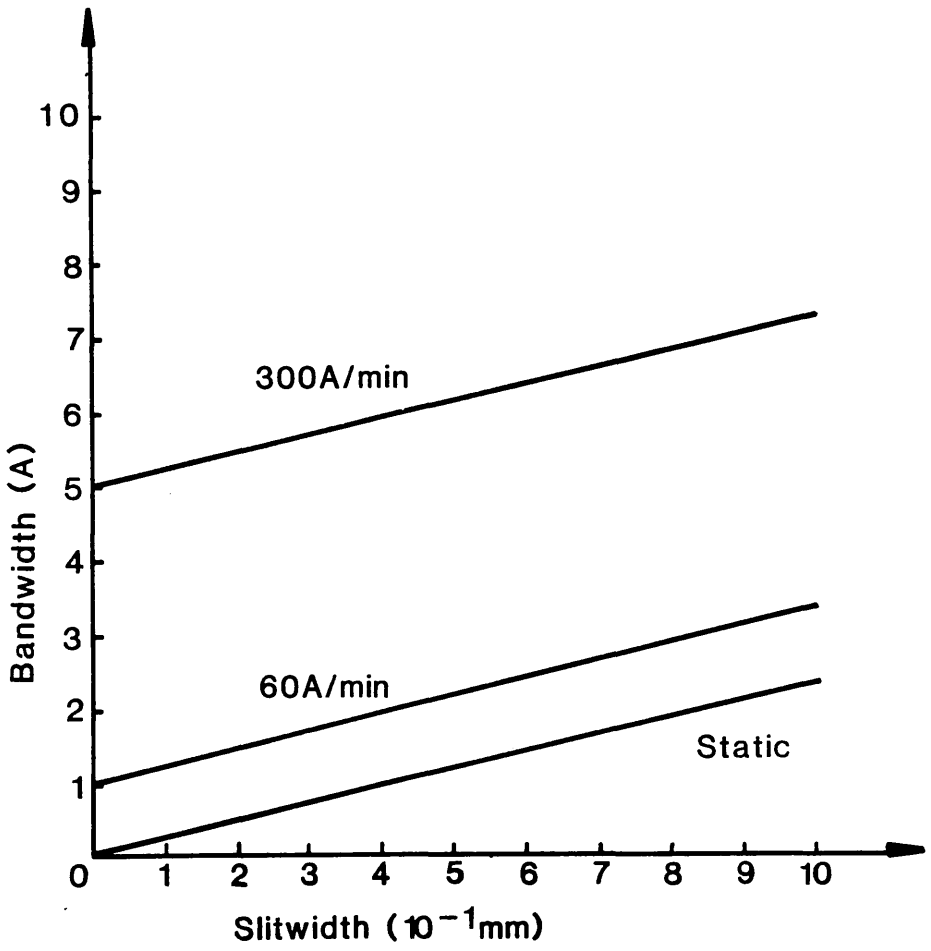

Figure 4.12 Values of the total resolution as a function of slitwidth for two scan speeds and a time constant of 1 second.

position of the spectrometer. There is also a manual wavelength readout on the spectrometer and these two numbers can be compared to ensure that there is no day–to–day loss of calibration. In order to calibrate the spectrometer absolutely, a monochromatic light source of known wavelength must be used, e.g. one of the lines of an arc lamp or a laser line. It is important to calibrate either every few days or every spectrum depending on the accuracy required. There is also a backlash effect when reversing the direction of travel of the spectrometer and so spectra need to be recorded always in the same direction and always approaching the start of the scan from the direction of travel of the scan.

4.5 Computerisation and Software

The machine recommended for the job of running the experiments under computer control was the IBM Model 30 which has a 20 MByte hard disk and one diskette drive. It also has one parallel port, one serial port and three expansion sockets. An Epson LX800 printer and a Benson 1002 4 pen plotter provided hard copy facilities while an analogue to digital converter (ADC) board together with a process control I/O timer and the programming language Turbo Pascal were used to control the experiment. The interface connections are shown schematically in figure 4.13. A flow diagram outlining the software for the Raman scanning program is given in figure 4.14. The program written to run a Raman scan is in Appendix C, and comments on each part of the program are included at each stage.

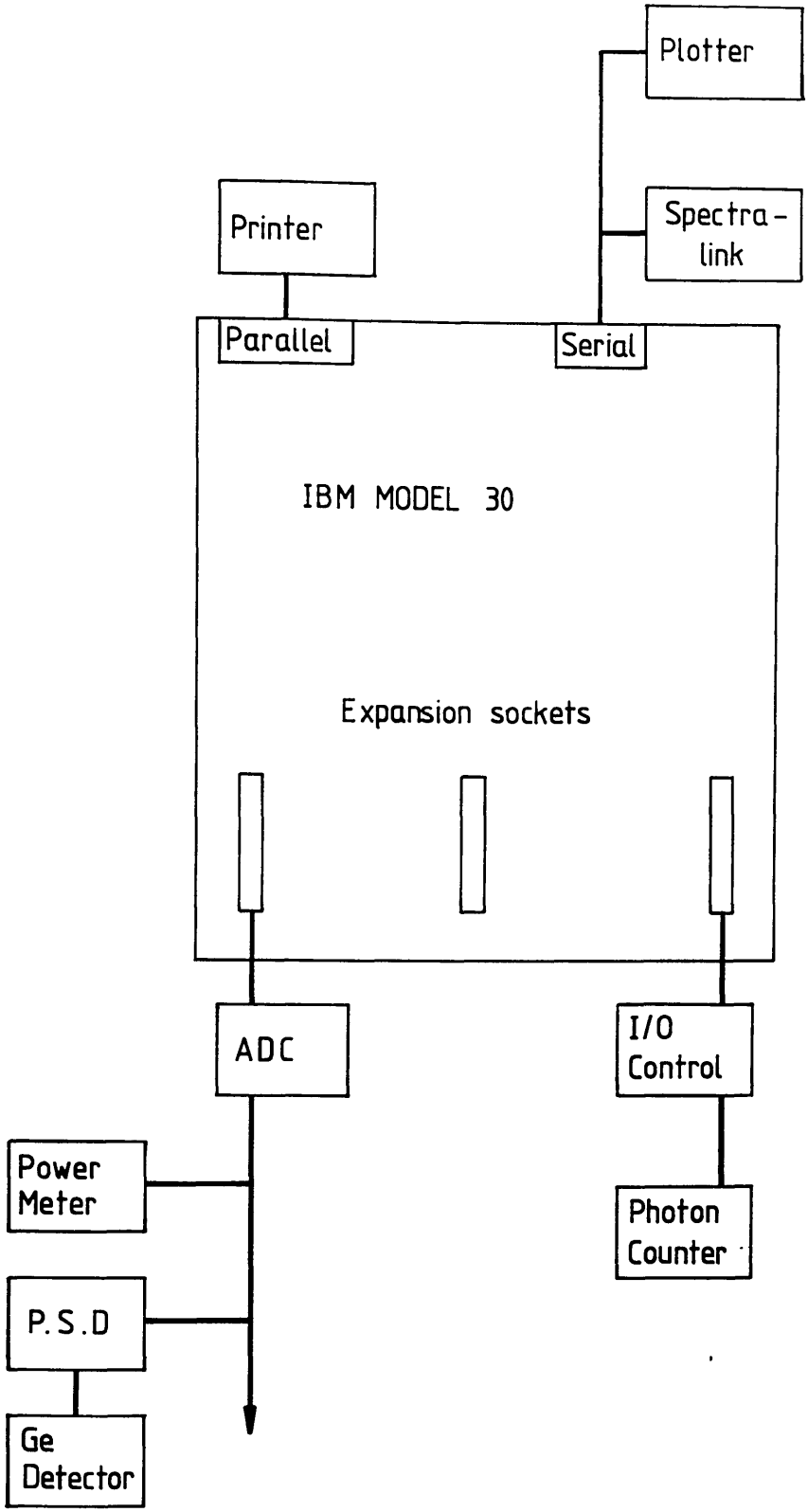

Figure 4.13 Schematic representation of the computer interface.

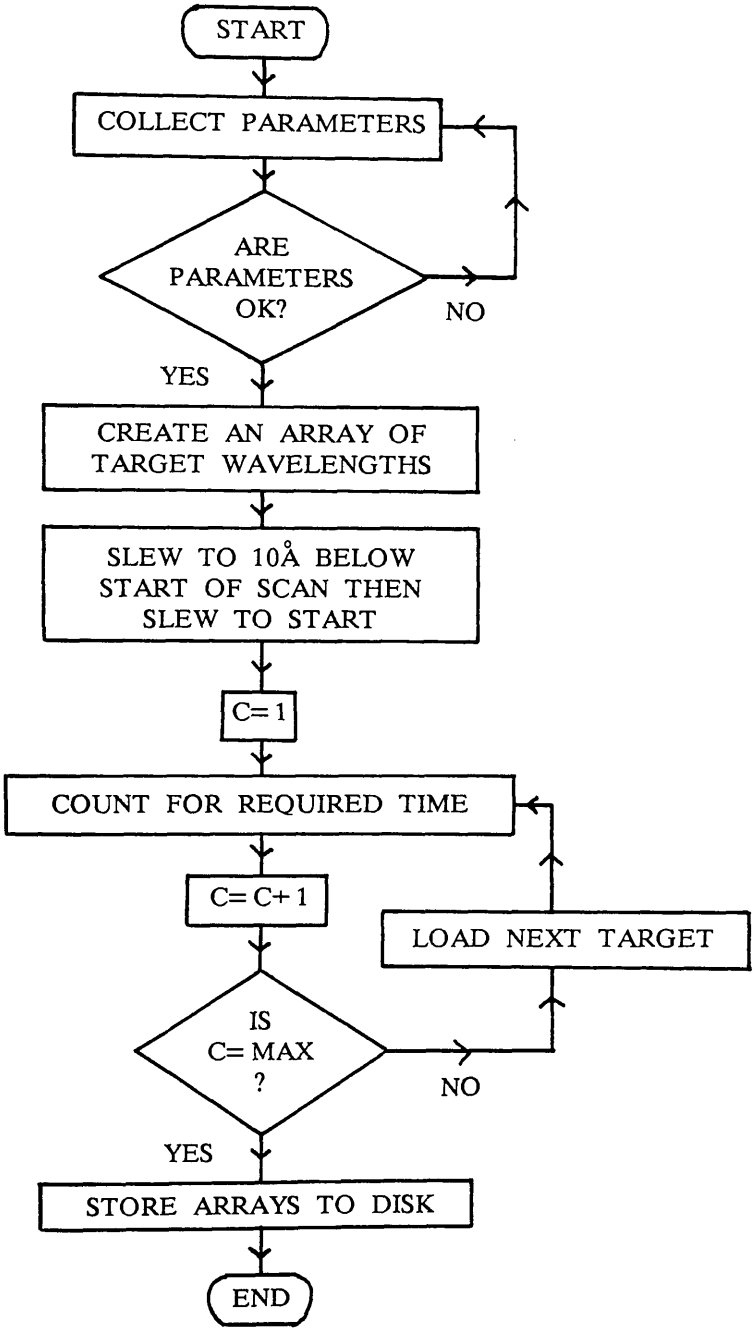

Figure 4.14 Flow diagram of Raman scanning program.

4.6 Cryostat

Some of the experiments in this work were carried out at cryogenic temperatures. This involved the use of a Quantum Electronics cryostat with optical access. Both the inner and the outer windows were made of Spectrosil WF (water free) which has a flat spectral response from 250nm to 2μm and a transmission in excess of 80% throughout this range. The cryostat could be operated in either bath or gas–flow modes, i.e., either by immersing the sample in liquid Helium and cooling to below the lambda point so that the liquid was still (temperature range 1.8 to 2.1 K) or else by maintaining a flow of cold gas sufficient to keep a constant temperature (temperature range 4.2 to 300 K). A schematic of the cryostat is given in figure 4.15. The temperature was maintained by balancing the cold gas/liquid input with the heat generated by a heater in the base of the cryostat. Temperature stabilities of ±2K in gas flow mode at around 60K or ±0.1K in bath mode below the lambda point were usual. It can be seen from figure 4.15 that the maximum solid angle subtended by the sample is limited. The two windows in the optical path also reduce the collection efficiency therefore resulting in weaker signals than in the unobstructed case. This meant that most experiments were done in air at room temperature unless either low temperatures or a sealed environment were needed.

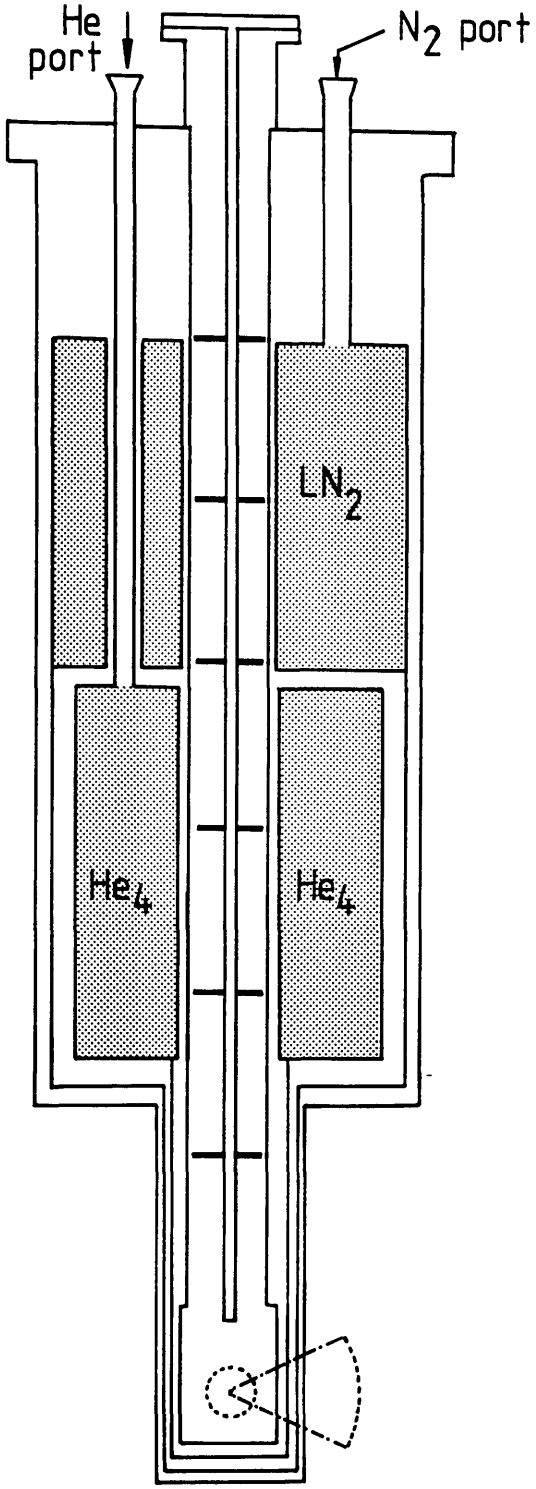

Figure 4.15 Schematic representation of the optical cryostat showing the liquid Nitrogen reservoir (LN_2), the liquid Helium reservoir (He_4) and the optical aperture (angular width 50°). The samples are held on a special block on the end of the insert such that they are centred on the optical aperture. Scale approx. 1:28.

R L Christensen and R J Potter; Appl Opt 2, 1049, 1963

R Foord, R Jones, C J Oliver and E R Pike; Appl Opt 8, 1975, 1969

M L Meade; J Phys E 14, 909, 1981

J K Nakamura and S E Schwartz; Appl Opt 7, 1073, 1968

"RCA Photomultiplier Handbook"; published by RCA Corporation, USA, 1980; p20

CHAPTER 5

GaInAs – InP HETEROSTRUCTURES

5.1 Introduction and Sample Details

The motivation to study the GaInAs– InP semiconductor system lies in the fact that the future of integrated circuitry is moving from electronics to optics. This trend is based on the optical capability for fast switching, low loss transmission and the improvement in parallel communication that is possible when electrical cross– talk is no longer a problem. Optical links using optical fibres will replace electrical wires as the data– carrying medium. At present, these optical fibres have maxima in their transmission at wavelengths around 1.3μm and 1.5μm – values which correspond to the energy gap range of GaInAs– InP heterostructures. The driving force behind work on this system is to produce laser sources, optical modulators and detectors in this material to take advantage of the low loss region of the fibres.

In this chapter, optical spectroscopy experiments are described aimed at understanding the effect of a layered structure on the lattice vibrations in GaInAs– InP. Experiments on the two bulk materials, GaInAs and InP, are described, followed by work on a comparatively simple heterostructure, a single quantum well (SQW) and lastly work on a more complex structure, a multiple quantum well (MQW).

The GaInAs–InP samples used in the work of this chapter were all grown by molecular beam epitaxy (MBE) in a VG 80 H reactor at the SERC III–V Semiconductor Facility at Sheffield University by Dr John S Roberts and Dr Peter A Claxton. All the samples were grown with an intended alloy composition of $Ga_{0.47}In_{0.53}As$ and are thus intended to be unstrained (see figure 3.2). X–ray analysis of two of the samples used is detailed in chapter 8 and shows that the actual composition is very close to the intended composition. This means that the overall strain in the epitaxially–grown layers is very low. The sample structures are given in table 5.1.

Table 5.1

Structures of GaInAs – InP Samples

Name	Type	Intended Structure	Actual Structure (if measured to be different)
PMB106	Bulk	3μm InP. Mobility(300K) = 4700 $cm^2V^{-1}sec^{-1}$	
PMB112	Bulk	2.5μm $Ga_{0.47}In_{0.53}As$ on 0.3μm InP buffer(u.d.) Mobility(300K)= 9700 $cm^2V^{-1}sec^{-1}$	
PMB116	SQW	500Å InP cap layer(u.d.) on 160Å $Ga_{0.47}In_{0.53}As$ QW on 0.3μm InP buffer (u.d.)	cap = 680Å, QW = 230Å [X–ray analysis; Ryan et al, 1987]
PMB117	MQW	0.1μm InP cap (u.d.) then 5 QW layers of $Ga_{0.47}In_{0.53}As$ of widths 5, 10, 20. 40, 80Å separated by 0.1μm InP barriers all grown on a 0.3μm InP buffer (u.d.)	QW sizes: 10, 20, 28, 50 and 110Å [TEM; Nash, 1987]
PMB121	MQW	0.1μm InP buffer (u.d.) then 50 periods of 25Å $Ga_{0.47}In_{0.53}As$ QW and 100Å InP barrier layers on 0.3μm InP buffer (u.d.)	

Notes:

1. u.d. = undoped
   background doping level = $3.2x10^{15}$ cm^{-3} (300K) for InP
   = $5.7x10^{15}$ cm^{-3} (300K) $Ga_{0.47}In_{0.53}As$

2. All substrates were [100] Fe–doped semi–insulating InP.

The sample studied as typical of the GaInAs grown at Sheffield was PMB112, a layer of $Ga_{0.47}In_{0.53}As$ which was 2.5μm thick (see table 5.1). The x−ray data, detailed in chapter 8, showed this sample to be of good crystalline quality and, although slightly distorted from the cubic, this produced no significant strain in the lattice (approx. 0.5 kbar in the plane of the interface).

The room temperature Raman spectrum of PMB112 is shown in figure 5.1. The spectrum obtained is qualitatively the same as those obtained from similar samples by Kakimoto and Katoda [1982], Jain et al [1985], Pearsall et al [1983], Davey et al [1987], Pinczuk et al [1978] and Soni et al [1986]. Of these, the first two demonstrate 2−mode alloy behaviour in $Ga_{0.47}In_{0.53}As$, the third, Pearsall et al, shows non−2−mode behaviour, Davey et al settle for "partial 2−mode phonon behaviour" while the latter two authors make no comment on the matter. A full account of the phonon behaviour of $Ga_{0.47}In_{0.53}As$ is given in section 2.6.3 where the phonon behaviour is interpreted in terms of a two−mode model.

Polarisation analysis was done on PMB112 and the results are shown in figure 5.2. In crossed polarisation, $z(y,x)\bar{z}$, first−order Raman scattering selection rules allow scattering from the LO mode; in parallel configuration, $z(y,y)\bar{z}$, the LO mode is forbidden. The TO mode is forbidden for both configurations. It is clear that the modes at 265 and 232 cm^{-1} obey the LO selection rules and these modes are therefore identified as the GaAs−like LO and the InAs−like LO modes respectively. The frequency of the GaAs−like LO compares favourably with that obtained by Pearsall et al (270 cm^{-1}, growth method LPE) and Davey et al (266 to 270 cm^{-1}, growth method MOVPE) for this particular alloy composition. It is possible that the small shift in the observed mode frequency might be related to growth method as this is the first Raman scattering study of MBE−grown $Ga_{0.47}In_{0.53}As$. Care should

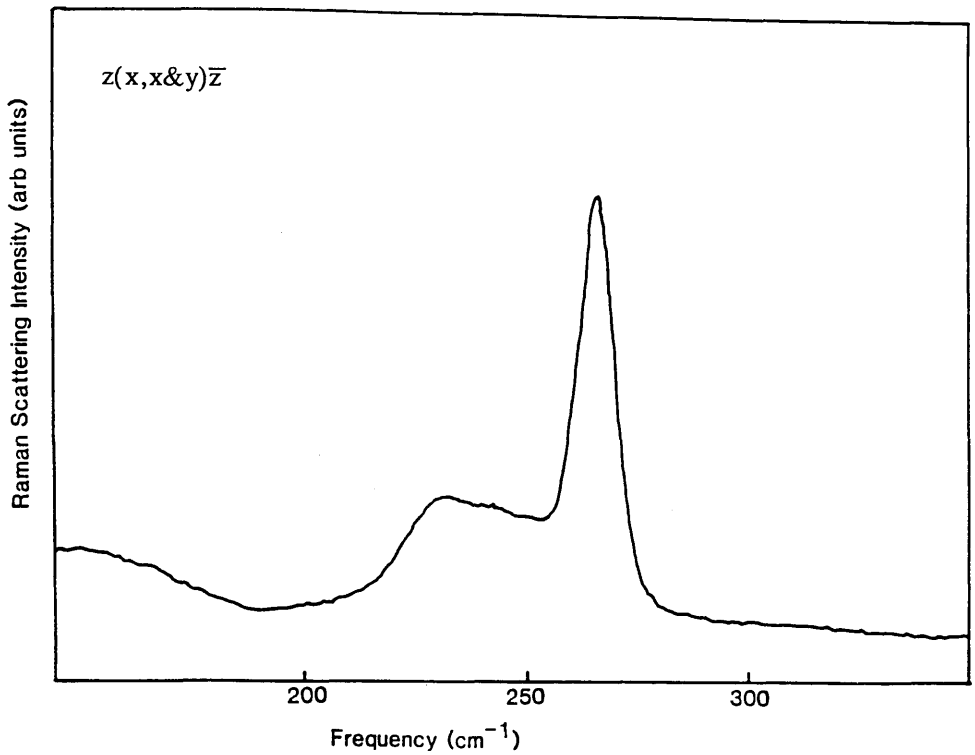

Figure 5.1 Room temperature Raman spectrum of PMB112, bulk GaInAs, $\lambda = 4880$Å, resolution= 5 cm^{-1}.
The dominant peak at 265 cm^{-1} is the "GaAs– like" LO and the peak at 232 cm^{-1} is the "InAs– like" LO.
Improving the spectral resolution to 2.5 cm^{-1} did not resolve any more features in this band.

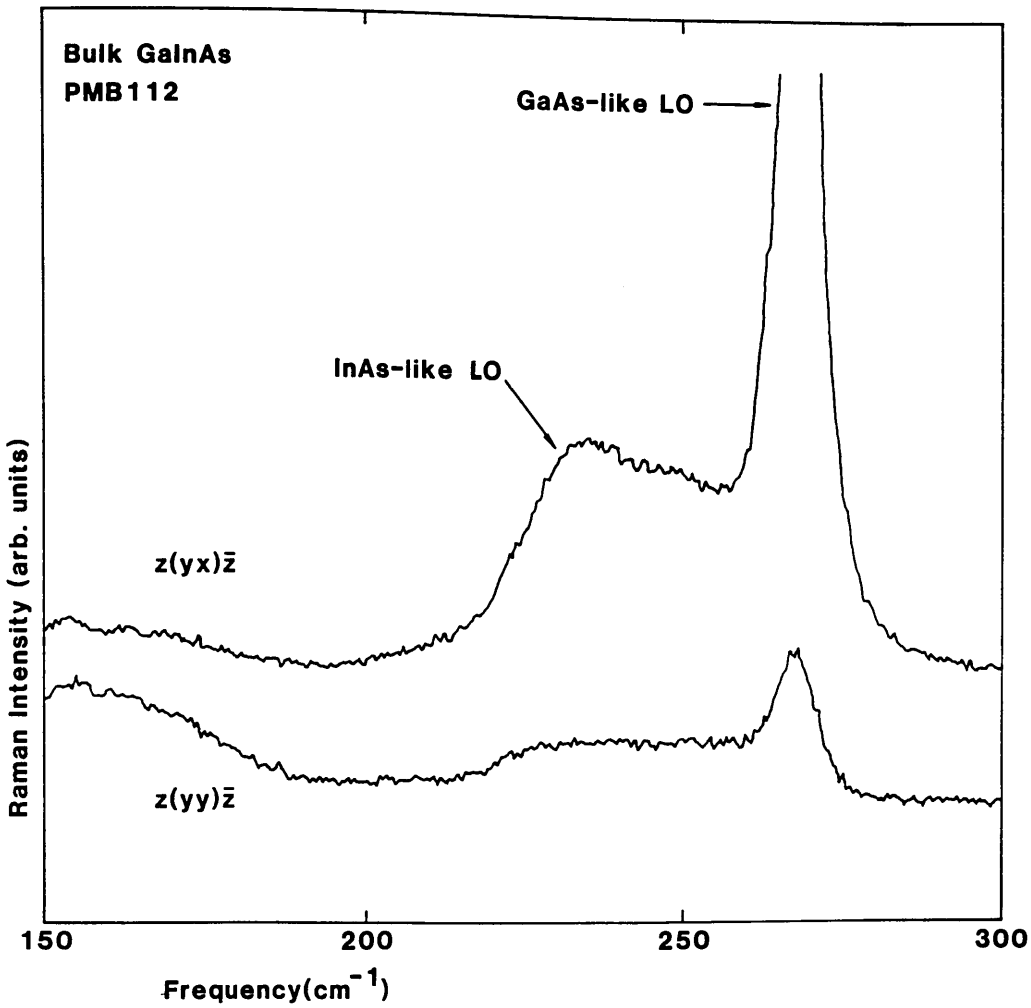

Figure 5.2 Polarisation analysis of PMB112. In the forbidden polarisation, $z(y,y)\bar{z}$, both LO modes have quenched. $\lambda = 4880$Å, resolution= 5 cm^{-1}.

be taken when comparing frequency data with that of Brodsky and Lucovsky [1968] as their material was grown on GaAs substrates and will therefore be in a state of strain [Marzin, 1987] which will shift the phonon frequencies [Nakashima et al, 1986].

The broad mode centred around 153 cm^{-1} is identified after Kakimoto and Katoda [1982] as a disorder–activated longitudinal acoustic phonon (DALA) of the alloy. Their interpretation is based on the fact that this mode is strongest in intensity at the mid–range of alloy composition where the alloy disorder is expected to be a maximum.

In an attempt to resolve the GaInAs phonon band, the sample was cooled to 10K in a Helium–flow cryostat. The data is compared with that recorded at room temperature in figure 5.3. Apart from a degradation in the signal strength due to the reduced collection efficiency allowed by the cryostat, there is no change in the spectrum.

Several laser lines were used to record spectra in order to choose the one closest to the E_1 energy gap of GaInAs and thus obtain resonant enhancement of the signal (see section 1.3.4). At room temperature, the energy gaps of $Ga_{0.47}In_{0.53}As$ are:

E_0	=	0.810 eV	=	1530 nm
E_1	=	2.62 eV	=	473 nm
$E_1+\triangle_1$	=	2.85 eV	=	435 nm

[Data from Landolt–Boernstein, 1982]

Three Argon ion laser lines were tried, 4579, 4880 and 5144Å. The spectra obtained are shown in figure 5.4. Trommer and Cardona [1978] demonstrated strongly resonant behaviour for both allowed and symmetry–forbidden phonon scattering in GaAs at both the E_1 and $E_1+\triangle_1$ energy gaps (see figure 1.5). As can

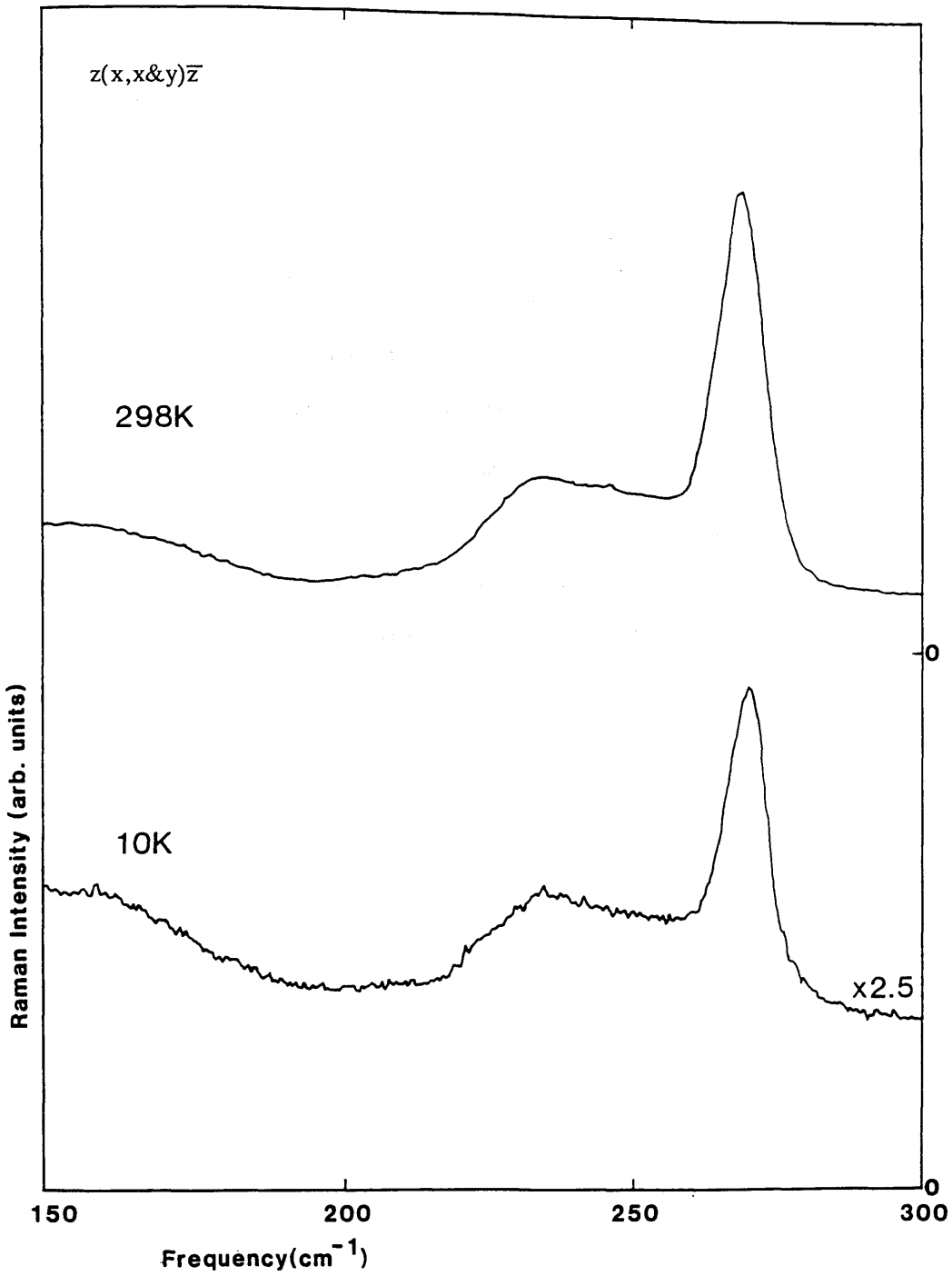

Figure 5.3 Raman spectra of PMB112 at room temperature and at 10K. The shape of the alloy band remains unchanged. $\lambda = 4880$Å, resolution= 5 cm^{-1}.

be seen from figure 5.4, there is a similar effect here, since the signal intensities have fallen for the 4579 and 5144Å lines by more than the decrease in power warrants. It was therefore decided to continue using the 4880Å line for subsequent measurements since this provided the strongest signal.

The sample heating caused by the laser beam was estimated for this sample using the Stokes/anti–Stokes intensity ratio described in section 1.3.2. The value obtained indicated that the sample temperature at the point of study was about 200°C above the ambient room temperature. This is a "worst–case" value obtained using 460mW of incident light in a point focus. The uncertainty in this value is likely to be about 20 – 40% as the calculated temperature has a logarithmic dependence on the measured intensity ratio. Using the data of Chang et al [1969] which gives a shift to lower energy of $0.16cm^{-1}$ per 10K for GaAs, a temperature of 200°C would cause a shift of the LO and TO phonon frequencies of about $3cm^{-1}$ to lower energy. This temperature shift probably accounts for the fact that the frequencies measured here for GaInAs are slightly lower than those reported elsewhere (see previous discussion).

As the absorption length in GaInAs is smaller than that in InP, this value of sample heating can be taken as the maximum which could be expected for any of the samples studied here. Since the value obtained is well below the growth temperature of either GaInAs or InP, it can be concluded that no degradation of the crystal will result from the laser powers used.

In summary, a high quality sample of bulk $Ga_{0.47}In_{0.53}As$ has been studied by Raman scattering at various temperatures and with various laser lines. The alloy Raman band has demonstrated the existence of one GaAs–like LO mode and one InAs–like LO mode in polarisation analysis, however the band has not been resolved further. The reasons for this are discussed fully in chapter 2.

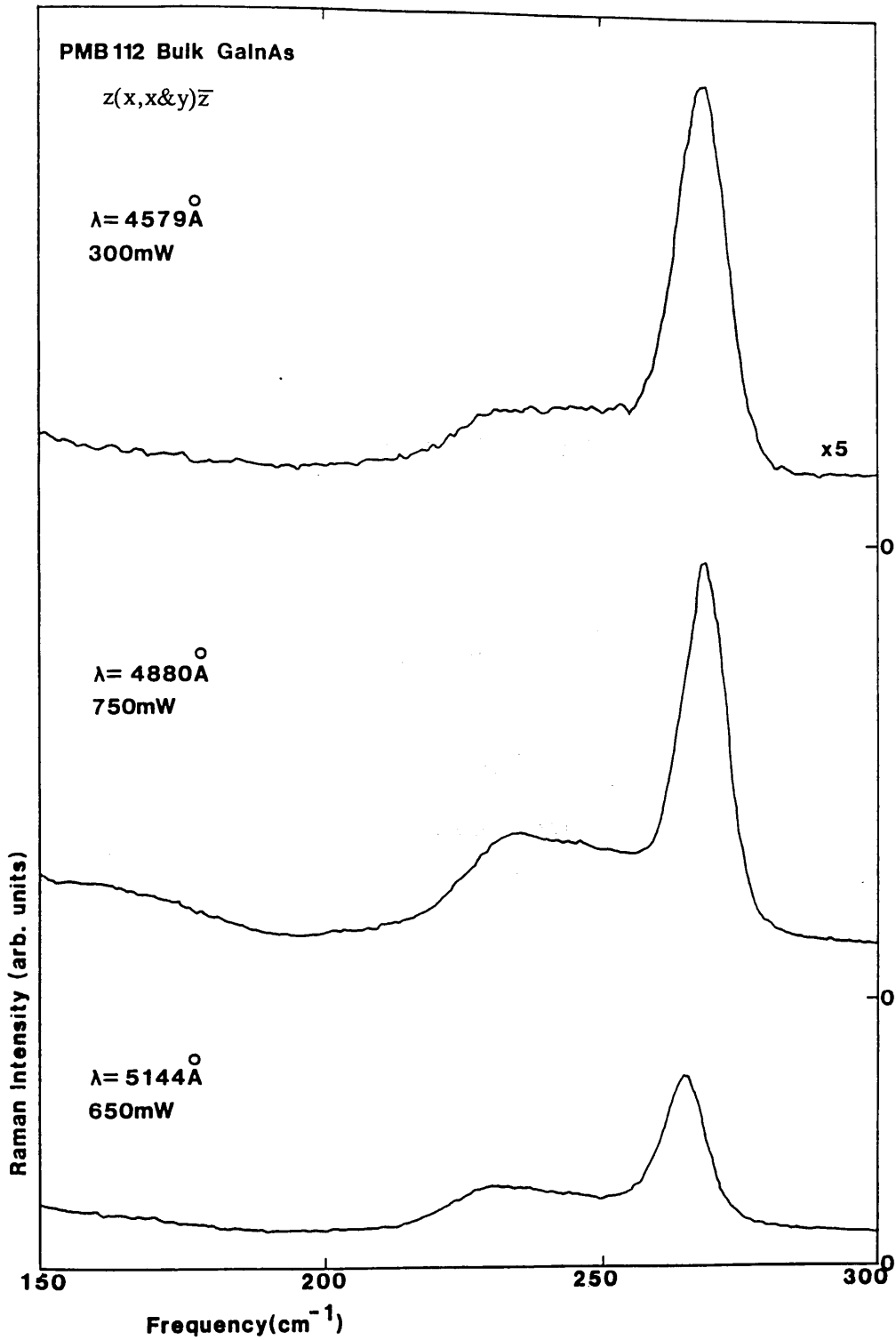

Figure 5.4 Room temperature Raman spectra of PMB112 for three different laser lines. Resolution= 5 cm^{-1}.

The sample used in this part of the work was PMB106, an epitaxially–grown layer of InP. The study of bulk InP was needed to form a basis for comparison with the InP barriers in the quantum well structures. The Raman spectra obtained from PMB106 are shown in figure 5.5 for two polarisation analysis configurations. The signal is not very strong, a fact that can be attributed to the off–resonance of the exciting light with any of the energy gaps in InP:

laser	=	2.514 eV	=	4880 Å
E_0 (InP)	=	1.34 eV	=	9250 Å
$E_0+\Delta_0$	=	1.45 eV	=	8550 Å
E_1	=	3.15 eV	=	3940 Å

[data at 300K from Landolt–Boernstein, 1982]

In the crossed configuration the allowed LO phonon can be seen at 348 cm^{-1} with a small contribution at 304 cm^{-1} from the symmetry–forbidden TO phonon. Also visible are three weak peaks at 185, 229 and 250 cm^{-1}. Similar structure has been seen by both Bedel et al [1986] at 191.5, 227 and 253 cm^{-1} and Alfrey and Borcherds [1972] at 189, 228 and 251 cm^{-1} in InP. Both authors agree that these peaks relate to second–order scattering from non–zone–centre phonons but their assignments are contradictory. Both assignments are listed in table 5.2. The interpretation of Bedel et al [1986] appears to be most consistent with both neutron scattering and infra–red absorption measurements and so these assignments are assumed for the peaks shown in figure 5.5. All three of these peaks follow the LO phonon symmetry of Γ_{15} thus agreeing with the experimental results of Bedel et al [1986].

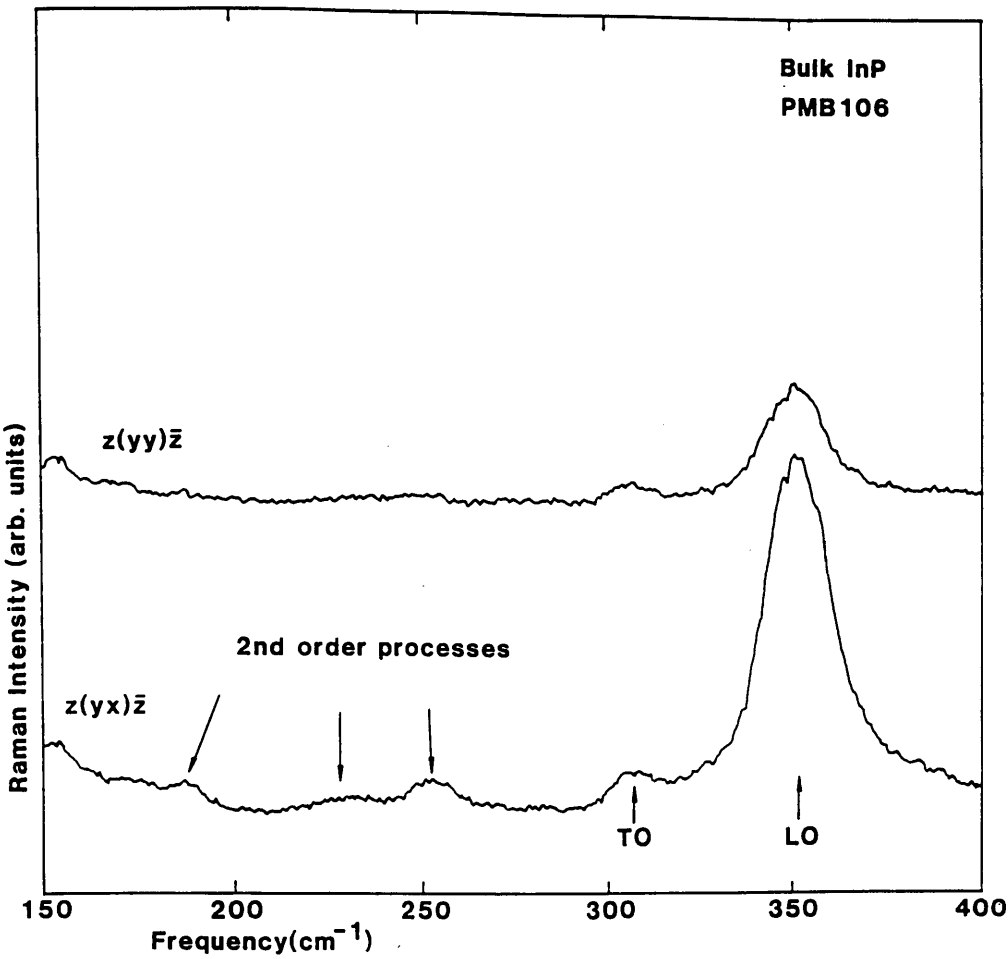

Figure 5.5 Room temperature Raman spectrum of PMB106, bulk InP, for two polarisation analyses. See text for identification of the second order processes. $\lambda = 4880$Å, resolution= 5 cm^{-1}.

Table 5.2

Identification of Second–Order Phonon Peaks in InP

This work (cm^{-1})	Alfrey (cm^{-1}) (a)	Bedel (cm^{-1}) (b)	Assignment (after Bedel) (c)
185 ± 4	189	191.5	$2\nu_2$ @ W
229 ± 4	228	227	$\nu_1 \pm \nu_3$ @ L $\nu_{12} + \nu_3$ @ L
250 ± 2	251	253	$\nu_{45} - \nu_{12}$ @ L $\nu_{45} - \nu_{12}$ @ X $\nu_2 + \nu_3$ @ W and K

Notes:

(a) Alfrey et al, 1972

(b) Bedel et al, 1986

(c) See figure 5.6 for the phonon dispersion curves of Bedel et al [1986] together with the notation they used.

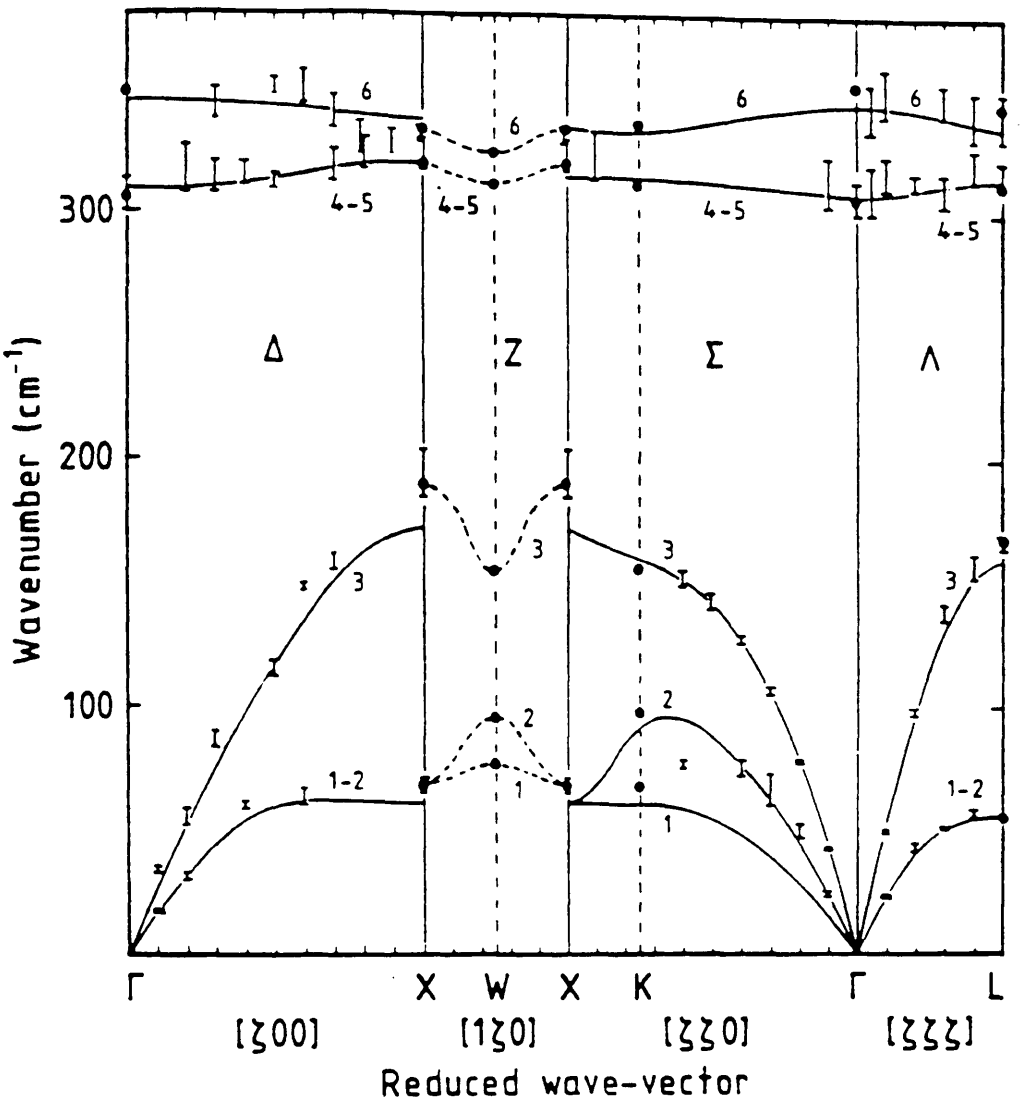

Figure 5.6 Phonon dispersion curves in InP. Figure 4 of Bedel et al [1986] showing the notation used in the second-order assignments.

In the parallel configuration, the LO mode intensity has decreased substantially although there is some breakthrough of signal in this forbidden polarisation. The three weak peaks which follow the LO symmetry are not apparent but the forbidden TO mode is still present as expected.

This work involved a sample grown to my specification, the aim of which was to provide a wide quantum well, so that the Raman scattering volume would be large, together with a thin cap layer to reduce absorption of both the incident laser beam and the scattered Raman signal. To this end, a sample was requested of well thickness 160Å with a cap layer of 500Å. X– ray measurements on the sample, PMB116, showed that the actual dimensions were 230Å and 680Å respectively for the well and cap layers, with a small tetragonal distortion of the epitaxial layer which did not degrade the crystallinity of the sample (see chapter 8 and Ryan et al [1987]).

Figure 5.7 shows the alloy phonon band for both the bulk sample (PMB112) and the QW sample (PMB116). Immediately it is obvious that the GaAs– like LO mode which dominated the bulk GaInAs spectrum has quenched although the phonon band remains in the same energy region. In order to investigate a possible contribution from the barriers to this quench, part of the sample was selectively etched and a spectrum was obtained at each stage. These spectra are shown in figure 5.8. Spectrum (a) is from PMB112, the bulk GaInAs. Spectrum (b) shows the scatter from the as– grown quantum well; the strong peak at 346 cm^{-1} is the InP LO phonon from the cap layer and the alloy band at 210 – 280 cm^{-1} is quenched as discussed above. Spectrum (c) is of the same sample but with the cap layer selectively etched off leaving the GaInAs layer uppermost. The etch used was a 3:1 mixture of H_3PO_4:HCl at room temperature giving an etch rate of about 0.2μm/min [Westland, 1986]. The GaInAs phonon band now resembles the bulk phonon band in both shape and frequency. Finally, in (d), the well layer was removed (with 80% 3:1 H_2SO_4:H_2O and 20% H_2O_2 for 1 – 2 minutes at room temperature [Westland 1986]) and the spectrum now shows only the InP LO mode.

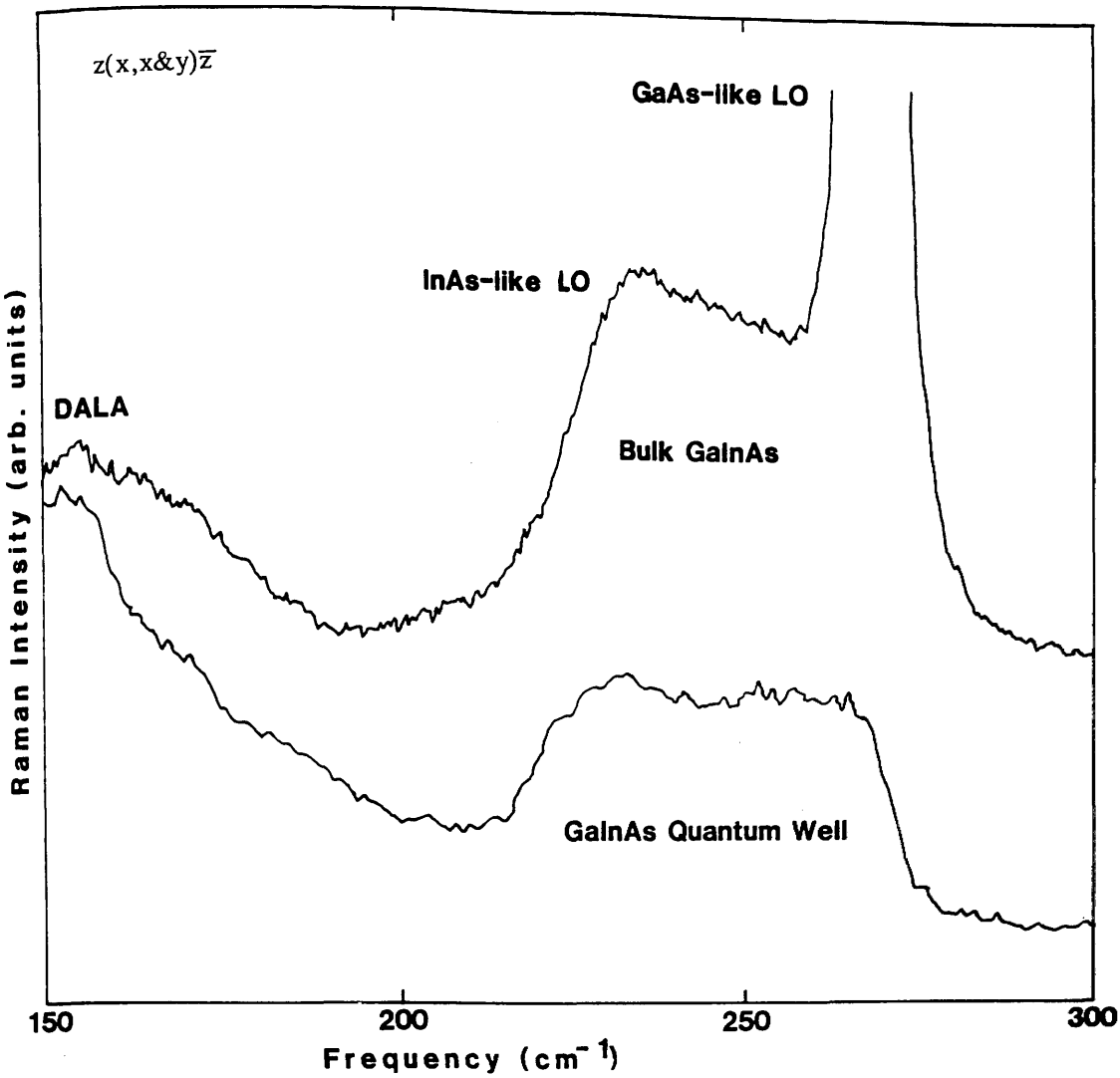

Figure 5.7 Comparison of the room temperature Raman spectra of PMB112, the bulk GaInAs, and PMB116, the quantum well. $\lambda = 4880\text{Å}$, resolution= 5 cm^{-1}.

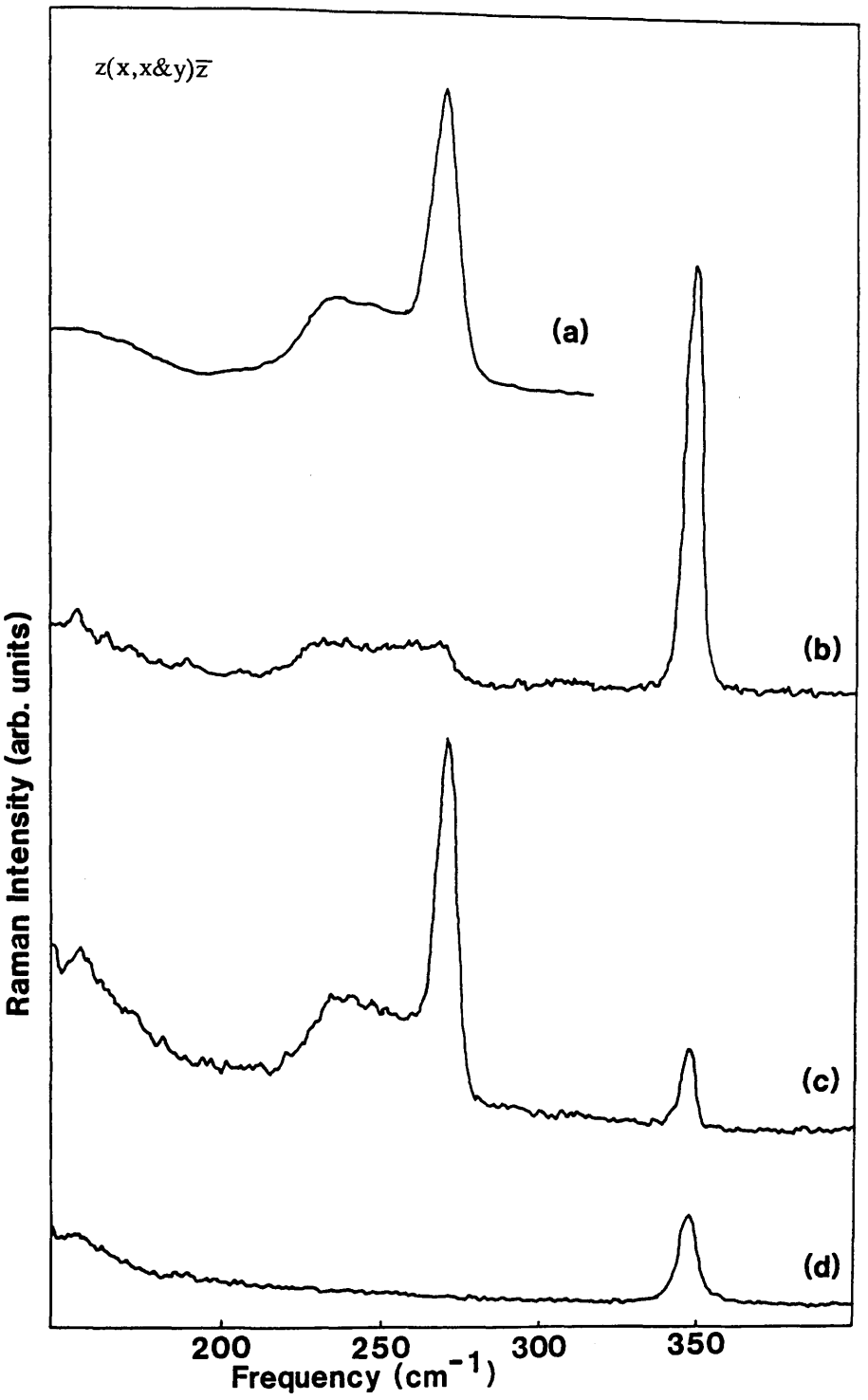

Figure 5.8 This shows the sequence of selective etching of PMB116. (a) The spectrum of bulk GaInAs. (b) Unetched PMB116. (c) PMB116 with the cap removed and the quantum well on the surface. (d) PMB116 with the well removed and the buffer layer on the surface. $\lambda = 4880$Å, resolution$= 5\ cm^{-1}$.

The purpose of this last etch was to show clear evidence that a) the etches were acting as intended and b) that the spectral region from 210 to 280 cm^{-1} in figure 5.8(b) was indeed due to the QW scattering.

A barrier contribution to the quench of the LO modes cannot be identified from these results. If significant tunnelling from the well into the InP had caused the quench of the GaAs–like LO mode in favour of the InP LO mode then the effect of removing the cap layer should have reduced the quench by half but not removed it entirely. As the LO intensity has fully recovered, tunnelling can be eliminated as the cause; in any case, at 230Å the well is too large for barrier penetration to be significant.

In order to investigate a screening mechanism for the quench, two experiments were performed: Raman scattering as a function of laser power and photoluminescence (PL) as a function of laser power. As the theory is different for each they will be discussed separately.

5.4.1 Photoluminescence Linewidth Measurements

This section begins with a brief introduction to the theory of PL as it relates to direct–gap semiconductors. The concept of PL is simple: an electron–hole pair is excited above the energy–gap by an incident photon, the excited carriers relax to the bottom of the bands and then recombine radiatively emitting a photon. Thus the energy spectrum of the emitted photons contains information about the energy levels at or near the semiconductor energy–gap (e.g. shallow impurity levels, bound or free exciton levels). PL spectra are usually recorded at low temperatures ($\lesssim$4K) in order to resolve these closely–spaced energy levels. As the sample temperature is increased, thermal broadening of the energy levels causes the PL emission to broaden and the peaks to overlap. In the absence of deep levels, the room

temperature PL emission consists of a single peak arising from the recombination of electrons at the bottom of the conduction band with holes at the top of the valence band. The lineshape of the emission depends on the shapes of the density of states functions of the electrons and holes. This has been illustrated by Thomas [1976] for various densities of photoexcited carriers, including the electron–hole liquid, where states of higher energy than in normal PL become occupied. The lineshape he deduced for the electron–hole liquid would apply equally well to an electron–hole plasma since Fermi–Dirac statistics apply in both cases. From the work of Thomas [1976], it can be seen that increased excitation of the sample will produce more carriers and therefore move the peak of the emission to higher energies. Sample heating is likely to cause a distortion of the high energy side of the emission thus it is the low energy half width that is used as a measure of the carrier concentration. Investigations of the PL linewidth were undertaken on PMB116 in order to investigate the density of the photoexcited carriers.

Room temperature PL spectra of PMB116 were recorded at various incident laser powers in the range 9 – 600 mW using all–lines blue/green Krypton laser output. Typical spectra, one from each end of the power range, are shown in figure 5.9. The emission lineshapes are qualitatively different for low and high power excitation. The low power emission spectrum is strongly reminiscent of the lineshape produced by excitonic emission where the excitation density is low enough for Maxwell–Boltzmann statistics to apply [Thomas et al, 1976]. The high power emission spectrum, on the other hand, closely resembles the PL lineshape observed by Sakar et al [1988] from a modulation–doped SQW of GaInAs–InP. In this case, the carrier density is such that Fermi–Dirac statistics must be used.

The integrated intensity of the PL spectra is plotted as a function of laser power in figure 5.10 and a predominantly linear relationship is observed. If the assumption is made that the radiative recombination efficiency is independent of the excitation intensity then this linear relationship is what would be expected since for

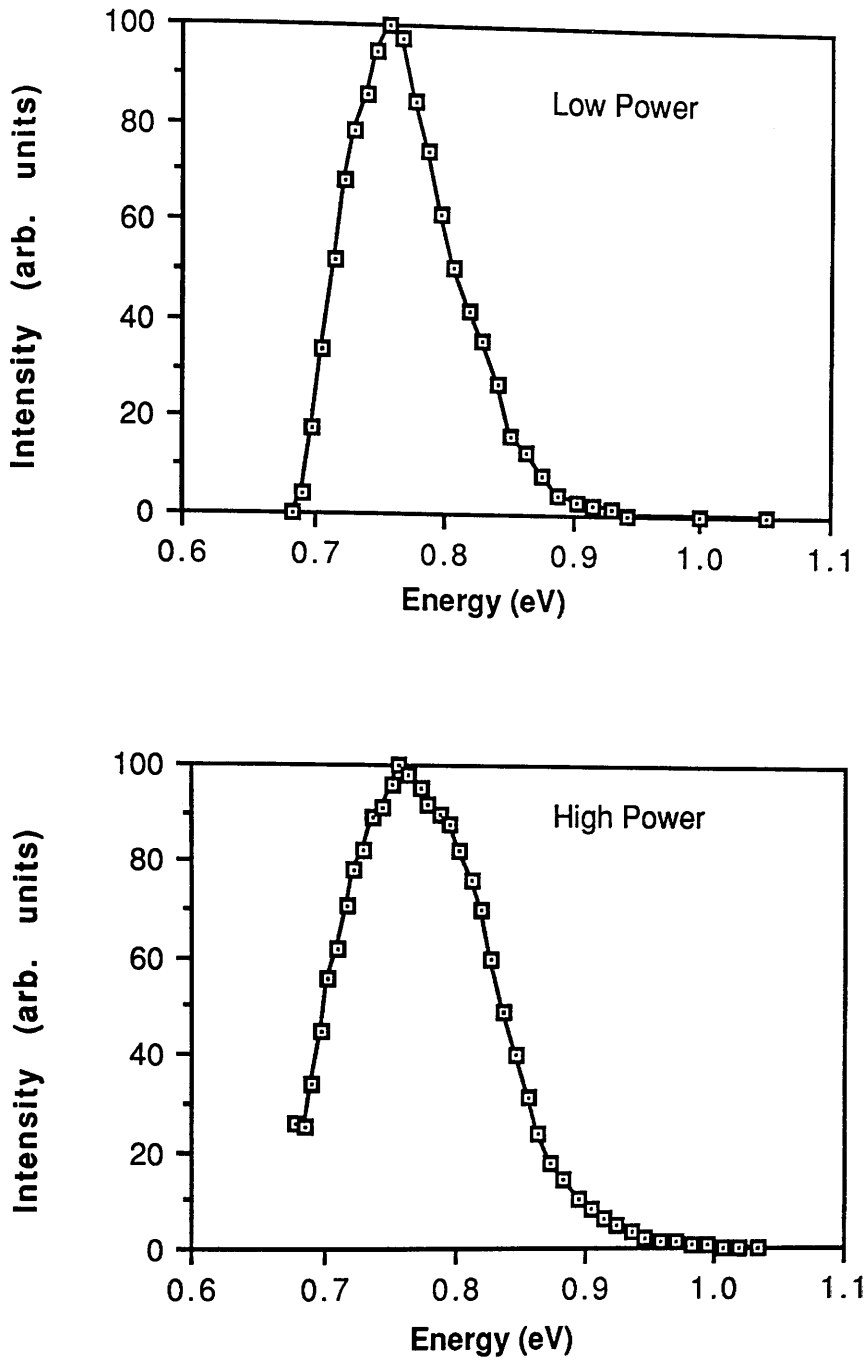

Figure 5.9 Spectral lineshape of photoluminesence from PMB116 at both low and high excitation intensity and at room temperature. The low power trace is an order of magnitude weaker than the high power trace. The spectra are corrected for instrumental spectral response.

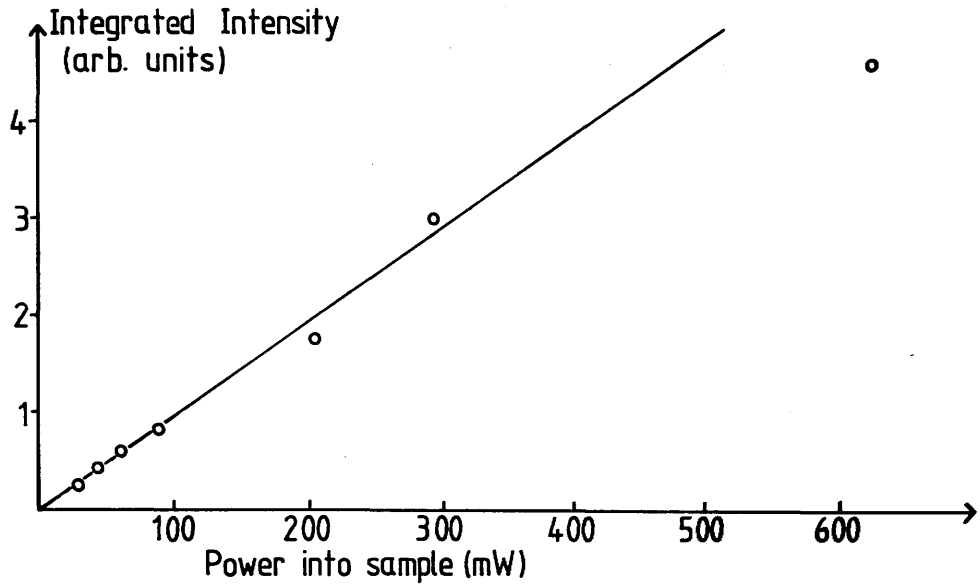

Figure 5.10 Integrated photoluminesence intensity as a function of incident laser power. The line is a linear regression analysis of the data except for the highest power point (see text). The regression coefficient is 0.993.

every photoexcited electron–hole pair, there would be a photon emitted at or near the energy gap. At very high excitation powers, the emission intensity becomes sub–linear as non–radiative processes become more significant. This is evident in the sub–linearity of the highest power point in figure 5.10. Figure 5.11 shows the low energy half width at half maximum (HWHM) of the spectra plotted as a function of laser power. A very different behaviour is observed here: initially, the HWHM increases with power and reaches saturation. Beyond this, no further increase in the HWHM is observed.

This behaviour can be interpreted in terms of a photoexcited electron–hole plasma (EHP): as the incident laser intensity increases, so the EHP density increases until an equilibrium is reached between the rate of excitation of electron–hole pairs and the recombination rate. At some point, the EHP density can no longer increase and the plasma expands to accommodate the extra electron–hole pairs with the result that the EHP density remains constant.

The expansion of EHPs in direct gap semiconductors is a well–documented phenomenon [see e.g. Romanek et al, 1981; Nather and Quagliano, 1984]. The expansion is driven by the Fermi pressure, p, given by:

$$p = n^2(\partial F(n,T)/\partial n)_T \qquad (5.1)$$

where

n = carrier density

T = carrier temperature

F(n,T) = free energy of the EHP

Thus for a fixed carrier temperature, the plasma expansion depends only on the carrier density.

A time–resolved PL study of EHPs in InGaAsP epitaxial films by Taylor and

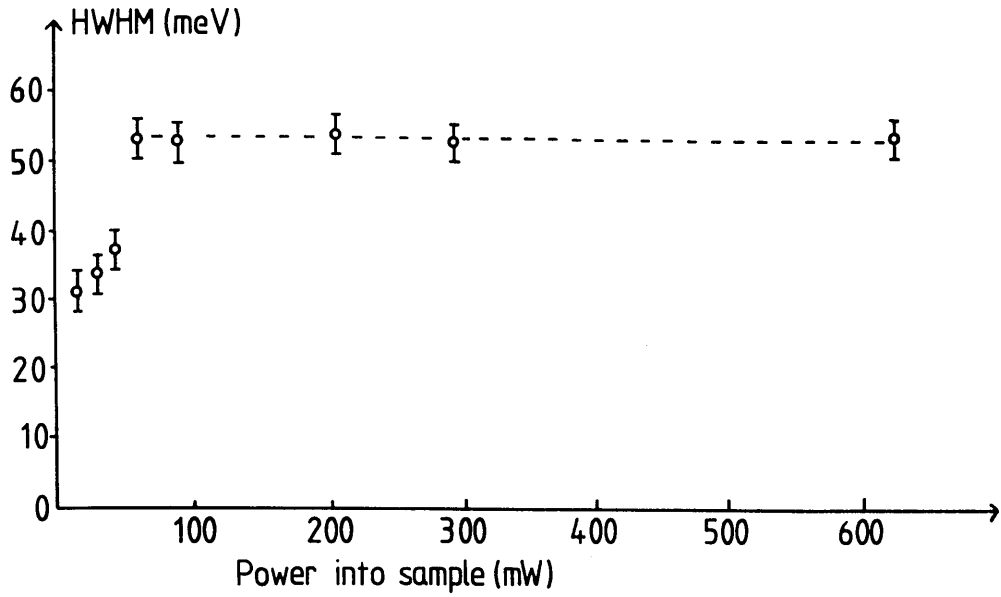

Figure 5.11 Low energy Half Width at Half Maximum of the photoluminesence peak as a function of laser power. The line is a guide to the eye.

Wiesenfeld [1987] showed that regardless of the initial excitation density, the carrier density of the EHP would decrease to less than $6x10^{18}$ cm^{-3} within 200 psecs by expansion of the EHP at a rate greater than 10^7 cm/sec. Their measurements showed that the integrated luminescence intensity was proportional to the size of the EHP after expansion where the size of expansion was determined by the initial excitation density: in short, the initial excitation density was proportional to the integrated luminescence intensity. This agrees very well with the data obtained from PMB116 plotted in figure 5.10. At low excitation intensities, this mechanism does not apply as the EHP density is insufficient to cause expansion of the plasma. At low excitation densities, therefore, the HWHM of the PL is seen to increase as the EHP density causes the conduction and valence bands to fill. At the saturation density, the bands no longer fill, instead, the excited carriers move outwards from the laser spot where they fill the lower energy states available thus causing the HWHM to remain constant.

In order to estimate the EHP saturation density, the following assumptions were made: each photon creates one electron–hole pair which decays to the bottom of the band in about 10 psecs, remains there for about 10 nsecs and then recombines radiatively. This yields a value of $2.4x10^{10}$ electron–hole pairs per Watt of incident power. From the absorption lengths in GaInAs and InP [Aspnes and Studna, 1983] it is possible to determine how deep within the sample the carriers are created. Figure 5.11 shows the onset of saturation at an incident power somewhere between 43 and 57mW. This yields a EHP density of $1.4 - 1.9$ $x10^{17}cm^{-3}$ in the InP cap layer and $9.8 - 13.0$ $x10^{11}cm^{-2}$ in the GaInAs QW. This density is certainly of the correct order of magnitude to populate the well and screen the phonons [Skolnick et al, 1987]. As a comparison, the EHP density is an order of magnitude greater than that measured experimentally for this sample under no illumination [S hubnikov–de Hass measurements at 4.2K; Al Dubuni, 1988] thus suggesting that in the limit of low incident laser power, the phonons in the sample would be unscreened.

5.4.2 Raman Scattering Intensity Measurements

High free carrier densities in bulk semiconductors give rise to plasma oscillations of the conduction band electrons which couple to LO phonons if their frequencies are sufficiently close [see e.g. Mooradian, 1972]. The theoretical cross-over point given in figure 22 of this reference lies at about $8x10^{17}$ cm^{-3} for GaAs. In practice, however, the excitations follow an anti-crossing behaviour and the higher frequency LO mode becomes plasma-like in character and moves to higher energy with increasing carrier density (L_+ mode) while the plasma mode develops phonon character and oscillates at the TO phonon frequency (L_- mode). In two dimensions (2D) this effect is different. The reduced dimensionality yields slab-like plasma oscillations of the 2D electron gas in the plane of the layer. In order to couple to these, there must be a component of the incident wavevector in the plane of the layers. As a nearly-backscattering geometry was used throughout these experiments, it is unlikely that it would have been possible to couple to these excitations. Instead, the incident light would couple to those intersubband excitations which exist as both single particle and collective intersubband excitations and which have wavevectors perpendicular to the QW plane. Previous experimental studies investigated this effect in GaAs-AlGaAs heterostructures and demonstrated that the collective intersubband excitations couple strongly to the LO phonon modes [Pinczuk et al, 1981; Zeller et al, 1982]. It therefore seems likely that a similar mechanism occurs here with the collective intersubband excitations coupling to the LO phonons and screening them. The experimental parameters used here are inappropriate to observe the coupled excitations as they are thermally smeared out at room temperature. Instead, at room temperature, the effect of the coupling is seen as a reduction in the intensity of the LO phonon.

In order to investigate the contribution of screening to the LO mode quench, Raman spectra were recorded at different laser powers. Figure 5.12 shows the

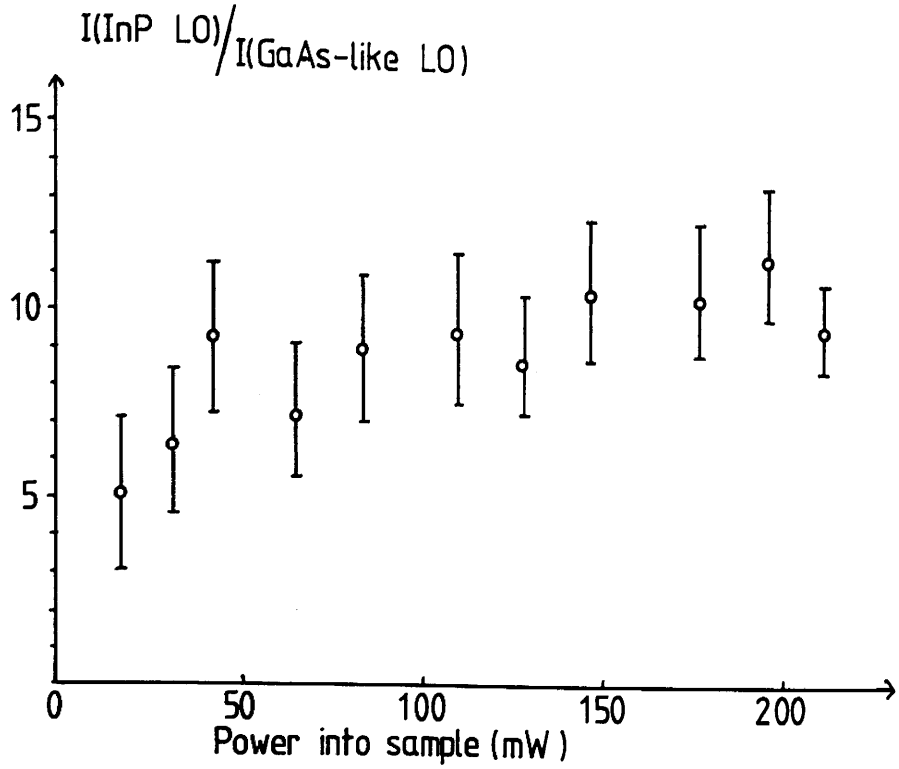

Figure 5.12 Raman scattering intensity of the InP LO mode divided by the GaAs– like LO mode intensity plotted as a function of incident laser power at room temperature.

intensity of the InP LO mode divided by the intensity of the GaAs–like LO mode plotted as a function of incident laser power (λ = 4825Å). Although the saturation behaviour is not as well–defined as in figure 5.11, there is a clear trend showing the strengthening of the GaAs–like LO mode as the incident power, and the EHP density, is decreased. This would suggest that screening is indeed causing the LO mode to quench.

It seems likely that a EHP screened the LO phonons in the quantum well thus yielding the spectrum of figure 5.8(b). With the cap layer removed and the power kept at the same level, the modes are no longer screened although the EHP density has not changed (see figure 5.8(c)). This fact can be attributed to depletion of the sample surface. Schubert et al [1984] give the following simple formula for the depletion width:

$$W_{ds} = \sqrt{[2\epsilon(\Phi_b - \xi)/qN_d]} \qquad (5.2)$$

where

ϵ = $\epsilon_r \epsilon_o$

ϵ_r = 12.6 (InP), 14.1 (GaInAs), [Landolt–Boernstein, 1982]

q = electronic charge

N_d $\simeq$ carrier concentration = EHP density

Φ_b = surface barrier height (eV)

ξ = $E_c - E_F$ = $-kT \ln(n/N_d)$ for $n \gg p$ and $N_d \gg N_a$

and

n = background doping level = 3.2×10^{15} cm^{-3}

T = 300K

(also see figure 5.13)

Using photoexcited carrier density values of 5.4×10^{23} m^{-3} for InP and

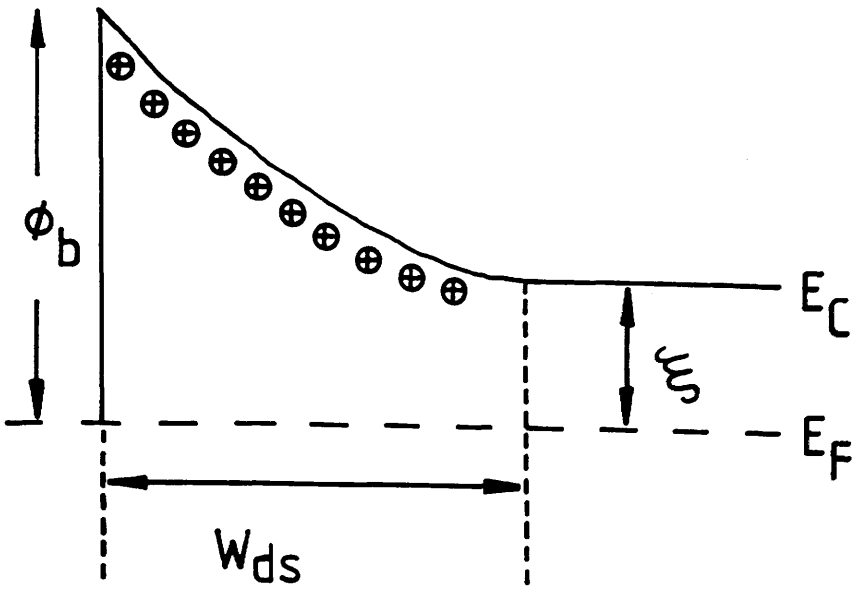

Figure 5.13 Schematic representation of depletion effects at the surface of the sample. The conduction band energy, E_C, the Fermi level, E_F, the surface potential, Φ_b, and the depletion width, W_{ds}, are shown.

5.3×10^{23} m^{-3} for GaInAs (corresponding to 100mW focussed onto an area 200μm square) and taking a Φ_b of 1eV for InP and 0.8eV for GaInAs, the following values are obtained:

$$\xi = 146\text{meV}, \quad W_{ds} = 470\text{Å} \text{ in InP}$$

$$\xi = 93\text{meV}, \quad W_{ds} = 460\text{Å} \text{ in GaInAs}$$

Hence the well phonons are screened when the well is buried beneath the cap layer since it is then beyond the surface depletion width. After removal of the cap, however, the well is on the surface and lies within the surface depletion width thus rendering the phonons unscreened.

In summary, the results on sample PMB116, a single quantum well, are consistent with QW phonons very similar to those in bulk GaInAs in which the LO modes are screened by the collective electronic excitations of a EHP when the layer is buried beyond the surface depletion width and which can recover the LO mode intensities when the screening is reduced either by reducing the optical excitation density or by depleting the well at the sample surface.

The first sample studied here was PMB121, a structure containing 50 periods of 25Å QWs of GaInAs separated by 100Å InP barriers. This sample initially had a capping layer of 1000Å and its Raman spectrum is shown in figure 5.14. The GaInAs alloy band is clearly visible although weak. Its intensity is comparable with that of the second order modes in the InP cap layer which occur at 185, 229 and 250 cm^{-1} (see also figure 5.5). Following the successful etching of PMB116 (see section 5.4) the cap layer of PMB121 was removed. The spectra obtained with the cap layer removed and then the first well removed are shown in figure 5.15. These spectra do not significantly differ in either mode frequency or intensity, moreover, the phonon modes of the alloy layers have the same frequencies as those in the bulk; there is no shift of the modes towards the spectrum of the quaternary alloy GaInAsP [see e.g. Soni et al, 1986] thus demonstrating that the layers are well–defined and the interfaces sharp. There is also no evidence of a GaAs–like LO mode quench which is further evidence that the InP barriers do not play a significant role in the quench process.

A second sample, PMB117, was also investigated but the very thick cap and barrier layers together with the narrow top well (10Å) precluded the observation of any useful information.

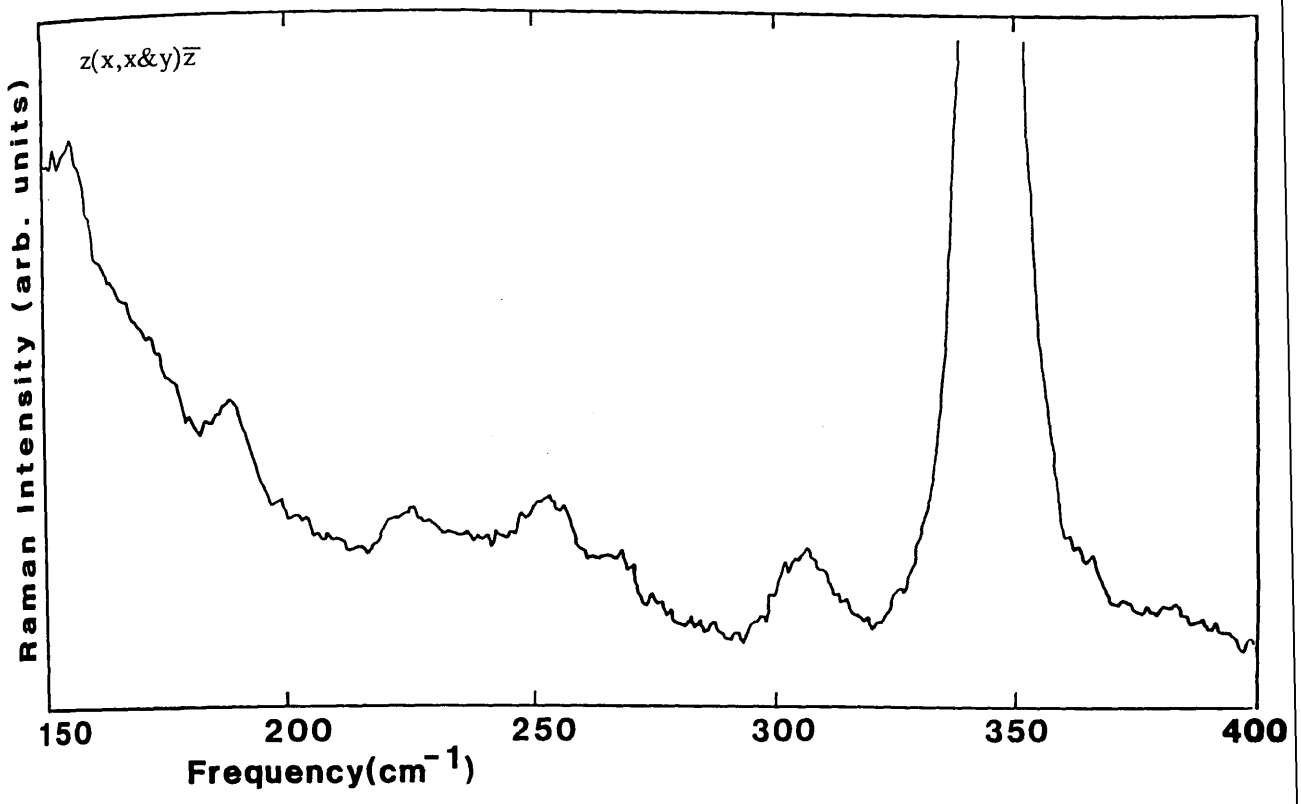

Figure 5.14 Room temperature Raman spectrum of PMB121 prior to etching, i.e., with a 1000Å cap layer. The alloy band is of the same order of magnitude as the InP second order modes. $\lambda = 4880$Å, resolution= 5 cm^{-1}.

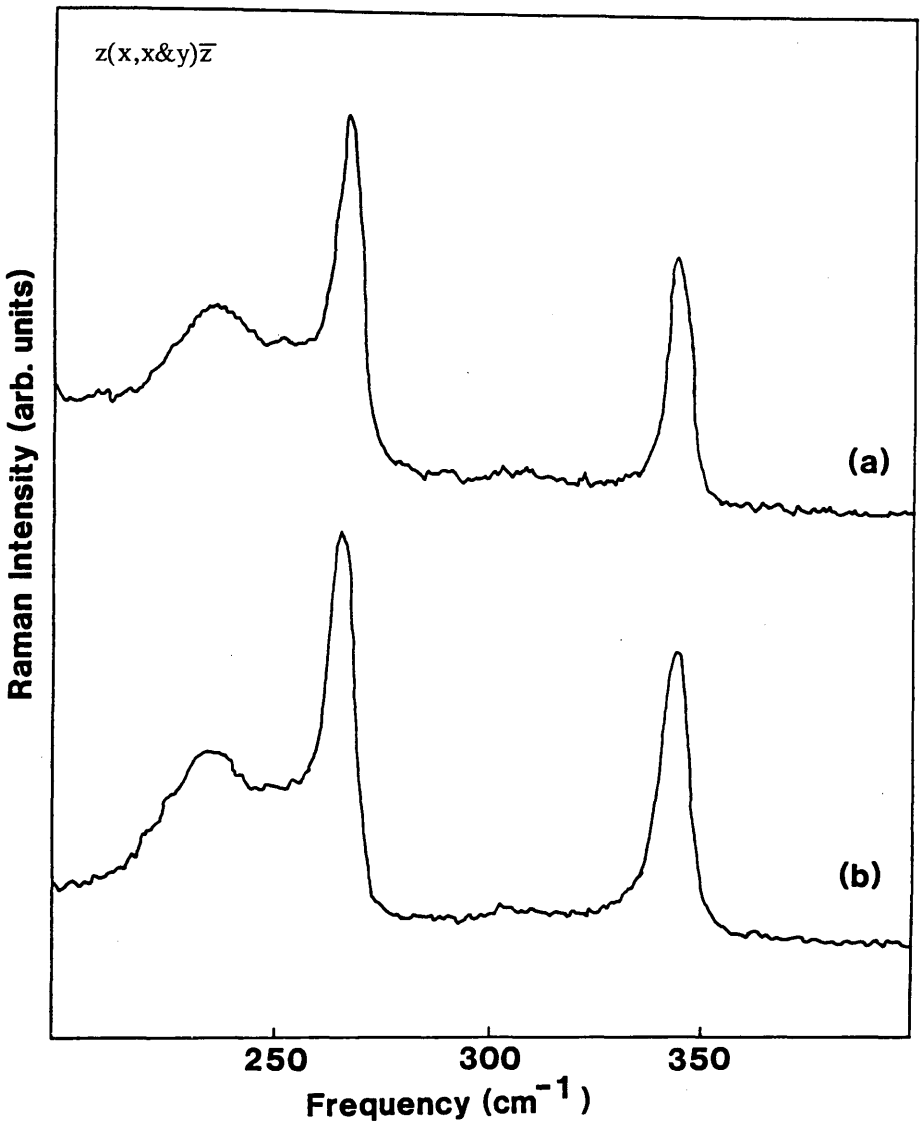

Figure 5.15 Room temperature Raman spectra of PMB121 after the cap layer was etched off. (a) With InP barrier layer on the surface. (b) With GaInAs well layer on the surface. These spectra do not significantly differ in either mode frequency or intensity ratio. $\lambda = 4880$Å, resolution= 5 cm^{-1}.

5.6.1 InP LO Mode Shift

In all the samples studied, there is a systematic shift of the InP LO phonon by about 2 cm^{-1} to lower energies when the mode exists in a cap or barrier layer grown on top of GaInAs as opposed to a buffer layer. This shift is independent of whether or not the barrier layer is buried. Four possible causes of this shift have been investigated. In addition, the sample heating effects discussed in section 5.2 could contribute to this shift.

1) Arsenic Contamination of Overgrown Layers

Contamination of the overgrown InP layers is possible due to a problem in the MBE growth process. There was found to be deposited Arsenic within the growth chamber which might have acted as an Arsenic source when the Arsenic was supposed to be blocked. Such contamination would produce the alloy InP_xAs_{1-x} whenever pure InP was expected. This alloy has been comprehensively studied using Raman scattering by Carles et al [1980]. Interpolation of their data to account for a 2 cm^{-1} shift of the InP LO mode gives an alloy composition with $x = 0.75$, i.e., 25% Arsenic. At this alloy composition, they observed a strong peak at 227 cm^{-1}. There is no such peak in our spectra and, besides, 25% Arsenic is much too high a value to be counted as a mere contaminant. Elsewhere in their paper it is noted without comment that "the pure InP spectrum recorded at 300K was shifted as a whole by 3 cm^{-1} to higher energies". This suggests a discontinuity in the otherwise smooth shift of modes from the InAs spectrum to the InP spectrum. If such a

discontinuity exists then a small contamination of Arsenic might be enough to move the LO mode. No indication was given by Carles et al [1980] of the amount of Arsenic needed to produce this shift. Nevertheless, it seems unlikely that such small quantities of Arsenic as are assumed here would influence the mode frequencies to such a degree. Gallium contamination of the overgrown layers can be ruled out as the work done by Beserman et al [1976] shows that any shift would be induced in the opposite direction, i.e., to higher energies.

2) GaInAsP Graded Interface Regions

This quaternary alloy was studied by Pinczuk et al [1978]. A shift of the InP LO energy by 2 cm^{-1} to lower energies by changing the InP into a quaternary of GaInAsP would require a composition of $Ga_{0.96}In_{0.04}As_{0.08}P_{0.92}$; clearly this is not feasible for our samples. If a more likely case is considered, that of 50:50 GaInAs:InP in a graded interface region, then the spectra observed by Pinczuk et al show that two Raman bands of equal intensity should be expected at around 260 and 340 cm^{-1}. It is clear from figure 5.15 that this is not the case. It has been suggested that graded interfaces may play a larger role in Raman scattering from MOCVD–grown material [Mowbray, 1987] but this work is not yet fully resolved.

3) Screening Effects

Nakamura and Katoda [1984] noted that "a shift in the LO phonon frequency from 346 to 350 cm^{-1} and an increase in the relative intensity of the LO phonon compared to the TO phonon are observed in the case of the sample without chemical etching because of damage and strain induced by mechanical polishing".

This suggests that a rougher surface (e.g., a substrate or buffer layer) will exhibit an LO phonon at a higher energy than a smoother surface (e.g., a cap or barrier layer). The authors explained this observation in terms of an increased surface recombination velocity for free carriers thus causing greater surface depletion and a reduction in screening for the rougher surface. This would be consistent with the data observed here since the buffer layer, although epitaxially–grown, is a means of improving subsequent growth by both smoothing the substrate and absorbing impurities from the growth chamber and its crystalline quality will be degraded by the dislocations produced by smoothing the substrate.

Good surface quality would also reduce the surface scattering of the laser beam thus enabling more of the incident light to be absorbed. This would cause an increase in the sample temperature thus moving the phonons to lower energies. This is consistent with experimental observations.

4) Strain in the Overgrown Layers

It is possible to calculate the strained lattice constant in the plane of a strained layer superlattice, $a_{||}$, by using the expressions derived by Osbourn [1982]:

$$a_{||} = a_1[1+fG_2d_2/(G_1d_1+G_2d_2)] \quad (5.3a)$$

$$= a_2[1-fG_1d_1/(G_1d_1+G_2d_2)] \quad (5.3b)$$

where

a_1 = lattice parameter of InP = 5.8687Å [Landolt–Boernstein, 1982]

a_2 = lattice parameter of $Ga_{1-x}In_xAs$

= 5.653 + 0.405x [Mikkelson and Boyce, 1983]

f = unstrained lattice mismatch

= $2[a_2 - a_1]/[a_2 + a_1]$

d_1 = layer thickness of InP = 100Å

d_2 = layer thickness of GaInAs = 25Å

and

G = shear modulus

= $[C_{11} + C_{12} - 2(C_{12})^2/C_{11}]$

where the C's are the elastic moduli

Using the values given in Landolt–Boernstein [1982] for the elastic moduli of InP, GaAs and InAs, the G values can be calculated (interpolating for GaInAs) as:

G_1 = 9.49×10^{10} Nm^{-2} for InP

G_2 = 9.97×10^{10} Nm^{-2} for GaInAs

It has been suggested [Adams, 1986] (although there is now some doubt) that the quaternary GaInAsP, and by extension the ternary GaInAs, could be up to five times softer than interpolation suggests thus yielding an alternative value for G_2:

G_2^* = 2×10^{10} Nm^{-2}

In this simple approximation the variable is the alloy composition, x, since it is this parameter that determines f, the lattice mismatch. Temperature effects that might influence the lattice mismatch have been neglected. This model holds for lattice mismatches of less than 7 – 9%.

Nakashima et al [1986] developed the following method to calculate phonon frequency shifts due to lattice strain. The strain tensor components parallel to the interface are:

$$\epsilon_{xx} = \epsilon_{yy} = (a_{||} - a)/a = (S_{11} + S_{12})X \qquad (5.4)$$

where S_{11} and S_{12} are the elastic compliance constants and X is the strength of the stress while the frequencies of the LO and TO phonons are given by:

$$\Omega(TO) = \omega_o(TO) + 2\Delta\Omega_H + 2\Delta\Omega/3 \qquad (5.5a)$$

$$\Omega(LO) = \omega_o(LO) + 2\Delta\Omega_H - \Delta\Omega/3 \qquad (5.5b)$$

where

$$\Delta\Omega_H = -\gamma(S_{11} + 2S_{12})\omega_o X \qquad (5.6a)$$

and

$$\Delta\Omega = \xi(S_{11} - S_{12})\omega_o X \qquad (5.6b)$$

with

ω_o = unstrained phonon frequency

$\gamma = -(p + 2q)/6\omega_o^2$

$\xi = (p - q)/2\omega_o^2$

The parameters, γ and ξ, have been determined for both InAs and GaAs by Cerdeira et al [1972]. In order to calculate the expected strain that would cause a 2 cm^{-1} shift in the LO mode, it is necessary to set

$$\Omega(LO) - \omega_o(LO) = -2\ cm^{-1} = 2\Delta\Omega H - \Delta\Omega/3 \qquad (5.7)$$

thus

$$-2\ cm^{-1} = -2\gamma(S_{11} + 2S_{12})\omega_o X - \xi(S_{11} - S_{12})\omega_o X/3 \qquad (5.8)$$

Solving this for X and substituting into equation (5.4) gives a value for $a_{||}$ of 5.908Å (in comparison with the unstrained, ideal case of $a_{||}$ = 5.8687Å,

corresponding to a lattice mismatch of 0.6%). Table 5.3 lists all the parameters used.

Using equations 5.3a and 5.3b, the following results are obtained: $a_2 = 6.060$Å for G_2 and $a_2 = 6.712$Å for G_2^* corresponding to lattice mismatches of 3.2% and 13.4%, respectively. Since the InAs lattice constant is only 6.058Å, these values are unrealistic in the sense that they cannot be achieved in GaInAs.

The x−ray measurements of chapter 8 contradict this value for $a_{||}$ showing it to be very close to the relaxed InP value of 5.8687Å. This suggests, very clearly, that it is not strain in the lattice that is the cause of the 2 cm^{-1} shift of the InP LO phonon. As a comparison, the high pressure data of Trommer et al [1980] on InP can be extrapolated to yield a lattice deformation value of $\Delta a = 0.16\%$ corresponding to a 2 cm^{-1} shift of the LO mode. This shift was achieved with an applied hydrostatic pressure of 3.4kbar at room temperature and is consistent with the value of Δa obtained above.

In summary, the strain needed to shift the InP LO mode by 2 cm^{-1} could be generated only if the alloy contained no Gallium and was therefore mismatched to the InP by about 3.2%. Since this entirely contradicts the measured values in the x−ray data (see chapter 8) and since there is no corroborating evidence for such an alloy composition, it is concluded that some mechanism other than lattice strain is causing the shift of the InP mode.

5.6.2 Magnetophonon Data Comparison

The magnetophonon resonance (MPR) technique is commonly used to investigate optic phonon frequencies thus making it an ideal comparison for Raman scattering results. The technique measures the resistance of a sample as a function of magnetic field: as the field is increased, the Landau levels separate in energy according to:

Table 5.3

Parameters used to calculate the lattice strain

Parameter	GaAs	InAs	InP
ω_0^2 ($x10^{27} sec^{-2}$)	2.56 [d]	1.69 [d]	4.29 [c]
C_{11} ($x10^{10} Nm^{-2}$)	11.8 [d]	8.33 [d]	10.22 [d]
C_{12} ($x10^{10} Nm^{-2}$)	5.4 [d]	4.53 [d]	5.76 [d]
S_{11} ($x10^{-11} m^2 N^{-1}$) [*]	1.19	1.95	1.65
S_{12} ($x10^{-12} m^2 N^{-1}$) [*]	− 3.73	− 6.86	− 5.94
$\gamma = -(p+2q)/6\omega_0^2$	0.90 ± 0.3 [a]	0.85 ± 0.13 [a]	[b]
$\xi = (p-q)/2\omega_0^2$	0.1 ± 0.1 [a]	0.57 ± 0.12 [a]	[b]

Notes:

[a] Cerdeira et al [1972]

[b] These parameters are unavailable. Trommer et al [1980] studied the mode Gruneisen parameters of a number of semiconductors. They found the values for InP to be very similar to those for GaAs at the gamma point therefore the values used here are those for GaAs.

[c] Values from Raman experiments

[d] Landolt– Boernstein [1982]

[*] $S_{11} = (C_{11} + C_{12}) / [(C_{11} - C_{12})*(C_{11} + 2C_{12})]$

$S_{12} = -C_{12} / [(C_{11} - C_{12})*(C_{11} + 2C_{12})]$

Landau level energy = $\bar{h}\,\omega_c$ = $\bar{h}$ eB/m* (5.9)

where

ω_c = cyclotron frequency of electrons

e = electronic charge

B = magnetic field

m* = effective mass of electrons

$\bar{h}$ = Planck's constant/2π

As the Landau level spacing is increased to sweep through the optic phonon frequency, ω_{LO}, the resonance condition is met allowing electrons to be scattered from one Landau level to the next by absorption of optic phonons. This changes the resistance by promoting the electrons into upper Landau levels, i.e.,

$\bar{h}\,\omega_{LO}$ = $N\bar{h}\,\omega_c$ = $N\bar{h}$ eB/m* (5.10)

where N is an integer.

For these resonances to be observed, the Landau level spacing must be greater than the thermal broadening ($\bar{h}\,\omega_c$ = $\bar{h}$ eB/m* > kT) which puts an upper limit on the experimental temperature. The temperature must also be high enough to ensure an adequate population of optical phonons and, since the number of phonons is proportional to exp(− Energy/kT), this constraint sets a lower limit on the temperature used. The compromise range is from about 77 − 200 K.

Magnetophonon resonance studies of GaInAs− InP heterostructures have been undertaken by a number of groups. Sarkar et al [1985] reported studies of bulk GaInAs grown lattice− matched to InP by MOCVD and MBE. Their data shows a dominant series of oscillations corresponding to the GaAs− like LO mode of the alloy. There is also evidence for a second set of oscillations in the splitting of one

of the MPR peaks at high magnetic field. They attribute the second set of oscillations to the InAs– like LO mode of the alloy.

Sugimasa et al [1986] performed MPR experiments on bulk $Ga_{0.47}In_{0.53}As$ in the temperature range 40 – 300 K. They observed only the GaAs– like LO phonon for temperatures above 77K but two sets of oscillations for temperatures below 77K. The authors were able to obtain both the GaAs– like and the InAs– like LO phonon oscillations at the lower temperatures because the occupation rate of the InAs– like phonon is expected to be greater than that of the GaAs– like phonon at lower temperatures.

Portal et al [1983] studied superlattice samples of 10 periods GaInAs – InP of QW thicknesses 80, 100 and 150Å and barriers of 400Å. Their samples also showed two sets of oscillations. They observed the dominant GaAs– like LO mode of the QWs. Equally strongly for the narrow wells, however, they also observed the LO mode of the InP barriers. They did not see evidence for the InAs– like mode. Their interpretation of the scattering by barrier phonons rests on four contributory factors: 1) the electric field associated with the InP phonon will penetrate into the well 2) the carrier wavefunctions in the well will penetrate into the barrier 3) some grading of the interface will enhance factors 1 and 2 and 4) the greater polarity of the InP means that it will couple more strongly than GaInAs.

Recently, Nash et al [1987] have investigated the electron phonon interaction in both bulk and low dimensional GaInAs. They considered the magnetophonon results in the context of many other experimental techniques. They calculated the electron phonon coupling for both the GaAs– like and the InAs– like LO modes and found that the dominant coupling is to the GaAs– like mode because the Froehlich coupling constant is much larger for the GaAs– like than for the InAs– like mode. This agrees well with the data of Sarkar et al [1985], Sugimasa et al [1986] and Portal et al [1983].

These MPR experiments demonstrate the fundamental difference between the

MPR and the Raman scattering techniques: unless in extreme resonance with the energy gap, Raman scattering involves virtual electron–hole pairs. Because of this, the scattered spectra reflect the phonons present with the scattering intensity of each type depending only on its Raman cross–section. MPR, on the other hand, involves real carriers in the semiconductor conduction band and the phonons are observed only via their interaction with these electrons. In the case of Portal et al [1983], for example, only GaAs–like phonons were observed for 150Å wells but both GaAs–like and InP phonons could be seen in 80Å wells. The Raman measurements presented in this chapter show GaAs–like, InAs–like and InP modes for wells from 230Å to 25Å with the added benefit of being able to demonstrate well–defined phonon modes in the 25Å wells. MPR is more appropriate when device applications are being considered. The reason for this is that the speed of devices at room temperature is limited by optical phonon scattering of the electrons; as only real electrons scatter phonons, MPR is the more appropriate technique.

5.6.3 Conclusions

MBE–grown samples of $Ga_{0.47}In_{0.53}As$ lattice matched to InP have been studied using Raman scattering techniques. The samples have been shown to be of good quality and they exhibit clear and well–defined phonon modes both in the bulk and heterostru cture case. The mode frequencies agree well with published values obtained by both Raman scattering and other techniques (e.g. infra–red reflectivity) and, where discrepancies arise, these have been investigated. A comparison with magnetophonon resonance methods highlights the different mechanism of the interaction and thus the complementary information that can be obtained by comparing both techniques.

For bulk GaInAs, a broad phonon band was observed in which the dominant

mode was the GaAs– like LO. The dominance of the GaAs– like scattering over that of the InAs– like scattering was attributed to a difference in their Froehlich coupling constants. The band was unable to be resolved into its constituent components because of broadening of the Raman lines as discussed in chapter 2.

The SQW sample of GaInAs exhibited a Raman spectrum in the region of the alloy phonons that was different from the bulk spectrum. The major change was the reduction in intensity of the GaAs– like LO phonon. This was investigated using both Raman scattering and room temperature PL techniques. The quench was attributed to screening of the mode by a photoexcited electron– hole plasma. An estimate of the 2D plasma density in the well gave a value of around $10x10^{11}$ cm^{-2} which is consistent with the values obtained by Skolnick et al [1987] for work on similar samples.

The discussion in section 5.6.1 centred on an observed shift of the InP LO frequency to lower energies. The shift was observed from a cap or barrier layer but not from a buffer layer. Four possible origins of the shift were discussed and the most likely origin involves the surface quality of the sample. Poor surface quality increases the surface recombination velocity thus causing a greater depletion effect at the sample surface. As the increased depletion reduces the free carrier density, coupling of the LO phonon to the free carriers is reduced and the mode moves to higher energies. A contribution from sample heating effects would also provide a shift in the right direction and it is probable that the origin of the observed shift of the InP LO phonon lies in some combination of these effects.

The data presented here show clearly why GaAlAs– GaAs and not GaInAs– InP has been the system in which so many low dimensional confinement effects on the phonons have been observed. AlGaAs has a well– defined two– mode alloy behaviour and the alloy composition can be varied across the the entire composition range without the effects of lattice strain. This enables clear resolution of the four components of the optical phonon spectrum which in turn enables the observation of

confined phonons as observed by Sood et al [1985]. It would be impossible to observe similar effects in the GaInAs– InP system because the broad alloy band would mask the weak, confined structure. In addition, GaAlAs can be regarded as a random alloy in comparison with GaInAs which tends to cluster. This, together with its higher mobility, has the effect of narrowing the Raman linewidth and enhancing the resolution still further.

The observation of folded acoustic phonons is not seriously hampered by choosing GaInAs– InP rather than GaAlAs– GaAs as demonstrated by Davey et al [1987]. The GaInAs– InP system is also better for investigating interface phonons as the GaP interface bond does not exist elsewhere in the sample unlike the bonds at the GaAlAs– GaAs interface. Continuation of the work on the phonons in GaInAs– InP heterostructures is therefore of importance for the study of fundamental vibrational behaviour and is likely to continue given the impetus of the need for devices in this material.

A R Adams; private communication, 1986

M Al Dubuni; PhD Thesis, St Andrews University, 1988

G F Alfrey and P H Borcherds; J Phys C5, L275, 1972

D E Aspnes and A A Studna; Phys Rev B27, 985, 1983

E Bedel, G Landa, R Carles, J P Redoutes and J B Renucci; J Phys C19, 1471, 1986

R Beserman, C Hirlimann, M Balkanski and J Chevallier; S S Comm 20, 485, 1976

M H Brodsky and G Lucovsky; Phys Rev Lett 21, 990, 1968

R Carles, N Saint-Cricq, J B Renucci and R J Nicholas; J Phys C13, 899, 1980

F Cerdeira, C J Buchenauer, F H Pollack and M Cardona; Phys Rev B5, 580, 1972

R K Chang, J M Ralston and D E Keating; in "Light Scattering Spectra of Solids", edited by G B Wright, published by Springer-Verlag, Berlin, Heidelberg, New York, 1969; p369

S T Davey, P C Spurdens, B Wakefield and A W Nelson; Appl Phys Lett 51, 758, 1987

K P Jain, R K Soni, S C Abbi and M Balkanski; Phys Rev B32, 1005, 1985

K Kakimoto and T Katoda; Appl Phys Lett 40, 826, 1982

"Landolt-Boernstein Numerical Data and Functional Relationships in Science and Technology. Group III: Crystal and Solid State Physics" Vol 17a: Physics of Group IV Elements and III-V Compounds, edited by O Madelung, published by Springer-Verlag, Berlin, Heidelberg, New York, 1982; sections 2.10, 2.11, 2.14 and 2.16

J Y Marzin; in "Optical Properties of Narrow-Gap Low-Dimensional Structures", edited by C M Sotomayor Torres, J C Portal, J C Maan and R A Stradling, NATO ASI Series B Physics Vol 152, published by Plenum Press, New York, London, 1987; p99

J Y Marzin; Proc Les Houches Winterschool on "Heterojunctions and Semiconductor Superlattices", edited by G Allan, G Bastard, N Boccara, M Lannoo and M Voos, published by Springer-Verlag, Berlin, Heidelberg, New York, 1986; p199

J C Mikkelson and J B Boyce; Phys Rev B28, 7130, 1983

A Mooradian; "Raman Spectroscopy of Solids" Laser Handbook Vol 2, edited by F T Arecchi and E O Schulz–DuBois, published by North Holland, Amsterdam, 1972; p1409

D J Mowbray; private communiction, 1987

T Nakamura and T Katoda; J Appl Phys 55, 3064, 1984

S Nakashima, Y Nakakura, H Fujiyashu and K Mochizuki; Appl Phys Lett 48, 236, 1986

K J Nash, M S Skolnick and S J Bass; Semicond Sci Technol 2, 329, 1987

K J Nash; LDS Workshop "Phonons and Plasmons in LDS", Egham, U.K., 1987

H Nather and L G Quagliano; S S Comm 50, 75, 1984

G C Osbourn; J Appl Phys 53, 1586, 1982

T P Pearsall, R Carles and J C Portal; Appl Phys Lett 42, 436, 1983

A Pinczuk, J Shah, A C Gossard and W Wiegmann; Phys Rev Lett 46, 1341, 1981

A Pinczuk, J M Worlock, R E Nahory and M A Pollack; Appl Phys Lett 33, 461, 1978

J C Portal, J Cisowski, R J Nicholas, M A Brummell, M Razeghi and M A Poisson; J Phys C16, L573, 1983

K M Romanek, H Nather, J Fischer and E O Goebel; J Lum 24/25, 585, 1981

T W Ryan, P D Hatton, S Bates, M Watt, C M Sotomayor Torres, P A Claxton and J S Roberts; Semicond Sci Technol 2, 241, 1987

M K Sakar, M S Skolnick, P A Claxton, J S Roberts and M J Kane; Semicond Sci Technol 3, 691, 1988

C K Sarkar, R J Nicholas, J C Portal, M Razeghi, J Chevrier and J Massies; J Phys C18, 2667, 1985

E F Schubert, K Ploog, H Dambkes and K Heime; Appl Phys A33, 63, 1984

M S Skolnick, K J Nash, P R Tapster, D J Mowbray, S J Bass and A D Pitt; Phys Rev B35, 5925, 1987

R K Soni, S C Abbi, K P Jain, M Balkanski, S Slempkes and J L Benchimol; J Appl Phys 59, 2184, 1986

A K Sood, J Menendez, M Cardona and K Ploog; Phys Rev Lett 54, 2111, 1985

T Sugimasa, T Yamasaki, H Hazama, T Imachi and C Hamaguchi; Jpn J Appl Phys 25–1, 55, 1985

A J Taylor and J M Wiesenfeld; Phys Rev B35, 2329, 1987

G A Thomas; Sci Am 234, 28, 1976

G A Thomas, A Frova, J C Hensel, R E Miller ans P A Lee; Phys Rev B13, 1692, 1976

R Trommer and M Cardona; Phys Rev B17, 1865, 1978

R Trommer, H Muller, M Cardona and P Vogl; Phys Rev B21, 4869, 1980

D J Westland; private communication, 1986

Ch Zeller, G Abstreiter and K Ploog; Surf Sci 113, 85, 1982

CHAPTER 6

OPTICAL ASSESSMENT OF DAMAGE IN REACTIVE-ION-ETCHED GaAs

6.1 Introduction and Etch Process

Reactive-ion-etching (RIE) is one step in a lithographic process designed to produce laterally structured devices. A polymeric resist is first deposited onto the sample surface. This radiation-sensitive layer is then exposed (either by optical or electron beams) to form a latent image which is then developed to produce a relief pattern on the sample. The pattern is transferred to the sample by etching. Various etches can be used depending on the type of material, whether an isotropic or an anisotropic etch is needed, the depth of etch required, whether material selectivity is required, the speed of etch, etc. RIE is used when an anisotropic etch is required. This is needed to ensure that the fine details of the mask or stencil are accurately reproduced, e.g. submicron grooves or dots.

In RIE, a relatively low pressure gas (of about 20mTorr) is ionised and this is done by the application of an r.f. field between two electrodes. One of the electrodes is earthed and an average d.c. self-bias of some 50 to 300 V builds up between the two because the electrons can move sufficiently fast to follow the r.f. field whereas the heavier ions cannot. This d.c. voltage accelerates the ions so that they arrive at the substrate (which is placed on the driven electrode) with a

significant energy. As the sample is located outwith the plasma, the etching tends to be anisotropic in nature with both a chemical and physical contribution. For typical power densities of $0.5 Wcm^{-2}$, a simple calculation of the incident ion flux yields a value of about 10^{16} ions per $cm^2 sec$.

A major concern with this etch technique is the ion bombardment damage to the sample caused by the ions. Raman scattering is one technique among many used to evaluate this damage. Other techniques are photoluminescence [Kawabe et al, 1978] and the ideality factors of Schottky diodes formed on the etched surface [Cheung et al, 1987]. Full evaluation of the damage produced requires the assimilation of several investigative techniques.

6.2 Effect of Reactive–Ion–Etch Damage

The effect of RIE on a perfectly crystalline starting material is the basis for all interpretations of the damage caused by this bombardment process. Most of the work done in this area, however, has been on ion–implanted material. The damage caused by ion–implantation is expected to be a great deal higher than that caused by RIE because of both the energy of impact of the ions and the intent of leaving the bombarding species within the crystal matrix. Typical studies of ion–bombarded GaAs have involved samples bombarded with H^+ (at wt 1) at 1.65 MeV [Anastassakis et al, 1988], Be^+ (at wt 9) at 45 – 100 keV [Rama Rao et al, 1983; Holtz et al, 1988(a)], Si^+ (at wt 28) at 120 – 300 keV [Holtz et al, 1986; Nakamura and Katoda, 1984; Nakamura and Katoda, 1982] and Xe^+ (at wt 131) at 400 keV [Peercy, 1971]. Typical doses are in the 10^{15} – 10^{16} ions/cm^2 range. In contrast, RIE involves molecular ions of $SiCl_4^+$ (at wt 170) which impact with energies of only some 0.3 keV [Arnot, 1988]. It is difficult to compare doses between etched and implanted samples because of the fundamentally different aims of the processes. In the ideal case, etched samples would receive zero implantation dose from the ions. It has been suggested by Semura et al [1984] that this is indeed the case (see discussion below) however, there is no corroborating data available to investigate implantation of the samples used in this work (e.g. SIMS analysis).

Few optical studies of etch–damaged samples have been performed. Kawabe et al [1978] investigated Argon ion milling techniques and discussed their results in terms of an amorphous layer of GaAs some 23 – 28 Å thick on an underlying defect–diffused layer. Their etch technique involved Argon ions with energies in the range 0.1 to 2 keV and the damage was studied using photoluminescence (PL) intensity, Helium backscattering and chemical etching techniques. Their model is somewhat simplistic as it provides for no gradual merging of the amorphous layer

into the defect–diffused layer, and indeed, no indication was given of the type of amorphicity expected or produced. The second study of etch damage was undertaken by Semura et al [1984] on GaAs samples using RIE gases of CCl_4/H_2 and CCl_4/O_2. The authors do not quote the energy of their etchant ions but the etch rates used were in the 0.1 – 1 μm/min range which is comparable to the etch rates used for the samples discussed in this work [Cheung, 1988]. The damage produced by etching was studied by means of Raman scattering and Auger electron spectroscopy. The Auger analysis revealed that no more than the top 10Å was implanted by the etchant ions. This is very close to the ideal case for etching discussed above. The Raman data obtained by Semura et al [1984] will be discussed in section 6.2.3. A study of RIE–induced damage was carried out by Tsang et al [1985] on Silicon samples etched with a CF_4/H_2 mixture. The authors found that shallow etching of about 500Å (typically a few tens of seconds) produced no detectable change in the Raman spectrum. When the sample was over–etched, however, say for 10 minutes, (etch rates were not given) then a weak contribution to the spectrum from amorphous Silicon could be detected. This spectral contribution was much weaker than that from a 60Å layer of amorphous Silicon deposited as a reference thus suggesting that the RIE–induced amorphicity was considerably less than 60Å deep. This point will be discussed further in section 6.2.3. Work by Kirillov et al [1986] on plasma etch damage to GaAs studied the effects of both Ar^+ plasma etching and $SiCl_4$ RIE of undoped and heavily–doped (10^{18} cm^{-3}) GaAs. It was reported that the Ar^+ plasma etch produced less damage in the GaAs than the RIE. This conclusion was based on observations of the Raman spectra of the coupled plasmon–phonon excitations of the n^+ GaAs where it was found that after RIE the electronic excitations were severely affected but were altered only marginally by Ar^+ etching. The spectra of the undoped material showed an increase in the forbidden TO intensity after RIE thus suggesting structural damage to the crystal.

6.2.1 Comparison of Microcrystalline and Amorphous Models

It is fairly common in the published literature to find that ion– bombarded and damaged material is referred to and regarded as amorphous [see e.g. Ashokan et al, 1986; Holtz et al, 1986; Burns et al, 1987; Anastassakis et al, 1988]. In fact, it is very seldom that the crystalline order is sufficiently destroyed to cause amorphisation. In general, an intermediate, microcrystalline and/or disordered crystalline state is formed which is distinguishable from the amorphous state down to samples with microcrystalline diameters of a few tens of Angstroms [Solin and Kobliska, 1974]. The advantage of using Raman scattering as the characterisation technique is that it discriminates between the separate crystalline and amorphous spectral components.

In this section, the various terms used will be defined: amorphous, microcrystalline, disordered crystalline and crystalline. Their spectral fingerprints will then be discussed together with examples taken from the literature.

Amorphous semiconductors are characterised by their lack of long– range order. Although strong short– range order exists on the scale of nearest– neighbour and next– nearest– neighbour interactions, no correlation exists beyond three or four bond lengths [Brodsky, 1982]. Amorphous semiconductors possess no crystallites large enough to yield sharp Bragg diffraction patterns. This limit on crystallite size is some 12 – 15 Å in Silicon [Brodsky, 1982] and can be expected to be at most double for III– V semiconductors due to their binary nature.

Crystalline semiconductors approximate very well to the infinite, perfect crystals discussed in section 1.2 and used to calculate the first order dipole selection rules for Raman scattering. A crystalline material has a long– range order as well as a short– range order and individual atoms occupy geometrically– regular lattice sites throughout the whole macroscopic crystal.

Disordered crystalline semiconductors are the less– than– perfect specimens of their crystalline counterparts. The disorder can be non– topological, for example, in

antisite defects or in an alloy where any given lattice site is occupied by one of a number of atom types. The disorder can also involve destroying the geometrical order, for example, by dislocation, vacancies or interstitial atoms. Disordered crystals preserve their macroscopic crystallinity, however, not so microcrystallites.

The term microcrystallite refers to an ensemble of small crystals where their individual size prohibits handling and orientation of just a single one of their number. The size of a single microcrystallite ranges from a few tens of Angstroms upwards. There is no ordering of the microcrystallites on a macroscopic scale and each is randomly oriented with respect to its neighbours.

The Raman spectrum of each of these four classes of semiconductor can be shown to possess distinctive features characteristic of each of the crystalline states although there is naturally an evolution from one form to the next.

The lack of long–range order in amorphous semiconductors prohibits selection rules based on a well–defined crystal momentum. The entire phonon density of states (DOS) can therefore participate in the Raman scattering process. Figure 6.1 shows the reduced Raman spectrum of amorphous GaAs compared with the calculated phonon DOS. The agreement is good. It is customary to represent Raman spectra of amorphous materials in the reduced form given by:

$$I_R(\omega) = \frac{\omega\, I(\omega)}{(\omega_L - \omega)^4\, [n(\omega,T) + 1]} \qquad (6.1)$$

where

$I(\omega)$ = the measured Stokes spectral intensity

$I_R(\omega)$ = the reduced spectral intensity

ω_L = the incident photon frequency

and

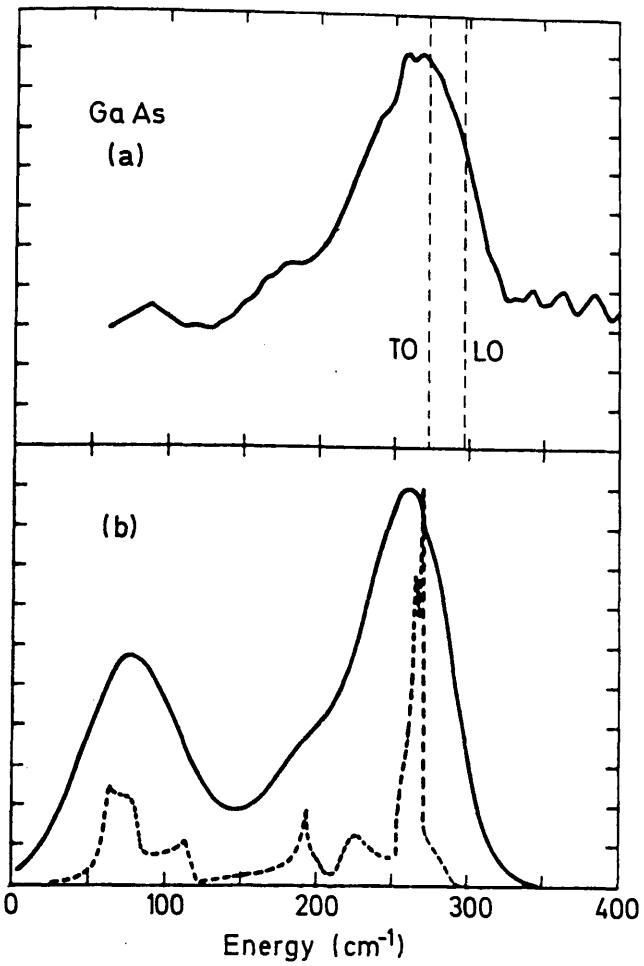

Figure 6.1 (a) Reduced Raman spectrum of amorphous GaAs. The dashed lines indicate the energies of the Raman active crystalline GaAs phonons

(b) The calculated density of states (DOS) of crystalline GaAs (dashed line). The solid line is the convolution of the crystalline DOS with a Gaussian broadening function.

[After Brodsky, 1982]

$$n(\omega,T) = [\exp(\hbar\omega/kT) - 1]^{-1}$$

$$= \text{the Bose–Einstein distribution function for temperature, } T$$

In contrast to the very broad structures shown in figure 6.1, spectral features arising from crystalline semiconductors are sharply defined (see figure 6.2). This results from the long–range ordering of the crystal in which there exists a well–defined crystal momentum which then gives rise to the associated dipole selection rules given in section 1.4.

As might be expected, Raman spectra from both microcrystalline and disordered crystals fall between these two extremes. A disordered crystal can be regarded as one in which the long–range order is not strictly preserved. As such, it is somewhat less than a perfect, infinite crystal therefore the "well–defined crystal momentum" mentioned above becomes less well–defined. As q relaxes from being a good quantum number, so the $q=0$ selection rule relaxes and the crystalline modes broaden. This is precisely the effect that broadens the Raman spectra of ternary and quaternary alloys (see discussion in section 2.5.4). Clearly, amorphicity, at the extreme end of this disordering process, can be achieved by sufficient bombardment of the crystal as illustrated by the work of Holtz et al [1988(b)] depicted in figure 6.3.

The case for microcrystallites is somewhat different. If possible surface disorder is ignored, then the microcrystals differ from the infinite crystal only in that they are finite in extent. They obey the same selection rules as macroscopic crystals but their random orientation with respect to one another prevents the selection rules being of any experimental use. The effect of their finite size mirrors the disorder–induced softening of the $q=0$ selection rule. The difference is that whereas for the microcrystalline case the crystalline correlation length is reduced to a value corresponding to the microcrystallite size, for the disordered case, it is only the average correlation length that is reduced. The size of a crystalline domain in a

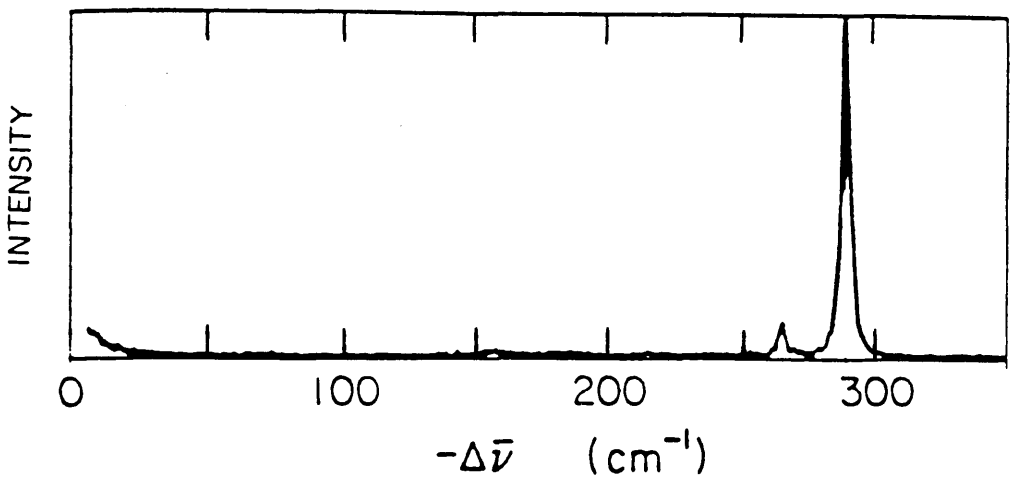

Figure 6.2 Raman spectrum of crystalline GaAs. Note that only two sharp peaks are present corresponding to the TO and the LO phonons at the centre of the Brillouin zone (at 269 and 292 cm^{-1}, respectively). The linewidth of the LO phonon in this figure is about $4cm^{-1}$ which approaches the natural linewidth of $3cm^{-1}$. [After Holtz et al, 1988(b)]

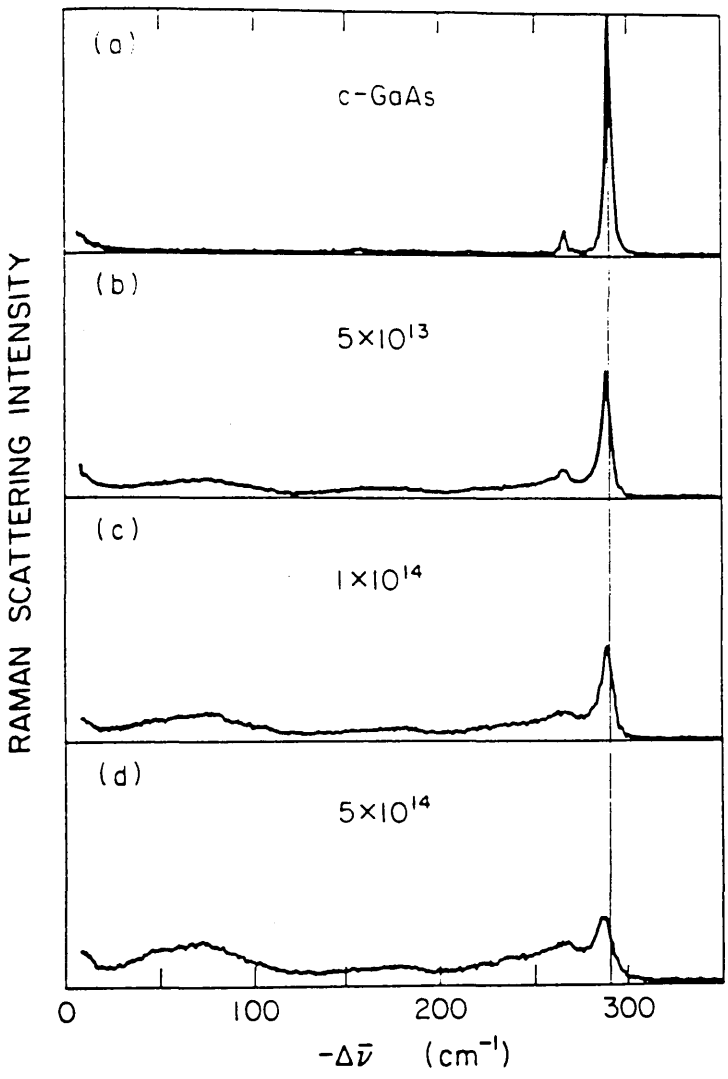

Figure 6.3 Effect of 45keV Be^+ ion bombardment on the Raman spectrum of GaAs showing the progression from the crystalline state (a) to an almost amorphous state (d). Each curve is labelled with the ion flux in units of ions/cm^2. [After Holtz et al, 1988(b)]

disordered crystal may vary widely from one domain to the next. The Raman spectrum of a microcrystalline semiconductor reflects the DOS accessible by a $q \leqslant d$ selection rule where d is the microcrystalline length. It is therefore very much better defined than the spectrum from a disordered crystal which has the same average correlation length, d. This latter spectrum will have contributions from both amorphous areas and crystalline areas of the sample thus broadening the spectral features. The difference between these spectra is illustrated in figure 6.4 which shows the spectrum from a Silicon film with the spectrum resolved into a disordered/amorphous part and a (micro)crystalline part.

The four crystal states and their corresponding Raman spectra have been described, it now remains to relate them to the type of damaged structure expected in RIE; this is done in section 6.2.3.

6.2.2 Theory of LO Phonon Lineshape and Shift

It is well documented that the LO phonon of crystalline GaAs softens (i.e. moves to lower energy) and broadens asymmetrically as the crystal becomes more and more disordered [see e.g. Peercy, 1971; Nakamura and Katoda, 1982; Holtz et al, 1988(a)]. Two interpretations of this effect have been proposed and both will be discussed in this section. The first interpretation involves a "phonon confinement" effect related to an average correlation length within the crystal and resulting in a softening of the $q = 0$ selection rule [Richter et al, 1981]. The second interpretation [Burns et al, 1987] is that the LO phonon shifts frequency as a result of changes in the effective charge induced in the crystal by the many defects involved in the disordering.

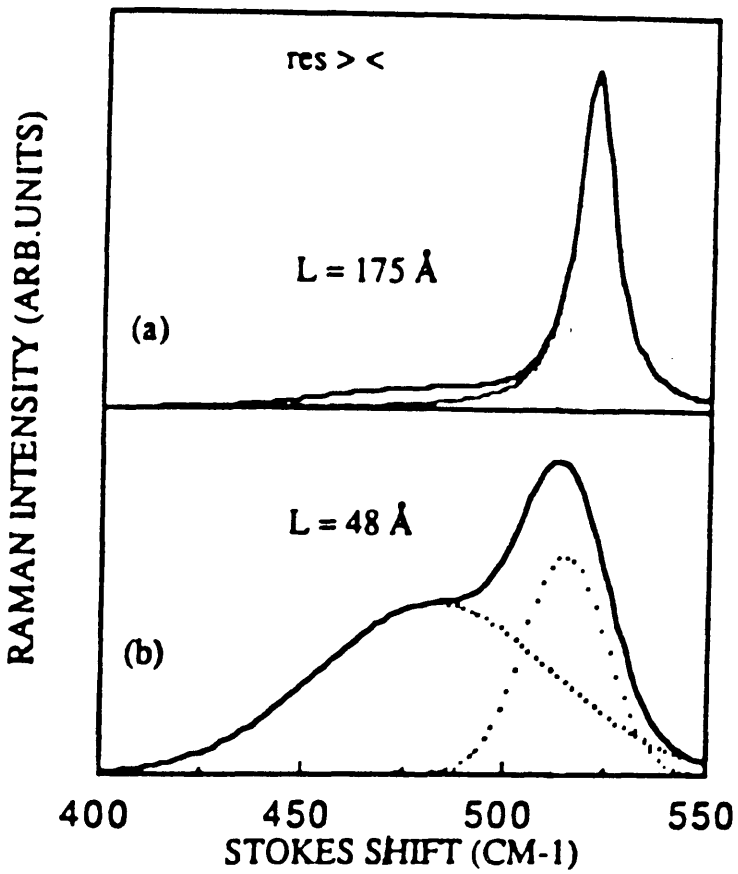

Figure 6.4 Raman spectrum from two microcrystalline Silicon films showing spectral contributions from the amorphous Silicon (broad feature at about 480 cm^{-1}) and the microcrystalline Silicon (feature at about 530 cm^{-1}) for two different sizes of microcrystal: (a) L= 48Å and (b) L= 175Å. [After Bustarret et al, 1988]

6.2.2.1 Phonon Confinement Model

The phonon confinement interpretation was developed by Richter et al [1981] to account for phonon linewidths and shifts in Silicon. The model was later used by Tiong et al [1984] to explain experimental observations of shifts and broadening of the LO modes in ion–bombarded GaAs. In this model, the long–range symmetry of the crystal is disordered leading to domains of undamaged material in a damaged matrix. The domains can be characterised by a correlation length, L, within which the phonons are confined. Confinement to L in real space gives rise to a broadened state in reciprocal space given by $\triangle q \approx 1/L$. This softens the $q=0$ dipole selection rule and allows a range of phonons to participate in the first–order Raman scattering process. The results obtained by Tiong et al [1984] are shown in figure 6.5 where 6.5(a) depicts the shift in LO frequency, $\triangle\omega_{LO}$, and the FWHM, Γ, of the LO peak as a function of the calculated correlation length, L. Figure 6.5(b) shows $\triangle\omega_{LO}$ together with the asymmetry of the peak, Γ_a/Γ_b, again as a function of L, where $\Gamma = \Gamma_a + \Gamma_b$, Γ_a is the low energy half width and Γ_b is the high energy half width. The fit to the experimental data is shown to be good.

The main objection to this model lies with the dispersion curve assumed for the LO phonon. The calculations shown in figure 6.5 are based on the formula for the Raman intensity, $I(\omega)$, given by

$$I(\omega) \propto \int_0^1 \frac{\exp(-q^2L^2/4)\quad d^3q}{[\omega - \omega(q)]^2 + [\Gamma_o/2]^2} \qquad (6.2)$$

where

q = phonon wavevector in units of $2\pi/a$

a = lattice constant

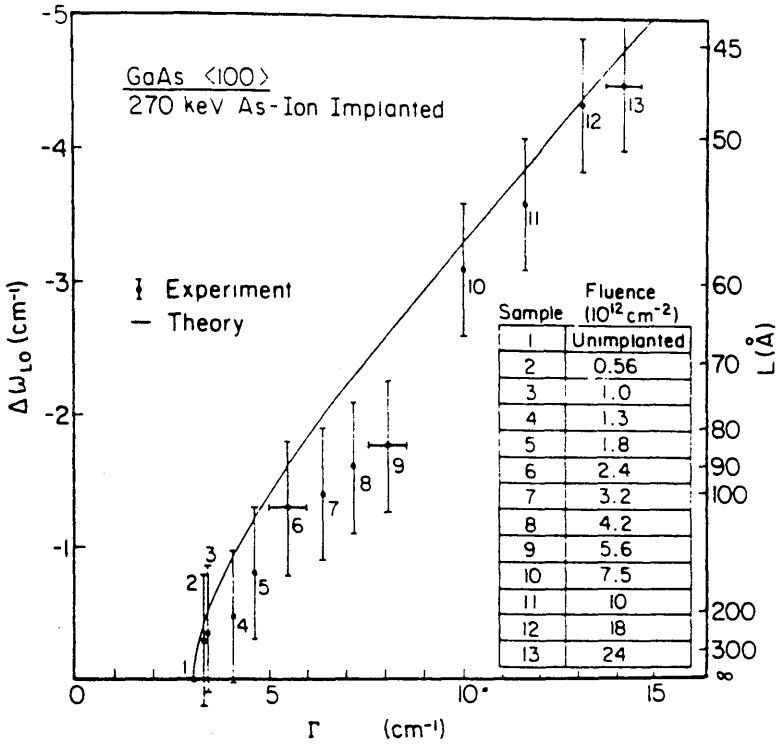

Figure 6.5(a) LO phonon Raman shift, $\Delta\omega_{LO}$, and broadening, Γ, as a function of L. The solid line is calculated from equations 6.2 and 6.3 and the points are experimental. [After Tiong et al, 1984]

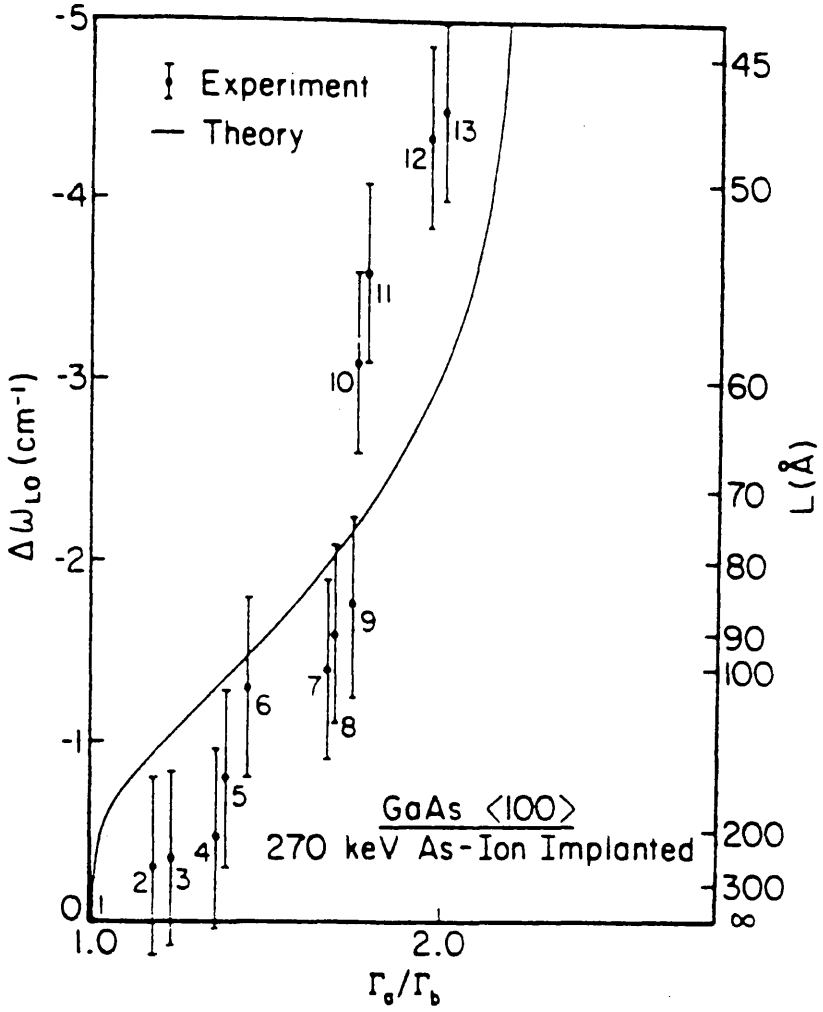

Figure 6.5(b) LO phonon Raman shift, $\Delta\omega_{LO}$, and asymmetry, Γ_a/Γ_b, as a function of L. The solid line is calculated from equations 6.2 and 6.3 and the points are experimental. [After Tiong et al, 1984]

Γ_o = unperturbed Raman FWHM

$\omega(q)$ is the phonon dispersion and has been approximated by Tiong et al [1984] by

$$\omega(q) = A + B\cos(\pi q) \tag{6.3}$$

with $A = 269.5\ cm^{-1}$ and $B = 22.5\ cm^{-1}$.

Figure 6.6(a) shows the cosine approximation of Tiong et al [1984] together with neutron scattering data by Dolling and Waugh [1965] and both Raman scattering data and a calculated dispersion curve taken from Sood et al [1985]. As a comparison, figure 6.6(b) shows the GaAs phonon dispersion curve from Landolt– Boernstein [1982]. Clearly, the approximation used by Tiong et al [1984] (equation 6.3 above) is not particularly appropriate. The dispersion would be much better mapped by an expression such as

$$\omega(q) = A + B\cos(\pi q/2) \tag{6.4}$$

with the same values for A and B. This, however, is not the main point of the disagreement.

In figure 6.6 it can be seen that the Raman scattering data of Sood et al [1985] predicts that both the LO and the TO phonon dispersions have qualitatively similar behaviour in the first quarter of the Brillouin zone. Both phonons should therefore respond to confinement affecting the first quarter of the Brillouin zone with similar shifts and broadening (say $L \approx 4a$, i.e., ≈ 20 Å or larger). Experimental results show that this is not the case [see e.g. Peercy, 1971] and that the shift is much greater for the LO than the TO phonon.

The argument of Tiong et al [1984], that the TO phonon dispersion is small in

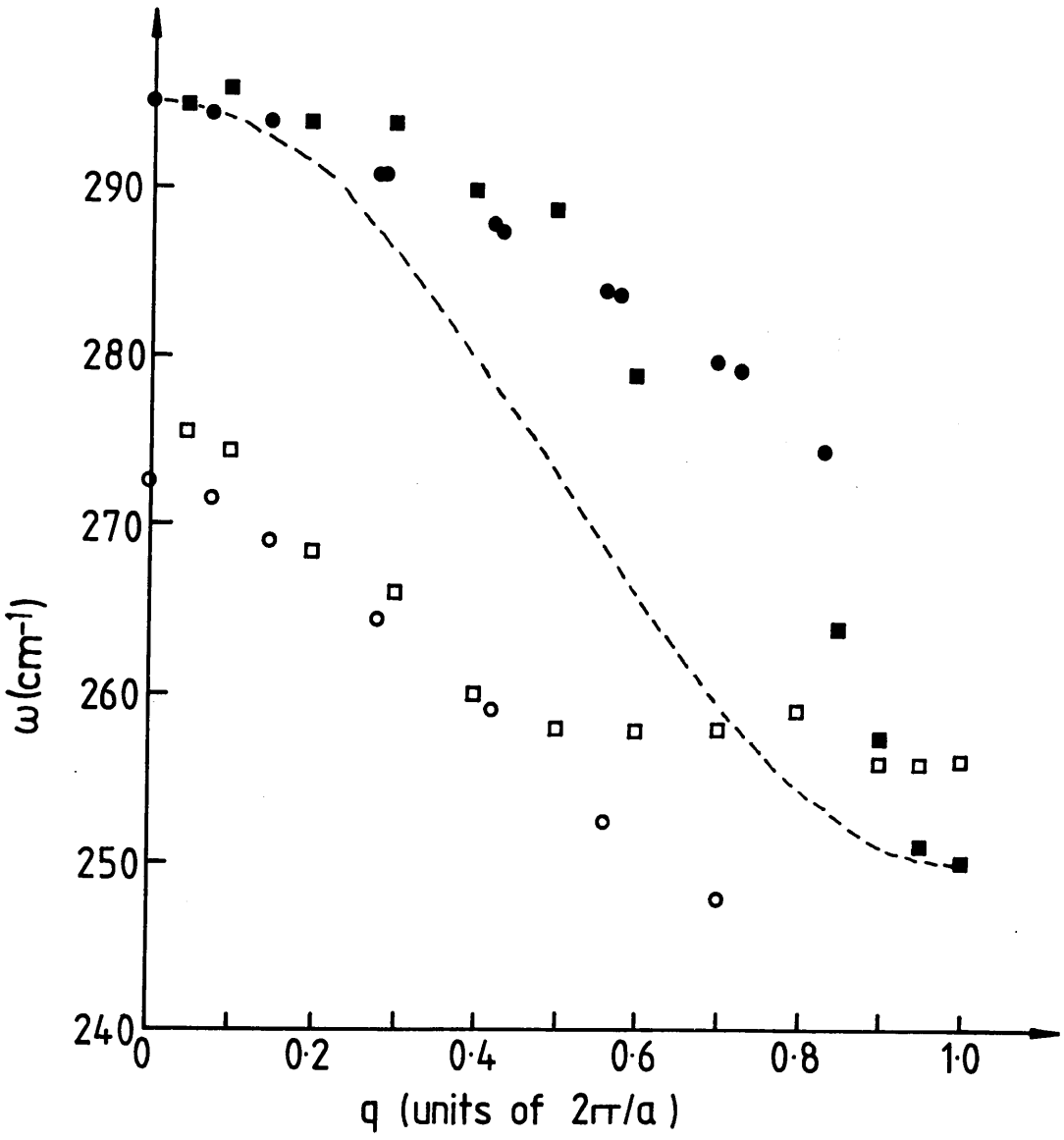

Figure 6.6(a) Phonon dispersion curve for GaAs. The circles correspond to the Raman scattering data of Sood et al [1985] and the squares to the neutron scattering data of Dolling and Waugh [1965]. The full symbols represent longitudinal modes while the open symbols represent transverse modes. The dashed line is the cosine approximation to the LO dispersion curve used by Tiong et al [1984] and given in equation 6.3. It has been moved up by 3.1 cm^{-1} in frequency to coincide with the $\Gamma = 0$ LO phonon value of Sood et al [1985].
The agreement of the Raman and neutron data is good below q = 0.5 but at larger q values, the two techniques show diverging results.

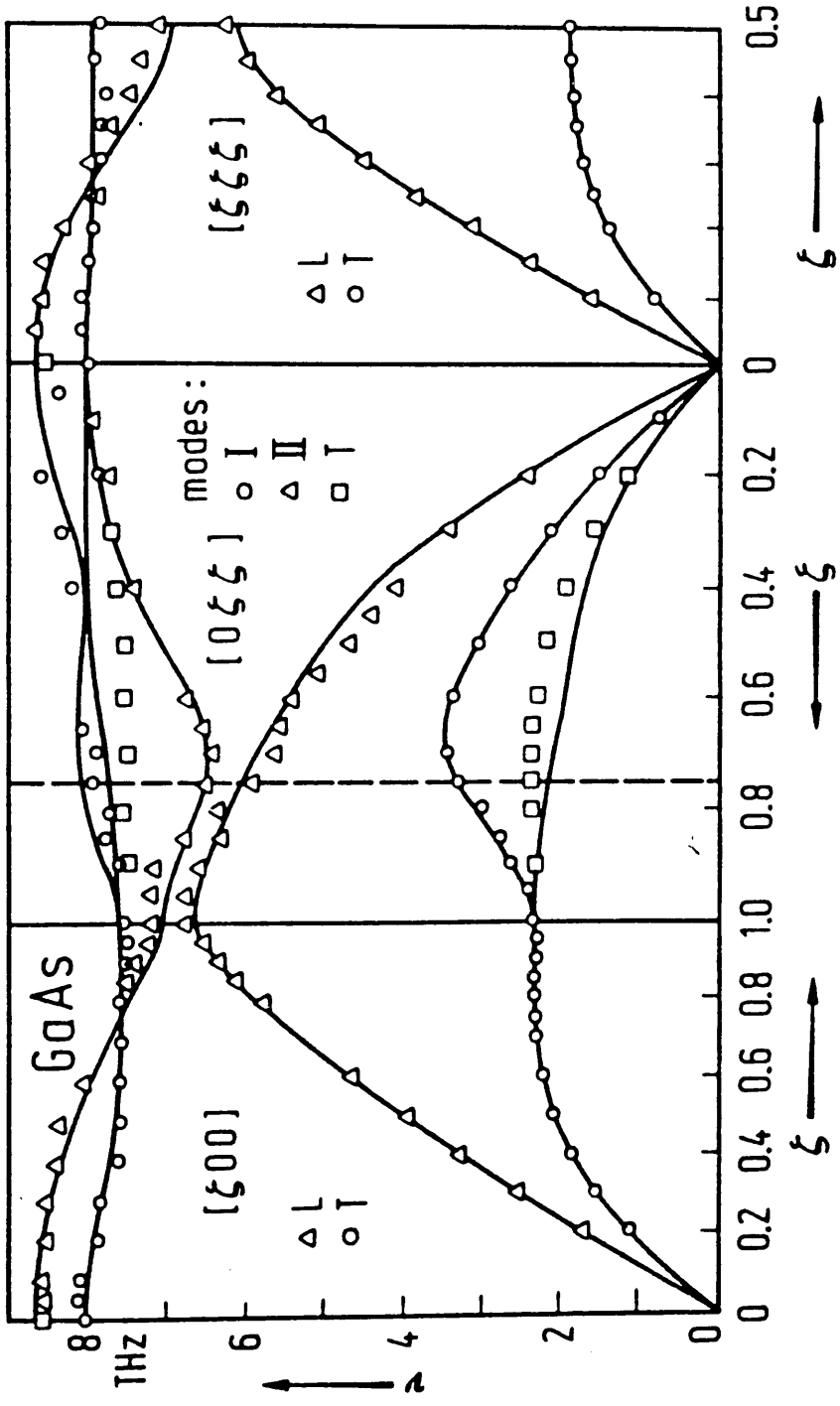

Figure 6.6(b) GaAs phonon dispersion. [After Landolt– Boernstein, 1982]

comparison with that of the LO and therefore yields only a small red shift of the mode, applies to correlation lengths smaller than about 20 Å, i.e., the full Brillouin zone. The phonon confinement model therefore cannot fully explain all the experimental observations.

6.2.2.2 Effective Charge Model

This model was proposed by Burns et al [1987] to resolve some of the inconsistencies of the phonon confinement model previously discussed. The authors studied ion–bombarded GaAs with Raman scattering techniques. The spectra that were obtained showed asymmetrical broadening and shifts of the LO phonon but little shift of the TO phonon (less than 1.5 cm^{-1} shift of the TO compared with greater than 4.5 cm^{-1} shift of the LO phonon). The authors measured the strain produced in the damaged layer using x–ray rocking curves and obtained a value of some 0.3 – 0.4% tensile strain perpendicular to the surface (i.e. parallel to the ion beam flux) with zero strain parallel to the surface. A calculation of the expected shifts of the phonon frequencies due to these strains yielded values which accounted for the shift of the TO phonons but which left a residual, unexplained, shift of the LO mode of about 4 cm^{-1}. The authors rejected the phonon confinement theory on the grounds discussed at the end of section 6.2.2.1 and instead, chose to investigate the shift in relation to a possible change in the effective charge of the material after bombardment. The idea behind this model is the fact that the LO – TO splitting results from the non–zero effective charge of a polar material. Changes in the LO – TO split might therefore be expected to be described in terms of a change in the effective charge of the material. From this basic concept, the authors proceeded after the method of Lucovsky et al [1971] to assign local, Q_l, and non–local, Q_{nl}, contributions to the effective charge where the total charge, Q =

$Q_l + Q_{nl}$. They then used the equations given by Lucovsky et al [1971], namely

$$(\omega_{TO})^2 = \omega_o^2 - 4\pi N(Q_l)^2/(3\mu V) = \omega_o^2 - \Omega_{DD}^2 \qquad (6.5)$$

and

$$(\omega_{LO})^2 = (\omega_{TO})^2 + 4\pi NQ^2/(\epsilon_\infty \mu V) = (\omega_{TO})^2 - \Omega^2 \qquad (6.6)$$

to deduce that

$$2\omega_{LO}d\omega_{LO} = \Omega^2 d(\ln[NQ^2]) - \Omega^2 d(\ln\epsilon_\infty) \qquad (6.7)$$

where

ω_{LO}, ω_{TO} = LO and TO phonon frequencies, respectively

N/V = density of Ga– As bonds

Ω = ionic plasma frequency of LO phonons (defined by the LO– TO split)

μ = GaAs reduced mass

ϵ_∞ = high frequency dielectric constant

and

$\mu\omega_o^2$ = short– range spring force constant

$\mu\Omega_{DD}^2$ = long– range dipole– dipole interaction force constant

Equation 6.7 describes the change in ω_{LO} arising from defect– induced changes in Q and ϵ_∞ which in turn produce changes in Ω, the LO– TO splitting. If the effect of defects on Q and ϵ_∞ can be quantified, then a change in Ω can be calculated and compared with the experimental value. The authors considered two types of ion– bombardment– induced defect: the vacancy/interstitial and the anti– site pair defects. For both cases they evaluated the number of bonds which would be affected by the defect and the corresponding contribution to the two terms on the right hand side of equation 6.7. Using this simple model, the authors were able to estimate the

defect density required for a 4 cm^{-1} shift of the ionic plasma frequency, Ω. Values of N_v/N of 6% and N_a/N of 4% were obtained where N_v is the number of vacancies and N_a is the number of antisites. They expected that some combination of defects would occur in practice but were unable to discriminate between the two contributions. The authors concluded that such values were reasonable and consistent with other findings for similar bombardment conditions. It has been pointed out by Anastassakis et al [1988], however, that this defect density would be consistent with a spatial correlation length of some tens to hundreds of Angstroms thus requiring the treatment of both the effective charge model and the phonon confinement model to maintain consistency. It is to be hoped that a dual treatment would account for the asymmetry of the LO phonon which was not discussed by Burns et al [1987] in their effective charge model. At present, such a full treatment is unavailable therefore careful use of both models is needed to interpret experimental data.

6.2.3 Discussion of Results

Raman scattering was used as the experimental technique to evaluate possible damage to GaAs crystals by the RIE processes discussed in section 6.1. The material used was GaAs doped to $2x10^{17}cm^{-3}$ with Si. Spectra were obtained in the nearly– backscattering geometry described in chapter 4. Samples were studied with various laser lines in order to change the penetration depth of the light and therefore probe different depths in the crystal. This process enabled evaluation of the depth dependence of the damage. Various etch powers of RIE were investigated and two etchant gases: $SiCl_4$ and CH_4/H_2.

The measurements are concentrated on a set of four samples etched in February 1987 in $SiCl_4$. These samples had the largest scattering efficiency possibly as a result of their doping density of $2x10^{17}cm^{-3}$ Si as opposed to the samples

subsequently etched in both $SiCl_4$ and CH_4/H_2, both sets of which showed almost no scattering efficiency whatsoever and both of which had a doping density of $6x10^{17}cm^{-3}$ Si. Two values of doping density are insufficient to yield a trend, however, and such a large change in scattering efficiency might be evidence for a contribution from another mechanism. Consequently, one of the recommendations for further work listed in section 6.2.4 involves studying a range of starting materials etched in both gases in order to look for consistency of results. In this context, the work presented in this chapter must be considered as a preliminary study.

Figure 6.7 shows the unanalysed Raman spectrum obtained from each of the four samples: the unetched control sample and three samples etched in $SiCl_4$ at powers of 20W, 50W and 100W. Immediately it is clear that although the TO phonon is a forbidden scattering process in this geometry, it appears in the spectra of the etched samples but not in that of the control sample. This suggests that the etch process has somehow disordered the crystal and relaxed the selection rules. A comparison of the TO:LO ratio for each of the etched samples yields a value of 0.30 for the 100W sample, 0.17 for the 50W sample and 0.40 for the 20W sample. It is instinctive to suppose that the larger the etch power, the more must be the damage to the crystal. In this context, such a high ratio for the 20W etched sample may seem surprising, however, subsequent study of the RIE process showed that at such a low power, deposition rather than etching was occurring. The surface produced on the 20W etched sample was particularly bad, being dull and rough, even to the naked eye. It is possible, therefore that the enhanced TO:LO ratio observed in the spectrum of this sample arose less from the greater damage inflicted and more from the overall reduction in intensity of the allowed scatter. Certainly, the LO phonon intensity from the 20W etched sample was far less than from any of the other three samples in the batch.

In the case of the other two samples, the 100W etched sample showed a larger TO:LO ratio than the 50W etched sample without degradation of the overall spectral

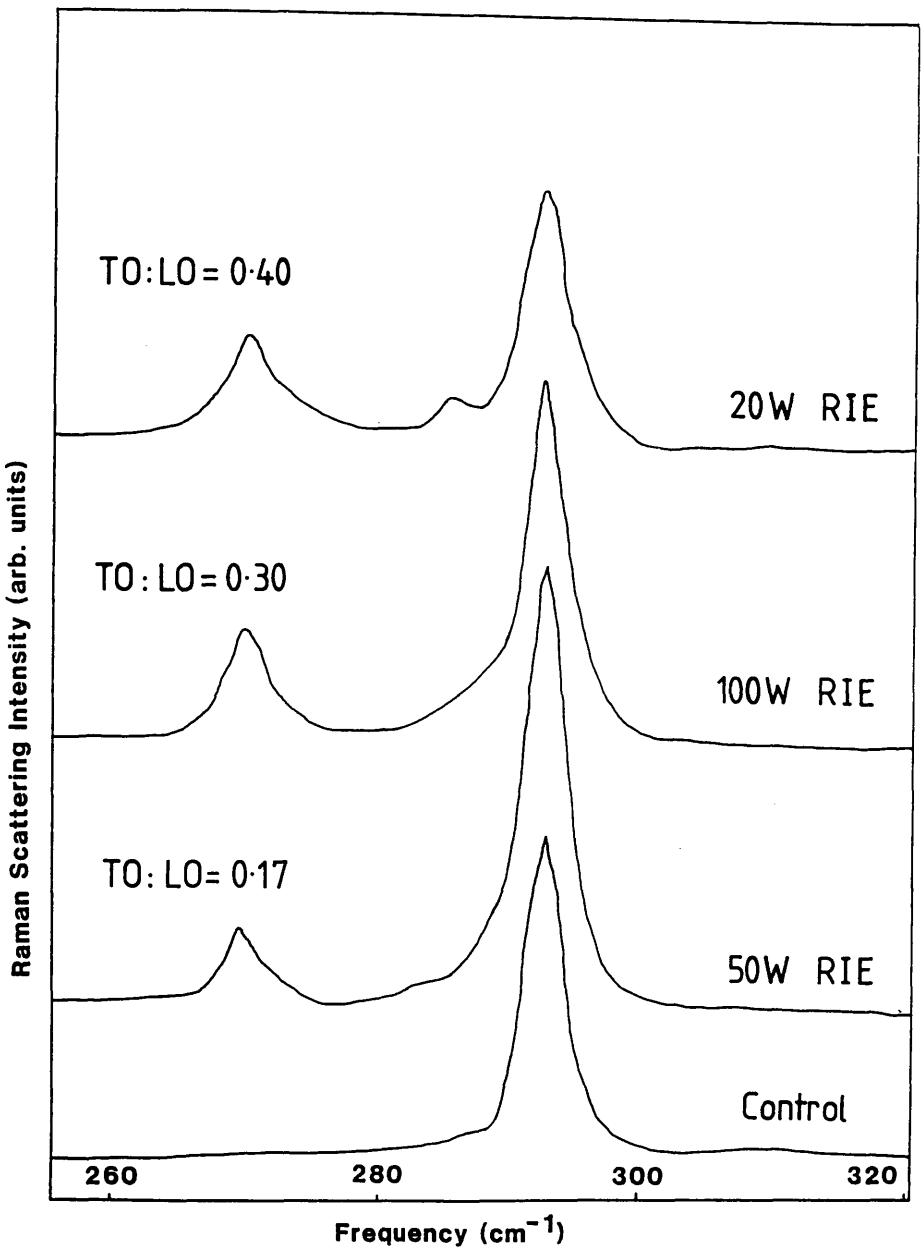

Figure 6.7 Raman scattering spectra from three etched samples and the control sample. The TO:LO ratios are given in the figure. Note the low energy tail on the LO mode of the etched samples. The small peak between the LO and TO modes of the 20W RIE spectrum is an experimental artifact discussed in the text. λ = 4825Å, Resolution = 2.4 cm^{-1}, scattering geometry = $z(x,x\&y)\bar{z}$

intensity (see figure 6.7). This can be regarded as evidence that the 100W etched sample suffered more crystalline damage than the 50W etched sample. This interpretation of the forbidden–TO presence as a signature of crystalline damage is corroborated by a number of authors [see e.g. Semura et al, 1984; Kirillov et al, 1986; Wagner and Hoffman, 1987]. The unanalysed Raman spectra of the control, 50W etched and 100W etched samples recorded with an excitation wavelength of 5309Å are shown in figure 6.8. Here the penetration depth of the laser into the sample is greater: $1/(2\alpha)$ = 650Å with the 5309Å line as opposed to 350Å with the 4825Å line [Aspnes and Stuna, 1983]. $1/(2\alpha)$ is taken as the penetration depth, rather than $1/\alpha$, to account for the absorption of both the incident and the scattered radiation [Holtz et al, 1988(b)]. Figure 6.8 shows that only the 100W etched sample, the one expected to show most damage, exhibits a TO mode; the TO mode for the 50W etched sample has disappeared. This change is indicative of crystalline damage that lies close to the surface of the material. As the penetration depth is increased, so the scattering volume is increased and the contribution to the scattered signal from the surface region is reduced. The Raman spectrum of the 100W etched sample recorded with 6471Å exciting light exhibited only an LO phonon with no evidence of a TO phonon ($1/(2\alpha)$ = 1450Å for 6471Å).

Thus two trends are perceived. Firstly, the TO mode appears when the crystal is damaged and as the damage increases, it grows stronger in intensity. Secondly, as the scattering volume is increased by increasing the laser penetration depth, so the TO phonon intensity decreases and thus the contribution to the spectrum from the damaged volume decreases. This result implies that the damaged volume is located in a region near the surface of the sample as might be expected. A qualitative estimate of the size of the damaged region can be obtained by considering the spectra at different penetration depths. For the 50W etched sample, the TO is present with 4880Å excitation but not with 5309Å excitation therefore on a scale of 350Å the damage is significant but on a scale of 650Å the damage is not significant.

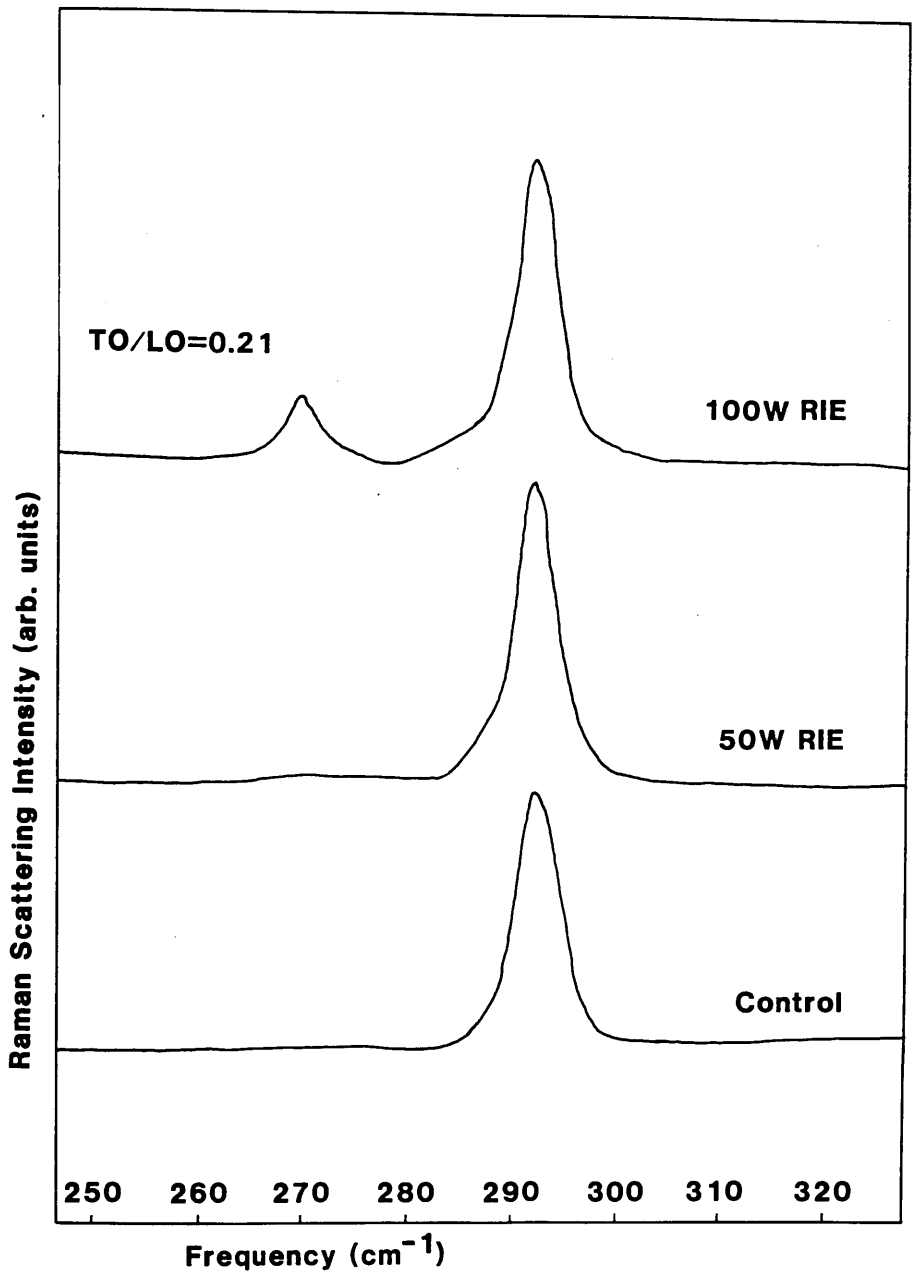

Figure 6.8 Raman scattering spectra from two etched samples and the control sample. The TO:LO ratios are given in the figure. Note the low energy tail on the LO mode of the etched samples. λ = 5309Å, Resolution = 4.2 cm^{-1}, scattering geometry = $z(x,x\&y)\bar{z}$

Naturally, this does not give more than an approximate idea of the damage caused by the RIE, however the method is very good for comparing the damage of one sample with that of another. Figure 6.9 shows a plot of the TO:LO intensity ratio as a function of penetration depth for the 100W etched sample. The straight line fit is the result of a linear regression analysis. Extrapolation of this line to either low or large penetration depths is physically inappropriate since for large penetration depths the TO:LO intensity ratio cannot be negative while for penetration depths tending to zero, surface effects rather than damage effects will dominate the spectra. Nevertheless, extrapolation to a penetration depth of some 1450Å (corresponding to 6471Å excitation) would predict a TO phonon scattering intensity of zero which is precisely what was observed experimentally.

In order to determine whether the damage to the crystal was isotropic normal to the sample surface, spectra were recorded with various rotations of the sample. Figure 6.11 shows the geometry of rotation. At each angle, a spectrum was recorded and the LO and TO intensities measured. Typical spectra are shown in figure 6.10 for the 50W etched sample. The small peak situated at around 286 cm^{-1} was not reproducible and is therefore identified as an experimental artifact. This identification is supported by the fact that the peak did not appear when different excitation lines were used. It might originate from the laser plasma tube although its measured frequency does not correspond to any of the tabulated values for Krypton. The phonon intensities as a function of angle are plotted in figure 6.11. For both etched samples, the LO phonon intensity follows the cosine dependence dictated by the selection rules while the TO phonon intensity remains constant thus indicating that the crystalline damage is indeed isotropic and does not preferentially lie along specific crystal planes.

If a quantitative estimate of the crystalline damage is required, the LO peak, rather than the TO peak, must be studied. As discussed in sections 6.2.1 and 6.2.2, there has been extensive work on the effect of ion damage to both the LO phonon

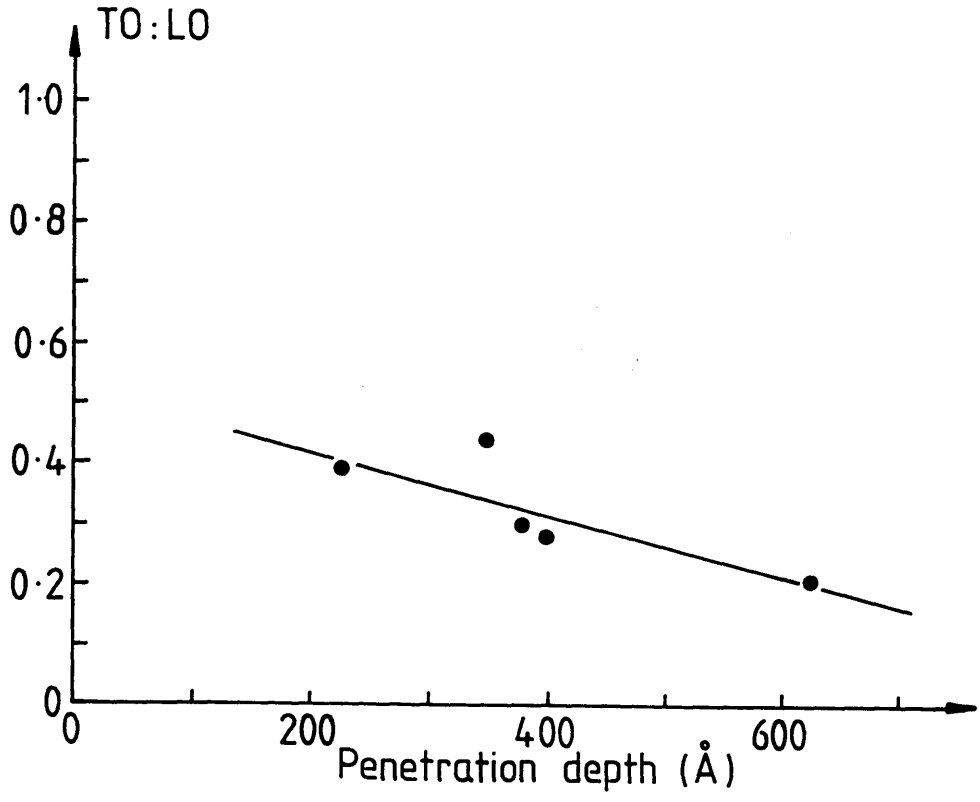

Figure 6.9 Plot of the TO:LO intensity ratio for the 100W etched sample. The straight line is a linear regression fit with a correlation coefficient of -0.805.

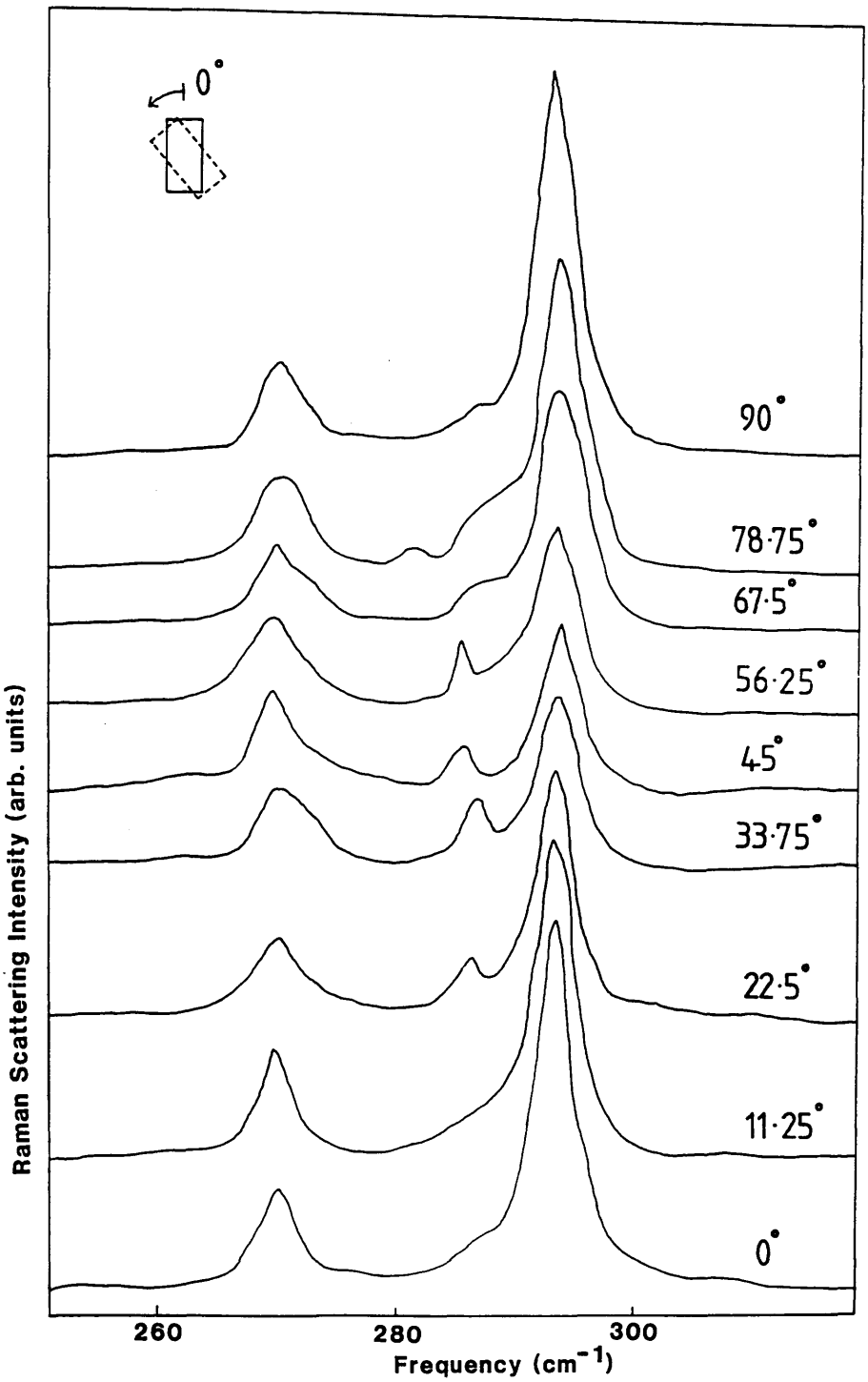

Figure 6.10 Raman scattering spectra of the 50W etched sample at different rotations (rotation geometry is given in figure 6.11). The small peaks between the LO and the TO modes are experimental artifacts as discussed in the text. λ = 4825Å, Resolution = 2.4 cm^{-1}, scattering geometry = $z(x,x\&y)\bar{z}$

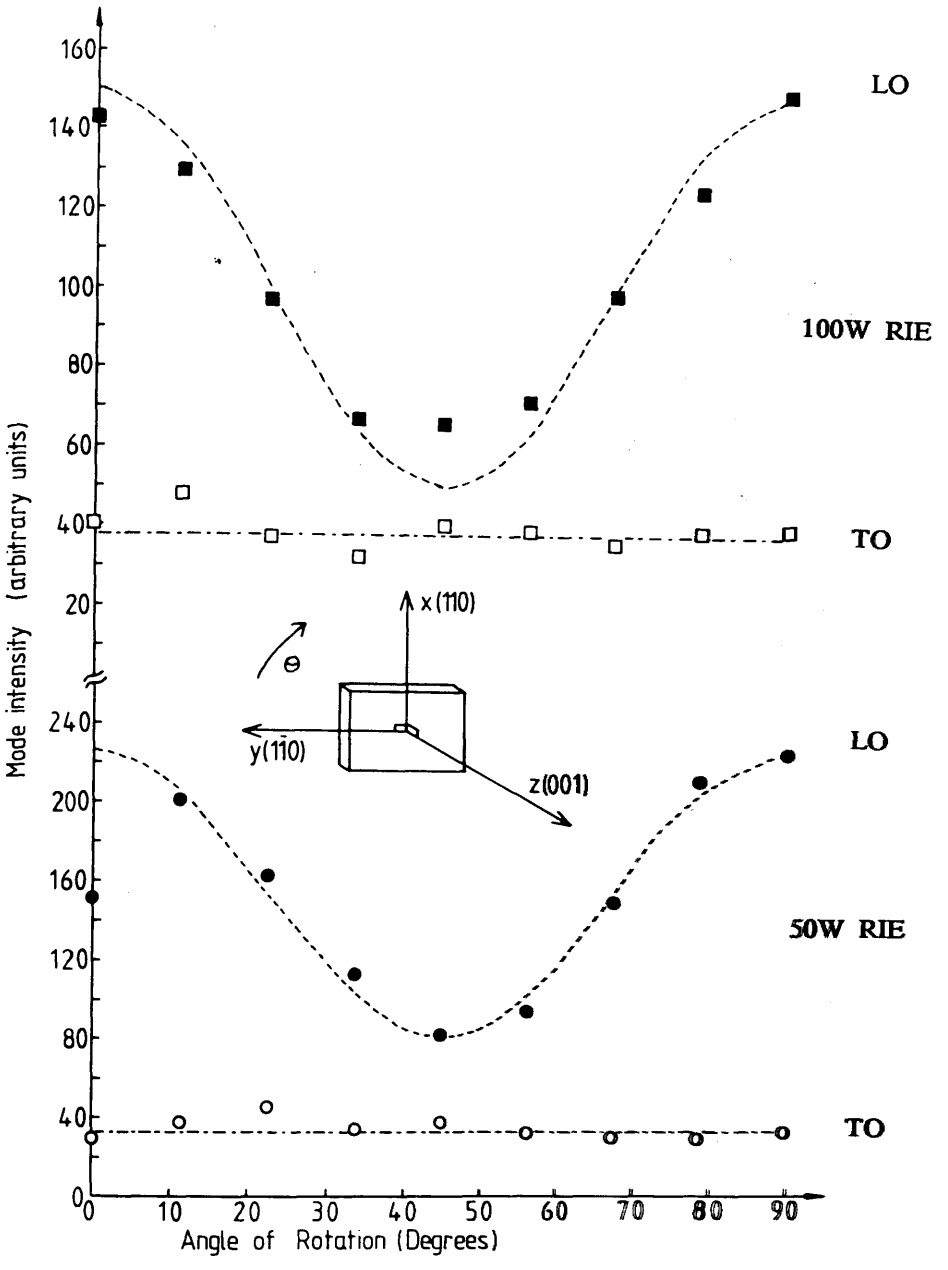

Figure 6.11 Dependence of the LO and TO phonon intensities on the sample orientation. The samples were rotated as shown in the inset. The dashed lines are a sinusoidal fit to the points and the dot–dashed lines are a guide to the eye. The two upper traces (squares) are of the 100W etched sample while the two lower traces (circles) are of the 50W etched sample. Full symbols are longitudinal modes while open symbols are the transverse modes.

peak position and lineshape. Observation of figures 6.7 and 6.8 shows that while the control sample exhibits a symmetric LO phonon peak, the etched samples all show a low energy tail on the LO mode. This is consistent with crystalline damage as discussed in section 6.2.2. None of the spectra of the etched samples show any contribution from an amorphous region of the sample thus indicati ng that the RIE processing does not produce a significant amorphous layer. Within the resolution of this experiment (see figures 6.7 and 6.8) no shift in the peak position of the LO phonon could be detected; the analysis, therefore, is of the asymmetry just mentioned. The effective charge model of Burns et al [1987] discussed in section 6.2.2.2 does not account for asymmetry of the mode, but merely for the shifts observed. The analysis followed here is that of the phonon confinement model of Tiong et al [1984] discussed in section 6.2.2.1 and bearing in mind the flaws.

Measurement of the LO phonon spectral features showed no difference in the high energy and low energy HWHM although a low energy tail was visible in the spectra. The resolution of the spectra would have allowed detection of an asymmetry of 7:6 or greater. If this asymmetry is compared with the calculations of Tiong et al [1984] (see figure 6.5(b)) it corresponds to a crystal correlation length of some 250Å. The spectra of the etched samples could therefore be interpreted as arising from crystalline areas with dimensions of between 250Å and infinity. Such a large value for L implies that these samples have suffered a low level of damage.

The data presented here are consistent with the published literature. Kirillov et al [1986], in their study of RIE of undoped GaAs, observed spectra very similar to those shown in figures 6.7 and 6.8 with the symmetry–forbidden phonon appearing for etched surfaces. They attributed this change to a modification of the selection rules produced by damage to the lattice. Semura et al [1984] used Raman scattering to characterise their etch parameters by comparing the spectrum of a wet–etched sample of GaAs, which exhibited no TO scattering, with those from variously dry–etched samples. They regarded samples as "badly–etched" when the TO

phonon became allowed, and this was one of the yardsticks they used to identify a "good" etch. The work of Tsang et al [1985] on dry–etched Silicon followed a different path since Silicon possesses degenerate LO and TO phonons at the Γ point thus it is not possible to compare the LO and TO intensities. The authors studied the RIE material in comparison with both bombarded and amorphous material. As stated in section 6.2, the RIE sample spectra showed evidence for an amorphous contribution but this was much weaker than for a 60Å amorphous layer. Since the Auger electron spectroscopy measurements of Semura et al [1984] demonstrated that implantation from the etchant gases occurred only in the first 10Å while normal atmospheric contamination (e.g. Oxygen and Carbon) existed to a depth of about 50Å, amorphicity of much less than 60Å can be regarded as comparable with an as–grown surface.

The work of Semura et al [1984], in conjunction with that presented here, suggestes that RIE causes minimal structural damage when the technique is properly optimised. Suggestions for future experimental work are included in section 6.2.4.

6.2.4 Conclusions

As discussed in the preceeding section, the work presented in this chapter must be regarded as a preliminary study, therefore the conclusions can be only preliminary. As such they contain a strong bias towards the work that has yet to be done to resolve and quantify the question of the RIE induced damage.

It has emerged from this work that samples of GaAs etched with $SiCl_4$ at a power of 100W suffer more damage than those etched at 50W. This is evidenced by the relative intensities of the symmetry–forbidden TO phonon scattering intensity. A sample etched at 20W was found to have a poor surface as a result of deposition of the etchant gases. Although a clear asymmetry of the LO lineshape was observed,

the corresponding change in half width was too small to be measured. This caused a lower limit of 250Å to be set on the dimensions of the crystallites remaining after etching. The small range of etch parameters studied enables no deduction of an optimum etch condition.

Future work in this area ought to investigate a wide range of etch conditions (power, etch time, etch gas, etch depth, etc.) for a variety of starting materials from undoped through to highly doped material. Studies of the LO and TO phonons of the undoped material could thereby be complemented by investigations of the coupled LO phonon– plasmon modes [after the manner of Kirillov et al, 1986] thus yielding information about the effect of the etch on the free electron gas. This information is important if the material is to be fabricated for device applications. Care should be taken to study CH_4/H_2 samples both before and after annealing as it is well known that Hydrogen in a sample is capable of passivating both shallow and deep impurities in GaAs and that the Hydrogen can be driven out by annealing at 400°C to reactivate the shallow levels and above 600°C to reactivate the deep levels [Pearton et al, 1987].

The data plotted in figure 6.9 should be extended to cover more samples and more values of the penetration depth. It would be particularly appropriate to obtain spectra using short wavelengths, e.g. the U.V. lines of the Argon ion laser at, say, 3638Å, thus allowing very low penetration depths of around 70Å in GaAs [Aspnes and Studna, 1983]. This is the penetration depth where the asymmetry and/or shift of the LO mode is likely to be sufficiently enhanced so as to be measurable thus yielding a quantitative value of the microcrystallite size. As this penetration depth is approaching the atmospheric contamination depth measured by Semura et al [1984] it would be interesting to look for evidence of the impurity vibrational modes of both Oxygen and Carbon which are expected to be present in measurably large quantities in the first 30Å of the surface. Raman scattering results could be compared with SIMS data on the samples to investigate the depth dependence of any impurities.

E Anastassakis, K M Biskupska, W Graeff, E Liarokapis, J Tatarkiewicz and K Wieteska; Proc. 19th Int. Conf. Phys. Semicond., Warsaw, 1988

H E G Arnot; Second year PhD report, Glasgow University, 1988

R Ashokan, K P Jain, H S Mavi and M Balkanski; J Appl Phys 60, 1985, 1986

D E Aspnes and A A Studna; Phys Rev B27, 985, 1983

M H Brodsky; in "Light Scattering in Solids I", edited by M Cardona, published by Springer– Verlag, Berlin, Heidelberg, New York, 1982; p205

G Burns, F H Dacol, C R Wie, E Burstein and M Cardona; Sol St Comm 62, 449, 1987

E Bustarret, M A Hachicha and M Brunel; Appl Phys Lett 52, 1675, 1988

R Cheung; Private Communication, 1988

R Cheung, S Thoms, S P Beaumont, G Doughty, V Law and C D W Wilkinson; Electron Lett 23, 857, 1987

G Dolling and J L T Waugh; in "Lattice Dynamics", edited by R F Wallis, published by Pergamon, London, 1965; p19

M Holtz, R Zallen, A E Geissberger and R A Sadler; J Appl Phys 59, 1946, 1986

M Holtz, R Zallen and O Brafman; Phys Rev B37, 2737, 1988(a)

M Holtz, R Zallen, O Brafman and S Matteson; Phys Rev B37, 4609, 1988(b)

M Kawabe, N Kanzaki, K Masuda and S Namba; Appl Opt 17, 2556, 1978

D Kirillov, C B Cooper and R A Powell; J Vac Sci Technol B4, 1316, 1986

"Landolt– Boernstein Numerical Data and Functional Relationships in Science and Technology. Group III: Crystal and Solid State Physics" Vol 17a: Physics of Group IV Elements and III– V Compounds, edited by O Madelung, published by Springer– Verlag, Berlin, Heidelberg, New York, 1982; sections 2.10, 2.11, 2.14 and 2.16

G Lucovsky, R M Martin and E Burstein; Phys Rev B4, 1367, 1971

T Nakamura and T Katoda; J Appl Phys 53, 5870, 1982

T Nakamura and T Katoda; Jpn J Appl Phys 23, L552, 1984

S J Pearton, J W Corbett and T S Shi; Appl Phys A43, 153, 1987

P S Peercy, Appl Phys Lett 18, 574, 1971

C S Rama Rao, S Sundraman, R L Schmidt and J Comas; J Appl Phys 54, 1808, 1983

H Richter, Z P Wang and L Ley; Sol St Comm 39, 625, 1981

S Semura, H Saitoh and K Asakawa; J Appl Phys 55, 3131, 1984

S A Solin and R J Kobliska; in "Amorphous and Liquid Semiconductors", edited by J Stuke, published by Taylor & Francis, London, 1974; p1251

A K Sood, J Menendez, M Cardona and K Ploog; Phys Rev Lett 54, 2111, 1985

K K Tiong, P M Amirtharaj, F H Pollak and D E Aspnes; Appl Phys Lett 44, 123, 1984

J C Tsang, G S Oerlein, I Haller and J S Custer; Appl Phys Lett 46, 589, 1985

J Wagner and Ch Hoffman; Appl Phys Lett 50, 682, 1987

C D W Wilkinson and S P Beaumont; in "The Physics and Fabrication of Microstructures and Microdevices", Proc. Winterschool, Les Houches, France, 1986; edited by C Weisbuch and M J Kelly, published by Springer– Verlag, Berlin, Heidelberg; p36

CHAPTER 7

GaAs QUANTUM CYLINDERS

7.1 Introduction and Fabrication

A natural extension of the progression from three dimensions to two, is the continuation to one or even zero dimensions. Whereas two dimensions can be achieved by growing layered structures, one dimensional structures consist of wires, situated either horizontally along a surface, or forming free–standing pillars at right–angles to a surface (see figure 7.1). Zero dimensional structures can be obtained by either crossing two sets of 1D wires, thus producing boxes, as shown in figure 7.2(a), or else by forming the pillars shown in figure 7.1(b) from quantum well material. This latter would produce disc–like confinement as shown in figure 7.2(b). Such structures are interesting both from the physics and the device point of view. There is a great interest at present in producing these structures and exploiting to the full techniques such as electron–beam lithography thus enabling very small patterns to be laid for etching.

The fabrication process used for the samples studied in this work involved first coating an undoped GaAs sample with a resist mask, secondly, exposing a pattern on the resist using an electron beam, thirdly, developing the pattern to leave a "stencil" on the sample and finally, etching through the stencil to form the required structure.

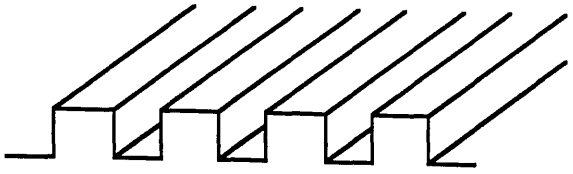

(a)

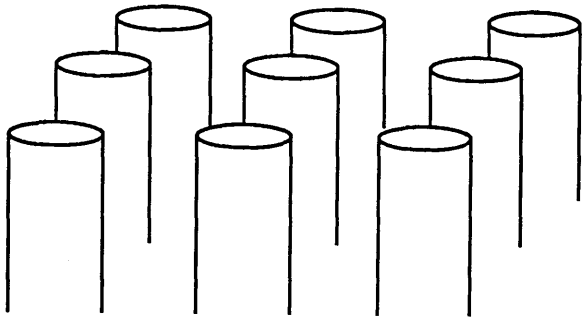

(b)

Figure 7.1 Schematic representation of 1D wires constructed (a) horizontally and (b) vertically.

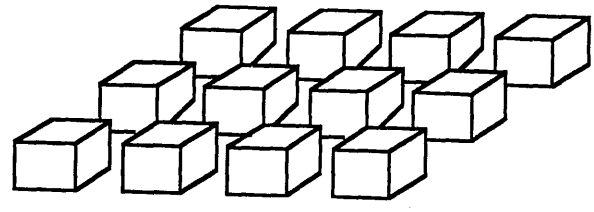

(a)

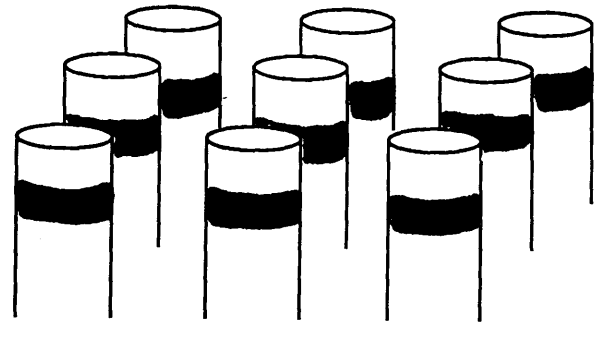

(b)

Figure 7.2 Schematic representation of 0D structures (a) boxes and (b) discs.

The structures formed in this way have the shape shown schematically in figure 7.1(b) and are therefore called quantum cylinders. All the fabrication was done by Hazel E G Arnot (PhD student at Glasgow University) as part of a collaborative study on the phonon modes of very small structures. The fabrication process is described fully elsewhere [Arnot, 1988] and only an outline will be given here.

The size of the structures that can be formed in this way is limited by the resolution of the electron beam. At present the resolution available limits the linewidth of a pattern to about 400Å. This linewidth comprises many factors: the beam spot, the resolution with which the beam can be moved (pixel size) and the proximity effect. This latter means that any exposure will be larger than intended because of electron scattering in both the resist and the substrate. Once patterned, the samples were reactive–ion–etched (RIE) using the process described in section 6.1. A typical SEM picture of the type of sample used in this work is shown in figure 7.3.

Alternative techniques used to fabricate similar structures are impurity induced disordering of the lattice [see e.g. Cibert et al, 1986], Argon ion milling as a replacement for the RIE step [Temkin et al, 1987] or doping of porous glass to produce microcrystallites [Luong, 1988]. Other authors have investigated microcrystallites produced by gas evaporation techniques [see e.g. Hayashi and Kanamori, 1982; Oktada et al, 1987]. The expected effect of the different processing techniques on the surfaces and hence on the surface phonons must be considered when drawing conclusions from the experimentally–observed phonon data.

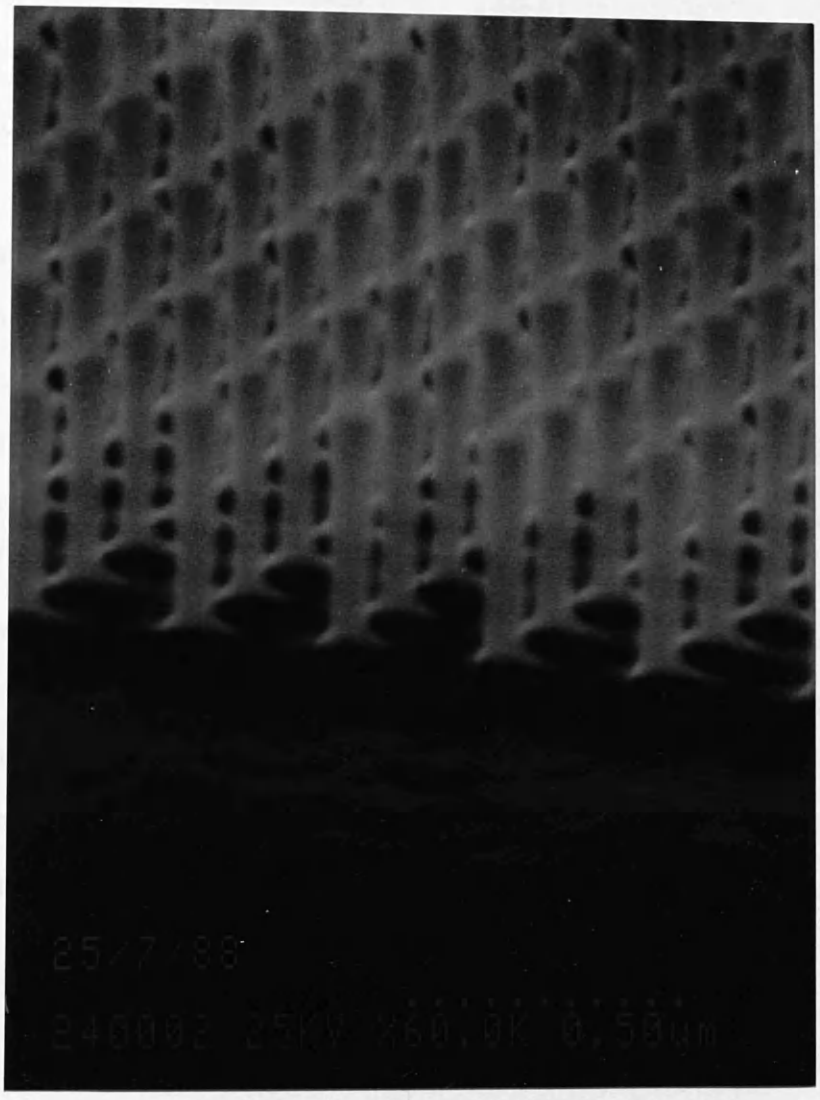

Figure 7.3 SEM micrograph of a typical quantum cylinder sample. The magnification is 60,000. [Micrograph courtesy of H E G Arnot]

As has been discussed in chapter 3, when sample dimensions become very small, concepts such as the infinite crystal approximation can no longer be used to calculate phonon frequencies. It was shown that 2D confinement resulted in confined and interface phonons. In one or zero dimensions, further effects can be expected. For the sample type shown in figure 7.3, the increased surface to volume ratio of the patterned structure compared to the plain unpatterned surface suggests that one of the major changes in the observed phonon behaviour would be an enhancement of the surface phonon intensity relative to that of the bulk. For the case of 500Å diameter cylinders of height 2000Å and pitch 5, the pattern enhances the surface to volume ratio by a factor of 1.5, where the pitch is defined as the distance between the cylinders divided by the cylinder diameter. In addition, the new structure enables the incident light to couple to the surface modes in a different way without altering the experimental geometry. This point will be discussed further in section 7.4.3.

7.2.1 Electrostatic Continuum Model

This model was developed by Englman and Ruppin [1966 and 1968] to describe the surface phonons of very small samples of arbitrary shape. They extended the work up to that time which had been restricted to the simpler geometries of sphere [Froehlich, 1949] and slab [Fuchs and Kliewer, 1965]. The authors derived, from first principles, general equations for the frequencies of the lattice vibrations, obtaining bulk LO, bulk TO and surface phonon solutions. They then applied suitable boundary conditions for a number of example geometries and calculated the frequencies of the surface phonons. They also included a comparison of their

expected modes with experimental data. The simplified geometry relevant to quantum cylinders is that of an infinitely long cylinder in which surface phonon modes propagate on the outside of the cylinder with decaying amplitude both inside and outside the surface. Two theoretical models were investigated: a full model which is applicable to samples of arbitary size and in which polariton effects are considered, and a simpler case of the full model in which polariton effects are neglected. The simpler theory is valid when the sample size is much smaller than the infrared radiation wavelength. In GaAs, optical phonon modes have an energy not exceeding $300cm^{-1}$ which is equivalent to about $34\mu m$, thus for quantum cylinders of GaAs, where the radius is typically $0.05\mu m$ and the length of the cylinder $0.5\mu m$, the polariton contributions to the surface mode frequency can be ignored and the simpler model will be adequate. The formula used to calculate the surface mode frequency for a cylinder is given by Ruppin and Englman [1970] as:

$$\frac{(\omega_{nh})^2}{(\omega_t)^2} = \frac{\epsilon_0 - \epsilon_m \rho_{nh}}{\epsilon_\infty - \epsilon_m \rho_{nh}} \qquad (7.1)$$

where

ω_{nh} = surface phonon mode frequency of order n

ω_t = bulk TO frequency ($269\ cm^{-1}$)

ϵ_0, ϵ_∞, ϵ_m = dielectric constants: static, dynamic and of the surrounding medium (taken as 12.85, 10.88 and 1.00 respectively ["Properties of GaAs", 1986])

and where

$$\rho_{nh} = \frac{K'_n(hR)\, I_n(hR)}{K_n(hR)\, I'_n(hR)} \qquad (7.2)$$

with

R	=	radius of cylinder
I_n, K_n	=	modified Bessel functions of order n
I'_n, K'_n	=	derivatives of I_n and K_n respectively

and

h	=	propagation constant along the cylinder = $2\pi n\cos\theta/\lambda$

where

n	=	refractive index for GaAs (4.33 [Aspnes and Studna, 1983])
λ	=	wavelength of incident light (4825Å)
θ	=	angle of incidence of the incident laser beam to the cylinder axis (estimated at 45°)

Equation 7.1 was used to calculate the surface modes expected for various radii of quantum cylinders using the cylinder radius as a variable. The Bessel functions were generated numerically using the methods given by Press et al [1986], together with recursion relations for the derivatives listed by Abramowitz and Stegun [1965]. The computer program is contained in Appendix D.

Figure 7.4 shows the theoretical surface phonon frequency plotted as a function of cylinder radius for the first three mode orders with the sample surrounded by air; the bulk GaAs LO and TO mode frequencies are also shown as a comparison. The calculated surface modes lie between the TO and LO modes as observed before in GaP microcrystals [Hayashi and Kanamori, 1982]. Equation 7.1 shows that the surface mode frequency depends on the dielectric constant of the surrounding medium. Figure 7.5 illustrates this dependence by plotting the frequency of the first order mode, ω_{0h}, for the cases of ϵ_m equal to 1, 2, 3 and 4. The effect of the increase in ϵ_m is to reduce the frequency of the surface mode.

It is clear that in order to make a positive identification of a surface mode, a

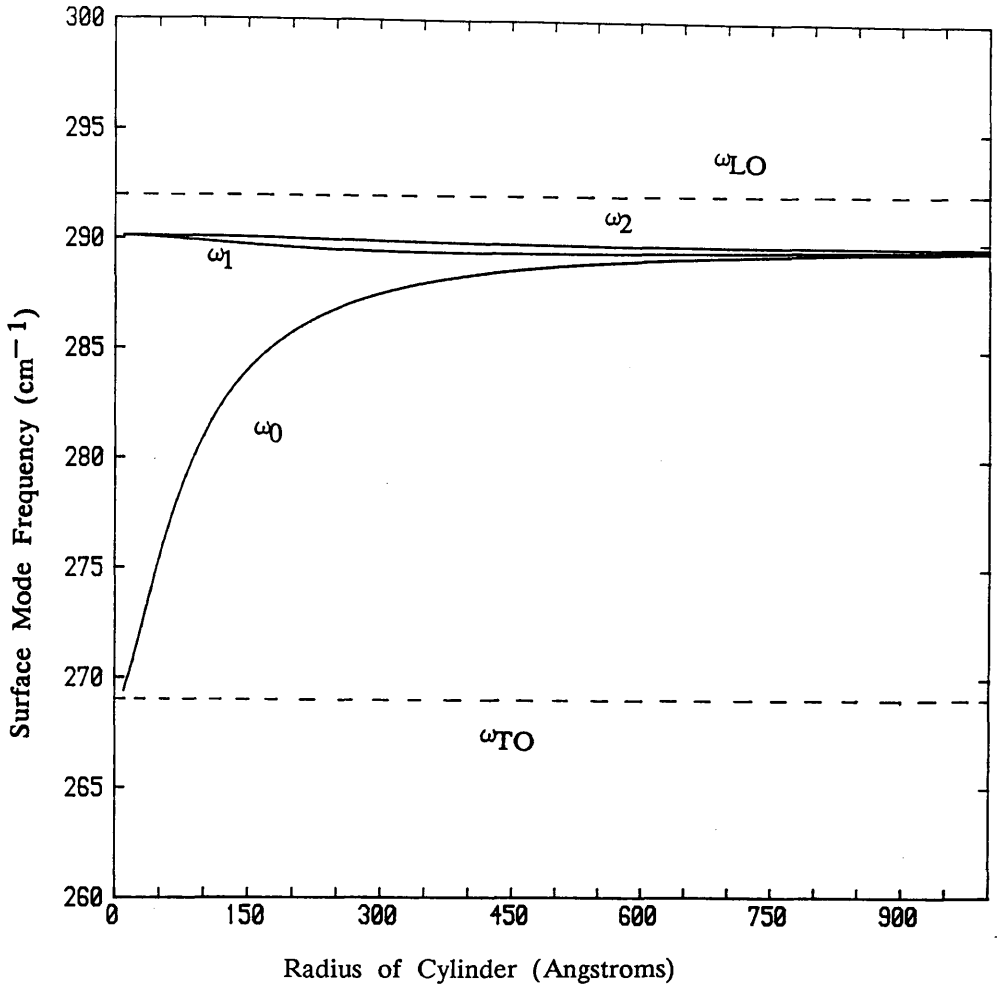

Figure 7.4 Calculated surface phonon frequencies as a function of quantum cylinder radius. The curves (solid lines) were obtained using equations 7.1 and 7.2 and the first three order modes are shown. The LO and TO bulk frequencies are given as a comparison (dashed lines).

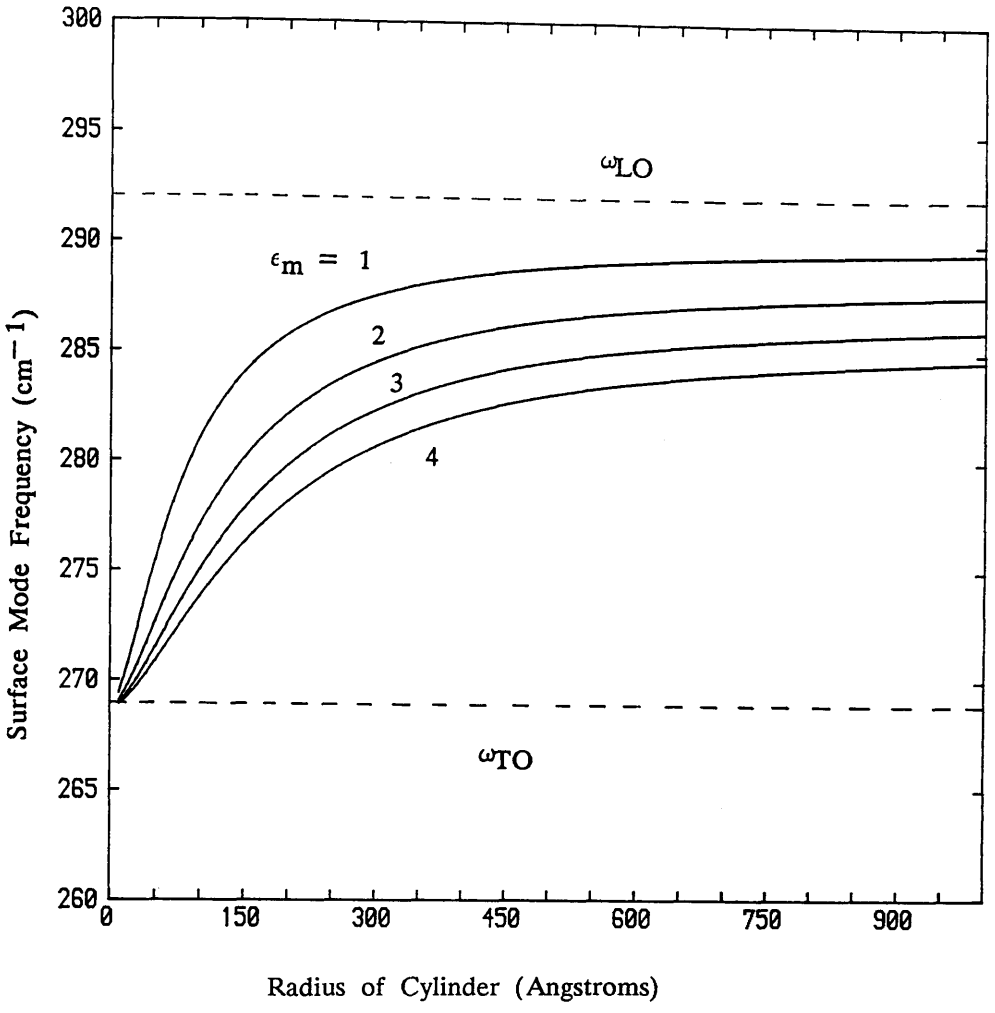

Figure 7.5 Calculated surface phonon frequencies as a function of quantum cylinder radius for the n= 0 mode. The curves (solid lines) were obtained using equations 7.1 and 7.2 and four values of the dielectric constant of the surrounding medium (ϵ_m) are shown. The LO and TO bulk frequencies are given as a comparison (dashed lines).

change of frequency with both sample radius and surrounding medium must be demonstrated. The model has been used successfully by Hayashi and Kanamori [1982] to fit the experimental data obtained from spherical microcrystals of GaP.

7.3 Experimental Data

A number of samples were investigated by Raman scattering with a view to observing the surface phonon mode of the quantum cylinders. A total of ten samples etched in $SiCl_4$ were studied. The geometry used to record the spectra was the nearly–backscattering geometry described in section 4.1. The samples can be divided into three categories according to their spectra. Two samples showed little or no difference in the spectra recorded from the patterned area (on–dots) and off the patterned area (off–dots). Their spectra are shown in figure 7.6. A further five samples exhibited strong shoulders to the low energy side of the LO mode in the on–dots spectra; these samples also showed enhanced TO phonon scattering intensities (see figure 7.7). The remaining three patterned samples showed a well–defined feature in the on–dots Raman spectrum at an energy between the LO and the TO phonons. These three samples are labelled QD01, QD07 and QD12 and scanning electron microscope (SEM) micrographs of the patterns are shown in figures 7.8 (a), (b) and (c), respectively. Their Raman spectra are shown in figure 7.9.

In order to study the effect of the surrounding medium on the frequency of the additional spectral feature, QD01 was immersed in Nujol, a mineral oil with a dielectric constant of 2.0 [Hayashi and Kanamori, 1982]. No change was observed in the recorded spectrum (see figure 7.10) and it was suspected that the Nujol might not be wetting the GaAs. The Nujol was removed with methanol and the sample was then coated with an etch resist (Polyimide XU 218) which had a dielectric constant of 2.6 [Ciba–Geigy, 1983], but no change was observed in the Raman spectrum (see figure 7.11). It was thought that this might be due to a native oxide of GaAs covering the sample surface and preventing interactions of the surface mode with the overlying coating. To investigate whether a surface mode might exist between the GaAs and its native oxide layer, the oxide was removed.

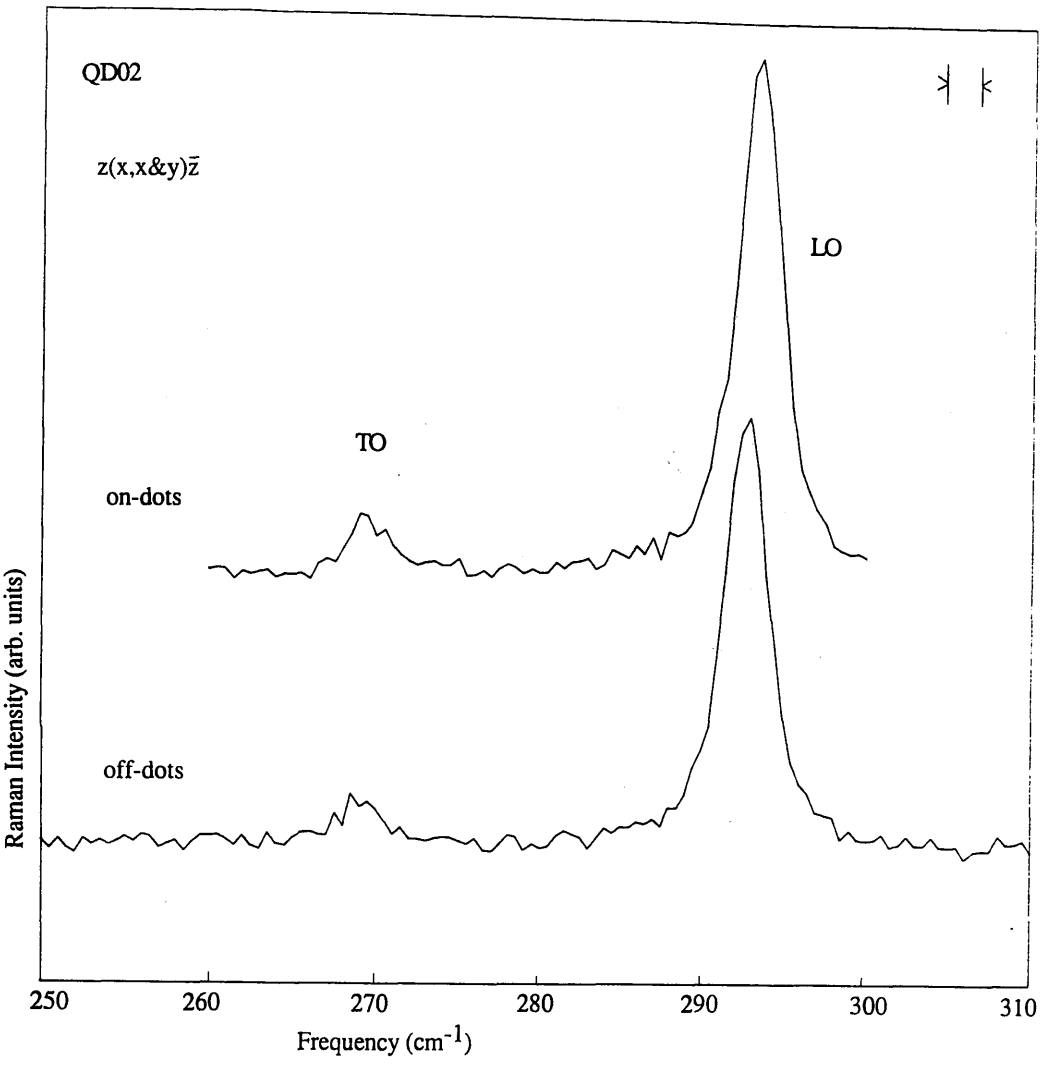

Figure 7.6 Raman spectra of QD02 both on and off the patterned area. No difference in the spectra is apparent. λ = 4880Å, resolution = 2.0 cm^{-1}, room temperature.

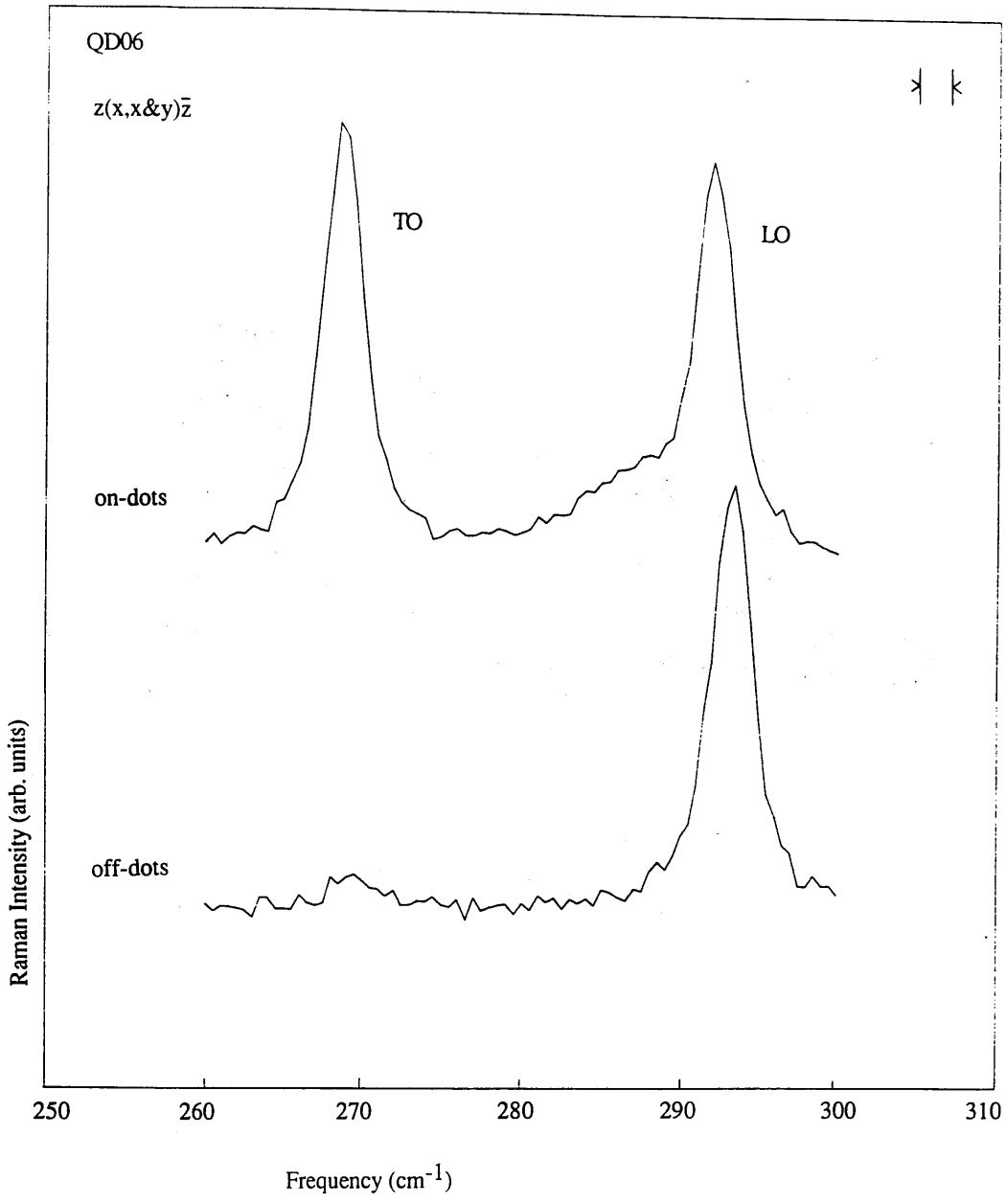

Figure 7.7 Raman spectra of QD06 both on and off the patterned area. The TO intensity is much stronger for the on–dots than the off–dots spectrum. Note also the shoulder to the low energy side of the LO phonon. λ = 4880Å, resolution = 2.0 cm^{-1}, room temperature.

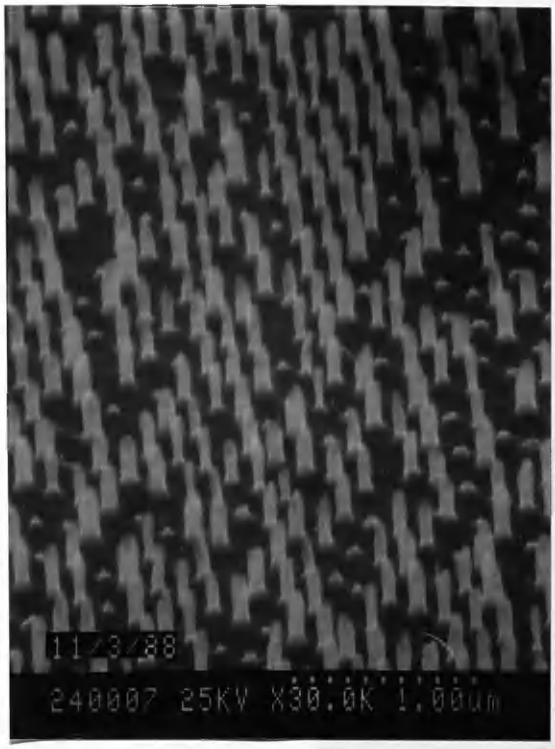

(i)

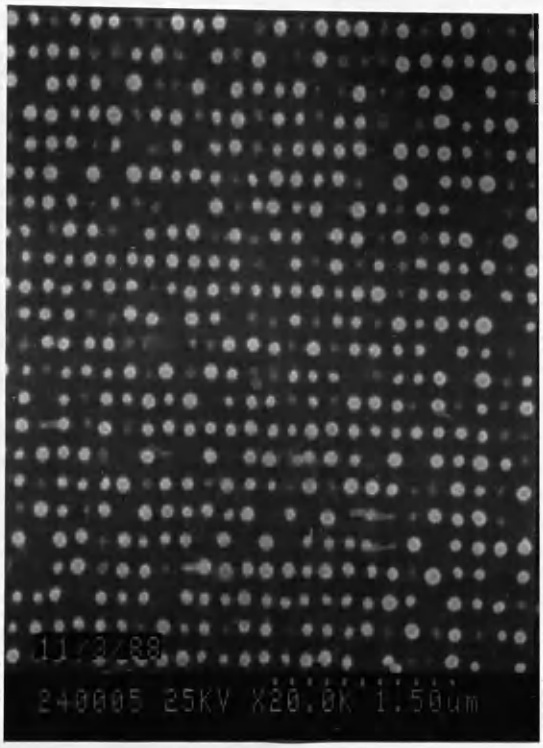

(ii)

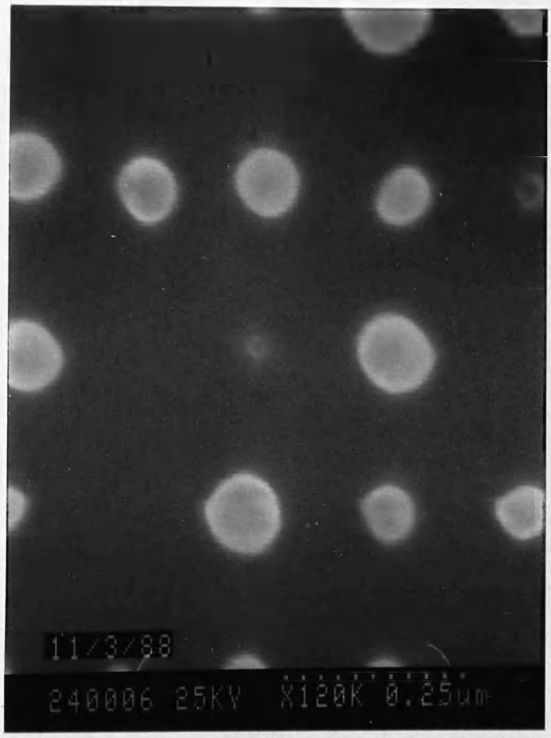

(iii)

Figure 7.8(a) SEM micrographs of QD01. The uneven size of the cylinders is evident. This is because this sample was one of the first produced and fabrication had not been optimised as it was for the later samples. (ii) shows the pattern from above illustrating the array and (iii) is an enlargement of part of (ii) to enable the cylinder diameters to be measured.

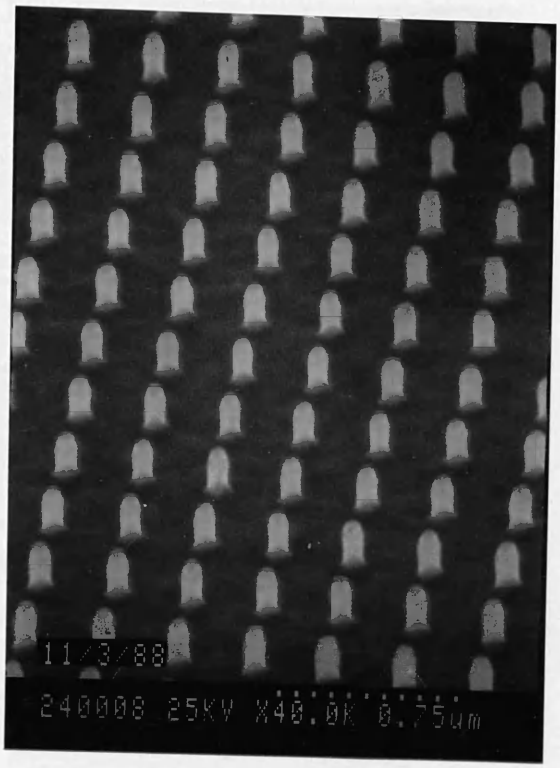

(i)

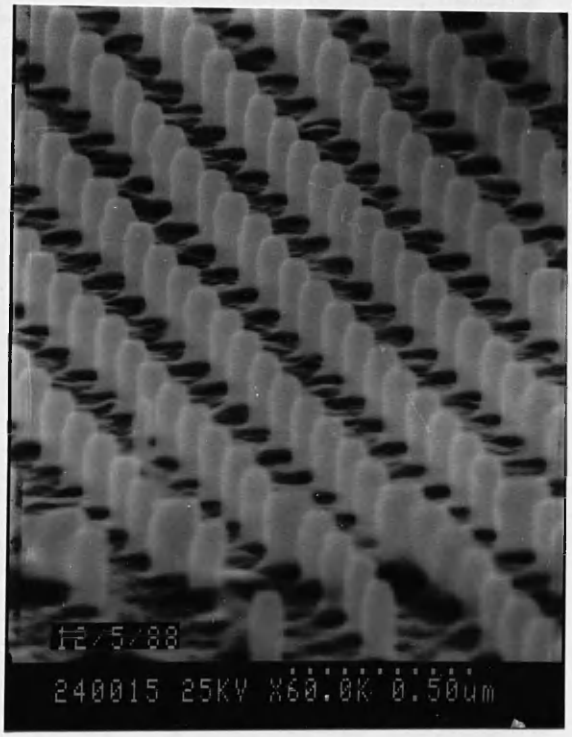

(ii)

Figure 7.8(b) SEM micrographs of QD07. This pattern has a very regular array and cylinder size. Micrographs (i) and (ii) were taken at different angles. Micrograph (ii) was taken after many Raman experiments on the pattern and therefore shows that no degradation has resulted from the experiments (e.g. no melting of the cylinders).

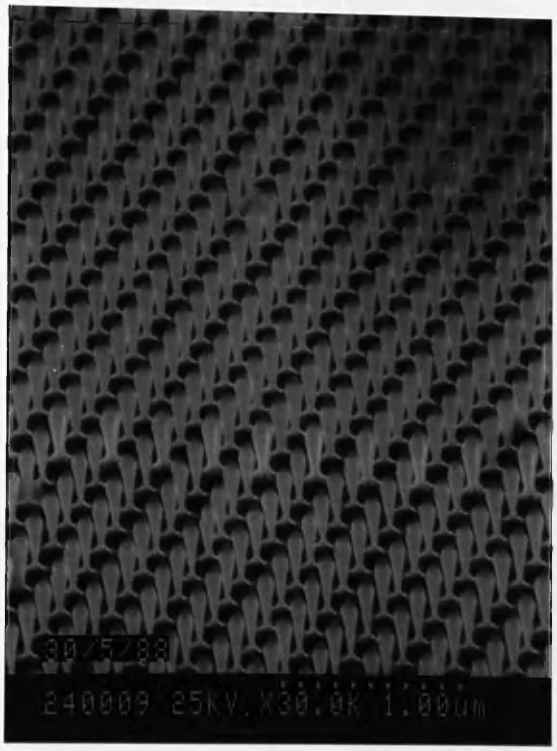

(i)

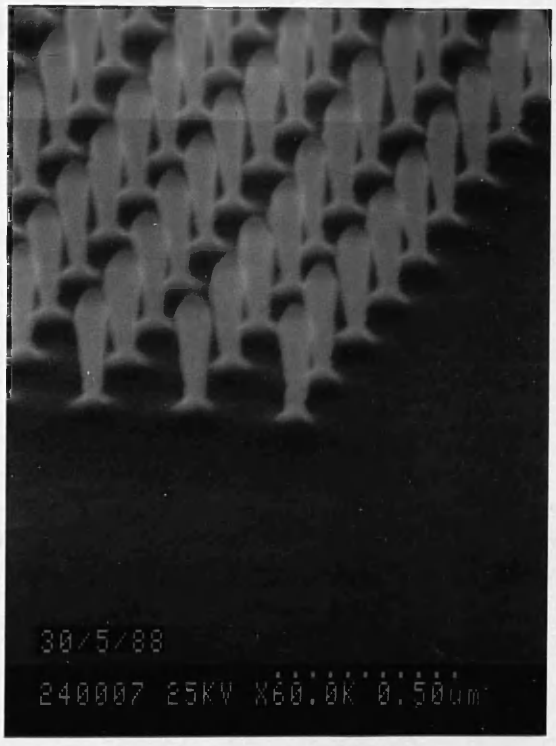

(ii)

Figure 7.8(c) SEM micrographs of QD12. This pattern has a very regular array and cylinder size. Micrograph (ii) shows the edge of the pattern.

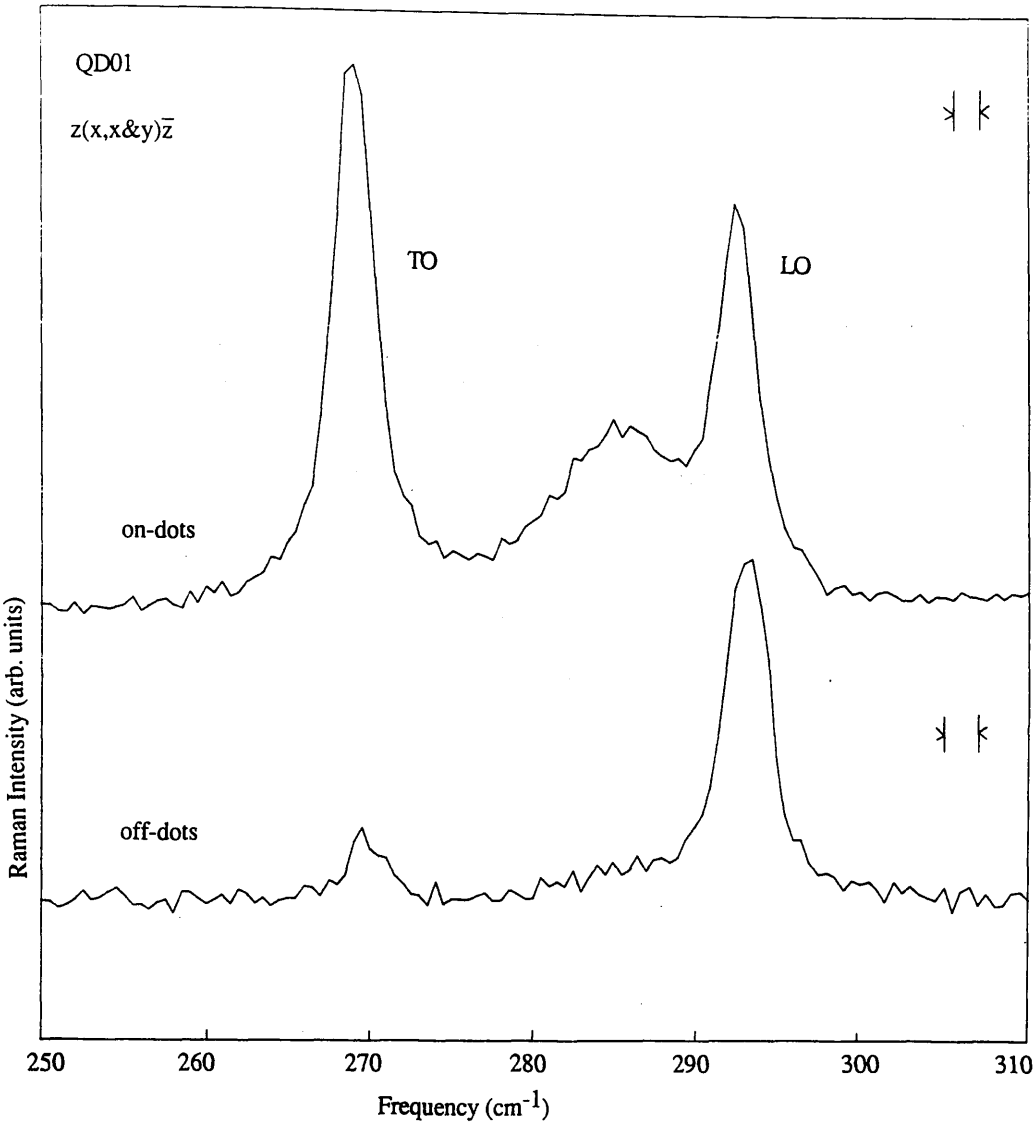

Figure 7.9(a) Raman spectra of QD01 both on and off the patterned area. λ = 4880Å, resolution = 1.5 cm^{-1} (upper trace), 2.0 cm^{-1} (lower trace), room temperature.

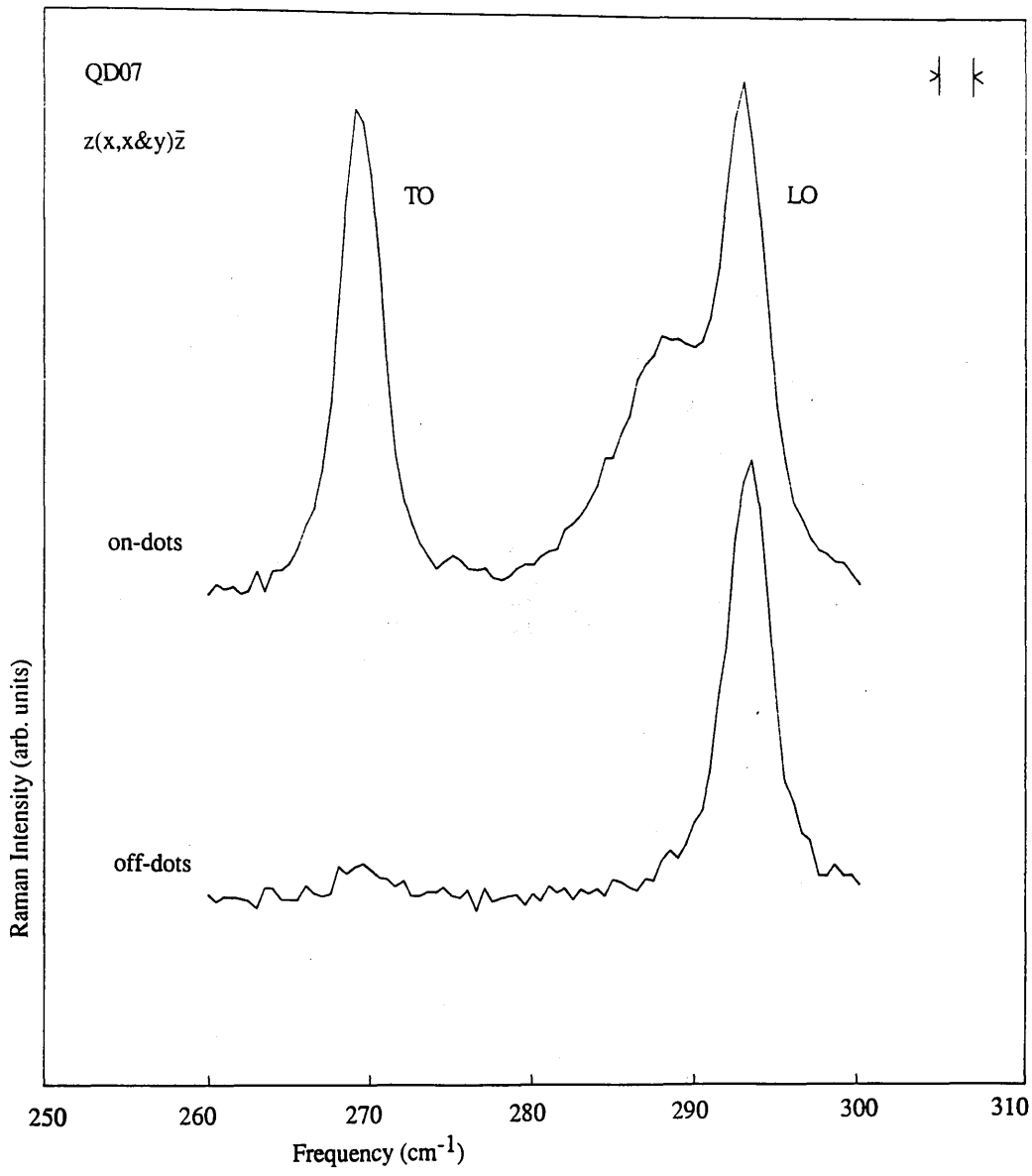

Figure 7.9(b) Raman spectra of QD07 both on and off the patterned area. λ = 4880Å, resolution = 2.0 cm^{-1}, room temperature.

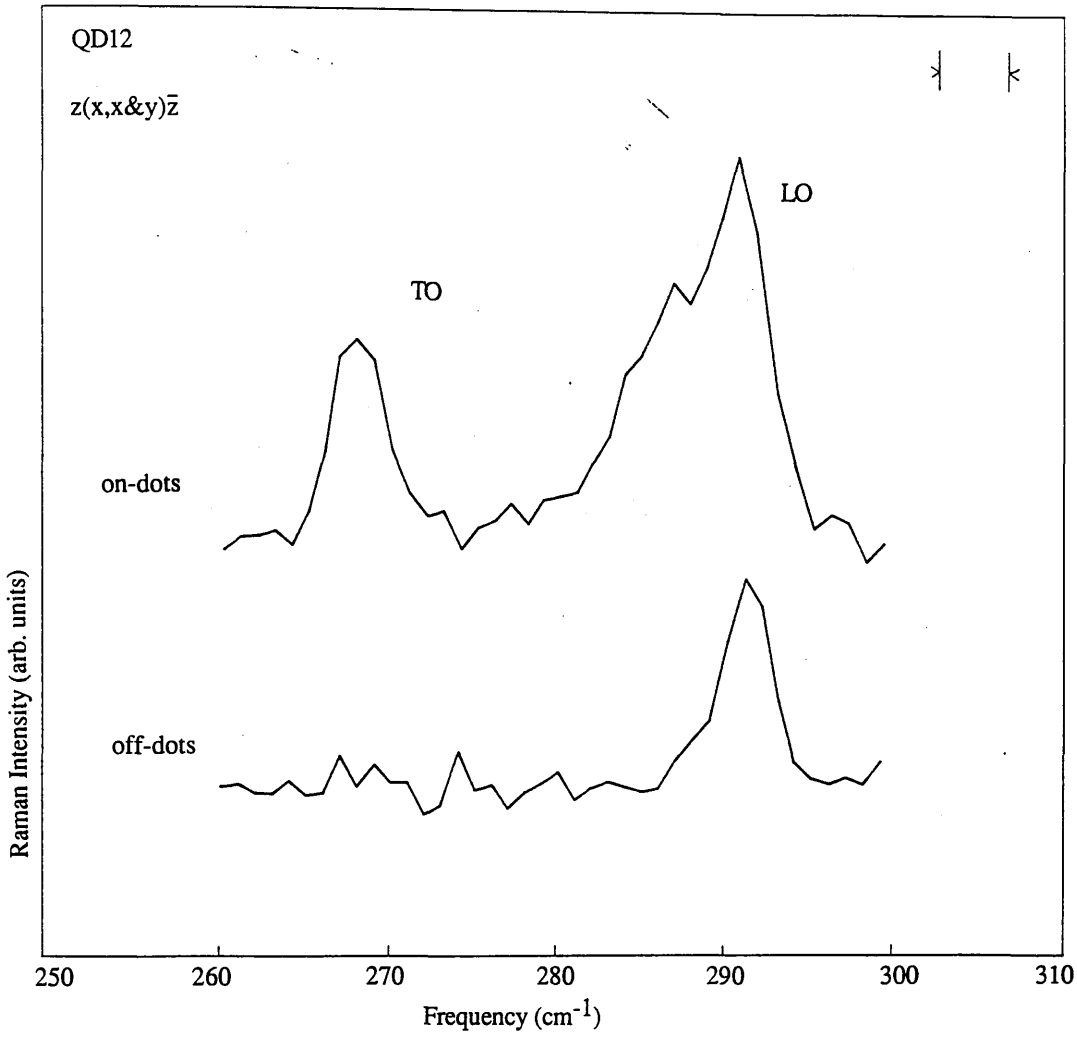

Figure 7.9(c) Raman spectra of QD12 both on and off the patterned area. λ = 4880Å, resolution = 4.0 cm^{-1}, room temperature.

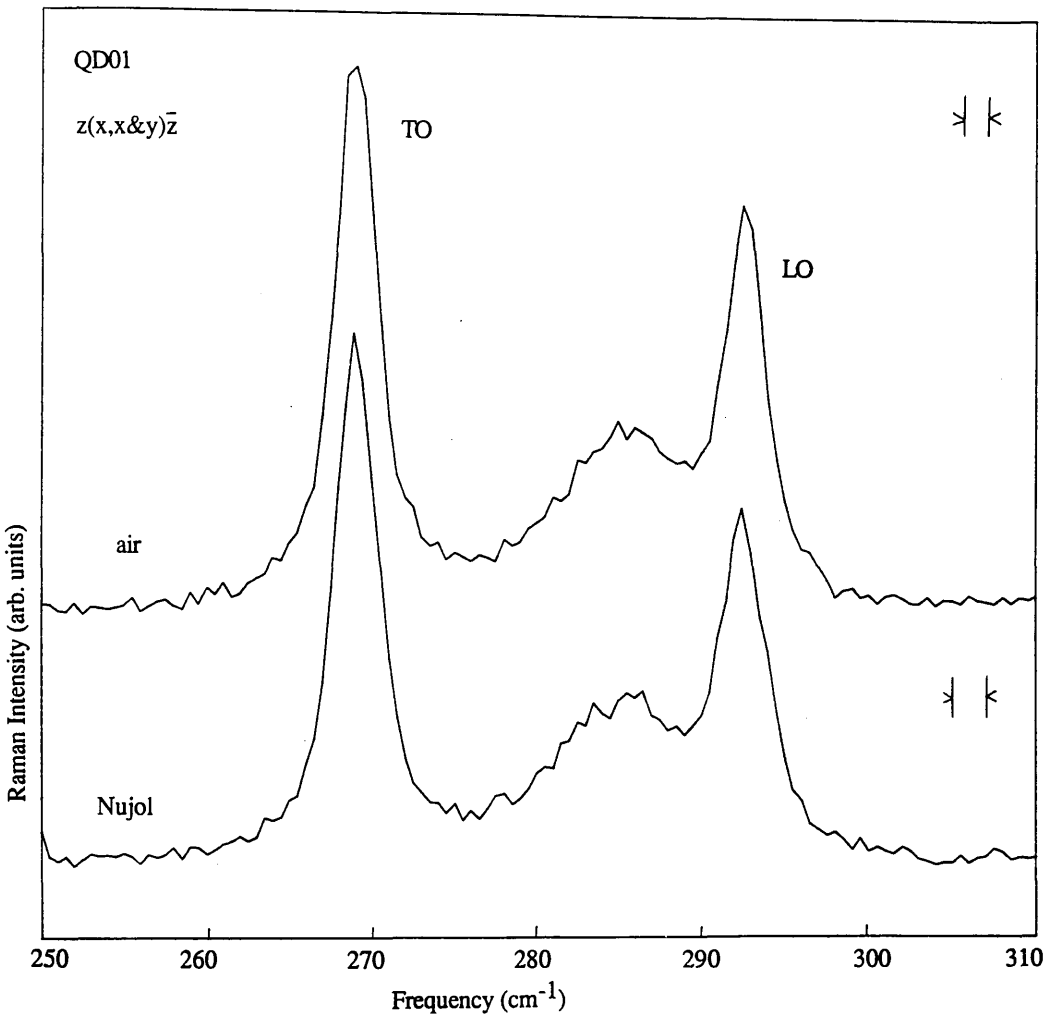

Figure 7.10 Raman spectra of QD01 surrounded by both air and Nujol. There is no measurable shift of the additional Raman feature. λ = 4880Å, resolution = 1.5 cm^{-1} (upper trace), 2.0 cm^{-1} (lower trace), room temperature.

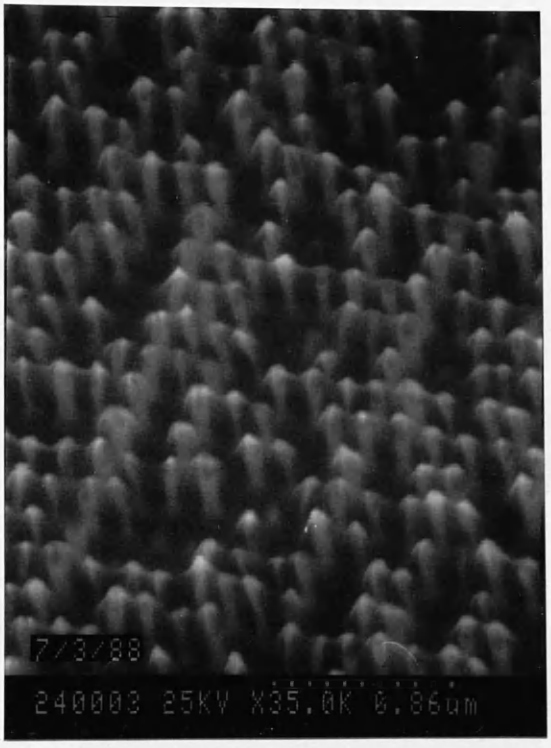

Figure 7.11(a) SEM micrograph of QD01 showing polyimide spun over the quantum cylinders. The polyimide can be seen to be coating the cylinders very well and to be penetrating between them.

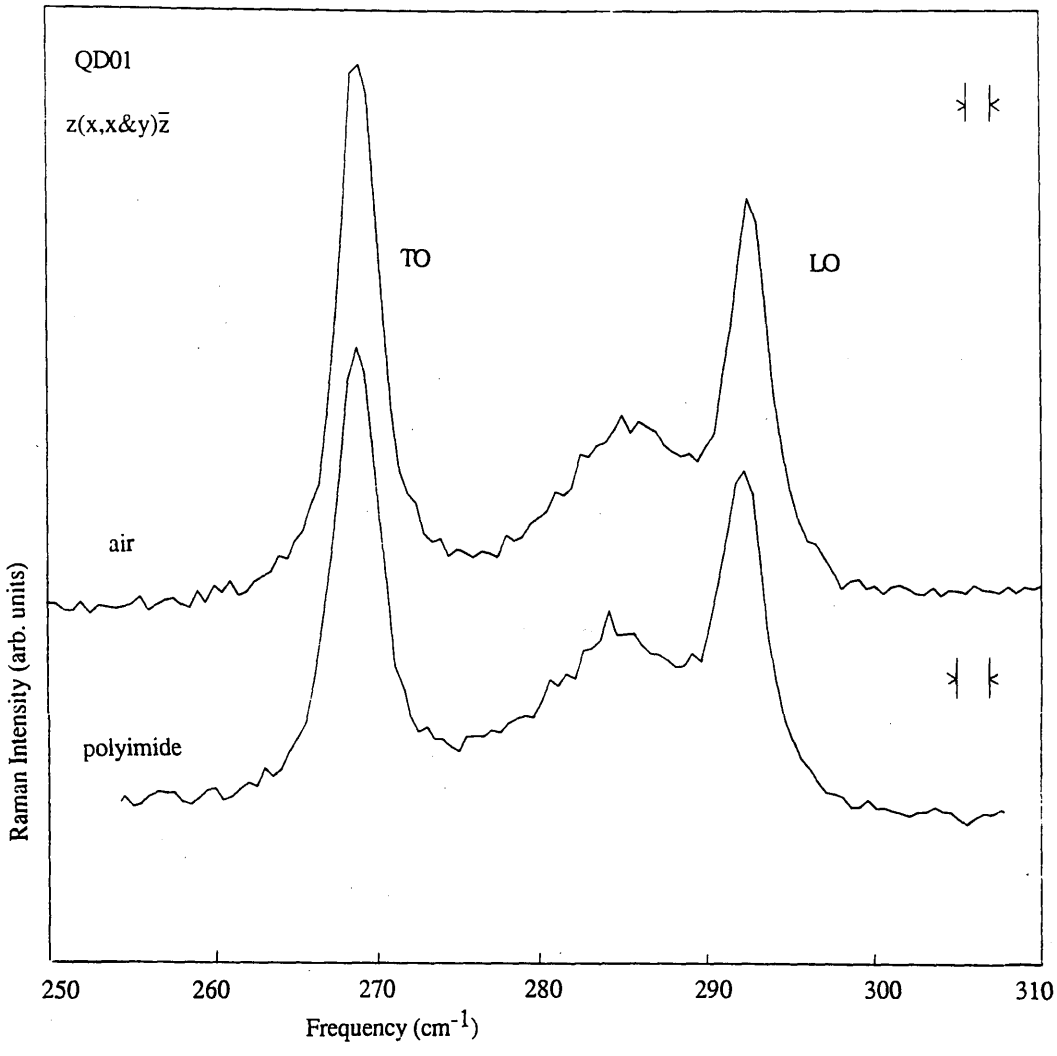

Figure 7.11(b) Raman spectra of QD01 with both air and polyimide surrounding the cylinders. There is no measurable shift of the additional Raman feature. λ = 4880Å, resolution = 1.5 cm^{-1} (upper trace), 2.0 cm^{-1} (lower trace), room temperature.

Sample QD07 was etched for 15 minutes in a concentrated solution of boiling HCl to remove the native oxide. It was then loaded into the cryostat which was rapidly pumped to vacuum level to prevent re-growth of the oxide layer. No change in the spectrum was observed (see figure 7.12).

Variation of the spectra with scattering geometry was investigated using QD12. As can be seen in figure 7.13, the nearly-backscattering geometry no longer holds good for these structured samples. The effect of the experimental geometry on the recorded spectra is shown in figure 7.14 for two scattering configurations. Here the spectra from the patterned area show a change in the intensity of the additional spectral feature as the scattering geometry changes. As the incident beam moves parallel to the cylinders, the additional spectral feature decreases in intensity and disappears. When the beam is almost at right angles to the cylinders, the intensity of the additional feature is greatest. This behaviour suggests that more efficient coupling to the source of the additional Raman feature is obtained when the beam is perpendicular to the cylinders.

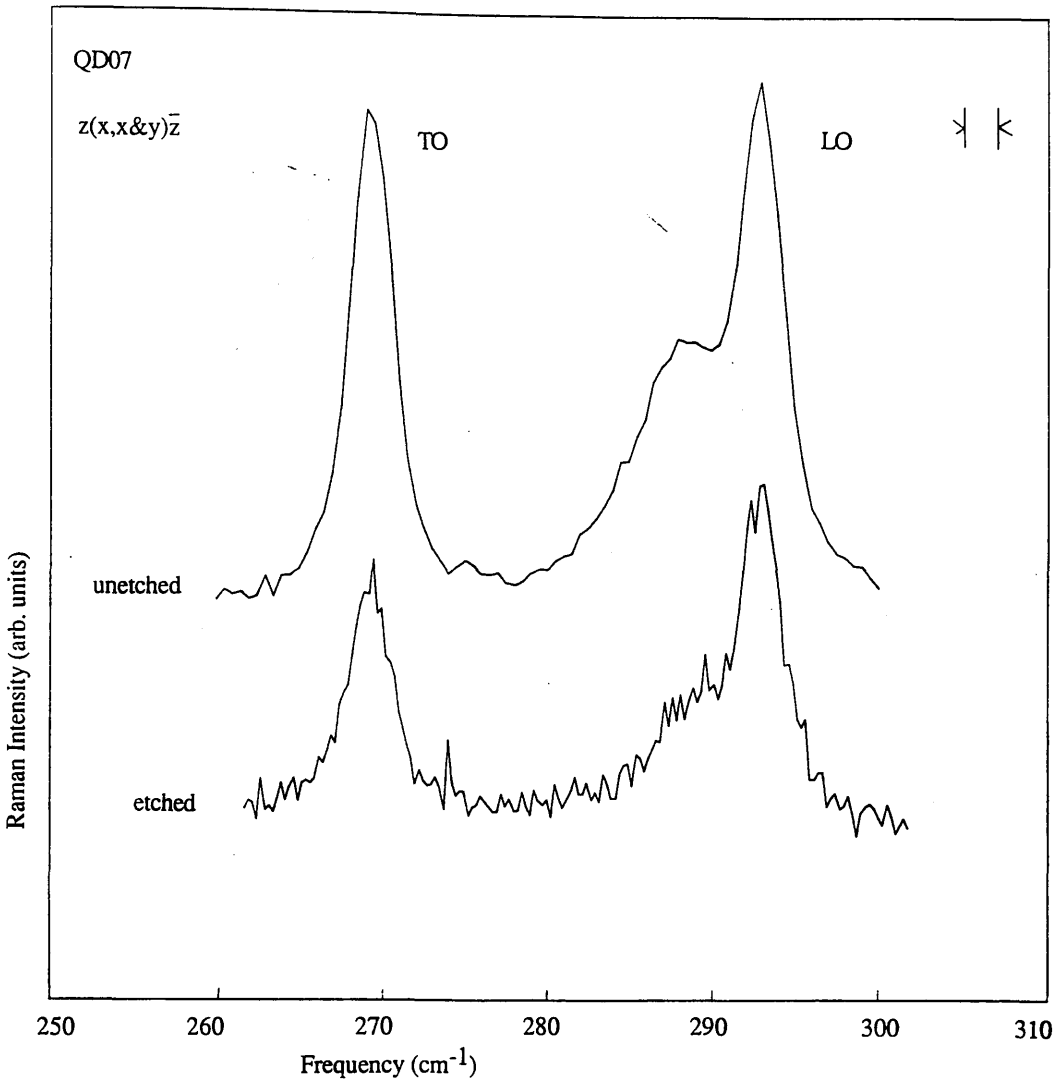

Figure 7.12 Raman spectra of QD07 both before and after etching off the native oxide. The etch procedure is described in the text. There is no measurable shift of the additional Raman feature. The lower trace is noisier than the upper trace because a) the count time per point was half and b) the signal was attenuated by the cryostat windows. λ = 4880Å, resolution = 2.0 cm^{-1}, room temperature.

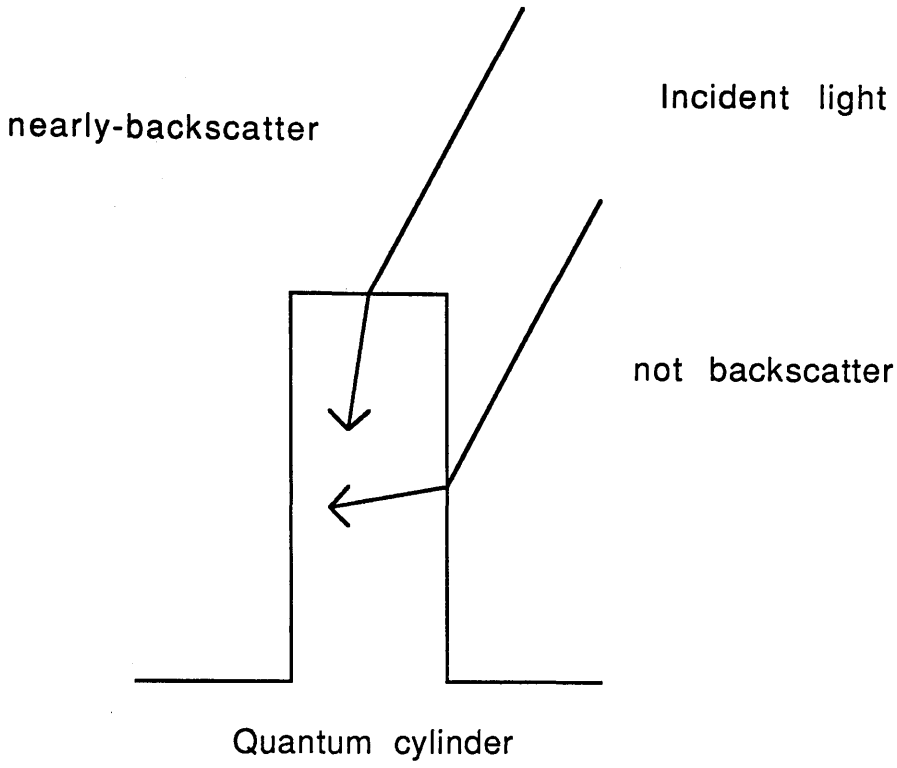

Figure 7.13 Schematic representation of the light path produced by a patterned surface in the nearly– backscattering geometry. It is clear that for light hitting the side of a cylinder, the approximation breaks down.

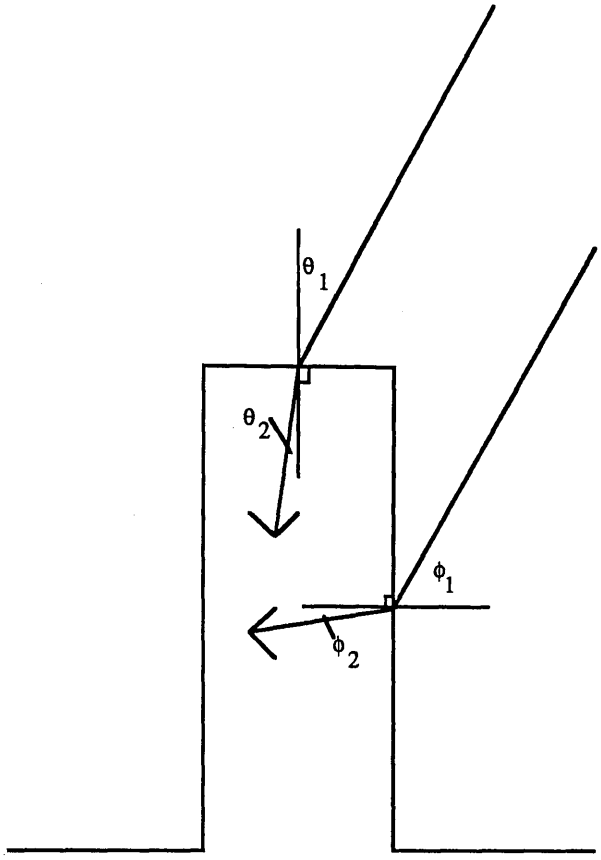

Figure 7.14(a) Definition of the angles used to record the spectra in 7.14(b)

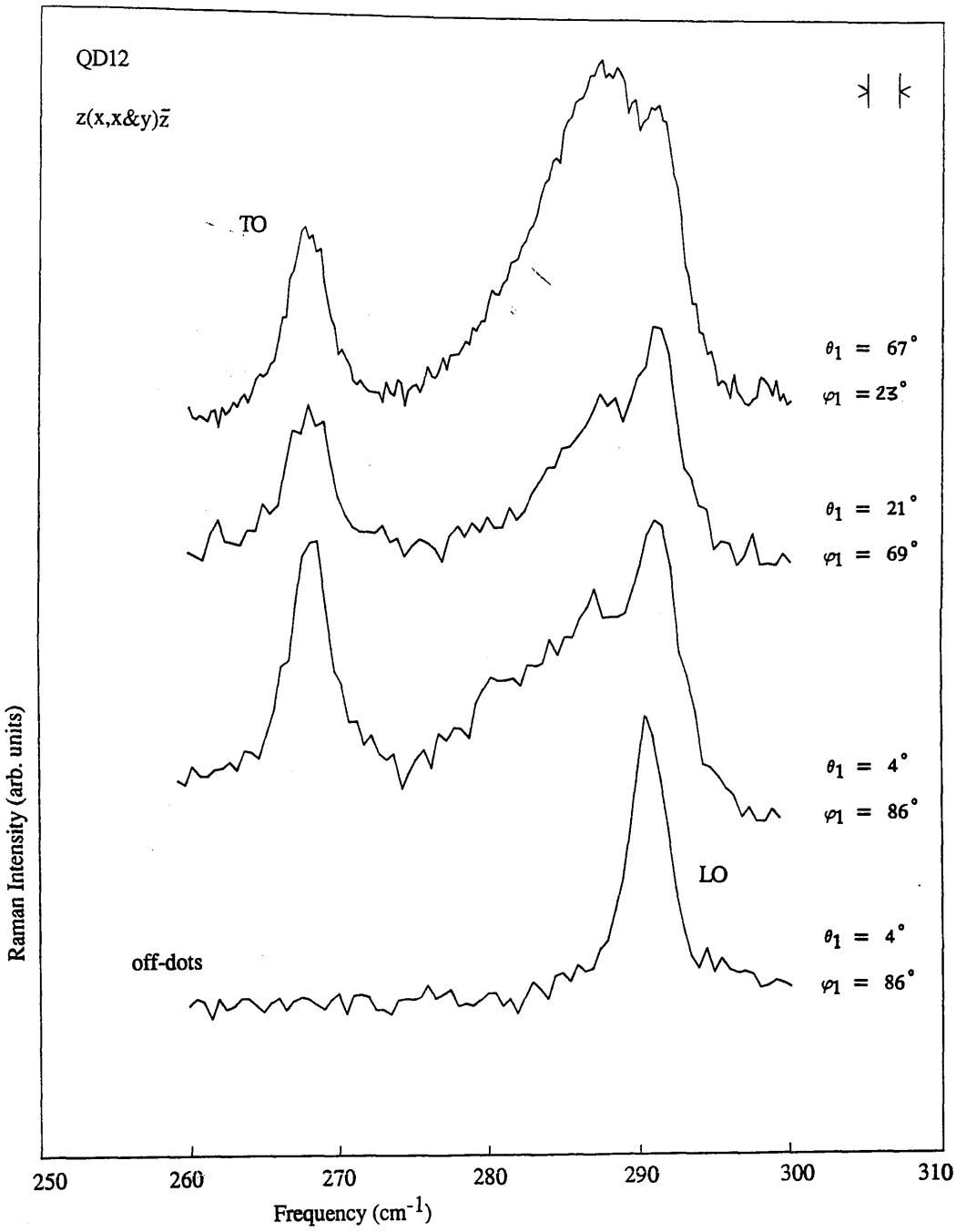

Figure 7.14(b) Raman spectra of QD12 for various scattering geometries. λ = 4880Å, resolution = 2.0 cm^{-1}, room temperature.

7.4 Discussion

Table 7.1 summarises the physical characteristics of the quantum cylinder samples studied. The samples are classified by their Raman spectra as given in the right hand column of the table. It can be seen that four of the five samples that gave a shoulder rather than a peak have cylinder diameters that are 1000Å or greater. This suggests that in these samples the cylinder size is not small enough to give rise to a well–defined spectral feature. The fifth sample, QD11, can be neglected as SEM micrographs showed that the cylinders had suffered severe undercut and were no longer vertical pillars. Of the two samples which showed no difference in the on–dots and the off–dots spectra, QD10 can be discounted as about 2/3 of the cylinders had fallen over as a result of very severe undercut. QD02 remains rather an anomaly as the cylinders were small (600Å) and vertical. It is possible that they were not etched sufficiently deeply (1500Å in comparison with >2100Å for the samples in category a) and that the cylinders were too short to sustain the mode corresponding to the additional spectral feature.

The three samples which showed the additional spectral feature have diameters of less than 1000Å (600, 600 and 800Å) and have etch depths in excess of 2000Å (2900, 2100 and 3100Å, respectively). They all have vertical or nearly–vertical sidewalls and therefore maintain the same diameter throughout the length of the cylinder. From these observations, it seems likely that any sample containing etched pillars of GaAs would show an additional feature in its Raman spectrum provided that (a) the cylinder was 800Å in diameter or smaller (b) the cylinder was 2000Å long or longer and (c) it had vertical sidewalls.

The next part of the discussion centres on the origin of the additional feature observed in the spectra of QD01, QD07 and QD12. The discussion will follow three paths: plasmon effects, amorphous or damage effects and surface phonon effects.

Table 7.1

Parameters of the Quantum Cylinder Samples

Number	Diameter (Å)	Height (Å)	Comment	Spectrum
QD01	600–1000	2900	Uneven sizes, Vertical	a
QD02	600	1500	Vertical	c
QD03	1000	1500	Vertical	b
QD06	1100	1400	Vertical	b
QD07	600	2100	Vertical	a
QD08	2000	5700	Vertical Etched 3 times	b
QD09	2000	4000	Vertical	b
QD10	600	2800	Undercut, 2/3 fallen over	c
QD11	600	2500	Undercut to 250Å at base	b
QD12	800	3100	Slightly undercut	a

Notes

a: Additional feature in the Raman spectrum of the on–dots area.

b: Shoulder to the LO mode and increased TO intensity in the Raman spectrum of the on–dots area.

c: No change in the Raman spectrum of the on–dots area.

7.4.1 Plasmon Effects

It has been suggested by Hansen and Kotthaus [1988(a)] that patterning the surface with a geometrically–regular pattern of the dimensions used here would cause modulations of the free electron gas near the surface of the sample thereby giving rise to resonances in the plasma oscillations. These effects have been observed with far infra–red transmission spectroscopy (FIR) in samples patterned with metallic gratings [Hansen and Kotthaus, 1988(b)]. The structured surface of the patterned samples affects the depletion layer across the sample and produces a corresponding modulation of the free electron gas. Several factors are sufficiently different between the experiments here and the work of Hansen and Kotthaus [1988(b)] to suggest that the extra Raman feature observed for some of the quantum cylinder samples is not plasmon–related.

The samples used by Hansen and Kotthaus were n^+ doped GaAs–AlGaAs heterojunctions with 2D carrier concentrations of $6x10^{11}cm^{-2}$. The samples were patterned with gratings of repeat distance 5000Å and wire widths of about 800Å. The plasma resonances were observed at temperatures of 2K and at frequencies in the 30 – 50 cm^{-1} range with full width at half maximum (FWHM) values of 5 – 8 cm^{-1}. By comparison, the samples used in this work were undoped bulk GaAs (except for QD01 which was n^+). The patterns that displayed the additional peak in the Raman spectrum had dot diameters of 600 – 800Å and separation about 3000Å. The additional feature was observed at room temperature and at around $286cm^{-1}$ with a FWHM of about $10cm^{-1}$. It therefore follows that the plasma density for these samples would be substantially lower than for the samples of Hansen and Kotthaus [1988(b)] because of the lower sample doping density. In addition, the modulated volume would be much less because of the much smaller surface area affected by the cylinders as opposed to the wires therefore the Raman scattering intensity can be expected to be small for such a small volume. It is worth

considering what might be expected if the results of Hansen and Kotthaus [1988(b)] were extrapolated to 0D.

When the 2DEG is squeezed from the 2D to the 1D regime by applying a negative gate voltage and squeezing the channel under the grating, the plasmon resonance is seen to move initially to lower energies as the channel is depleted and subsequently to higher energies as the channels begin to behave like an array of isolated electron channels. If the process were continued by squeezing the 1D channel into segments, via a cross–patterned grating, then the segments could be squeezed into dots (of about 700Å diameter). Since this confinement from 1D to 0D would be gradual and of the same order as the confinement from 2D to 1D, the shifts of the observed plasma frequency can be expected to be of the same order too (i.e. about 30 cm^{-1}). This size of shift would not put the plasma frequencies observed by Hansen and Kotthaus [1988(b)] into the optical phonon frequency range. As noted previously, since the carrier density is much lower in the samples studied here, the initial 2D plasma frequency can be expected to be lower and thus the observed resonances would be moved as a whole to lower energies. This would enhance the disparity in the frequencies observed in the two experiments.

Two other factors also make it unlikely that the additional Raman feature is plasmon–related. The first is the temperature of the measurement. The FIR measurements were taken at 2K therefore the electronic plasmon would be well–defined. At higher temperatures, the plasmon is expected to be thermally broadened. The room–temperature Raman FWHM, however, is of the same order as the 2K FIR FWHM thus demonstrating no thermal broadening effects and suggesting that its origin does not lie with a plasma excitation. The second factor is the fact that the additional Raman feature is only apparent for very small cylinders. A plasmon effect would be expected to be observed for all cylinder sizes and indeed more strongly for the larger cylinders because of the larger scattering volume and greater modulation of the free electron gas. Non–vertical sidewalls on the cylinders

and cylinder height could be expected to have no significant effect on the formation of a modulated plasma. It seems reasonable to conclude that the additional Raman feature does not arise from modifications to the plasmons of the free electron gas.

7.4.2 Amorphous or Damage Effects

It has been suggested [Sapriel, 1987] that the additional Raman feature observed in the spectra of the small quantum cylinder samples could be an amorphous signal from a damaged layer resulting from the RIE processing. This is unlikely to be the case for the reasons discussed below.

In the study of RIE–induced damage (see chapter 6), no evidence was found that the processing produced an amorphous layer on the sample surface. Indeed, the data suggested that with optimised RIE conditions (such as were used here) minimal damage would occur to the crystal structure. This can be seen to be the case for these samples by considering the off–dots spectra (see figure 7.9). The method used to produce the patterned areas involved producing a mask of dots and etching the whole sample surface to produce the quantum cylinders. This is shown in figure 7.15. Any damage due to the RIE could therefore be expected to show up in both the on–dots and the off–dots spectra. Figure 7.9 shows clearly that the additional Raman feature is present only in the on–dots spectra and that the off–dots spectra show little evidence of crystalline damage. Specifically, the LO mode has neither broadened nor softened and the symmetry–forbidden TO mode is weak.

The additional Raman feature cannot be explained by the theoretical predictions of Tiong et al [1984] for a damage–induced shift of the LO mode. Their prediction is that a $\Delta\omega_{LO}$ of about $7cm^{-1}$ to lower energies should correspond to a peak with FWHM of about $21cm^{-1}$ (the peaks in figure 7.9 have FWHM in the range 8 – 10 cm^{-1}). The theory also predicts that broadening of the LO mode to a FWHM

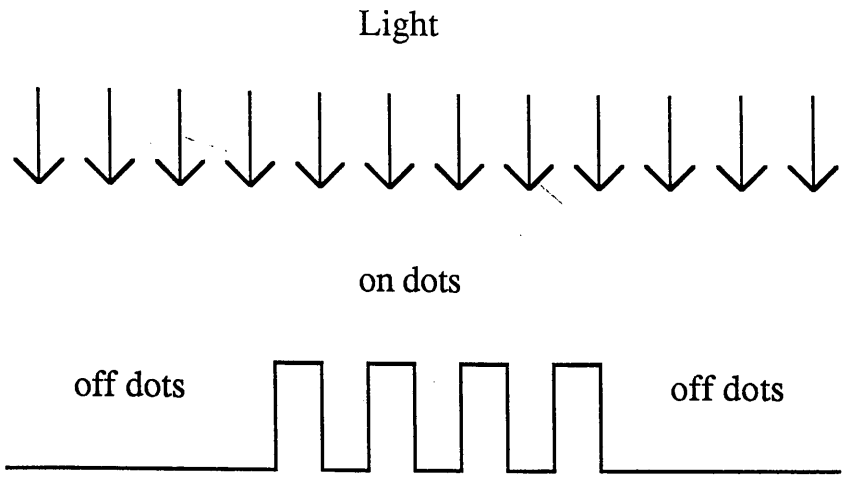

Figure 7.15 Schematic representation of a quantum cylinder sample showing the patterned area (on dots) and the unpatterned area (off dots). It can be seen that the off dots area has also been subjected to RIE.

of 8 – 10 cm^{-1} should result in a corresponding shift of $\triangle\omega_{LO}$ of less than 4.5cm^{-1}. As a comparison, Nakamura and Katoda [1984] ion implanted GaAs with $10^{16}cm^{-2}$ of 175 keV Si^{+} and observed a shift of the LO mode from 291 to 286 cm^{-1}. At this implantation level, however, they also observed strong, broad spectral features at 80, 175 and 250 cm^{-1} which were comparable in intensity with the softened LO mode. These broad features can be regarded as contributions from an amorphous region of the sample as they reflect very well the amorphous spectral features shown in figure 6.1. A Raman spectrum of QD01 was recorded in the region 25 – 310 cm^{-1} in order to look for evidence of these low energy amorphous modes and this spectrum is shown in figure 7.16. It can be seen that there is no evidence of broad, low energy amorphous modes. The sharp low energy features are identified as Raman scattering from air surrounding the sample. This identification is based on a comparison of the Raman spectra of the rotations of N_2 and O_2 bonds obtained by Weber et al [1967] (see figure 7.17) and the theoretical energy level calculations by Herzberg [1945]. These calculations give an energy displacement of 7.99cm^{-1} and 11.50cm^{-1} for the rotational energies of the N_2 and O_2 bonds respectively. The sharp air–induced Raman lines are not superimposed on any broad background structure as it can be seen that the background level is flat from 25 – 260 cm^{-1}.

In summary, the additional Raman feature cannot be identified as an amorphous spectral contribution because the spectrum of amorphous GaAs would contain a broad band reflecting the phonon density of states and this is observed in none of the samples studied here.

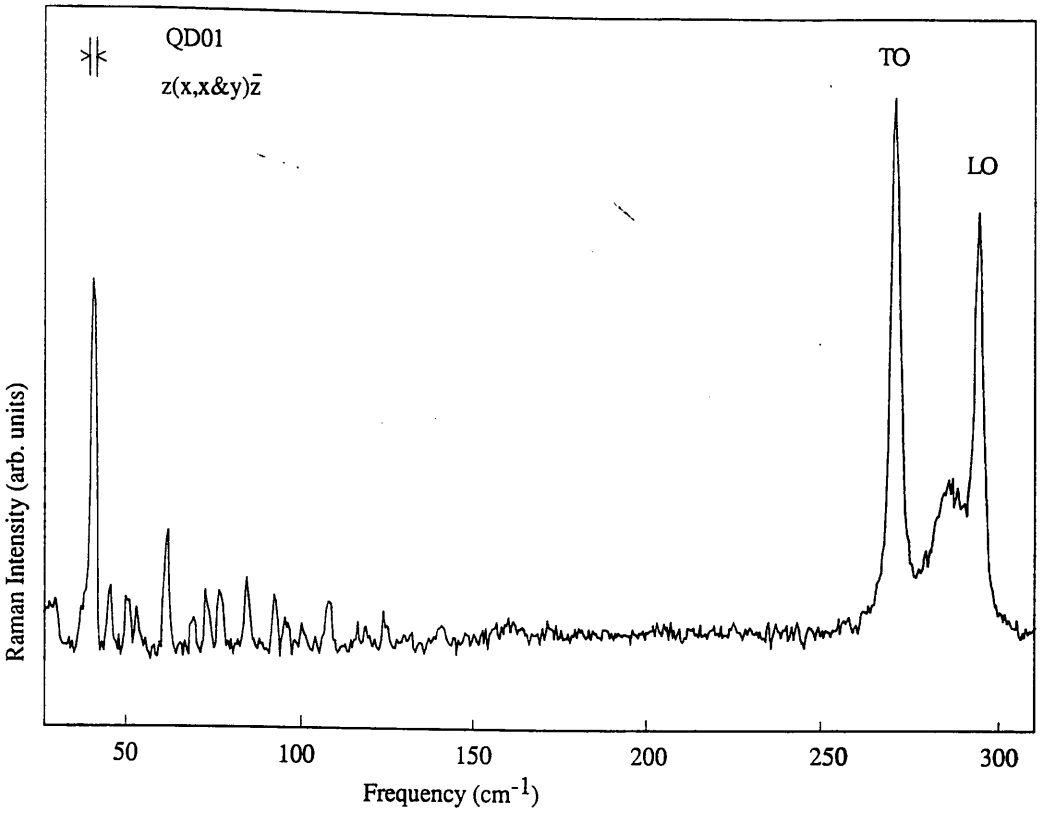

Figure 7.16 Raman spectrum of QD01 from 25 to 310 cm^{-1}. λ = 4880Å, resolution = 2.0 cm^{-1}, room temperature.

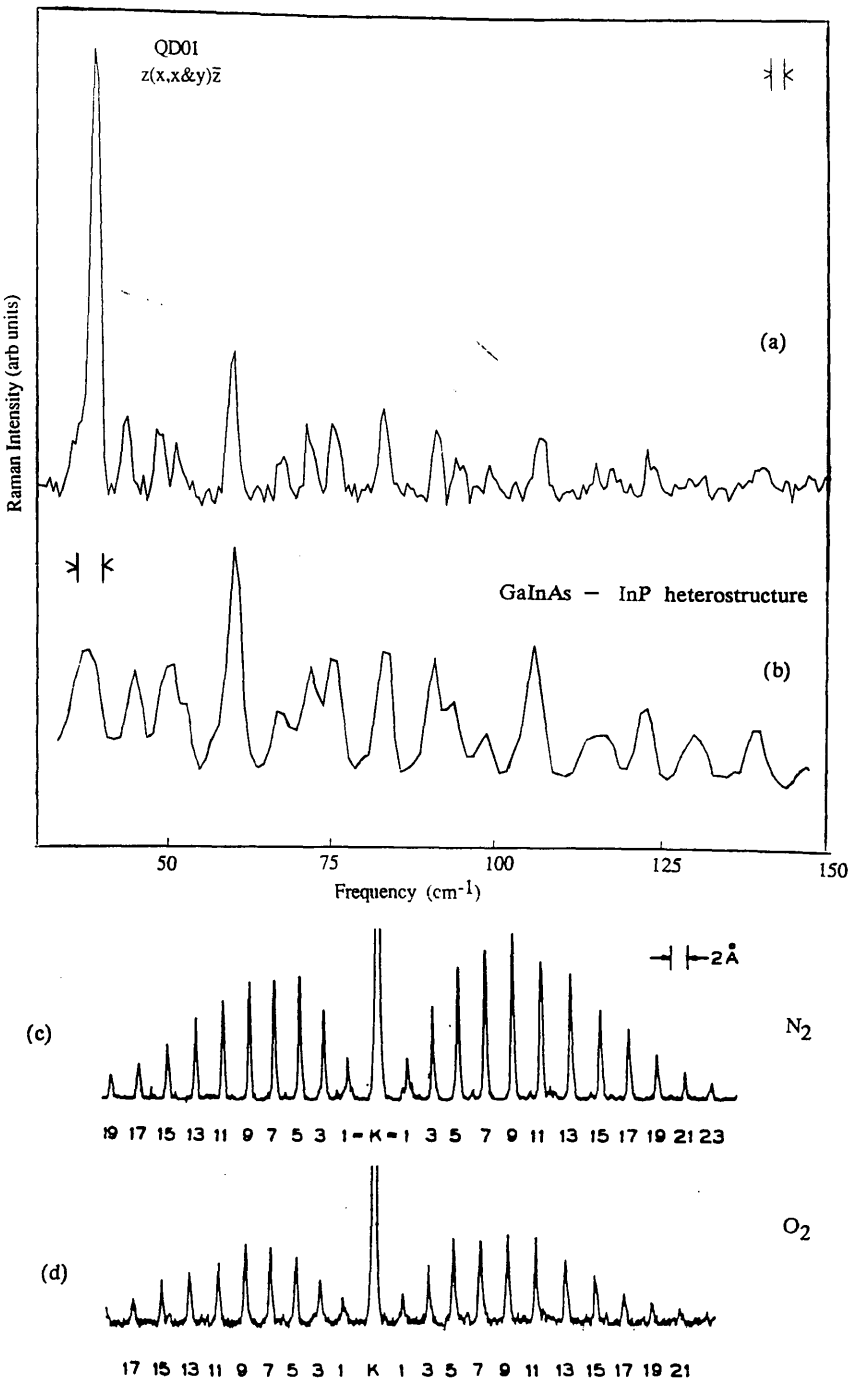

Figure 7.17

(a) Low energy region of the Raman spectrum of QD01 from 30 to 150 cm^{-1}. λ = 4880Å, resolution = 2.0 cm^{-1}, room temperature.

(b) Raman spectrum from PMB121, a GaInAs– InP heterostructure (see chapter 5) showing the same features as observed in (a). λ = 4880Å, resolution = 5.0 cm^{-1}, room temperature.

(c) & (d) Stokes and Antistokes Raman spectra of N_2 and O_2 respectively showing the rotational modes labelled by their k numbers. If the frequencies are measured, they compare very well with those observed in (a) and (b) above.
[after Weber et al, 1967]

7.4.3 Surface Phonon

This section discusses the experimental evidence for and against the identification of the additional Raman scattering feature as a surface phonon mode of the GaAs pillars. The experimental data is plotted on the graph of theoretical surface mode frequency as a function of cylinder radius showing good agreement (see figure 7.18). The error bars in figure 7.18 arise from the uncertainty in the radius which is dependent on the accuracy with which the SEM micrographs can be measured and the uncertainty in the frequency which depends on the spectral resolution.

The experiments described in section 7.3 had the aim of demonstrating a shift to lower energy of the additional Raman feature as the dielectric constant of the surrounding medium was increased. It is possible that each cylinder may consist of a core material covered by several layers: the core being crystalline GaAs covered by an etch–deposited layer (discussed below) and further covered by a native oxide layer. In this case, the additional Raman feature might arise from the interface between the GaAs and the etch–deposited layer, the interface between the etch–deposited layer and the oxide or the oxide–air interface. The experiments of section 7.3 remove the possibility that the oxide layer participates in the appearance of the additional Raman feature but do not investigate the role of any etch–deposited layer.

It is possible that all the sample surfaces were coated with an etch–deposited layer. No evidence for such a layer has been seen in the Raman spectra but other evidence does exist with regard to QD08. This sample was reactive–ion–etched three times. It was removed from the etch chamber to allow the Raman spectra to be recorded for different etch depths of the same sample. The cylinder diameter did not change during the second or third etch stages, in contrast to a sample which was etched to the same depth but in one stage. This latter sample suffered severe

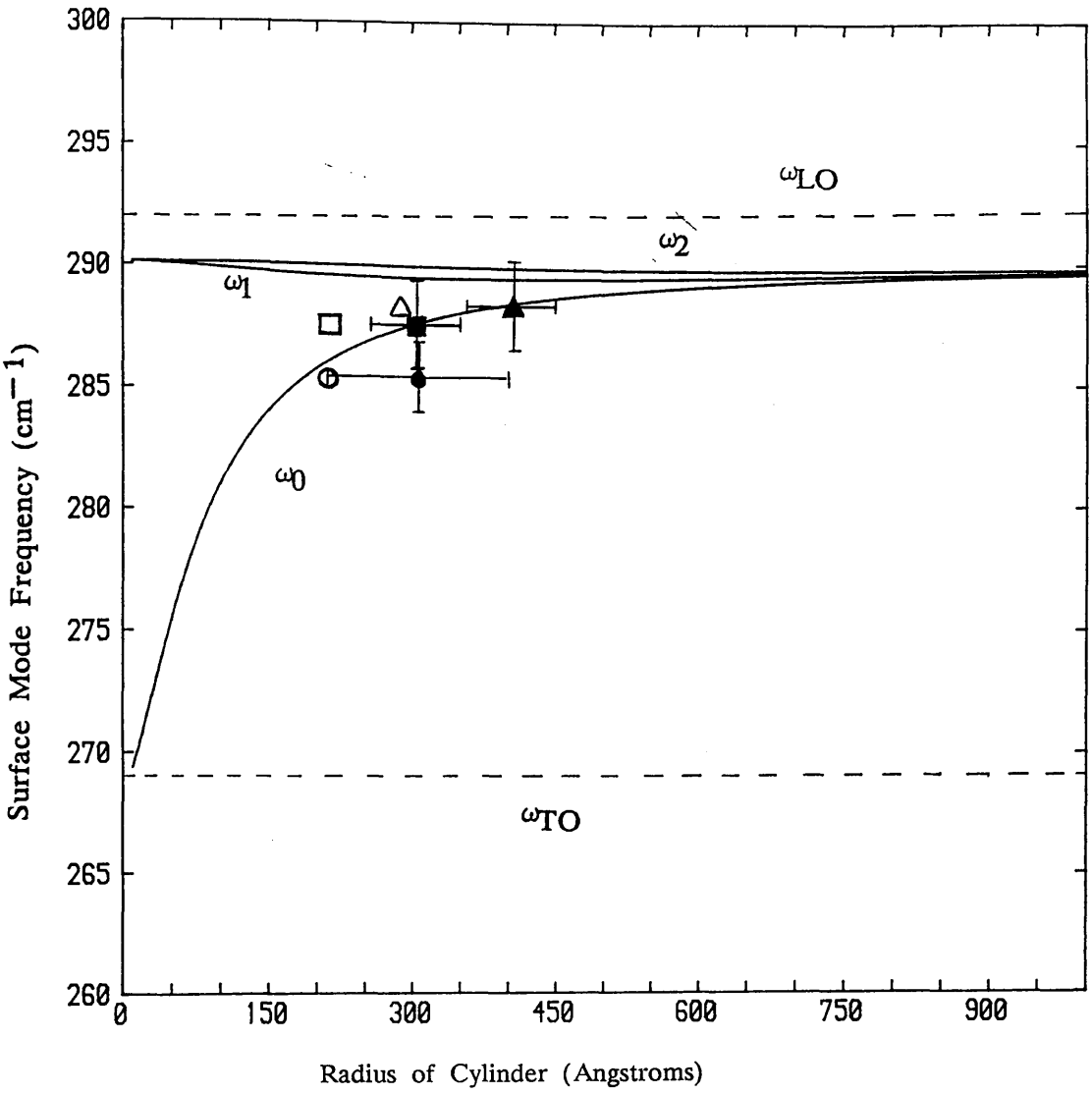

Figure 7.18 This is a plot of the experimental data points of the additional Raman feature and the theoretical calculations for the surface phonon frequency. The circles represent QD01, the squares, QD07 and the triangles, QD12. The theory was calculated using equations 7.1 and 7.2 with $\cos\theta = 1/\sqrt{2}$, where θ is the angle of incidence. In order to account for experimental deviations from this, the solid symbols correspond to the measured radii while the open symbols are plotted using cylinder radii which have been scaled to compensate for a $\cos\theta$ value of 1. It can be seen that the agreement between theory and experiment is good.

undercut. The implication of this result is that removing the sample from the etch chamber enabled a chemical reaction with the air which formed a protective coating on the sidewalls of the cylinders. This protective coating was sufficiently hard to prevent significant lateral etching of the already–etched portions of the dots during subsequent etching. It is possible that the coating contained Chlorine as Hu and Howard [1984] observed excess Chlorine adhering to the sidewalls of GaAs samples reactive–ion–etched with Cl_2 gas by using Auger electron spectroscopy techniques. If such a coating were present, it would obviously affect the properties and behaviour of a surface phonon mode and might thereby explain the observation that the frequency of the additional Raman feature did not change when the dielectric constant of the surrounding medium was altered.

Figure 7.14 showed the effect of changing the angle of incidence of the exciting laser beam with respect to the sample surface. Englman and Ruppin [1968] derived an expression for a surface phonon with three degenerate orthogonal modes. In cylindrical co–ordinates, these correspond to modes that vibrate in the r, θ and z directions as shown in figure 7.19. Light incident parallel to the cylinders would couple only to the vibrations oscillating in the z direction. Light incident at right angles to the cylinder, would couple to both the oscillations in the r direction and those in the θ direction (see figure 7.20). This suggests that a stronger intensity would be expected from a right–angle scattering geometry thus agreeing with experimental observations. The reason for the loss of intensity in true backscattering geometry can be related to the low absorption of photons in the appropriate direction. In figure 7.8(c), the SEM micrograph of QD12, it can be seen that the top of each pillar is not flat. Each cylinder has a conical cap of etch mask left after the dry etching process. If the effect of these residual etch masks is considered with regard to the light coupling, then it would appear that much of the light that is incident parallel to the cylinders may be reflected from the etch masks (see figure 7.21). This would drastically reduce the number of photons absorbed into the surface

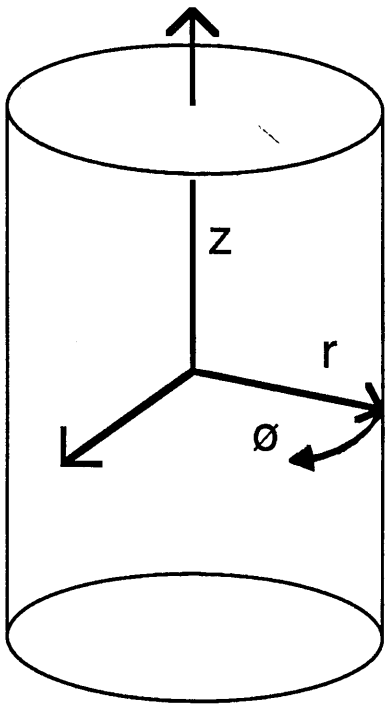

Figure 7.19 Schematic representation of the cylindrical co-ordinate system showing the directions of vibration of the three surface modes.

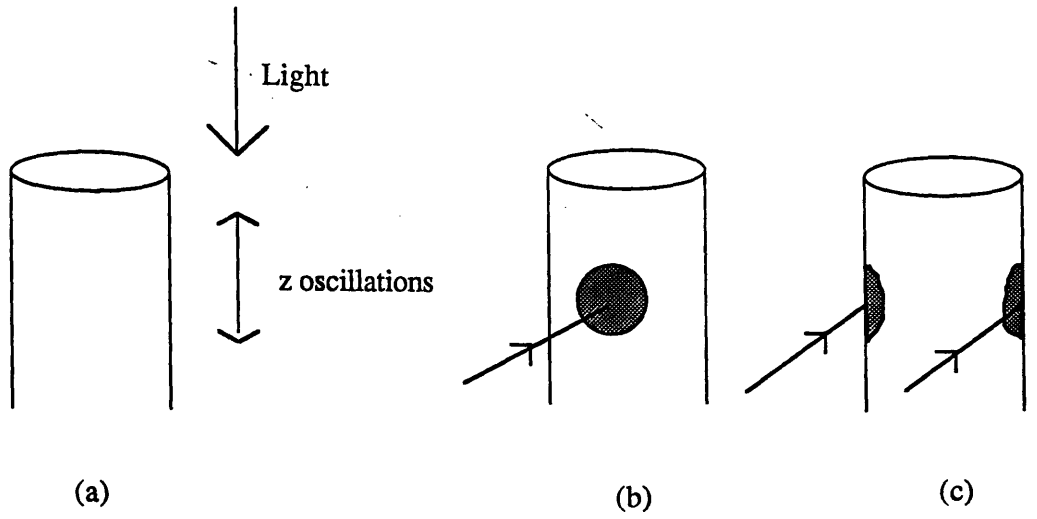

Figure 7.20 Schematic representation of the various ways in which light can couple to the surface modes. Light incident vertically can only couple to the z oscillations (a). Light incident horizontally can couple to both the r oscillations (b) and the θ oscillations (c) by simultaneously illuminating the whole side of a cylinder.

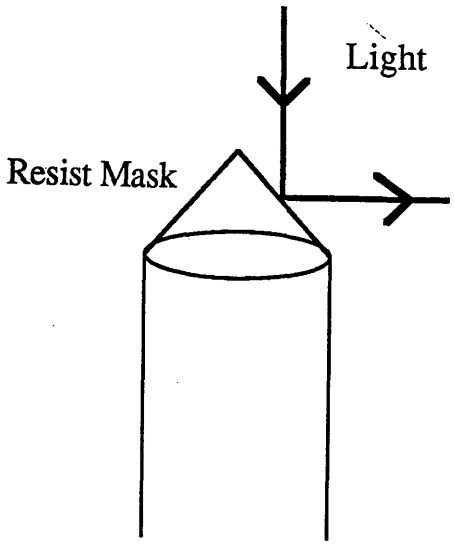

Figure 7.21 Schematic representation of how light incident normal to the surface might be reflected by the residual resist mask.

of the cylinders and therefore reduce the scattering intensity. This would explain the fact that the spectra obtained in the true backscattering geometry show a loss of the additional Raman feature rather than a reduced intensity as would otherwise have been expected.

7.4.4 Conclusions

Three possible origins of the additional feature observed in the Raman spectra of very small quantum cylinders have been considered. A plasmon contribution has been discounted because a) the frequency of the observed Raman feature does not correspond to the expected frequency of a plasmon–phonon interaction in these particular samples and b) the temperature of the Raman scattering experiments is too high to allow observation of a well–defined plasmon–related feature. A contribution from an amorphous layer has also been rejected as a possible source of the additional Raman feature based on two facts: a) spectra of amorphous GaAs exhibit several strong, broad features not observed here and b) the optimised RIE conditions used would be unlikely to produce amorphisation of the sample surface. The third possibility considered was that of a surface phonon of the quantum cylinders. This is the most likely option although positive identification has not been made. The experimentally–observed frequencies were found to be in good agreement with the theoretically–predicted frequencies of an infinite cylinder. The change of intensity of the additional spectral feature with angle of incidence can also be well explained by regarding the mode as a surface phonon.

Positive identification of the additional feature in the Raman spectrum as a surface phonon can only be made if the mode is seen to move with varying external surrounding media. In this context, the next work to be done in this area should involve investigations of the possible surface layer which is preventing coupling of

the mode to the external media. This could consist of, for example, more experiments on coating the cylinders ensuring that the samples are thoroughly cleaned and wet–etched between RIE and coating. One of the methods that will be used to change the dielectric constant of the surrounding medium will be overgrowth of the samples with Silicon nitride. It is intended to obtain and study polarisation analysed Raman spectra to investigate further the coupling of the incident light to the surface modes. It is also hoped to fabricate smaller diameter cylinders since smaller masks can now be made using the new electron microscope that is being commissioned at present. This work will be done in conjunction with H E G Arnot.

In the context of device applications (such as the quantum dot laser), the low level of damage implicit in the observation of a surface phonon suggests that the processing of such structures has reached a sufficiently advanced level for the fabrication of working devices to be feasible. Consideration of all the other characterisation techniques, both optical and electrical, suggests that Raman scattering is uniquely able to investigate the crystallinity of fabricated nano–structures.

M Abramowitz and I A Stegun, editors; "Handbook of Mathematical Functions", published by Dover Publications Inc. N.Y., 1965; p358

H E G Arnot; Second year PhD report, Glasgow University, 1988

D E Aspnes and A A Studna; Phys Rev B27, 985, 1983

Ciba–Geigy Corporation; Datasheet on Polyimide XU 218, published by Ciba–Geigy Corporation, New York, 1983

J Cibert, P M Petroff, G J Dolan D J Werder S J Pearton A C Gossard and J H English; Superlatt Microstr 3, 35, 1987

R Englman and R Ruppin; Phys Rev Lett 16, 898, 1966

R Englman and R Ruppin; J Phys C1, 614, 1968

H Froehlich; "Theory of Dielectrics", published by Clarendon, Oxford, 1949; p32

R Fuchs and K L Kliewer; Phys Rev 140, A2076, 1965

W Hansen and J P Kotthaus; Private Communication, 1988(a)

W Hansen and J P Kotthaus; in "Physics and Technology of Submicron Structures" Springer Series in Solid State Sciences Vol 83, edited by H Heinrich, G Bauer and F Kuchar, published by Springer–Verlag, Berlin, Heidelberg, 1988(b); p187

S Hayashi and H Kanamori; Phys Rev B26, 7079, 1982

G Herzberg; "Molecular Spectra and Structure Volume 2", published by Van Nostrand, New York, 1945; p133

E L Hu and R E Howard; J Vac Sci Technol B2, 85, 1984

Inspec; "Properties of GaAs: EMIS Datareview No. 2", 1986; section 8.2

C Kittel; "Introduction to Solid State Physics", 5th edition, published by John Wiley & Sons, New York, 1976; p289

J C Luong; Superlatt Microstr 4, 385, 1988

T Nakamura and T Katoda; Jpn J Appl Phys 23, L552, 1984

T Okada, H Sasaki, S Hayashi, S S Kim and K Yamamoto; Sol St Comm 61, 671, 1987

A Pinczuk, M G Lamont and A C Gossard; Phys Rev Lett 56, 2092, 1986

W H Press, P B Flannery, S A Teukolsky and W T Vetterling; in "Numerical Recipes:The Art of Scientific Computing", published by Cambridge University Press, 1986; p176

R Ruppin and R Englman; Rep Prog Phys 33, 149, 1970

J Sapriel; Private Communication, 1987

H Temkin, G J Dolan, M B Panish and S N G Chu; Appl Phys Lett 50, 413, 1987

R Uyeda; J Cryst Growth 24/25, 69, 1974

A Weber, S P S Porto, L E Ceesman and J J Barrett; J Opt Soc Am 57, 19, 1967

CHAPTER 8

TRIPLE CRYSTAL X-RAY EXPERIMENTS

8.1 Introduction

In 1913, it was first observed by Bragg and Bragg that crystalline substances give characteristic x-ray scattering patterns that do not appear in similar experiments on liquids. This phenomenon was explained by a diffraction mechanism in which the crystal was assumed to consist of regularly-spaced atoms in a periodic array. X-rays scattered by any atom in the array would interfere, either constructively or destructively, with scattered radiation from all the other atoms. The perodic nature of the crystal would impose what is now known as the Bragg condition for constructive interference:

$$n\lambda = 2d\sin\theta \tag{8.1}$$

where λ is the wavelength of the incident x-rays, n is the order of diffraction and $2d\sin\theta$ is the path difference between the two rays as defined in figure 8.1. In this way, the reflected or diffracted pattern is built up according to the crystalline structure. Since the Bragg condition relates the spatial positions of the intensity maxima of the diffracted pattern to the lattice constant, this latter can be evaluated

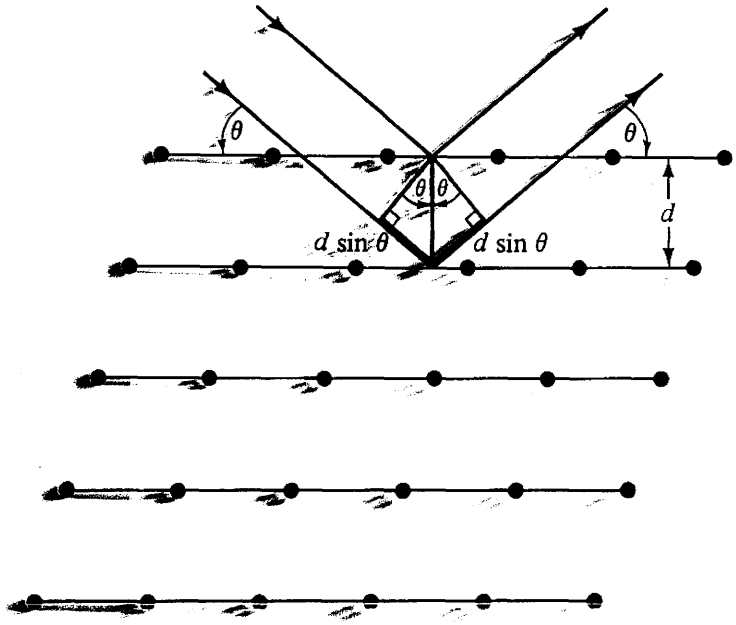

Figure 8.1 Schematic representation of a Bragg reflection from a particular family of crystal lattice planes separated by a distance d. Incident and reflected rays are shown for the two neighbouring planes. The path difference is $2d\sin\theta$. [After Ashcroft and Mermin, 1976]

from experimental data. It is the assimilation of the lattice constants measured for various scattering directions which gives the full crystal structure.

X– ray diffraction is now a widely– used technique. One specialised application of its use has been the study of semiconductor superlattices via rocking curve measurements. In this case, the superlattice has an additional periodicity, superimposed on the lattice constant, which produces additional Bragg reflection conditions. These act as a modulation on the diffraction pattern observed from a sample without the superperiodicity. A rocking curve is obtained by measuring the intensity modulation of a single Bragg peak. From this it is possible to determine both the thickness of each of the repeated layers in the superlattice and the composition of the layers. The experimental apparatus required to record rocking curves is shown in figure 8.2. Here it can be seen that a double crystal diffractometer is used. The first crystal is a reference substrate, usually of Si(111) or Ge(111), encased in a housing with an exit slit. This can be regarded as a monochromator as one of the main Bragg reflections of this crystal is used to select one of the lines of the x– ray source and reject everything else including the Bremsstrahlung radiation. The monochromatic beam is then incident on the sample which is the second crystal. The beam is diffracted from the sample and passes through a slit to a detector (either a proportional or a scintillation counter). It is usually found to be easier to move (or rock) the sample and keep the detector fixed while recording the rocking curve.

A typical rocking curve is shown in figure 8.3 for a 100 period multi– quantum well of GaInAs– InP. Here, the central peak is due to diffraction from both the substrate and the average lattice parameter of the overgrown layer. The splitting of the peak shows that the epitaxially– grown layer does not have exactly the same lattice constant as the substrate. The small satellite peaks are due to the superlattice periodicity. The composition of the GaInAs, can be deduced from the measured lattice constant. For other, more difficult, material systems (e.g. GaAs– AlGaAs) this

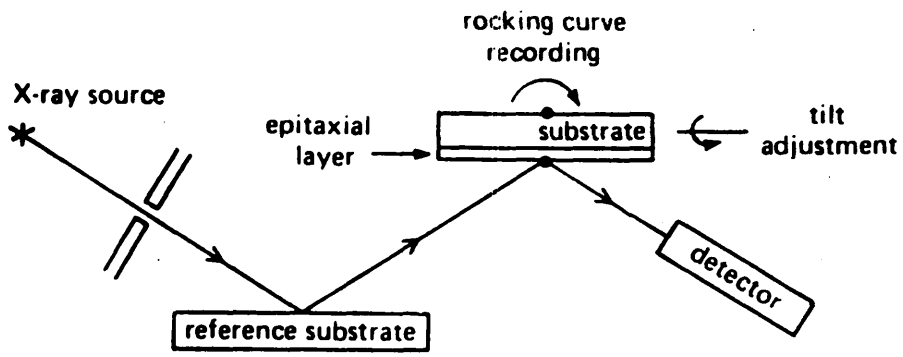

Figure 8.2 Schematic representation of a double crystal diffractometer suitable for recording rocking curves. [After Halliwell et al, 1985]

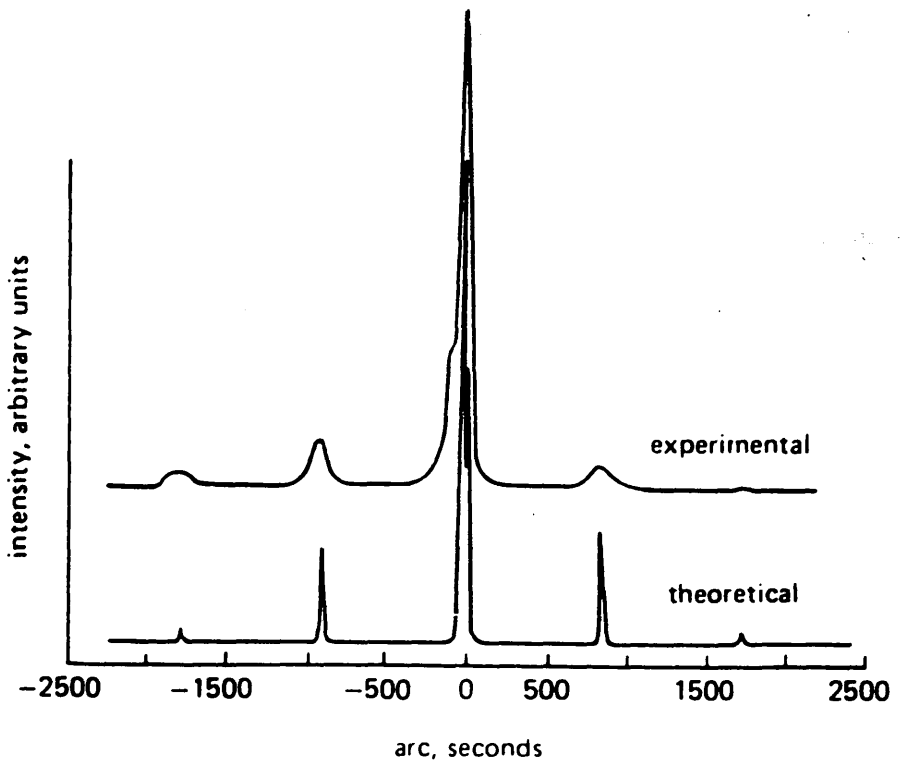

Figure 8.3 Experimental and theoretical rocking curves for a multi quantum well of 100 periods of GaInAs– InP (of layer thicknesses 112 and 76 Å respectively) on an InP substrate. The satellites are the small peaks to either side. The split of the central peak shows a lattice mismatch between the epitaxial layer and the substrate. The theoretical curve is a fit by the authors.
[After Halliwell et al, 1985]

information can still be obtained. Although the lattice constant does not vary by more than 0.2% from GaAs to AlAs, resolutions of 20ppm (i.e. 0.002%) can be attained [Halliwell et al, 1985] thus resolving the AlGaAs composition to the nearest 1%.

Double crystal diffractometry lacks sensitivity when investigating single layers thinner than 1000Å. Using a triple crystal diffractometer, however, it is possible to measure the thickness of layers down to a few hundred Angstroms.

The triple crystal diffractometer is an extension of the double crystal diffractometer. A third crystal is placed after the sample and performs the function of an analyser. This is shown schematically in figure 8.4. The effect of the third crystal is to remove the spatial dependence of the scattered beam. This works because the analyser intercepts all the scattered beam, unlike a slit, thus an analyser crystal can improve resolution without loss of intensity. This means that only the direction and energy of the scattered beam affect the detected signal. Easier analysis of the diffracted pattern and better resolution result since contributions to the detected signal from effects such as the source size, intensity distribution and beam penetration are eliminated. The construction, operation and resolution of a triple crystal diffractometer are discussed fully by Ryan [1986].

The geometry used for a triple crystal diffraction experiment is such that some of the Bragg reflections are blocked by the crystal orientation. This eliminates the number of reflections that are accessible as depicted in figure 8.5.

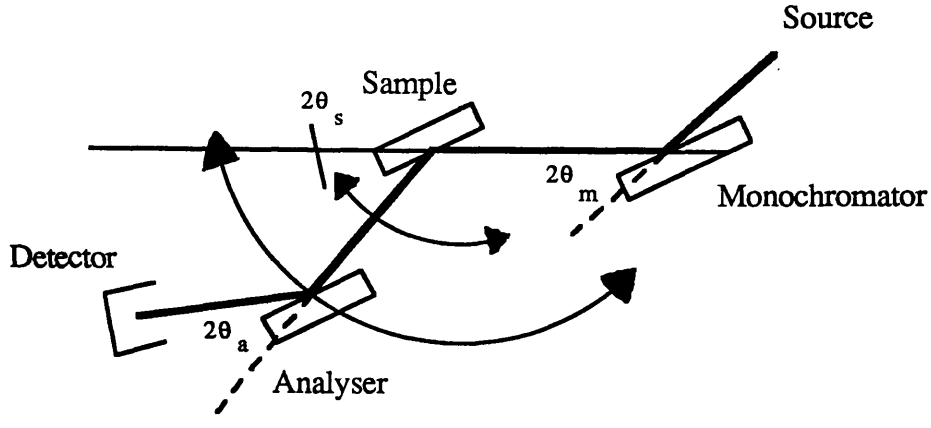

Figure 8.4 Schematic of the essential elements of a triple crystal diffractometer as given by Ryan [1986].

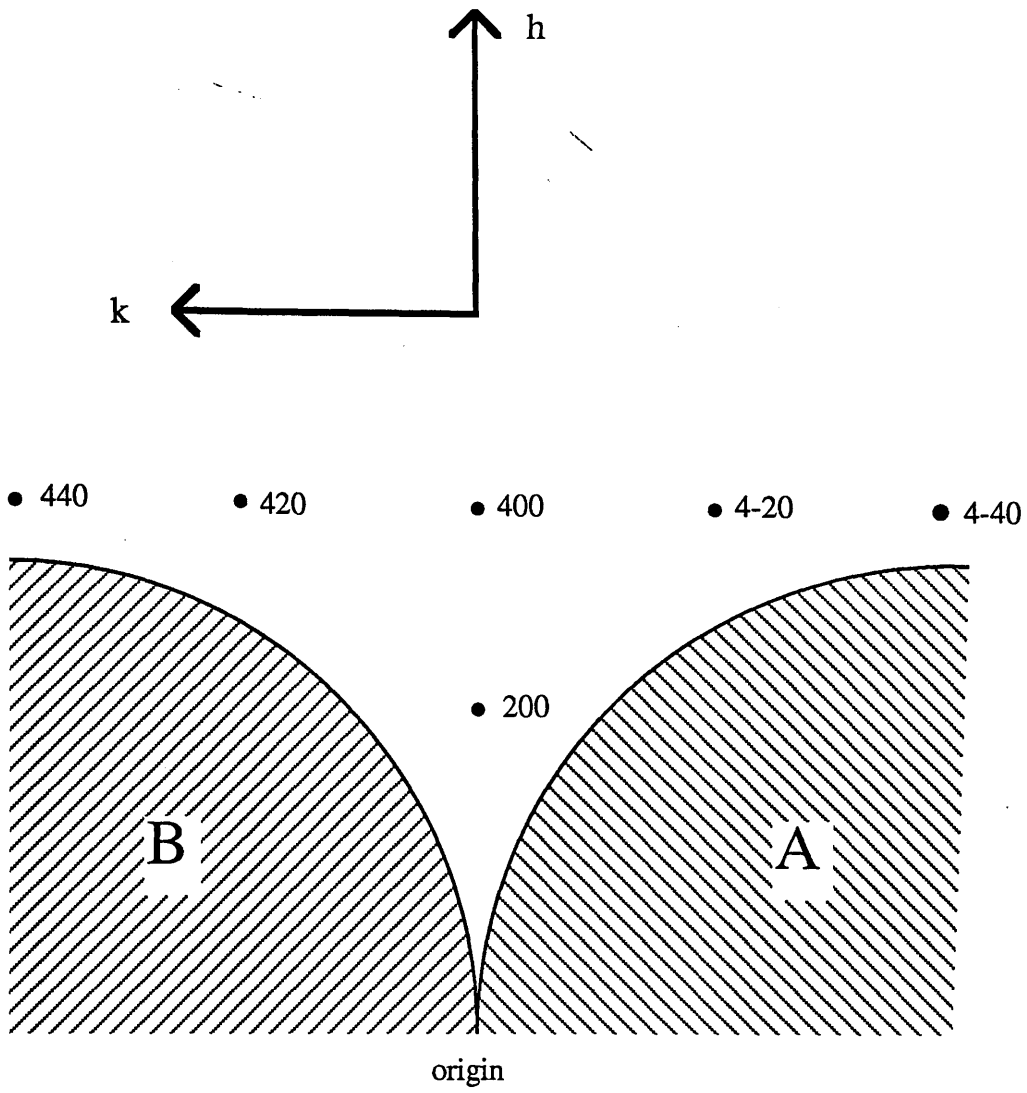

Figure 8.5 An Ewald sphere diagram illustrating the accessible and forbidden regions of reciprocal space. In region A, the incident beam is obscured by the crystal face as is the diffracted beam in region B. h and k are two of the axes in reciprocal space. h is parallel to the 100 direction and k is parallel to the 010 direction. As given by Ryan [1986].

The work presented in this section was done in collaboration with Drs Tom W Ryan, Peter D Hatton and Simon Bates at Edinburgh University Physics Department. The triple crystal x-ray diffractometer was based on a Huber 430/440 goniometer using a GEC Avionics GX21 x-ray generator with a copper target producing two main emission lines at 1.540511 and 1.544551 Å. The monochromator and analyser were flat Ge(111) crystals and either a NaI(Tl) scintillation counter (for fine triple crystal work) or a $Xe(CH_4)$ proportional counter (for coarse double crystal work) was used to detect the signal. When looking at thin layer samples it is usual to keep the incident beam at nearly glancing incidence to reduce its penetration depth into the crystal.

Three samples of GaInAs-InP were studied using x-ray analysis. The purpose of the study was to determine the lattice constant of the alloy and thereby determine its composition and state of strain. The first sample studied was PMB106, a bulk epitaxially-grown layer of InP grown on an InP substrate. Table 5.1 contains the details of both this and the other two samples studied, PMB112, a thick GaInAs layer grown on InP, and PMB116, a single quantum well of GaInAs-InP.

Figure 8.6 shows the 2D plot of the 440 Bragg reflection from PMB106. This represents an area of reciprocal (hkl) space scanned by the detector. The experimental geometry is such that the h direction corresponds to the direction of growth, i.e., the (100) direction, while the k and l directions correspond to the plane of the layer or surface. The samples were studied in cross section where l was always chosen to be zero. In figure 8.6, a central peak can be seen with tails in several directions. The star shape is characteristic consisting of three well-resolved streaks that result from the monochromator, sample and analyser as discussed by Ryan [1986] and shown in the inset.

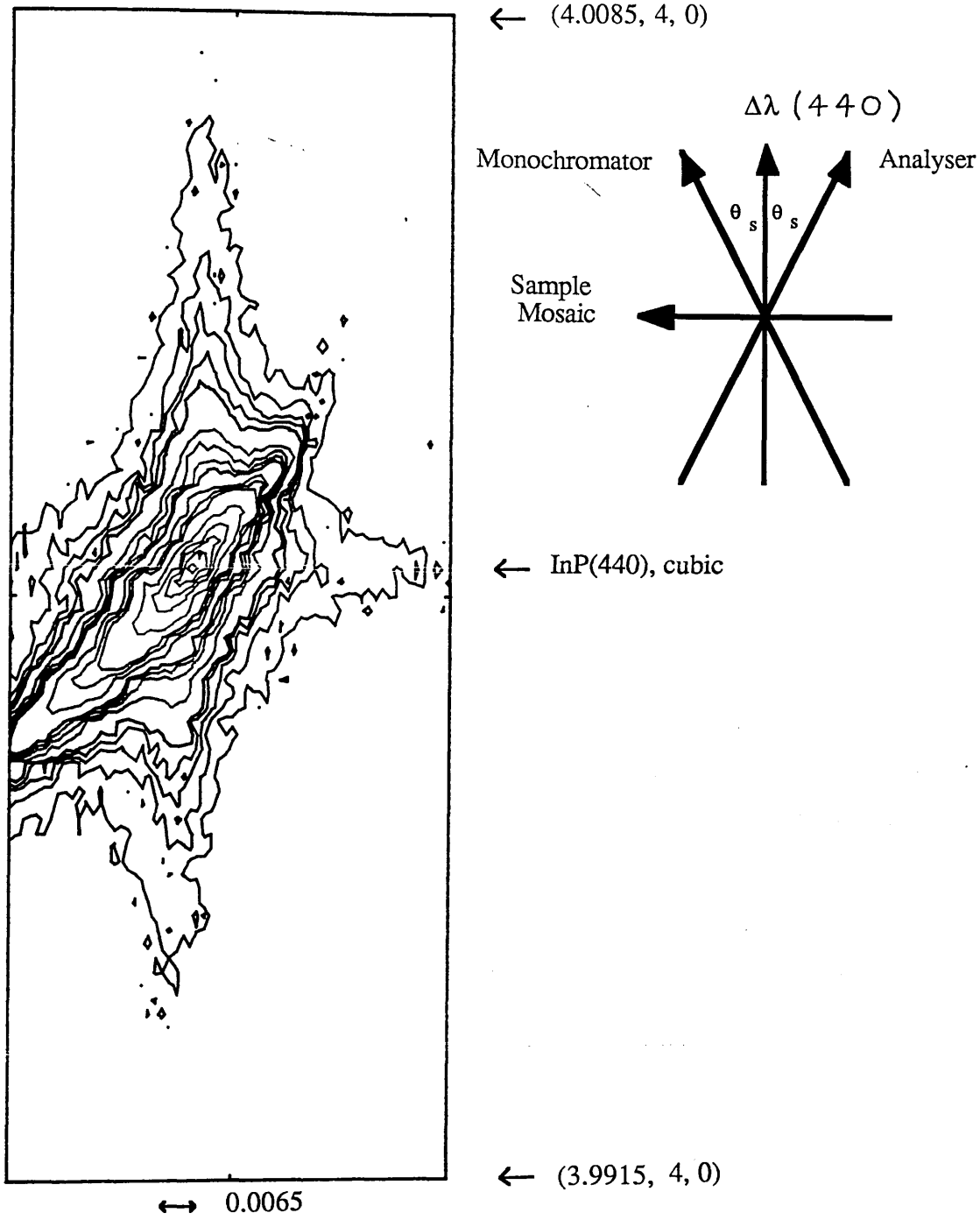

Figure 8.6 An iso–intensity contour plot of the observed x–ray diffraction in the region of the InP (440) Bragg reflection from the bulk InP sample, PMB106. The data are presented on a quasi–logarithmic scale over 4 decades of intensity to avoid over–contouring the main peak. The axes are plotted in reciprocal lattice units. The inset shows the origin of the streaks around the Bragg peak.

A lattice constant value can be obtained from the position of the peak. A more accurate figure can be determined by scanning several Bragg reflections and using an iterative method to calculate the best–fit value of the lattice constant in each direction. Values of a = 5.8677Å and a = 5.8670Å were calculated for the InP of PMB106 using this iterative method with four Bragg reflections (the 400, 420, 4–20 and 600). These values of a show that the lattice is cubic to within the error limit and the values compare well with that of 5.8687Å given by Landolt–Boernstein [1982]. Resolution in all these experiments ≙ 0.0025Å or 0.04%.

Figure 8.7 shows a plot of the 420 Bragg reflection from PMB112, the thick, 2.5μm, GaInAs layer (nominally $Ga_{0.47}In_{0.53}As$) grown on an InP substrate and buffer. Here two peaks can be seen. These are aligned in the k direction but are displaced along h. This implies that although the lattice constant is single valued in the plane of the layer, it has two values in the direction of growth. If these values are measured and compared with the single–valued lattice constant in the plane of the layer, it is found that one of the peaks corresponds to a cubic state while the other peak corresponds to a non–cubic state. The cubic contributon exhibits a lattice constant of 5.8689Å (refined over the 200, 400 and 600 reflections) in the growth direction and 5.8710Å (refined over 420 and 4–20) in the plane of the layer. The non–cubic crystal has a lattice constant of 5.8855Å in the growth direction (refined over the 200, 400 and 600 Bragg reflections) and 5.8712Å (refined over 420 and 4–20) in the plane of the layer. This corresponds to a change in the lattice constant of $\triangle a/a$ = 0.3% in the direction of growth. Since it can be assumed that the InP substrate is a bulk crystal in a relaxed state with no inherent lattice strain then the cubic peak can be assigned to the 420 Bragg reflection of the substrate. In addition, this lattice constant value agrees with that of 5.8687Å given by Landolt–Boernstein [1982] for InP. The Bragg peak corresponding to the tetragonally–distorted lattice must therefore arise from the GaInAs epitaxial layer. This suggests that although it was intended to grow an alloy layer perfectly

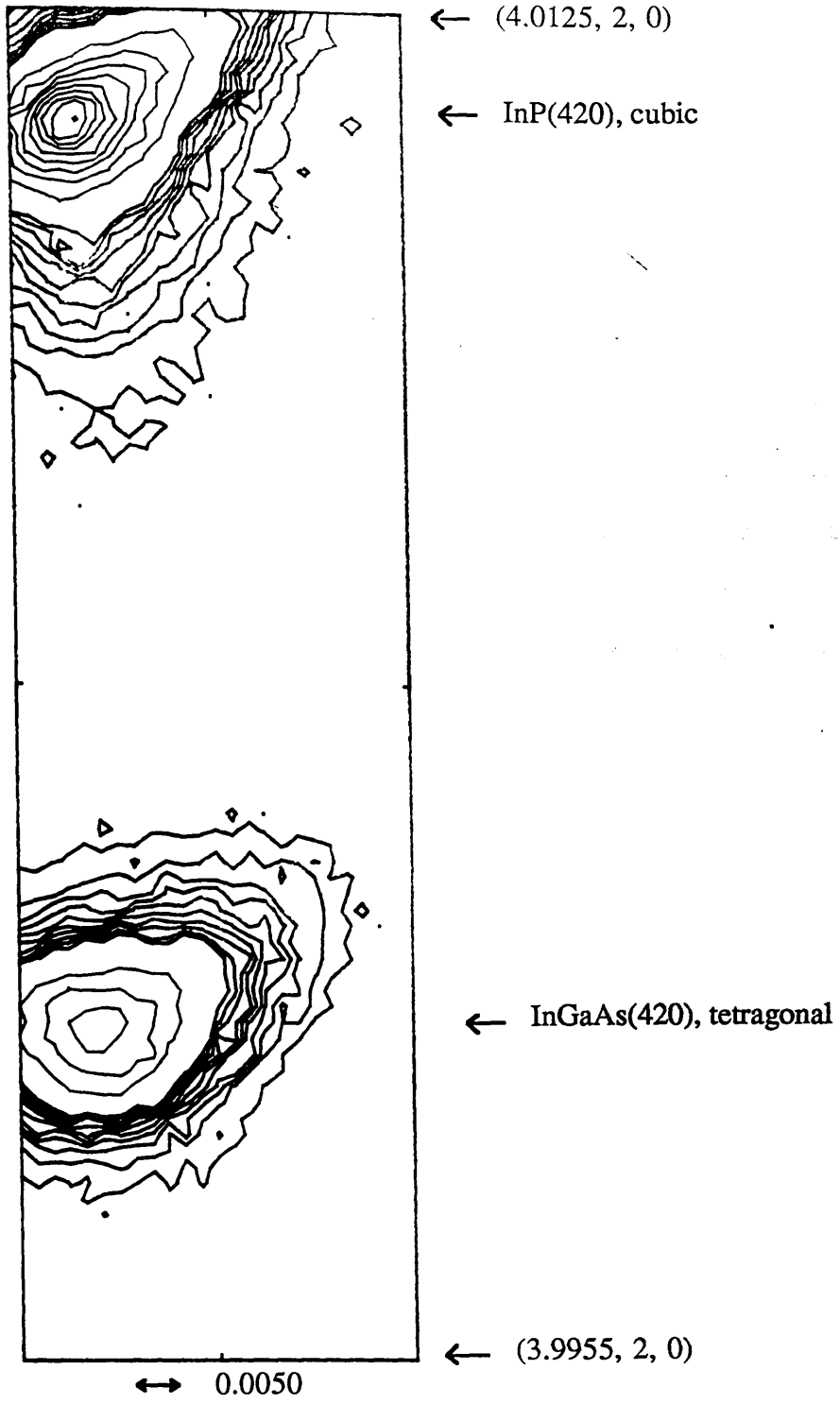

Figure 8.7 An iso–intensity contour plot of the observed x–ray diffraction in the region of the InP (420) Bragg reflection from the epitaxial GaInAs sample, PMB112. The data are presented on a quasi–logarithmic scale over 2 decades of intensity to avoid over–contouring the main peak. The axes are plotted in reciprocal lattice units.

lattice–matched to the substrate, the alloy layer is distorted and in a state of strain. The distortion is equivalent to a lattice mismatch of 0.11% (note that the maximum mismatch is 3.7%, obtained with pure GaAs on InP) and therefore corresponds to a composition change of 1.6% giving a revised alloy composition of $Ga_{0.45}In_{0.55}As$.

This 1.6% error in alloy composition is quite large although the corresponding mismatch is small in comparison with the lattice mismatches of up to 1% which are tolerated in deliberately strained superlattices [see e.g. Marzin, 1985]. Part of the reason for the mismatch can be attributed to a temperature effect.

A study of the thermal expansion parameters of GaInAs and InP was conducted by Bisaro et al [1979] in the temperature range 25 – 400 °C. Using this data, and linearly extrapolating to a value of 630°C, which is the growth temperature of the samples under study, it can be calculated that GaInAs which is perfectly lattice matched to InP at 630°C, will be mismatched by 0.07% at 25°C with the GaInAs lattice constant being the larger. This effect alone explains most of the mismatch observed in PMB112. This is not something which can be circumvented by better growth conditions or tailoring of the structure parameters. If temperature effects are included in the calculations of the alloy composition of PMB112, then the actual composition meets the intended composition to within 1%. This compares well with the work of Vandenberg et al [1986] on MOMBE–grown GaInAs–InP heterostructures in which the authors observed lattice mismatch values in the growth direction of $\triangle a/a = 0.5 - 1.2 \times 10^{-3}$ (for PMB112, a value of $\triangle a/a = 0.4 \times 10^{-3}$ is obtained when temperature effects are removed).

The third sample to be studied with triple crystal x–ray diffraction was a single quantum well of GaInAs grown on InP with an InP capping layer, PMB116. The alloy was intended to be lattice matched to the InP and the layer thicknesses deduced from the growth times were 160Å for the well and 500Å for the cap. The plot of the 440 Bragg reflection is shown in figure 8.8. This Bragg peak shows much more structure than those from PMB106 and PMB112 with two main peaks

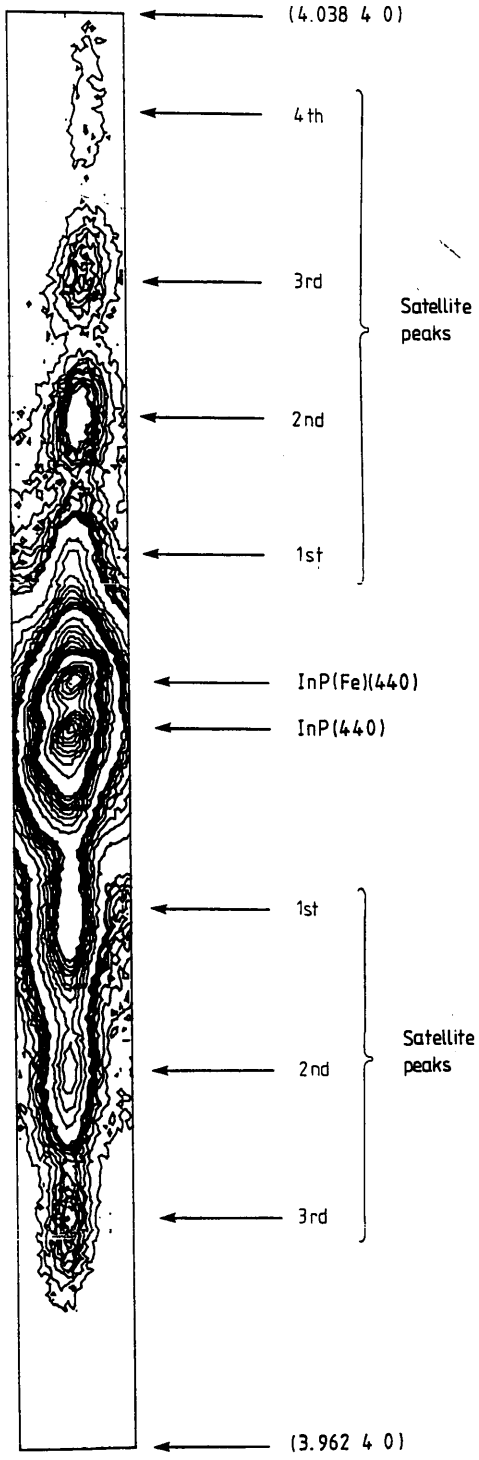

Figure 8.8 An iso– intensity contour plot of the observed x– ray diffraction in the region of the InP (440) Bragg reflection from a single quantum well of GaInAs– InP, sample PMB116. The data are presented on a quasi– logarithmic scale over 4 decades of intensity to avoid over– contouring the main peak. The axes are plotted in reciprocal lattice units. [After Ryan et al, 1987]

and a number of satellite peaks, all displaced along the h axis but aligned along the k axis. A plot of the intensity distribution along the h axis is given in figure 8.9(a). The split of the main InP Bragg peak can be attributed to scattering from both the InP substrate and the epitaxially–grown InP. This is demonstrated by the dependence of the diffraction pattern on the angle of incidence of the x–ray beam. Figure 8.10 shows a plot of the 440 Bragg reflection. Here the x–ray beam made an angle of 1° with the sample hence the penetration depth into the sample was small and a single peak was observed. In figure 8.11, the 420 Bragg reflection is plotted and shows two strong peaks close together. In this case the x–rays were incident at an angle of 8° and thus penetrated much deeper into the sample. For both scattering geometries, the Bragg peak corresponding to the epitaxial InP is present, but the Bragg peak corresponding to the substrate only appears when the x–rays penetrate far enough into the sample. The InP substrate peak was measured to be cubic with a lattice constant of 5.8694Å (refined over the 200,400, 600, 420, 4–20, 440 and 4–40 Bragg reflections) while the peak corresponding to the epitaxially–grown InP was measured to have a lattice constant of 5.8733Å in the direction of growth and 5.8695Å in the plane of the layer (both refined over the 200, 400, 420, 4–20 and 600 Bragg reflections). The epitaxially–grown InP is therefore tetragonally–distorted by a small amount ($\Delta a/a$ in the direction of growth is 0.06%). This could be accounted for by a small amount of Arsenic contaminating the lattice of the epitaxial layer as this was a problem encountered by the growers. The distortion could also be a result of the Iron doping of the substrate material which tends to shrink the lattice. In practice, the tetrahedral distortion may result from a combination of these two possibilities.

The satellite peaks surrounding the two main Bragg peaks can be assigned to scattering from thin crystalline slabs of material within the sample. X–ray scattering from thin, single–crystal slabs is a well–understood phenomenon which has been observed by a number of authors [see, e.g., Hashizume et al, 1970]. It gives rise to

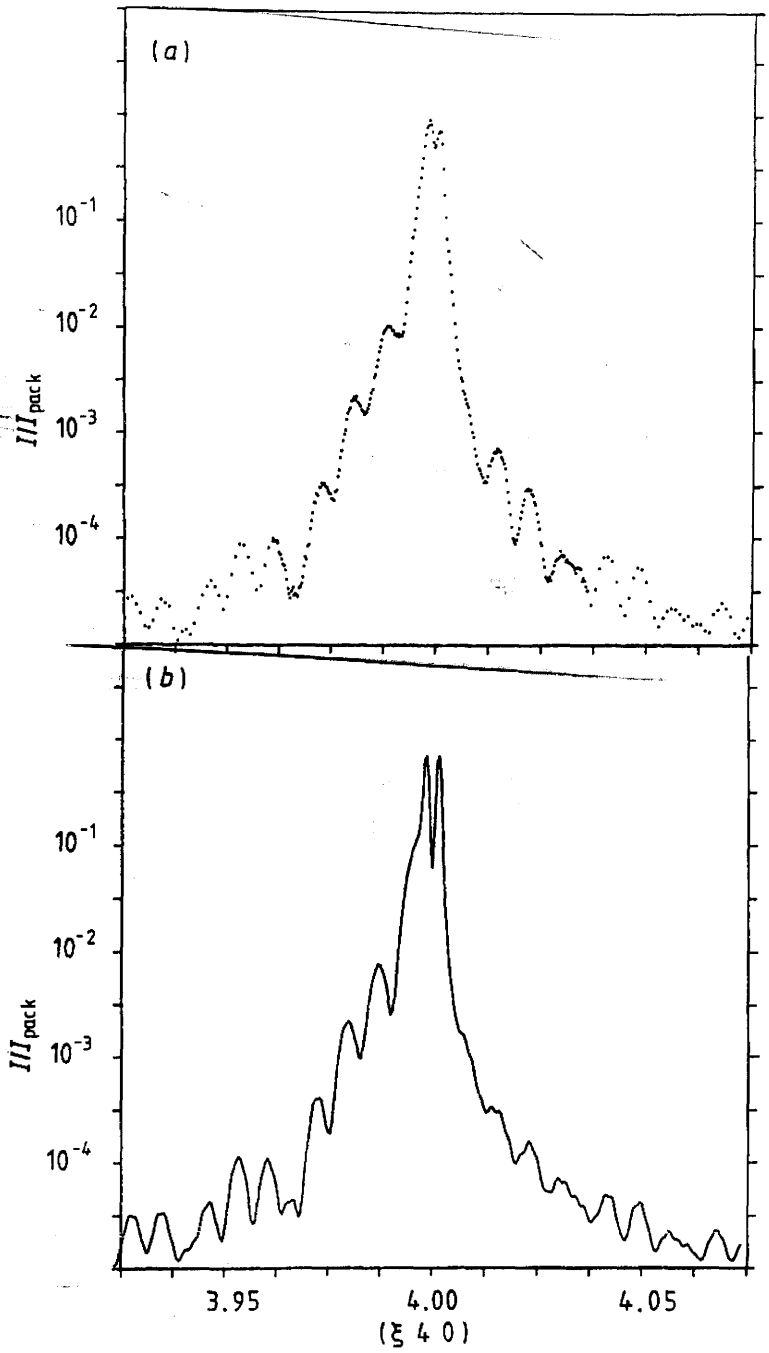

Figure 8.9 (a) The intensity distribution along [100], the growth direction, through the InP(440) Bragg peak. The intensity is shown on a logarithmic scale. The scan range is shown in reciprocal lattice units.

(b) A simulation of the data shown in (a) based on a kinematical scattering model. The simulation parameters are given in table 8.1. [After Ryan et al, 1987]

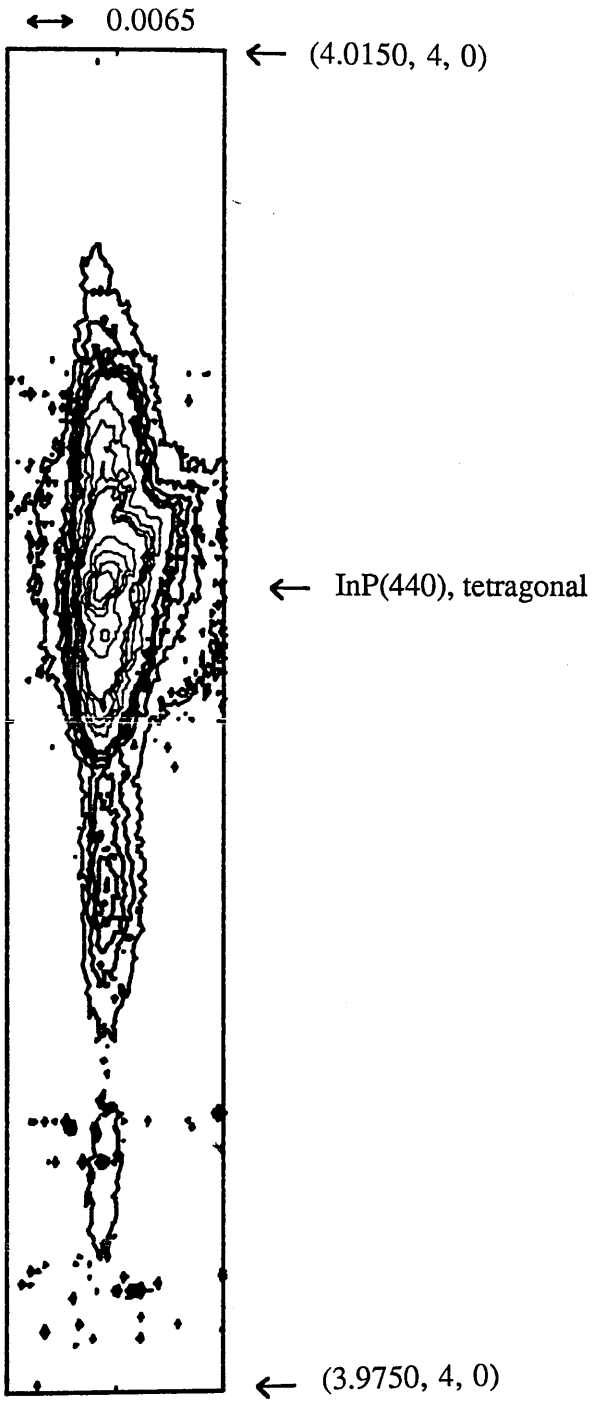

Figure 8.10 An iso– intensity contour plot of the observed x– ray diffraction in the region of the InP (440) Bragg reflection from the GaInAs– InP quantum well, sample PMB116. The data are presented on a quasi– logarithmic scale over 3 decades of intensity to avoid over– contouring the main peak. The axes are plotted in reciprocal lattice units. The angle of incidence of the beam was 1°.

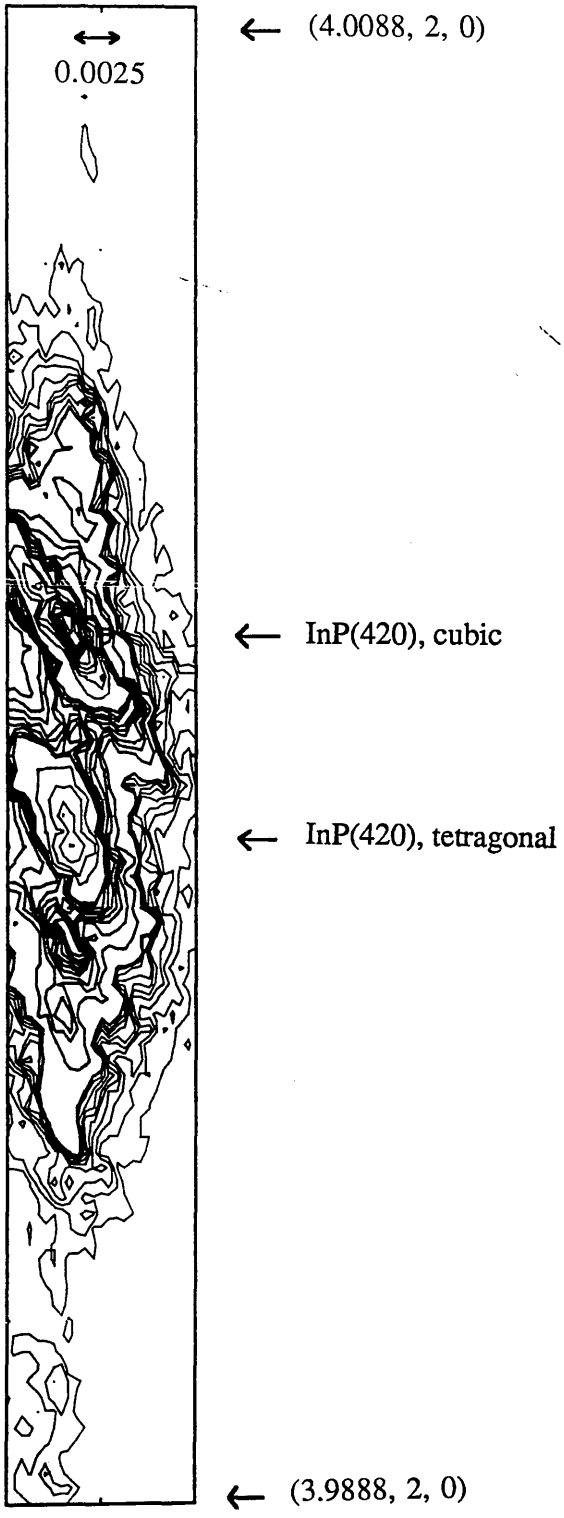

Figure 8.11 An iso– intensity contour plot of the observed x– ray diffraction in the region of the InP (420) Bragg reflection from the GaInAs– InP quantum well, sample PMB116. The data are presented on a quasi– logarithmic scale over 3 decades of intensity to avoid over– contouring the main peak. The axes are plotted in reciprocal lattice units. The angle of incidence of the beam was 8°. The cubic peak corresponds to the substrate while the tetragonal peak is from the epitaxially– grown InP.

a series of diffraction maxima about the main Bragg peak. The spacing of these satellite peaks is related to the slab thickness in much the same way as the spacing of the diffraction maxima produced by diffraction of an optical beam by a single slit is related to the slitwidth. In this case it can be seen in figure 8.9(a) that the satellite peaks do not have a regular behaviour with regard to their intensites. The satellites to the low h side of the main Bragg peaks have a higher intensity than those on the high h side and on both sides, some peaks are missing. This can be interpreted as an interference effect arising from the two interference patterns originating in the two layers within the sample: the cap layer and the quantum well. The main satellite peaks originate in the InP capping layer but these are modulated by a weaker set of satellite peaks from the GaInAs layer. The experimental data shown in figure 8.9(a) has been simulated by Ryan et al [1987]. The result of this simulation is shown in figure 8.9(b). It is clearly a very good representation of the experimental data. The parameters used by Ryan et al [1987] to obtain the simulated profile are given in table 8.1. From this table it can be seen that the experimental data suggests that PMB116 had a 230Å rather than a 160Å well with a 680Å rather than a 500Å capping layer.

It is important to know the structure of a sample if any comparison is to be made between experiment and theory. Such comparisons could involve fitting quantum well energy levels to a quantum mechanical model, where the energy levels had been obtained by photoluminescence (for the lowest), photoluminescence excitation or electronic intersubband Raman spectroscopy. In such a case, if both the well width and the energy levels can be measured then information can be obtained regarding the shape of the confining potential. Equally, if a sample structure has been carefully designed for a specific device application, it is important to know how accurately the grown structure matches the design before conclusions can be drawn from the device performance.

Table 8.1 also shows a 12Å interface roughness assumed in the model

Table 8.1

Structural Parameters used by Ryan et al [1987] to Simulate the Triple Crystal X-ray Scattering from PMB116, a GaInAs-InP Quantum Well Sample

Parameter	Value used by Ryan et al [1987]	Nominal Value from Growth Conditions
InP cap thickness	680(10)Å	500Å
InGaAs layer thickness	230(10)Å	160Å
Lattice parameter mismatch ($\Delta a/a$)	$2.73(1)\times10^{-3}$	–
Surface roughness	20(2)Å	–
Internal surface roughness	12(2)Å	–

simulation of Ryan et al [1987]. This compares very well with the spectroscopic ellipsometry measurements of Erman et al [1986]. In this latter work it was found that the InP on GaInAs interface was of the order of 30 – 60 Å while the GaInAs on InP interface was about 9Å.

8.3 Conclusions

Triple crystal x–ray diffraction has been shown to be a technique which can be used to measure epitaxial layer thicknesses down to a few hundred Angstroms with a resolution of some 10Å. In addition, surface and interface roughnesses have been measured to within 2Å. This technique is much more sensitive than either conventional double crystal x–ray measurements or SIMS work, neither of which has a comparably good depth resolution. Triple crystal x–ray has two advantages over TEM measurements. The first is that the technique is non–destructive and involves minimal sample preparation. The second is that the data is collected from a large sample area of several millimeters. TEM measurements are made on a microscopically small area of the sample and cannot yield information about the variation of well width across a sample. The type of x–ray measurements undertaken here will show up such non–uniformity as a broadening of the satellite structure.

With respect to the samples under study, it has been shown by the sharpness of the Bragg reflections that all three have good crystalline quality. In particular, the GaInAs quantum well in PMB116 has demonstrated its crystal quality by behaving as a single–crystal layer of thickness 230Å. This information is used in the discussion of its Raman scattering behaviour in chapter 5. In addition, the lattice constant of the thick GaInAs layer in PMB112 has been determined and from this, the lattice mismatch, state of strain and alloy composition have all been calculated. It was found that PMB112 had a tetragonally–distorted layer of GaInAs with a change of the lattice constant in the direction of growth of $\Delta a/a = 0.04\%$ once temperature effects had been removed. This corresponds to an alloy composition which is within 1% of that intended. This information is used extensively in the discussion of the Raman scattering behaviour of PMB112 which is presented in chapter 5.

N W Ashcroft and N D Mermin; "Solid State Physics", published by Holt, Rinehart and Winston, New York, 1976; chapter 6

R Bisaro, P Merenda and T P Pearsall; Appl Phys Lett 34, 100, 1979

W H Bragg and W L Bragg; Proc Roy Soc A88, 428, 1913

M Erman, J P Andre and J LeBris; J Appl Phys 59, 2019, 1986

M A G Halliwell, M R Taylor and T Ambridge; Br Telecom Technol J 3, 30, 1985

H Hashizume, K Nakayama, T Matushita and K Kohra; J Phys Soc Japan 29, 806, 1970

"Landolt–Boernstein Numerical Data and Functional Relationships in Science and Technology. Group III: Crystal and Solid State Physics" Vol 17a: Physics of Group IV Elements and III–V Compounds, edited by O Madelung, published by Springer–Verlag, Berlin, Heidelberg, New York, 1982; sections 2.10, 2.11, 2.14 and 2.16

J Y Marzin; in "Heterojunctions and Semiconductor Superlattices", Proc Winterschool, Les Houches, France, 1985, edited by G Allen, G Bastard, N Boccara, M Lannoo and M Voos, published by Springer–Verlag, Berlin, Heidelberg; p199

T W Ryan; PhD Thesis, Edinburgh University, 1986

T W Ryan, P D Hatton, S Bates, M Watt, C M Sotomayor Torres, P A Claxton and J S Roberts; Semicond Sci Technol 2, 241, 1987

J M Vandenberg, R A Hamm, A T Macrander, M B Panish and H Temkin; Appl Phys Lett 48, 1153, 1986

CHAPTER 9

CONCLUSIONS

The main effort of the GaInAs– InP work has been to investigate the confined and propagating phonons expected in low dimensional systems. The optical phonon spectrum of $Ga_{0.47}In_{0.53}As$ consists of a single broad band in which the GaAs– like LO phonon dominates. This band cannot be resolved because of broadening of the component phonon peaks resulting from alloy potential fluctuations inherent in this material. The Raman spectra of GaInAs quantum wells exhibited screening of the LO phonons by the free carriers, a situation that was aggravated by the high power densities needed to obtain significant signal intensity. The 2D plasma density in the quantum well at the onset of screening was estimated to be about $1x10^{12}$ cm^{-2}.

Although the GaInAs– InP samples were of good quality, as demonstrated by their optical properties, the Raman scattering data posed questions with regard to the exact alloy composition and lattice strain. These questions were addressed using triple crystal x– ray diffraction. It was found that the epitaxially– grown layers were tetragonally distorted, exhibiting a change in the lattice constant of $\Delta a/a = 0.04\%$ in the direction of growth. This evidence for strain is important, not only for strained layer systems, but also for nominally lattice– matched systems. It has emerged from this work that the combination of Raman scattering and high resolution x– ray diffraction provides a powerful analytical tool for the investigation of strain in heterostructures.

The continuation of this work involved a further reduction in dimensionality with the study of sub-micron cylinders of GaAs. These nanostructures exhibited an additional feature in the optical phonon region of their Raman spectra. Several possible interpretations of this feature were considered: plasmon-phonon interactions, amorphous contributions and oxide layers, however none provided an adequate or consistent explanation of the mode. Identification of the additional Raman feature as a surface phonon of the cylinders was based on the shape of the structures observed in the SEM micrographs and the good agreement of the experimentally-observed frequencies with those predicted by theory. The theoretical calculations of the surface phonon frequency were based on the model of a small, geometrically-regular, crystalline cylinder. Suggestions have been made for further work in this area.

As reactive-ion-etching (RIE) provided one of the major steps in the fabrication process of the quantum cylinders, a study was made of the etch-damage due to this process. As the etch power was varied, the crystalline symmetry selection rules were observed to change thereby introducing phonon scattering from the symmetry-forbidden TO phonon. The intensity of this mode correlated well with the extent of the RIE-induced damage measured by depth profiling of the samples. Optimised RIE conditions, such as were used in the fabrication of the quantum cylinders were observed to produce negligible crystalline damage.

The study of the phonons in the 2D GaInAs-InP material system can be regarded as a prerequisite for the study of lattice vibrations in nanostructures fabricated in this material. Such structures are currently of much interest as GaInAs-InP is a promising system in which to study zero-dimensional confinement effects.

Appendix A

Program to Calculate Superlattice Acoustic Phonon Frequencies

```
C       THIS PROGRAM IS DESIGNED TO CALCULATE THE FOLDED
C       DISPERSION CURVES OF SUPERLATTICES
C       USING THE RYTOV MODEL

C       DEFINITION OF PARAMETERS FOR PMB121
C       WITH GaInAs AS LAYER 1 AND InP AS LAYER 2

C       C=COMPLIANCE CONST
C       ROH=DENSITY
C       D=LAYER THICKNESS
C       V=SOUND VELOCITY

        DOUBLE PRECISION YDP,WDP

        DIMENSION Y(500)
        DIMENSION YDP(500)
        DIMENSION W(500)
        DIMENSION WDP(500)

        C1=9.96E10
        C2=10.22E10
        ROH1=5.503E+3
        ROH2=4.81E+3
        D1=25E-10
        D2=100E-10
        V1=4.25E3
        V2=4.61E3

        E=(C1*ROH1-C2*ROH2)/(C1*ROH1+C2*ROH2)
        K=0
        DO 25 J=1,500

        K=K+1
        W(K)=J*1.0E10
        Y(K)=COS(W(K)*(D1/V1+D2/V2))
        Y(K)=Y(K)-E*E*SIN(W(K)*D1/V1)*SIN(W(K)*D2/V2)/2
        IF (Y(K).GT.1.0) Y(K)=1.0
        IF (Y(K).LT.-1.0) Y(K)=-1.0
        Y(K)=ACOS(Y(K))/(D1+D2)

        WDP(K)=W(K)/1.0D10
        YDP(K)=Y(K)*1.0D0

   25 CONTINUE
```

```
C*SELECT GRAPHICAL OUTPUT DEVICE

      WRITE (2,10)
      READ (1,89) N
      IF (N.EQ.1) THEN
       CALL B1302
       ELSEIF (N.EQ.2) THEN
       CALL T4010
       CALL PICCLE
       ELSEIF (N.EQ.3) THEN
       CALL HP747
       CALL CHASWI(1)
      ENDIF
   89 FORMAT (I1)
   10 FORMAT (`TYPE 1 FOR BENSON, 2 FOR T4010, 3 FOR HP `)

C*INITIALISE NAG GRAPHICS

      CALL J06WAF

C*MAP USER DATA REGION ONTO PLOTTING SURFACE


      CALL J06WBF (1.0D0, 2.6D8, 1.0D0, 5.0D2, 1)
      CALL J06AMF(1,0)

C*LABEL X AXIS

      CALL J06AJF (1,`WAVEVECTOR                          `)

C*LABEL Y AXIS

      CALL J06AJF (2,'FREQUENCY                           ')

C*PLOT

      IFAIL=0
      CALL J06BAF(YDP,WDP,500,1,2,IFAIL)
      IF (IFAIL.NE.0) WRITE (4,*) `ERROR IN PLOT ROUTINE`

C*TERMINATE GRAPHICAL OUTPUT

      CALL J06WZF


      STOP
      END
```

Appendix B

Program to Calculate Superlattice Interface Phonon Frequencies

```
C       THIS PROGRAM IS DESIGNED TO CALCULATE THE
C       INTERFACE MODES ASSOCIATED WITH PMB121 GaInAs-InP
C       USING THE DIELECTRIC CONTINUUM MODEL

        DOUBLE PRECISION KZDP1,KZDP2,KZDP3,WDP1,WDP2,WDP3
        REAL KX,KZ1,KZ2,KZ3

        DIMENSION W1(100),W2(100),W3(100)
        DIMENSION E1(100)
        DIMENSION E2(100)
        DIMENSION ETA(100)
        DIMENSION Y(100)
        DIMENSION KZ1(100),KZ2(100),KZ3(100)
        DIMENSION KZDP1(100),WDP1(100),KZDP2(100),
       *WDP2(100),KZDP3(100),WDP3(100)

        KX=1.0E5
        CONV=2.99792E10
        WL1=232*CONV
        WL2=265*CONV
        WL=348*CONV
        WT1=226*CONV
        WT2=254*CONV
        WT=304*CONV

        EINF1=11.62
        EINF2=9.61
        D1=25E-10
        D2=100E-10

        DO 99 J=1,87

        W1(J)=(304+0.5*J)*CONV

        E1(J)=EINF1*(WL1**2-W1(J)**2)*(WL2**2-W1(J)**2)
        E1(J)=E1(J)/(WT1**2-W1(J)**2)/(WT2**2-W1(J)**2)

        E2(J)=EINF2*(WL**2-W1(J)**2)/(WT**2-W1(J)**2)

        ETA(J)=E1(J)/E2(J)

        Y(J)=(ETA(J)**2+1)/2/ETA(J)*SINH(KX*D1)*SINH(KX*D2)
        Y(J)=Y(J)+COSH(KX*D1)*COSH(KX*D2)

        KZ1(J)=ACOS(Y(J))*2*3.14159/(D1+D2)
        W1(J)=W1(J)/CONV

        KZDP1(J)=KZ1(J)*1.0D0
        WDP1(J)=W1(J)*1.0D0

   99 CONTINUE
```

```
      DO 101 J=1,20

      W2(J)=(254+0.5*J)*CONV

      E1(J)=EINF1*(WL1**2-W2(J)**2)*(WL2**2-W2(J)**2)
      E1(J)=E1(J)/(WT1**2-W2(J)**2)/(WT2**2-W2(J)**2)

      E2(J)=EINF2*(WL**2-W2(J)**2)/(WT**2-W2(J)**2)

      ETA(J)=E1(J)/E2(J)

      Y(J)=(ETA(J)**2+1)/2/ETA(J)*SINH(KX*D1)*SINH(KX*D2)
      Y(J)=Y(J)+COSH(KX*D1)*COSH(KX*D2)

      KZ2(J)=ACOS(Y(J))*2*3.14159/(D1+D2)
      W2(J)=W2(J)/CONV

      KZDP2(J)=KZ2(J)*1.0D0
      WDP2(J)=W2(J)*1.0D0

  101 CONTINUE

      DO 103 J=1,23

      W3(J)=(226+0.25*J)*CONV

      E1(J)=EINF1*(WL1**2-W3(J)**2)*(WL2**2-W3(J)**2)
      E1(J)=E1(J)/(WT1**2-W3(J)**2)/(WT2**2-W3(J)**2)

      E2(J)=EINF2*(WL**2-W3(J)**2)/(WT**2-W3(J)**2)

      ETA(J)=E1(J)/E2(J)

      Y(J)=(ETA(J)**2+1)/2/ETA(J)*SINH(KX*D1)*SINH(KX*D2)
      Y(J)=Y(J)+COSH(KX*D1)*COSH(KX*D2)

      KZ3(J)=ACOS(Y(J))*2*3.14159/(D1+D2)
      W3(J)=W3(J)/CONV

      KZDP3(J)=KZ3(J)*1.0D0
      WDP3(J)=W3(J)*1.0D0

  103 CONTINUE
```

```
C*SELECT GRAPHICAL OUTPUT DEVICE

      WRITE (2,10)
      READ (1,89) N
      IF (N.EQ.1) THEN
       CALL B1302
       ELSEIF (N.EQ.2) THEN
       CALL T4010
       CALL PICCLE
       ELSEIF (N.EQ.3) THEN
       CALL HP747
       CALL CHASWI(1)
      ENDIF
   89 FORMAT (I1)
   10 FORMAT (`TYPE 1 FOR BENSON, 2 FOR T4010, 3 FOR HP `)

C*INITIALISE NAG GRAPHICS

      CALL J06WAF

C*MAP USER DATA REGION ONTO PLOTTING SURFACE


      CALL J06WBF (0.0D0, 5.0D6, 2.2D2, 3.5D2, 1)
      CALL J06AMF(0,0)

C*LABEL X AXIS

      CALL J06AJF (1,`WAVEVECTOR,  KZ,  IN  METERS**-1 `)

C*LABEL Y AXIS

      CALL J06AJF (2,'FREQUENCY  IN  CM**-1  ')

C*PLOT

      IFAIL=0
      CALL J06BAF(KZDP1,WDP1,87,1,2,IFAIL)
      IF (IFAIL.NE.0) WRITE (4,*) `ERROR IN PLOT ROUTINE`
C*PLOT

      IFAIL=0
      CALL J06BAF(KZDP2,WDP2,20,1,2,IFAIL)
      IF (IFAIL.NE.0) WRITE (4,*) `ERROR IN PLOT ROUTINE`
C*PLOT

      IFAIL=0
      CALL J06BAF(KZDP3,WDP3,23,1,2,IFAIL)
      IF (IFAIL.NE.0) WRITE (4,*) `ERROR IN PLOT ROUTINE`

C*TERMINATE GRAPHICAL OUTPUT

      CALL J06WZF

      STOP
      END
```

Appendix C

Data Collection Program

```
{$C+,C-,U-}
PROGRAM AUTORAMAN;

{
*****************************************************************************
*                                                                           *
*  THIS PROGRAM WILL GIVE ANTISTOKES RAMAN SCANS IN WAVENUMBERS             *
*  USING THE PHOTON COUNTING SYSTEM. TO GET WAVELENTH SCANS, USE THE PLSCAN  *
*  PROGRAM.                                                                 *
*                                                                           *
*  LAST UPDATED 4.10.88                                                     *
*****************************************************************************
}
TYPE
    NAME=STRING[66];


VAR
   A, COUNT, I, II, ZZ, STEPNUM, INC, SECS, RESPONSE  : INTEGER;
   LASERCM, STARTANG, ENDANG, SCANTIME, STEPANG : REAL;
   XYZ, ZYX, NEXT, BOX, STARTCM, ENDCM, SLEWANG : REAL;
   KOUNT, RCOUNT, TEST, SLITS, POWER : REAL;
   ANGVAL,C10VAL, LPOWER  : ARRAY[0..2000] OF REAL;
   TARGL, TARGI, TARGM : ARRAY[1..2000] OF INTEGER;
   CONTC : CHAR;
   ANS, ANS2, ANS3 : STRING[1];
   FILNAM : STRING[7];
   NAMETEST:BOOLEAN;
   DATFILE : FILE OF REAL;

CONST
     LASERLINE :REAL=3638.0;
     SCANSTART :REAL=100.0;
     SCANEND   :REAL=200.0;
     SCANSTEP  :REAL=20.0;
     ICOUNTIME :INTEGER=5;
     RCOUNTIME :REAL=5.0;

{*****************************************************************************}

PROCEDURE ENDUP;

BEGIN
     WRITELN('THIS IS THE END OF THE PROGRAM');
END;

{*****************************************************************************}

FUNCTION CHANGEPARAM : REAL;
{This function is used to change one of the scan parameters to a new value.}

VAR
   NEWPARAM :REAL;

BEGIN
```

```
      WRITELN('INPUT THE NEW VALUE: ');
      READLN(NEWPARAM);
      CHANGEPARAM:=NEWPARAM;
END;

{*****************************************************************************}

PROCEDURE BEEPWARNING;
{This procedure is carried out at the start of the scan and reminds the user
audibly that the laser beam must be blocked prior to the spectrometer slewing
outside the scan range.}

BEGIN
      WRITELN;
      WRITELN('***** FILTERS !!!!! *****');
      WRITELN;
      FOR I:= 1 TO 20 DO
      BEGIN
      SOUND(550);
      DELAY(100);
      NOSOUND;
      DELAY(100);
      END;
END;

{*****************************************************************************}

PROCEDURE ENDBEEP;
{This procedure tells the user audibly that the scan is over.}

BEGIN
      WRITELN;
      WRITELN('***** SCAN OVER *****');
      WRITELN;
      FOR I:=1 TO 4 DO
      BEGIN
      SOUND(I*100);
      DELAY(200);
      NOSOUND;
      DELAY(200);
      END;
      SOUND(550);
      DELAY(300);
      NOSOUND;
      DELAY(100);
      SOUND(550);
      DELAY(100);
      NOSOUND;
      DELAY(50);
      SOUND(550);
      DELAY(100);
      NOSOUND;
      DELAY(200);
      SOUND(550);
      DELAY(300);
```

```
     NOSOUND;
END;

{*****************************************************************************}

PROCEDURE ANGSEND(VAR X: INTEGER);
{This procedure sends information to the spectralink and reads the echo
as required by protocol.}

VAR
   CBACK: CHAR;

BEGIN
     WRITE(AUX,CHR(X));
     READ(AUX,CBACK);
END;

{*****************************************************************************}

FUNCTION RDSEND(VAR X: INTEGER): CHAR;
{This function reads information fromthe spectralink and stores the value
in the character value RDSEND.}

VAR
   CBACK:CHAR;
   Y: ARRAY[0..16] OF CHAR;

BEGIN
     WRITE(AUX,CHR(X));
     READ(AUX,CBACK);
     IF (CBACK=' ') THEN CBACK:='0';
     RDSEND:=CBACK;

END;

{*****************************************************************************}

FUNCTION ANGREAD : REAL;
{This function uses ANGSEND and RDSEND to interrogate the spectralink
and determine the current wavelength.}

LABEL
     DUMMY;

VAR
   X,I,A,RESULT:INTEGER;
   CALIB,LSB, ISB, MSB:REAL;
   CMSB,CISB,CLSB:CHAR;
   OK : BOOLEAN;
   NUM:STRING[8];
   Y: ARRAY[0..17] OF CHAR;

BEGIN
      DUMMY:
      X:=58;
```

```
        ANGSEND(X);
        ANGSEND(X);
        ANGSEND(X);
        X:=0;
        ANGSEND(X);
        X:=97;
        ANGSEND(X);
        X:=3;
        ANGSEND(X);
        X:=63;
        CLSB:=RDSEND(X);
        CISB:=RDSEND(X);
        CMSB:=RDSEND(X);
        X:=58;
        ANGSEND(X);
        ANGSEND(X);
        ANGSEND(X);
        LSB:=ORD(CLSB);
        ISB:=ORD(CISB);
        MSB:=ORD(CMSB);
        IF (LSB=63) AND (ISB=63) AND (MSB=63) THEN
          BEGIN
          WRITELN('ERROR READING WAVELENGTH');
          GOTO DUMMY;
          END;
        CALIB:=(LSB+(256*ISB)+(6.5536E4*MSB))/200;
        ANGREAD:=CALIB;

END;

{*****************************************************************************}

FUNCTION C1OREAD : REAL;
{This function interrogates the photon counter unit (the C-10) via the
PC-14 I/O board and buffer to read the current digital display.}

VAR
    RESULT : INTEGER;
    DISP : REAL;
    X,Y,Z: BYTE;
    DIGIT : ARRAY[0..7] OF BYTE;
    NUM : STRING[8];

CONST
      DATA = $1f1;
      CONTROL = $1f0;
      READ = 128;
      MASK = 15;
      CUT = 127;

BEGIN
      REPEAT
        Z:=PORT[DATA];
      UNTIL Z>CUT;
      FOR X:= 0 TO 7 DO
```

```
        BEGIN
        REPEAT
          PORT[CONTROL]:=READ+X;
          Y:=PORT[DATA];
        UNTIL Y>CUT;
        Y:=PORT[DATA];
        Y:=Y AND MASK;
        DIGIT[X]:=Y;
        PORT[CONTROL]:=READ;
        END;
      DISP:=0;
      DISP:=DISP+DIGIT[0];
      DISP:=DISP+DIGIT[1]*10;
      DISP:=DISP+DIGIT[2]*100;
      DISP:=DISP+DIGIT[3]*1000;
      DISP:=DISP+DIGIT[4]*1E4;
      DISP:=DISP+DIGIT[5]*1E5;
      DISP:=DISP+DIGIT[6]*1E6;
      DISP:=DISP+DIGIT[7]*1E7;
    C10READ:=DISP;
    PORT[$1f0]:=2;
    DELAY(10);
END;

{*****************************************************************************}

PROCEDURE C10START;
{This procedure starts the C-10 counting.}

CONST
    CONTROL = $1f0;
    START = 2;
    NUL = 0;

BEGIN
    PORT[CONTROL]:=START;
    DELAY(10);
    PORT[CONTROL]:=NUL;
END;

{*****************************************************************************}

PROCEDURE C10INIT;
{This procedure initialises the C-10.}

CONST
    COMD = $1f3;
    CONTROL = $1f0;
    INIT = $8b;
    RESET = 1;
    NUL = 0;

BEGIN
    PORT[COMD]:=INIT;
    PORT[CONTROL]:=RESET;
```

```
      DELAY(30);
      PORT[CONTROL]:=NUL;
END;

{*****************************************************************************}

PROCEDURE LOADTARGET(VAR TARGL,TARGI,TARGM : INTEGER);
{This procedure loads the spectralink with the next
wavelength in the scan sequence.}

VAR
   X : INTEGER;

BEGIN
      X:=58;
      ANGSEND(X);
      ANGSEND(X);
      ANGSEND(X);
      X:=0;
      ANGSEND(X);
      X:=84;
      ANGSEND(X);
      X:=3;
      ANGSEND(X);
      X:=TARGL;
      ANGSEND(X);
      X:=TARGI;
      ANGSEND(X);
      X:=TARGM;
      ANGSEND(X);
      X:=58;
      ANGSEND(X);
      ANGSEND(X);
      ANGSEND(X);
END;

{*****************************************************************************}

PROCEDURE SENDGO;
{This procedure tells the spectralink to go to the target wavelength.}

VAR X: INTEGER;

BEGIN
      X:=58;
      ANGSEND(X);
      ANGSEND(X);
      ANGSEND(X);
      X:=0;
      ANGSEND(X);
      X:=71;
      ANGSEND(X);
      X:=0;
      ANGSEND(X);
      X:=58;
```

```
      ANGSEND(X);
      ANGSEND(X);
      ANGSEND(X);
      DELAY(5000);
END;

{*****************************************************************************}

PROCEDURE SLEWSTART(VAR SLEWANG : REAL);
{This procedure causes the spectrometer to slew to 10 Angstroms
below the scan start and then 10 Angstroms back to the scan start
so that backlash effects are eliminated.}

VAR
   X : INTEGER;
   TARG1,TARG2,TARG3 : INTEGER;

BEGIN
      NEXT:= SLEWANG;                  {IN ANG.}
      NEXT:= NEXT*200;                 {IN SCAN UNITS}
      BOX:= (NEXT/256/256);

      TARG3:=TRUNC(BOX);         {MSB}
      BOX:=TARG3*256;
      BOX:=BOX*256;

      NEXT:= NEXT-BOX;
      BOX:=NEXT/256;
      TARG2:=TRUNC(BOX);         {ISB}
      BOX:=TARG2*128;

      NEXT:= NEXT-2*BOX;
      TARG1:=ROUND(NEXT);        {LSB}

      LOADTARGET(TARG1,TARG2,TARG3);
      SENDGO;

      DELAY(1000);

      NEXT:=STARTANG;                  {IN ANG.}
      NEXT:= NEXT*200;                 {IN SCAN UNITS}
      BOX:= (NEXT/256/256);

      TARG3:=TRUNC(BOX);         {MSB}
      BOX:=TARG3*256;
      BOX:=BOX*256;

      NEXT:= NEXT-BOX;
      BOX:=NEXT/256;
      TARG2:=TRUNC(BOX);         {ISB}
      BOX:=TARG2*128;

      NEXT:= NEXT-2*BOX;
      TARG1:=ROUND(NEXT);        {LSB}
```

```
      LOADTARGET(TARG1,TARG2,TARG3);
      SENDGO;

END;

{*****************************************************************************}

PROCEDURE TIMESCAN;
{This procedure prints the C-10 value, averaged over 10 second intervals,
on the line printer.}

            BEGIN
            WRITELN('REMEMBER TO SET "MODE LPT1" PRIOR TO DOING THIS ');
            WRITELN;
            WRITE('INPUT YOUR FILENAME: ');
            READ(FILNAM);
            WRITELN(LST,FILNAM);
            ASSIGN(DATFILE,FILNAM);
            WRITELN;
            REWRITE(DATFILE);
            C10INIT;
            DELAY(30);
            KOUNT:=0;
            COUNT:=0;
            REPEAT
                  KOUNT:=0;
                  COUNT:=COUNT+1;
                  FOR I:=1 TO 10 DO
                  BEGIN
                  C10START;
                  KOUNT:=KOUNT+C10READ;
                  END;
                  KOUNT:=KOUNT/10;
                  RCOUNT:=COUNT*1.0;
                  WRITELN(LST,COUNT:5,'   ',KOUNT:10:0);
                  WRITE(DATFILE,RCOUNT,KOUNT);
             UNTIL KEYPRESSED;

             PORT[$1f0]:=2;
             DELAY(10);
             WRITELN('REMEMBER TO RESET "MODE LPT1:=COM1"');
             END;

{*****************************************************************************}

PROCEDURE STARTCOUNT;
{This procedure sets the control line to the C-10 such that it is always on.}

             BEGIN
             C10INIT;
             PORT[$1f0]:=2;
             DELAY(10);
             END;

{*****************************************************************************}
```

```
PROCEDURE READLAMBDA;
{This procedure reads the current wavelength of the spectrometer and
displays the value on the screen.}

      BEGIN
            TEST:=ANGREAD;
            WRITELN;
            WRITELN('THE WAVELENGTH IS  ',TEST:12:2);
            WRITELN;
            WRITELN('PRESS ANY KEY TO RETURN TO MENU');
            READ(KBD,CONTC);
      END;

{*****************************************************************************}

PROCEDURE OPTIONS;
{This procedure displays the options menu.}

  BEGIN
        CLRSCR;
        WRITELN;
        REPEAT
              WRITELN('      CHOOSE ONE OF THE FOLLOWING:');
              WRITELN;
              WRITELN('      1     SCAN WITH TIME');
              WRITELN('      2     START PHOTON COUNTER');
              WRITELN('      3     READ ABSOLUTE WAVELENGTH');
              WRITELN;
              WRITELN('      0     QUIT');
              READLN(RESPONSE);
        UNTIL RESPONSE IN [0..3];

        CASE RESPONSE OF
             0:ENDUP;
             1:TIMESCAN;
             2:STARTCOUNT;
             3:READLAMBDA;
        END;

    END;

{*****************************************************************************}

PROCEDURE LOADPARAM;
{This procedure enables the user to input the scan parameters.}

BEGIN
        REPEAT
          CLRSCR;
          ICOUNTIME:=ROUND(RCOUNTIME);
          WRITELN;
          WRITELN('THE SCAN PARAMETERS ARE: ');
          WRITELN;
          WRITELN('A:  LASER WAVELENGTH = ',LASERLINE:8:2,' ANGSTROMS');
```

```
            WRITELN;
            WRITELN('B:  SCAN START        = ',SCANSTART:8:2,' CM-1');
            WRITELN('C:  SCAN END          = ',SCANEND:8:2,' CM-1');
            WRITELN;
            WRITELN('D:  STEP              = ',SCANSTEP:8:2,' CM-1');
            WRITELN('E:  COUNT TIME        = ',ICOUNTIME:8,' SECONDS');
            WRITELN;
            IF ((SCANEND-SCANSTART)/SCANSTEP)>2000 THEN
            WRITELN('*****WARNING THIS ARRAY IS TOO BIG*****');
            WRITELN;
            WRITELN ('PRESS A,B,C,D,OR E TO CHANGE OR Q TO QUIT');
            READLN(ANS);

                IF (ANS='A') OR (ANS='a') THEN LASERLINE:=CHANGEPARAM
                ELSE
                IF (ANS='B') OR (ANS='b') THEN SCANSTART:=CHANGEPARAM
                ELSE
                IF (ANS='C') OR (ANS='c') THEN SCANEND :=CHANGEPARAM
                ELSE
                IF (ANS='D') OR (ANS='d') THEN SCANSTEP:=CHANGEPARAM
                ELSE
                IF (ANS='E') OR (ANS='e') THEN RCOUNTIME:=CHANGEPARAM
                ELSE
                IF (ANS<>'Q') AND (ANS<>'q') THEN BEGIN
                   WRITELN('ILLEGAL ENTRY');
                   ANS:='N';
                   LOADPARAM;
                   END

    UNTIL  (ANS='Q') OR (ANS='q');
END;

{*****************************************************************************}

FUNCTION FILEXIST(FILENAME: NAME): BOOLEAN;
{This function checks to see if there is already a datafile with
the same name as the new one.}

VAR
       FIL: FILE;

BEGIN
      ASSIGN(FIL,FILENAME);
      {$I-}
      RESET(FIL);
      CLOSE(FIL);
      {$I+}
      FILEXIST:=(IORESULT=0)
END;

{*****************************************************************************}

PROCEDURE RUNSCAN;
{This procedure carries out the scan by
 1) calculating an array of target wavelengths
```

```
2) initiating the scan
3) carrying out the scan
4) storing the data to disk.)

        BEGIN

        REPEAT

        WRITELN;
        WRITE('INPUT YOUR FILENAME: ');
        READ(FILNAM);
        NAMETEST:=FILEXIST(FILNAM);
        IF NAMETEST=TRUE THEN
        BEGIN
             WRITELN('OVERWRITE OLD ',FILNAM,' ?  Y/N');
             READLN(ANS3);
             IF (ANS3='Y') OR (ANS3='y') THEN NAMETEST:=FALSE;
        END
        UNTIL (NAMETEST=FALSE);

        ASSIGN(DATFILE,FILNAM);
        REWRITE(DATFILE);
        WRITE(DATFILE,LASERLINE,SCANSTART,SCANEND,SCANSTEP,RCOUNTIME);
        WRITELN;
        WRITELN('SLITS USED: ');
        READLN(SLITS);
        WRITELN;
        WRITELN('POWER USED: ');
        READLN(POWER);
        WRITE(DATFILE,SLITS,POWER);
        WRITELN;
        WRITELN;
        WRITELN('MOVE TO START WAVELENGTH AND ');
        WRITELN('HIT ANY KEY TO START SCAN');
        READ(KBD,CONTC);

        STARTCM:=LASERCM-SCANSTART;
        ENDCM:=LASERCM-SCANEND;
        STEPNUM:=ROUND((STARTCM-ENDCM)/SCANSTEP);
        WRITELN;
        WRITELN('STEPNUM = ',STEPNUM:6);
        FOR INC:= 0 TO STEPNUM DO
        BEGIN
             NEXT:=STARTCM-(SCANSTEP*INC); {IN CM-1}
             ANGVAL[INC]:=LASERCM-NEXT;
             NEXT:= 1E8/NEXT;              {IN ANG.}
             NEXT:= NEXT*200;              {IN SCAN UNITS}
             BOX:= (NEXT/256/256);

             TARGM[INC]:=TRUNC(BOX);       {MSB}
             BOX:=TARGM[INC]*128;
             BOX:=BOX*128;

             NEXT:= NEXT-4*BOX;
             BOX:=NEXT/256;
```

```
        TARGI[INC]:=TRUNC(BOX);          {ISB}
        BOX:=TARGI[INC]*128;

        NEXT:= NEXT-2*BOX;
        TARGL[INC]:=ROUND(NEXT);         {LSB}
    END;

    BEEPWARNING;
    C10INIT;
    PORT[$1f0]:=2;
    DELAY(10);
    SLEWSTART(SLEWANG);

    FOR I:= 0 TO STEPNUM DO
    BEGIN
        LOADTARGET(TARGL[I],TARGI[I],TARGM[I]);
        SENDGO;
        KOUNT:=0;
        FOR SECS:=1 TO ICOUNTIME DO
          BEGIN
          C10START;
          KOUNT:=KOUNT+C10READ;
          END;
        C10VAL[I]:=KOUNT;
        POWER:=0;
        FOR II:= 1 TO 5 DO
        BEGIN
            PORT[$702]:=(12 SHL 4)+2;
            PORT[$702]:=(12 SHL 4)+3;
            FOR ZZ:= 1 TO 6 DO
                BEGIN
                END;
            POWER:=POWER+((PORT[$701] AND $0F) SHL 8) + PORT[$700];
        END;
        LPOWER[I]:=POWER/5;

        WRITELN('STEP ',I:4,' OF ',STEPNUM:4,'   COUNT =   ',KOUNT:8:0);
    END;

    PORT[$1f0]:=2;
    DELAY(10);

    WRITELN;
    FOR COUNT := 0 TO STEPNUM DO
    BEGIN
    WRITE(DATFILE,ANGVAL[COUNT],C10VAL[COUNT],LPOWER[COUNT]);
    END;

    ENDBEEP;
    ENDUP;
    END;

{*****************************************************************************}

PROCEDURE DEFINESCAN;
```

```
{This procedure takes the user-input parameters and calculates
the start, end, step and time of the scan. The user may then change
the parameters, start the scan or quit.}

            BEGIN

            LASERCM:=1E8/LASERLINE;
            STARTANG:=LASERCM-SCANSTART;
            ENDANG:=LASERCM-SCANEND;
            SCANTIME:=(SCANEND-SCANSTART)/SCANSTEP*(ICOUNTIME+5);
            STARTANG:=1E8/STARTANG;
            SLEWANG:=STARTANG-10.0;
            ENDANG:=1E8/ENDANG;
            STEPANG:=(ENDANG-STARTANG)/(SCANEND-SCANSTART)*SCANSTEP;

            WRITELN;
            WRITE('SCAN IS ',STARTANG:8:1);
            WRITE('  TO ',ENDANG:8:1,'  ANGSTROMS.');
            WRITELN('  IT WILL TAKE ',(SCANTIME/60):8:1,' MINUTES.');
            WRITELN;
            WRITELN('STEP SIZE IS ',STEPANG:8:3,' ANGSTROMS');
            WRITELN;
            WRITELN('IS THIS OK Y/N OR Q TO QUIT ?');
            READLN (ANS2);
            IF (ANS2='N') OR (ANS2='n') THEN LOADPARAM;
            IF (ANS2='Y') OR (ANS2='y') THEN RUNSCAN;

            END;

{*****************************************************************************}

PROCEDURE SCAN;

BEGIN
     LOADPARAM;
     DEFINESCAN;
END;

{*****************************************************************************}

{.............................................................................}
{.........................MAIN PROGRAM.......................................}
{.............................................................................}
{This is the main menu display.}

BEGIN

     REPEAT
     CLRSCR;
       REPEAT
            WRITELN;
            WRITELN('      CHOOSE ONE OF THE FOLLOWING OPTIONS:');
            WRITELN;
            WRITELN('      1  SCAN');
            WRITELN('      2  OPTIONS');
```

```
            WRITELN('      0  QUIT');

            READLN(A);

        UNTIL (A IN [0..2]);

        CASE A OF
           0:ENDUP;
           1:SCAN;
           2:OPTIONS;
        END;

    UNTIL (A=0);
END.
```

Appendix D

Program to Calculate Surface Phonon Frequencies

```
C      THE ROUTINES CAME FROM THE BOOK
C      'NUMERICAL RECIPIES'
C      BY W H PRESS, B P FLANNERY, S A TEUKOLSKY
       AND W T VETTERLING
C      PUB BY CAMBRIDGE UNIVERSITY PRESS, 1986
C
C*************************************************************
C
C      THIS IS THE MAIN PROGRAMME
C
C*************************************************************
C
       DOUBLE PRECISION X,R,ROH0,ROH1,ROH2,ROH3,FREQ0,FREQ1,
      *FREQ2,FREQ3
       DIMENSION FREQ0(51)
       DIMENSION FREQ1(51)
       DIMENSION FREQ2(51)
       DIMENSION FREQ3(51)
       DIMENSION R(51)
C
       DO 50 J=1,50
       R(J)=J*10.0D00
       X=R(J)*2.0**0.5*3.1415*4.33/4880.0
C
       ROH0=-1.0*BESSK1(X)*BESSI0(X)/(BESSK0(X)*BESSI1(X))
       FREQ0(J)=SQRT(268.7*268.7*(12.85-ROH0)/(10.88-ROH0))
C
       ROH1=(-1.0*BESSK(2,X)/BESSK1(X)+1.0/X)/
      *(BESSI(2,X)/BESSI1(X)+1.0/X)
       FREQ1(J)=SQRT(268.7*268.7*(12.85-ROH1)/(10.88-ROH1))
C
       ROH2=(-1.0*BESSK(3,X)/BESSK(2,X)+2.0/X)/
      *(BESSI(3,X)/BESSI(2,X)+2.0/X)
       FREQ2(J)=SQRT(268.7*268.7*(12.85-ROH2)/(10.88-ROH2))
C
   50 CONTINUE
C
C*SELECT GRAPHICAL OUTPUT DEVICE
C
       WRITE (2,10)
       READ (1,89) N
       IF (N.EQ.1) THEN
        CALL B1302
        ELSEIF (N.EQ.2) THEN
        CALL T4010
        CALL PICCLE
        ELSEIF (N.EQ.3) THEN
        CALL HP747
        CALL CHASWI(1)
       ENDIF
   89 FORMAT (I1)
   10 FORMAT (`TYPE 1 FOR BENSON, 2 FOR T4010, 3 FOR HP`)
```

```
C
C*INITIALISE NAG GRAPHICS
C
      CALL J06WAF
C
C*MAP USER DATA REGION ONTO PLOTTING SURFACE
C
      CALL J06WBF (0.0D0, 0.5D3, 2.60D2, 3.00D2, 1)
C
C*REDUCE PLOT
C
      CALL J06WCF (0.0D0, 1.0D0, 0.0D0, 1.0D0)
C
C*PUT TICK MARKS IN BORDER
C
      CALL J06AFF (5.0D1,0.1D0)
C
C*SCALE CHARACTERS UP BY 1.5
C
      CALL J06XGF (1.5D0,1.5D0)
C
C*LABEL X AXIS
C
C      CALL J06AJF (1,'RADIUS IN A. ')
C
C*LABEL Y AXIS
C
C      CALL J06AJF (2,'SURFACE PHONON FREQ. ')
C
C*PLOT
C
      IFAIL=0
      CALL J06CAF(R,FREQ0,50,1,IFAIL)
      IF (IFAIL.NE.0) WRITE (4,*) 'ERROR IN PLOT ROUTINE'
C
      IFAIL=0
      CALL J06CAF(R,FREQ1,50,1,IFAIL)
      IF (IFAIL.NE.0) WRITE (4,*) 'ERROR IN PLOT ROUTINE'
C
      IFAIL=0
      CALL J06CAF(R,FREQ2,50,1,IFAIL)
      IF (IFAIL.NE.0) WRITE (4,*) 'ERROR IN PLOT ROUTINE'
C
C*TERMINATE GRAPHICAL OUTPUT
C
      CALL J06WZF
C
      STOP
      END
```

```
C
C*****************************************************************
C
C     THESE ARE THE FUNCTIONS
C
C*****************************************************************
C
      FUNCTION BESSI0(X)
C
      DOUBLE PRECISION Y, P1, P2, P3, P4, P5, P6, P7,
     *Q1, Q2, Q3, Q4, Q5, Q6, Q7, Q8, Q9

C
      DATA P1, P2, P3, P4, P5, P6, P7/1.0D00, 3.5156229D00,3.0899424D00,
     *1.2067492D00, 0.2659732D00, 0.360768D-01, 0.45813D-02/
      DATA Q1,Q2, Q3, Q4, Q5, Q6, Q7, Q8, Q9/0.39894228D00,
     *0.1328592D-01, 0.225319D-02, -0.157565D-02, 0.916281D-02,
     *-0.2057706D-01, 0.2635537D-01, -0.1647633D-01, 0.392377D-02/
C
      IF (ABS(X).LT.3.75) THEN
        Y=(X/3.75)**2
        BESSI0=P1+Y*(P2+Y*(P3+Y*(P4+Y*(P5+Y*(P6+Y*P7)))))
      ELSE
        AX=ABS(X)
        Y=3.75/AX
        BESSI0=(EXP(AX)/SQRT(AX))*(Q1+Y*(Q2+Y*(Q3+Y*(Q4+Y*(Q5+Y*(
     *  Q6+Y*(Q7+Y*(Q8+Y*Q9)))))))
      ENDIF
      RETURN
      END

C
C*****************************************************************
C
      FUNCTION BESSK0(X)
C
      DOUBLE PRECISION  Y, P1, P2, P3, P4, P5, P6, P7,
     *Q1, Q2, Q3, Q4, Q5, Q6, Q7
C
      DATA  P1, P2, P3, P4, P5, P6, P7/-0.57721566D00, 0.42278420D00,
     *0.23069756D00, 0.3488590D-01, 0.262698D-02, 0.10750D-03, 0.74D-05/
      DATA Q1, Q2, Q3, Q4, Q5, Q6, Q7/1.25331414D00, -0.7832358D-01,
     *0.2189568D-01, -0.1062446D-01, 0.587872D-02, -0.251540D-02,
     *0.53208D-03/
C
      IF (X.LE.2.0) THEN
        Y=X*X/4.0
        BESSK0=(-LOG(X/2.0)*BESSI0(X))+(P1+Y*(P2+Y*(P3+Y*(P4+Y*(
     *  P5+Y*(P6+Y*P7))))))
      ELSE
        Y=(2.0/X)
        BESSK0=(EXP(-X)/SQRT(X))*(Q1+Y*(Q2+Y*(Q3+Y*(Q4+Y*(Q5+Y*(
     *  Q6+Y*Q7))))))
      ENDIF
      RETURN
      END
```

```
C
C*********************************************************************
C
      FUNCTION BESSI1(X)
C
      DOUBLE PRECISION Y, P1, P2, P3, P4, P5, P6, P7,
     *Q1, Q2, Q3, Q4, Q5, Q6, Q7, Q8, Q9

C
      DATA P1, P2, P3, P4, P5, P6, P7/0.5D00, 0.87890594D00,
     *0.51498869D00, 0.15084934D00, 0.2658733D-01, 0.301532D-02,
     *0.32411D-03/
      DATA Q1,Q2, Q3, Q4, Q5, Q6, Q7, Q8, Q9/0.39894228D00,
     *-0.3988024D-01, -0.362018D-02, 0.163801D-02, -0.1031555D-01,
     *0.2282967D-01, -0.2895312D-01, 0.1787654D-01, -0.420059D-02/
C
      IF (ABS(X).LT.3.75) THEN
        Y=(X/3.75)**2
        BESSI1=X*(P1+Y*(P2+Y*(P3+Y*(P4+Y*(P5+Y*(P6+Y*P7))))))
      ELSE
        AX=ABS(X)
        Y=3.75/AX
        BESSI1=(EXP(AX)/SQRT(AX))*(Q1+Y*(Q2+Y*(Q3+Y*(Q4+Y*(Q5+Y*(
     *  Q6+Y*(Q7+Y*(Q8+Y*Q9))))))))
      ENDIF
      RETURN
      END
C
C*********************************************************************
C
      FUNCTION BESSK1(X)
C
      DOUBLE PRECISION  Y, P1, P2, P3, P4, P5, P6, P7,
     *Q1, Q2, Q3, Q4, Q5, Q6, Q7
C
      DATA  P1, P2, P3, P4, P5, P6, P7/1.0D00, 0.15443144D00,
     *-0.67278579D00, -0.18156897D00, -0.1919402D-01, -0.110404D-02,
     *-0.4686D-04/
      DATA Q1, Q2, Q3, Q4, Q5, Q6, Q7/1.25331414D00, 0.23498619D00,
     *-0.3655620D-01, 0.1504268D-01, -0.780353D-02, 0.325614D-02,
     *-0.68245D-03/
C
      IF (X.LE.2.0) THEN
        Y=X*X/4.0
        BESSK1=(LOG(X/2.0)*BESSI1(X))+(1.0/X)*(P1+Y*(P2+Y*(P3+Y*(P4+Y*(
     *  P5+Y*(P6+Y*P7))))))
      ELSE
        Y=(2.0/X)
        BESSK1=(EXP(-X)/SQRT(X))*(Q1+Y*(Q2+Y*(Q3+Y*(Q4+Y*(Q5+Y*(
     *  Q6+Y*Q7))))))
      ENDIF
      RETURN
      END
```

```
C
C*****************************************************************
C
      FUNCTION BESSK(N,X)
C
      IF (N.LT.2) PAUSE `BAD ARGUMENT N IN BESSK`
C
      TOX=2.0/X
      BKM=BESSK0(X)
      BK=BESSK1(X)
C
      DO 89 J=1,N-1
       BKP=BKM+J*TOX*BK
       BKM=BK
       BK=BKP
  89  CONTINUE
C
      BESSK=BK
      RETURN
      END
C
C*****************************************************************
C
      FUNCTION BESSI(N,X)
C
      PARAMETER(IACC=40, BIGNO=1.0E10, BIGNI=1.0E-10)
C
      IF (N.LT.2) PAUSE `BAD ARGUEMENT N IN BESSI`
C
      TOX=2.0/X
      BIP=0.0
      BI=1.0
      M=2*((N+INT(SQRT(FLOAT(IACC*N)))))
C
      DO 99 J=M,1,-1
       BIM=BIP+FLOAT(J)*TOX*BI
       BIP=BI
       BI=BIM
       IF (ABS(BI).GT.BIGNO) THEN
          BESSI=BESSI*BIGNI
          BI=BI*BIGNI
          BIP=BIP*BIGNI
       ENDIF
       IF (J.EQ.N) BESSI=BIP
   99 CONTINUE
C
      BESSI=BESSI*BESSI0(X)/BI
      RETURN
      END
```